Evaluation of structural integrity of steel components by non-destructive magnetic methods

Lukasz Mierczak

Wolfson Centre for Magnetics

School of Engineering

Cardiff University

A thesis submitted for the degree of

Doctor of Philosophy

April 2015

Declaration

This work has not previously been accepted in substance for any degree and is not concurrently submitted in candidature for any other degree.

Signed: (candidate)   Date: 27/04/2015

Statement 1

This thesis is being submitted in partial fulfilment of the requirements for the degree of PhD.

Signed: (candidate)   Date: 27/04/2015

Statement 2

This thesis is the result of my own independent work/investigation, except where otherwise stated. Other sources are acknowledged by explicit references.

Signed: (candidate)   Date: 27/04/2015

Statement 3

I hereby give consent for my thesis, if accepted, to be available for photocopying and for inter-library loan, and for the title and summary to be made available to outside organisations.

Signed: (candidate)   Date: 27/04/2015

Acknowledgements

I would like to express my sincere gratitude to my supervisor Prof. David Jiles for providing me with an opportunity to pursue research at Cardiff University and for his continuous guidance and motivation. I would also like to express my sincere appreciation to my second supervisor Dr Yevgen Melikhov for his invaluable support, encouragement and contribution throughout this study. I am grateful to my third supervisor Dr Jeremy Hall for his essential help and advice.

I am thankful to all my friends and colleagues from Wolfson Centre for Magnetics for many insightful discussions and memorable time.

I would like to acknowledge my industrial sponsors AgustaWestland and Sperry Rail for their financial and technical support for this research.

Finally, I would like to dedicate this thesis to my family, my wife Marta and daughter Natalia, my parents Adam and Halina, and my sister Monika. I will be forever grateful for your love, support and belief in me.

Abstract

Magnetic non-destructive methods utilising the Magnetic Flux Leakage (MFL) and Magnetic Barkhausen Noise (MBN) phenomena are widely used in the evaluation of the structural integrity of steel components. The MFL method is effectively applied for in-service flaw monitoring of oil and gas pipelines, fuel storage tank floors and rails; whereas the MBN method, due to high sensitivity of Barkhausen emission to residual and applied stress, has become one of the most popular NDE tools for investigating this condition of steels. Despite the affirming research and successful applications, which helped these methods to gain acceptance as a viable non-destructive tools, there is still a requirement for establishing a quantitative links between magnetic and mechanical properties of steel which would enable their further understanding and optimisation.

In this thesis the applications of MFL and MBN methods for flaw and stress detection are analysed via analytical and numerical modelling.

A new model relating the MBN amplitude and stress for materials having different magnetostrictive behaviour under load is proposed and validated in the quantitative stress evaluation of different grades of steel. Moreover, a new method for determining depth dependence of stress from measured magnetic Barkhausen signals is presented. A complete set of newly derived equations describing the detected Barkhausen signals in terms of the actual emissions that are generated inside the material and how these appear when they propagate to the surface is given.

The results from finite element modelling of magnetic flux leakage signals above unflawed and flawed rails energised in various directions are presented. These results enabled to identify the most effective current injection procedure and optimise the probability of transverse flaw detection in the rail inspection. The agreement between modelled and measured electromagnetic signals indicating presence of transverse rail defects has been justified.

Table of Contents

Nomenclature

Greek Symbols

α	Domain coupling
γ	Coefficient of proportionality in stochastic model of Barkhausen Noise
δ	Skin depth
ε	Mechanical strain
θ	Angle between direction of stress and magnetisation
λ	Magnetostriction
μ	Magnetic permeability
μ_r	Relative permeability
μ_0	Permeability of free space
ν	Poisson's ratio
ρ	Electric charge density
σ	Mechanical stress
σ_a	Applied stress
σ_r	Residual stress
σ_e	Electrical conductivity
ϕ	Magnetic flux
ϕ_l	Flux linkage
χ	Magnetic susceptibility
χ'	Differential susceptibility
χ'_{Hc}	Maximum differential hysteretic susceptibility
χ'_{an}	Maximum differential anhysteretic susceptibility
ω	Frequency

Other Symbols

a	Domain density
b, b'	Magnetostriction coefficients
B	Magnetic Flux Density
B_r	Remanence
d	Atomic lattice spacing

E	Young's modulus
H	Magnetic field
H_e	Effective magnetic field
H_{ex}	Exchange field
H_σ	Stress-equivalent field
H_c	Coercive field
I	Current
J	Current density
k_B	Boltzmann's constant
m	Magnetic moment
M	Magnetisation
M_s	Spontaneous magnetisation
M_{sat}	Saturation magnetisation
M_{an}	Anhysteretic magnetisation
M_{irr}	Irreversible magnetisation
M_{rev}	Reversible magnetisation
MBN_{pk}	Peak amplitude of Barkhausen Noise
MBN_{RMS}	Root-mean-square of Barkhausen Noise
MBN_{ppos}	Peak positon of Barkhausen Noise
MBN_{AREA}	Area under Barkhausen Noise envelope
t	Time
T	Temperature
T_c	Curie temperature
V	Voltage

Acronyms

ABBM	Alessandro, Beatrice, Bertotti and Montorsi
JSW	Jiles, Sipahi and Williams
MBN	Magnetic Barkhausen Noise
MFL	Magnetic Flux Leakage
XRD	X-ray diffraction

1. Introduction

1.1 Scope, motivation and contribution

Structural integrity of steel components is considered as one of the main concerns in the design and operating performance of railway and building systems, gears and transmissions, reactor pressure vessels and power plants, or any other types of systems which are subjected to stress during their service life. Applied and residual stresses, as well as the presence of defects are some of the main mechanical factors affecting this integrity and therefore their early detection and reliable evaluation are of great importance. This thesis focuses on contributing to two industrially accepted non-destructive magnetic methods commonly used in the structural integrity assessment, which are based on the relation between the Barkhausen emissions and stress (MBN method), and detection of magnetic flux leakage generated in the vicinity of defects (MFL method).

The main aims of this thesis include:

- Development of an analytical model capable of evaluating mechanical stress from the measured Barkhausen emissions
- Development of method for determining depth dependence of stress using magnetic Barkhausen noise measurements
- Optimisation of the transverse flaw detection in the rail inspection involving current injection

In order to meet the above aims both theoretical and experimental work has been carried out, which involved various magnetic measurements, as well as analytical and numerical modelling. This work was additionally supported by the industrial partners including AgustaWestland helicopter design and manufacturing company, and Sperry Rail Ltd the provider of rail flaw detection services.

The outcome of this thesis provides mathematical models and testing methodologies which are directly implementable in the currently performed structural integrity monitoring of steel components.

1.2   Organisation of the thesis

This thesis is organised into six chapters which cover theoretical and experimental aspects of the stress and flaw detection using Magnetic Barkhausen Noise and Magnetic Flux Leakage methods.

Chapter 2 introduces the physics of ferromagnetism and implementation of numerical methods in modelling of electromagnetic circuits comprising ferromagnetic materials using Finite Element Analysis.

Chapter 3 provides the insight into industrial motivations for this research related to evaluation of integrity of steel components.

In **Chapter 4** a new model relating the MBN amplitude and stress for materials having different magnetostrictive behaviour under load is proposed and validated. The derivation of underlying equations is presented, followed by description and discussion on the verifying experimental procedure and results from MBN evaluation of surface hardened steel samples. The newly developed MBN model is applied to previously published results to demonstrate its generality. Moreover, a new method for determining depth dependence of residual stress from measured magnetic Barkhausen signals is proposed.

In **Chapter 5** the various aspects of detection of transverse rail defects using MFL method involving current injection are discussed and analysed. The underlying principles of generation and distribution of magnetic field within and around a current carrying conductor is given. Subsequently, the flaw detection methodology of induction sensing unit (ISU) currently applied by Sperry Ltd. in railway inspection is presented. The details of developed FEM model used for magnetic flux leakage analysis are described. This chapter also provides results on the distribution of magnetic flux leakage above various cases of flawed rails, as well as types of voltage signals recorded by inductive sensors during rail inspection involving alternative current injection procedures.

Chapter 6 summarises the achievements and conclusions from this research. The directions for future work are also discussed.

2.   Ferromagnetism

2.1   Introduction

This chapter introduces the physics of ferromagnetism by providing information on its origin on the atomic scale as well as the types of fundamental micromagnetic energies governing domain configuration in ferromagnetic bodies (Section 2.2). It also explains the mechanisms of the magnetisation processes and hysteretic behaviour of magnetic materials by describing the domain processes under influence of external magnetic field and mechanical stress (Sections 2.3 to 2.5). Section 2.6 is focused on the phenomenon of Magnetic Barkhausen Noise where detailed information regarding its origin is given. The previously developed analytic models characterising the stochastic nature of Barkhausen jumps are also presented. Section 2.7 describes the basis and implementation of numerical methods in modelling of electromagnetic circuits comprising ferromagnetic materials using Finite Element Analysis. Finally, the introduced ferromagnetic phenomena and their physical models are summarised in Section 2.8.

2.2   Micromagnetic theory

The distinctive feature of ferromagnetic metals such as iron, nickel and cobalt is their unfilled 3d atomic subshell leading to unpaired electron spins on neighbouring atoms [1]. The atomic magnetic moments associated with these unpaired electron spins are aligned in regions, called magnetic domains [2]. In each such domain, all magnetic moments **m** are aligned parallel to each other, giving rise to a spontaneous magnetisation **Ms** even in the absence of external magnetic field. This spontaneous magnetisation **Ms** is equal to sum of all magnetic moments **m** within a domain divided by its volume V_d, which can be written as:

$$\mathbf{Ms} = \frac{\Sigma \mathbf{m}}{V_d} \qquad\qquad (2.1)$$

The value of **Ms** is the same within all magnetic domains but its orientation varies from one domain to another. The total net magnetisation **M** for a given magnetic domain configuration is the vector sum of all the local spontaneous magnetisation vectors **Ms**. Therefore the net magnetisation over the total volume of ferromagnetic material will depend on the relative orientation of magnetic domains within it.

An example representation of magnetic domain structure in silicon steel (3% Si-Fe) is shown in Fig. 2.1.
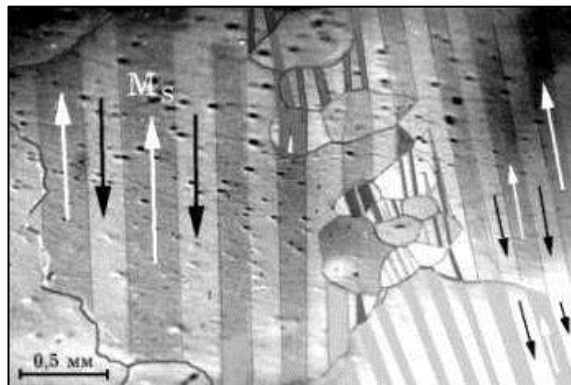

Fig. 2.1 Illustrative representation of domain structure in silicon steel (3% Si-Fe) [3].

Due to thermal agitation, the atomic magnetic moments can lose their ferromagnetic order at a certain temperature, which is called the Curie temperature [4]. This temperature is a material dependent property and for iron, nickel and cobalt

it is 770°C, 358°C and 1130°C respectively [5]. Above these temperatures they become paramagnetic materials.

The modern theory of magnetic domains is based on total magnetic free energy E_{tot} equation proposed by Landau and Lifshitz in 1935 [6]. For a crystal of magnetic material this total energy combines five main contributing components: exchange energy E_{ex}, magnetocrystalline anisotropy energy E_k, magnetostatic energy E_m, magnetoelastic energy E_λ and the energy associated with externally applied field E_H. There is also another sixth term, called domain wall energy E_{dw}, determined by energy balance between exchange and magnetocrystalline energies, which can be added as a component to the overall magnetic energy. Therefore the complete expression for the total magnetic free energy can be written as:

$$E_{tot} = E_{ex} + E_k + E_m + E_\lambda + E_H + E_{dw} \tag{2.2}$$

The effective domain structure of a material is the one minimizing the sum of these components called the magnetic Gibbs free energy of material. Each of the contributing energies is described in the following sub-sections.

I. Exchange energy

The exchange energy E_{ex} in ferromagnetic materials is closely related to the coupling of adjacent atomic magnetic moments and their tendency to align parallel to each other. In its simplest form this interaction energy per moment can be defined by Equation 2.3:

$$E_{ex} = -2J\boldsymbol{S_i} \cdot \boldsymbol{S_j} = -2JS^2 \cos \phi_S \tag{2.3}$$

where J is the exchange integral which is positive for ferromagnetic materials, $\boldsymbol{S_i}$ and $\boldsymbol{S_j}$ are the total spin angular momenta vectors of neighbouring atoms of the same magnitude and ϕ_S is the angle between them [5].

According to Equation 2.3 in order to minimise the exchange energy all the neighbouring magnetic moments within a ferromagnetic crystal body should be aligned parallel for all spatial directions in which the crystal can be magnetized.

II. Magnetocrystalline anisotropy energy

Magnetic properties of ferromagnetic single crystals demonstrate anisotropy with respect to crystallographic main axes. In other words the spontaneous magnetisation vectors tend to align along energetically favourable crystallographic directions. In the single crystal of body-centred cubic (bcc) iron we can distinguish three principal crystallographic directions:

- <100> which is the direction along the cube edges of the unit cell
- <110> being the direction along the diagonals of cubes faces
- <111> which is the direction along the diagonals of unit cell
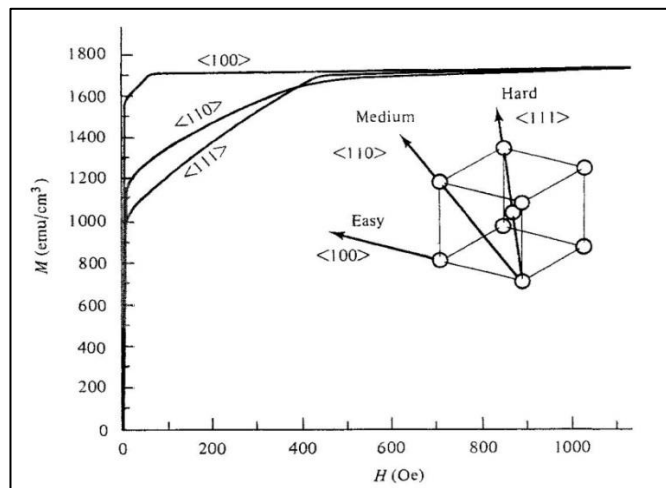
Fig. 2.2 Representation of effects of magnetocrystalline anisotropy energy in bcc iron on the magnetisation curves obtained along principal crystallographic directions [1].

It can be seen in Fig. 2.2 that when magnetic field is applied along the <100> direction magnetic saturation is reached at relatively low field strength. Therefore this crystallographic axis is called an 'easy magnetic direction'. In case of the <110> and <111> directions the field strengths needed to obtain saturation are progressively higher. Hence, they are called 'medium' and 'hard' magnetic crystallographic directions respectively.

The expression for the magnetocrystalline anisotropy energy in the bcc structure is given by:

$$E_k = K_1(\alpha_1^2\alpha_2^2 + \alpha_2^2\alpha_3^2 + \alpha_3^2\alpha_1^2) + K_2(\alpha_1^2\alpha_2^2\alpha_3^2) \tag{2.4}$$

where α_1, α_2, α_3 are the direction cosines of the magnetisation vectors with respect to the three easy cubic orthogonal axes, and K_1 and K_2 are the first and second order anisotropy coefficients. For bcc iron at room temperature the values of anisotropy coefficients are: $K_1=48kJ/m^3$ and $K_2=5kJ/m^3$ [5].

Basing on the Equation 2.4 it can be concluded that the magnetocrystalline anisotropy energy in bcc materials is minimized when all the magnetic moment vectors are aligned along one of the easy orthogonal axes of the cube.

III. Magnetostatic energy

The magnetostatic energy E_m arises when a magnetic moment is subjected to magnetic field. In the case where a ferromagnetic crystal is a single domain, spontaneously magnetized along the easy axis as shown in Fig. 2.3a, there is a formation of magnetic free poles on its ends which are the source of large demagnetizing field $\mathbf{H_d}$. This demagnetizing field can be described by the following equation:

$$H_d = -N_d\mathbf{Ms} \qquad (2.5)$$

where N_d is the shape dependent demagnetising factor and $\mathbf{Ms}$ is the spontaneous magnetisation within a domain.
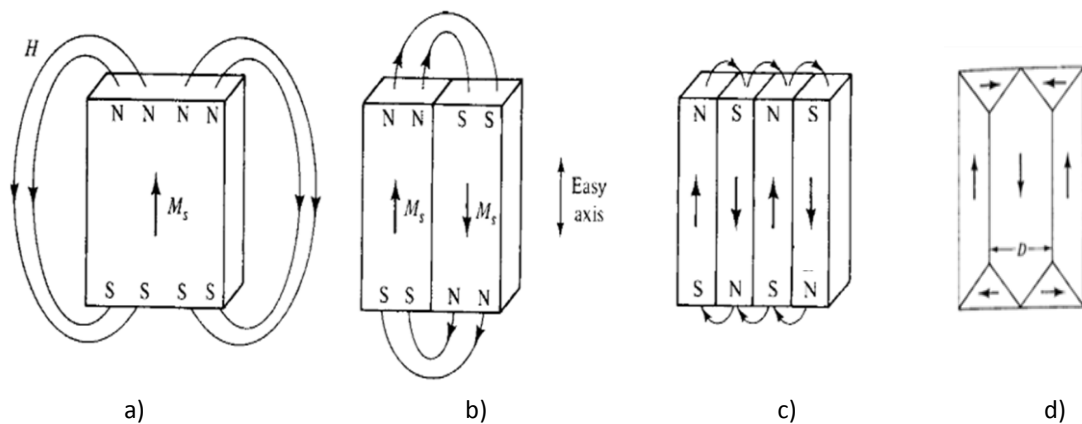

Fig. 2.3 Division of ferromagnetic crystal into domains. Only external H fields are shown [1].

For the single-domain crystal the magnetostatic energy E_m per unit volume of the magnetic dipoles of magnetisation **Ms** in their own demagnetizing field is given by:

$$E_m = -\mu_0 \int \boldsymbol{H_d} \, d\mathbf{Ms} = \mu_0 N_d \int \mathbf{Ms} \, d\mathbf{Ms} = \frac{\mu_0}{2} N_d \mathbf{M}_s^2 \qquad (2.6)$$

where μ_0 is the permeability of free space ($4\pi*10^{-7}$ H/m), $\mathbf{H_d}$ is the demagnetising field, N_d is the demagnetising factor and **Ms** is the spontaneous magnetisation within domain.

This energy can be reduced by nearly factor of 2 if the crystal is divided into two domains magnetized anti-parallel as shown in Fig. 2.3b, because it decreases the demagnetizing field by bringing the south and north poles closer to one another. Simultaneously if the domain structure splits into four domains as shown in Fig. 2.3c, the magnetostatic energy will be reduced to about one fourth of its initial energy [1]. However this division cannot continue indefinitely because the transition regions between domains, called domain walls, have additional energy associated with them which adds to the total magnetic energy of the system. The magnetostatic energy is minimized by creation of additional domains, called closure domains, which allow enclosing the magnetic flux within the material and consequently eliminates magnetic free poles. This type of structure is shown in Fig. 2.3d.

In bcc iron the magnetic moments in closure domains are aligned perpendicular to the antiparallel main domains in order to minimise the anisotropy energy. In such a configuration all the domains are oriented along one of the three easy orthogonal axes of the bcc crystal unit. However there is an increase in anisotropy and exchange energy associated with the 90° and 180° domain walls. Nevertheless this additional domain wall energy is less than the reduction in total magnetostatic energy of the system. The width and energy of domain walls are discussed in the following sub-section IV.

There is also another additional energy related to existence of closure domains called magnetoelastic energy E_λ. In iron the closure domains would be strained magnetostrictively as shown by dotted lines in Fig. 2.4b, if not restrained by the main domains on either side [1].
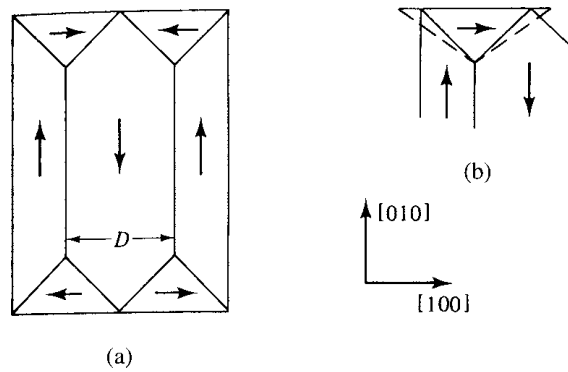
Fig. 2.4. Closure domains of cubic crystal in iron [1].

The magnetoelastic energy stored in the closure domains is proportional to their volume. Therefore the domain structure will split into given number of main and closure domains for which the sum of magnetoelastic and domain wall energies becomes a minimum. The concept of magnetoelastic energy in ferromagnetic crystal is further discussed in sub-section V.

IV. Domain wall energy

Magnetic domains in ferromagnetic materials are separated by transition regions, called domain walls, where the magnetic moments undergo reorientation from one crystallographic direction to another. The existence of these transition regions was first suggested by Bloch [7]. The Bloch wall commonly refers to a 180° domain wall which separates two domains of antiparallel magnetisation. The structure of this type of domain wall is shown in Fig. 2.5.
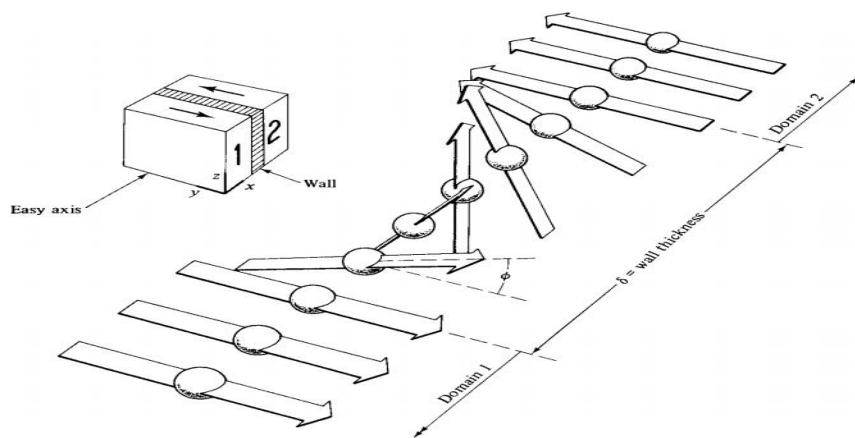

Fig 2.5 Structure of a 180˚ domain wall (Bloch wall) [1].

The total energy E_{dw} of Bloch wall per unit area is the sum of its exchange and anisotropy energies given by Equation 2.7:

$$E_{dw} = \frac{\mu_0 \xi \boldsymbol{m}^2 \pi^2}{l_{dw} d} + K_1 l_{dw} \qquad (2.7)$$

where μ_0 is the permeability of free space, ξ is the interaction between nearest magnetic moments, $\boldsymbol{m}$ is the individual magnetic moment, d is the lattice spacing, l_{dw} is the thickness of the domain wall being the product of number of magnetic moments n in domain wall and lattice spacing a (l_{dw}=nd) and K_1 is the anisotropy constant.

From Equation 2.7 it can be seen that if the exchange energy (first component in equation) is dominant then energy is minimised at a large domain wall width l_{dw} whereas if the anisotropy energy is dominant then energy is minimised at small domain wall thickness l_{dw} [5]. The effective domain thickness will be then determined by the energy balance between those two energies.

V. Magnetoelastic energy

The magnetoelastic energy in a ferromagnetic body is related to the presence of strain in its domain structure. The existing strain can originate from the following sources:

- spontaneous strain caused by ordering of the atomic magnetic moments when the ferromagnetic material is cooled through its Curie temperature. In such a case the spontaneous magnetisation appears within the domains and with it an associated spontaneous strain e and spontaneous magnetostriction λ_0 (as shown in Fig. 2.6b). The relation between these two measures is given by Equation 2.8:

$$\lambda_0 = \frac{e}{3} \qquad (2.8)$$

a) Disordered

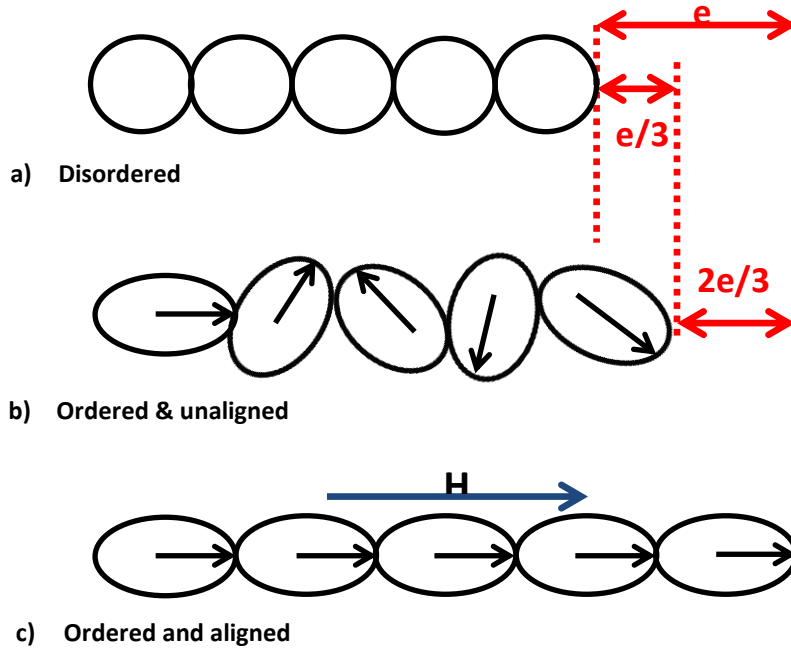b) Ordered & unaligned

c) Ordered and aligned

Fig 2.6 Schematic diagram illustrating the magnetostriction in: a) disordered paramagnetic state, b) demagnetised ferromagnetic state, c) ferromagnetic state magnetised to saturation (image reproduced from [5]).

- field induced strain which can be considered in terms of realignment of strained domains each of which has saturation magnetostriction λ_s of ferromagnetic material in which all magnetic domains are aligned parallel to the magnetic field direction as shown in Fig. 2.6c. The relation between spontaneous strain e and saturation magnetostriction λ_s is as follows:

$$\lambda_s = \frac{2e}{3} \tag{2.9}$$

The saturation magnetostriction λ_s in a cubic single crystal is given by:

$$\lambda_s = \frac{3}{2}\lambda_{100}\left(\alpha_1{}^2\beta_1{}^2 + \alpha_2{}^2\beta_2{}^2 + \alpha_3{}^2\beta_3{}^2 - \frac{1}{3}\right) + 3\lambda_{111}(\alpha_1\alpha_2\beta_1\beta_2 + \alpha_2\alpha_3\beta_2\beta_3 + \alpha_3\alpha_1\beta_3\beta_1) \tag{2.10}$$

where α_1, α_2 and α_3 are the direction cosines of the magnetisation direction and β_1, β_2 and β_3 are the directions cosines of the strain direction with respect to the cube edges. λ_{100} and λ_{111} are the saturation magnetostriction constants in the [100] and [111] directions respectively. The values of magnetostriction coefficients for iron are as follows: $\lambda_{100} = 21*10^{-6}$ and $\lambda_{111} = -21*10^{-6}$ [5].

In case of saturation magnetostriction measured along magnetisation (field) direction Equation 2.10 can be further simplified to:

$$\lambda_s = \lambda_{100} + 3(\lambda_{111} - \lambda_{100})(\alpha_1^2\alpha_2^2 + \alpha_2^2\alpha_3^2 + \alpha_3^2\alpha_1^2) \qquad (2.11)$$

In iron with bcc structure the field induced strain is caused by motion of 90° domain walls and 90° domain magnetisation rotation. The 180° domain wall motion or 180° domain rotation do not produce any magnetostrictive change in dimensions [1].

- strain related to presence of residual or/and applied mechanical stress σ

The overall magnetoelastic energy E_λ for material with isotropic magnetostriction subjected to unidirectional stress is given by:

$$E_\lambda = -\frac{3}{2}\lambda_s\sigma cos^2\theta \qquad (2.12)$$

where λ_s is the isotropic saturation magnetostriction, σ is the uniaxial stress and θ is the angle between direction of stress and magnetisation **Ms**.

Based on Equation 2.12 it can be concluded that the magnetoelastic energy in randomly oriented multi-domain ferromagnetic material with positive magnetostriction is minimised when the magnetic moments are aligned along the unidirectional tensile stress axis. Consequently in the case of materials with negative magnetostriction the magnetoelastic energy is minimised when magnetisation **Ms** is perpendicular to the unidirectional tensile stress axis. The mechanism of reconfiguration of domain structure under influence of stress is further explained in Section 2.5.

VI. Energy associated with externally applied magnetic field

The energy associated with interaction between the spontaneous magnetization vectors **Ms** of magnetic domains and externally applied field **H** can be expressed by the following equation:

$$E_H = -\mu_0 \boldsymbol{H} \cdot \mathbf{Ms} = -\mu_0 H \mathrm{Ms} \cos \phi_{HM} \tag{2.13}$$

where μ_0 is the permeability of free space, **H** is the external magnetic field, **Ms** is the spontaneous magnetisation and ϕ_{HM} is the angle between the field and magnetisation vectors.

According to this equation the energy E_H is minimised when all magnetic moments within the ferromagnetic body are aligned in the direction of externally applied magnetic field **H**. The sum of fully aligned magnetic moments in ferromagnetic material is called saturation magnetisation **M$_{sat}$** and can be obtained under sufficiently high external magnetic field **H**. However before reaching this state the material undergoes a set of intermediate stages of magnetisation involving reversible and irreversible domain wall motion, and domain magnetisation rotation. A complete description of magnetisation processes of ferromagnetic materials subjected to external magnetic field is given in Section 2.3.

2.3   Magnetisation processes and magnetic hysteresis

Application of external magnetic field **H** causes a realignment of magnetic domains within a ferromagnetic body. The new field induced domain configuration is the one for which the total magnetic energy is a minimum. Therefore the particular domain structure depends on the strength and direction of magnetic field **H** at which the increase in total energy components such as exchange energy E_{ex}, magnetocrystalline anisotropy energy E_k and domain wall energy E_{dw} is balanced by the reduction of energy associated with an externally applied field E_H.

As shown in Fig. 2.7a the initial magnetisation process of ferromagnetic material, such as pure iron, under the influence of an external field **H** can be represented by the virgin magnetisation curve **B(H)** with three distinguishable sections related to the main magnetisation stages.

The particular stages of initial magnetisation process can be described as follows:

I.   Reversible domain wall motion at low field values. In this stage the energetically favourable domains with magnetisation directions closest to

direction of applied field expand at the expense of neighbouring domains by means of translational domain wall motion (as shown in Fig. 2.7c). However in this phase when the external field is removed the magnetic domains return to their original demagnetised structure (Fig 2.7b).
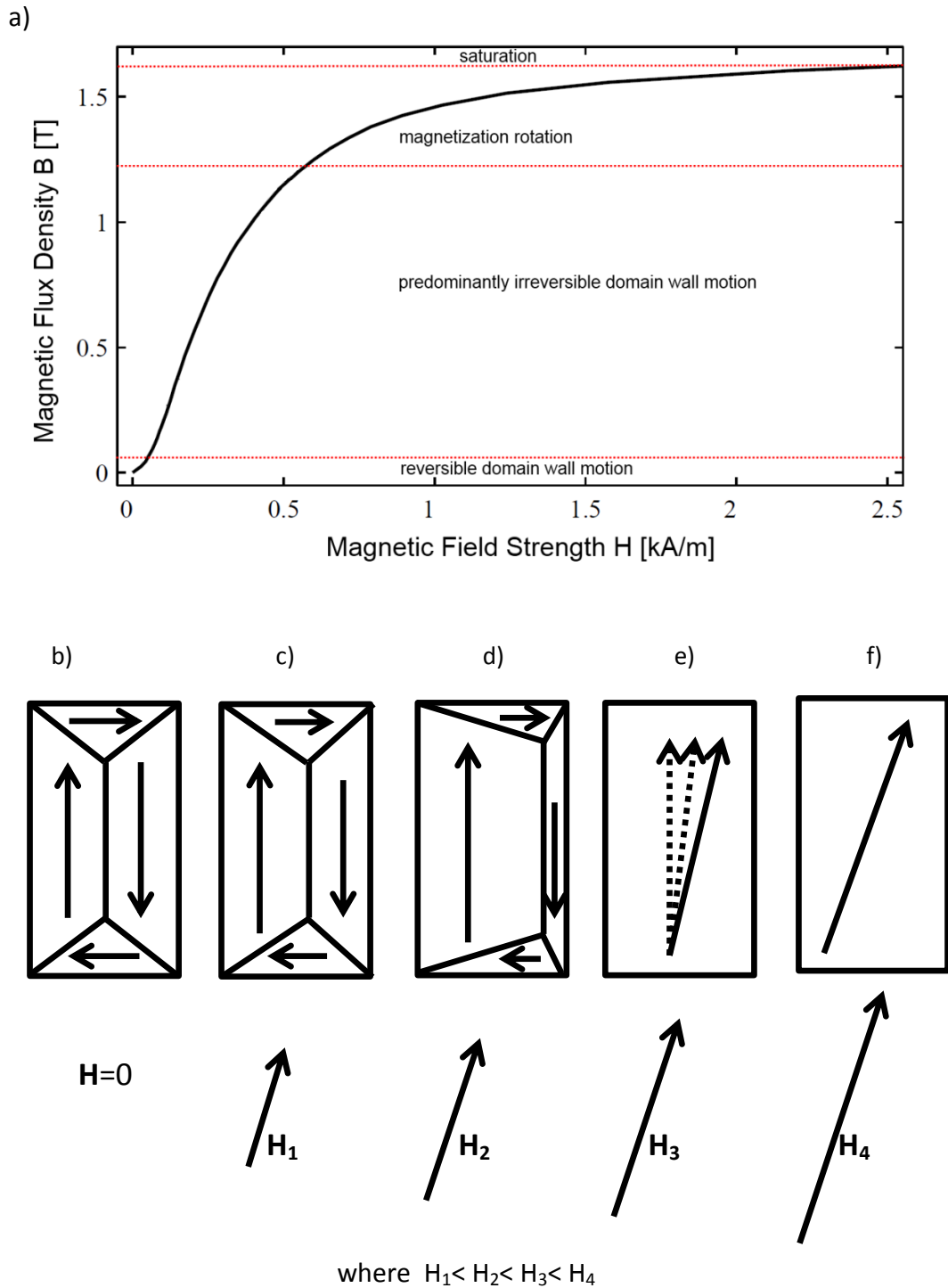

Fig. 2.7 Illustration of magnetisation process in ferromagnetic material: a) initial magnetisation curve for pure iron, b) domain structure in demagnetised state, c) reversible domain wall motion, d) irreversible domain wall motion, e) magnetisation rotation, f) ferromagnetic material in saturated state.

II.   Predominantly irreversible domain wall motion at moderate field values. Similarly to previous phase the magnetisation process takes place by domain wall motion and volume growth of energetically favourable domains (as shown in Fig. 2.7d). Nevertheless the main difference being here is that after field removal most of the magnetic domains will not revert to their initial demagnetised configuration; thus giving rise to remanent magnetisation.

III. In the final phase the magnetisation process is continued by rotation of domains magnetisation vectors towards the direction of applied field (as shown in Fig 2.7e). In iron and steels this mechanism requires high enough field to overcome the strong magnetocrystalline anisotropy and force the magnetisation vectors to rotate out of the easy crystallographic axes. Ferromagnetic material reaches its saturation when all magnetisation vectors are aligned along the direction of external field (Fig. 2.7f).

The total net magnetisation **M** is linked with external applied field **H** through a quantity called magnetic susceptibility χ which can be written as:

$$\boldsymbol{M} = \chi \boldsymbol{H} \qquad (2.14)$$

whereas the magnetic flux density **B** is related to magnetic field **H** by permeability μ given by:

$$\boldsymbol{B} = \mu \boldsymbol{H} \qquad (2.15)$$

Another important measure used to quantify the magnetic response of ferromagnetic materials to applied field is the relative permeability μ_r defined by:

$$\mu_r = \frac{\mu}{\mu_0} \qquad (2.16)$$

where μ is the permeability and μ_0 is the permeability of free space.

The relative permeability is closely related to susceptibility according to following equation:

$$\mu_r = \chi + 1 \qquad (2.17)$$

Finally the flux density can be defined in the following ways:

$$\boldsymbol{B} = \mu_0(\boldsymbol{H} + \boldsymbol{M}) = \mu_0\mu_r\boldsymbol{H} = \mu_0(1 + \chi)\boldsymbol{H} = \mu\boldsymbol{H} \qquad (2.18)$$

For paramagnetic and diamagnetic materials subjected to magnetic field the absolute values of susceptibility are of order -10^{-3} to 10^{-5} and consequently relative permeability is approximately 1 ($\mu_r \approx 1$). In case of ferromagnetic materials the magnitudes of maximum susceptibility and relative permeability are of much higher orders, for example $\mu_r \approx 2000$ for low carbon steel or $\mu_r \approx 100000$ for permalloy [1].

The initial magnetisation curve for ferromagnetic materials clearly demonstrates their strong non-linear response to magnetic field and magnetic saturation at high field levels. However there is another characteristic feature of this group of materials known as magnetic hysteresis. This phenomenon was first described by Ewing in 1890 [8]. The mechanism of hysteresis is closely related to the irreversible magnetisation processes. The microstructure of bulk polycrystalline soft magnetic materials, such as iron and steel, contains randomly distributed lattice imperfections, i.e. dislocations, grain boundaries, precipitates, second phase boundaries, which act as energy barriers and result in pinning of domain walls. Therefore in order to enable the domain wall to overcome these pinning sites a high enough external magnetic field has to be applied which will supply sufficient unpinning force.

The unpinning of a domain wall is an irreversible process as when the external field is removed the reverse domain wall motion is impeded and consequently domain walls do not return to their initial positions. This gives a rise to non-zero remnant magnetisation in the absence of external magnetic field. In order to cancel this remnant magnetisation and bring the ferromagnetic material back to demagnetised state a high enough reverse field needs to be applied. The other factors which can additionally contribute to hysteresis are the anisotropy and stress in the material [5]. The continuous magnetisation process can be represented by the major hysteresis loop, as shown for pure iron in Fig. 2.8a.

The distinctive subsequent phases of the magnetisation cycle in a ferromagnetic body can be described as following:

- The virgin curve illustrates the initial magnetisation process under external applied field. This phase starts from the demagnetised state where magnetic

domains are randomly oriented and consequently net magnetization is zero. At the end of this process the material is magnetically saturated as all domains are aligned parallel to field direction. This is marked in Fig. 2.8a as saturation S.

- When reducing the field to zero, a considerable number of magnetic domains are still aligned hence the material retains substantial net magnetisation, which is depicted in Fig. 2.8a as remanent flux density **B$_r$**
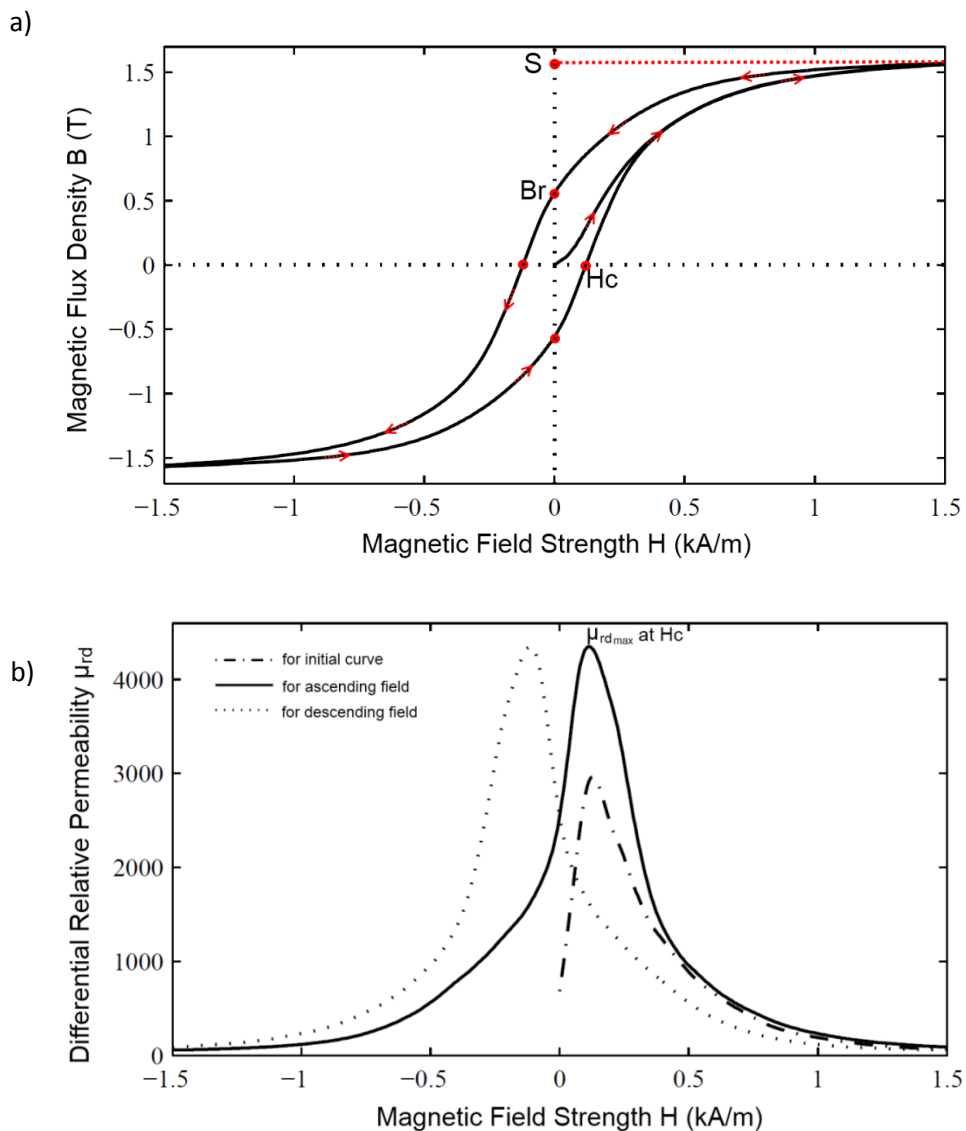
a)

b)

Fig. 2.8 Graphical illustration of magnetisation process in pure iron: a) initial magnetisation curve and hysteresis loop for pure iron; b) differential relative permeability as function of applied field in pure iron.

- When applying reverse field the magnetisation is reduced and reaches zero at amount of magnetic field corresponding to the coercivity of the system, which

is marked as H_c in Fig. 2.8a. At this point the material is brought back to zero net magnetisation state.

- When further increasing the strength of reverse field the material again approaches magnetic saturation in the opposite direction with magnetisation parallel to field direction

- Continuous application and reversal of external magnetic field results in repetition of the magnetisation cycle pattern where the value of flux density **B** changes with magnetic field strength **H** along the hysteresis curve

- The area enclosed by the **BH** loop corresponds to energy density loss per magnetisation cycle which is often referred to hysteresis loss

The dynamics of the magnetisation process along the hysteresis loop can be described in terms of differential relative magnetic permeability. This measure is defined by:

$$\mu'_r = \frac{1}{\mu_0} \frac{dB}{dH}$$

(2.19)

The graphical representation of differential magnetic permeability, as a non-linear function of applied field, corresponding to the initial magnetisation curve and hysteresis loop for pure iron is shown in Fig. 2.8b. When analysing the magnetic response of ferromagnetic materials to applied field it is more reliable to use differential relative permeability μ'_r or differential permeability μ' and corresponding differential susceptibility χ' rather than relative permeability μ_r, as the μ_r can become zero or infinite along the hysteresis loop at B_r and H_c respectively. Therefore in this work these quantities will be predominantly employed.

2.4   Anhysteretic magnetisation

As mentioned in the previous section the hysteresis and coercivity of isotropic soft ferromagnetic materials are associated mainly with the presence of lattice imperfections acting as pinning sites impeding the domain wall motion. Therefore it can be assumed that in the absence of all these imperfections the ferromagnetic material would be hysteresis free. In such a case the magnetic induction **B** and

magnetisation **M** would be single-valued functions of the magnetic field **H** and consequently the magnetisation process fully reversible. This type of magnetic behaviour is represented by the anhysteretic magnetisation curve as shown in Fig. 2.9.
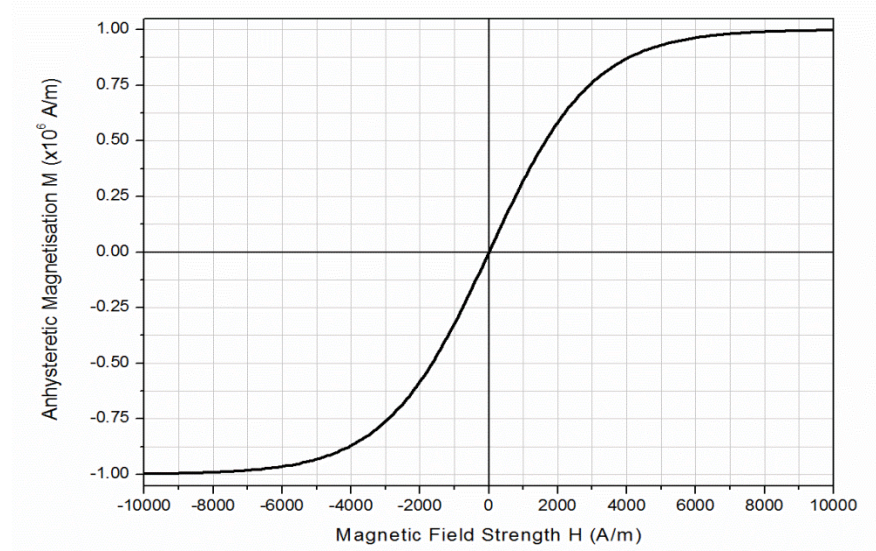

Fig. 2.9 Typical anhysteretic magnetisation curve for ferromagnetic material.

The anhysteretic magnetisation as a function of applied field for isotropic materials can be described by the modified Langevin equation proposed by Jiles in [9]:

$$M_{an} = M_{sat}\left[\coth\left(\frac{H+\alpha M}{a}\right) - \frac{a}{H+\alpha M}\right] \tag{2.20}$$

where **M**$_{an}$ is the anhysteretic magnetisation, **M**$_{sat}$ is saturation magnetisation, **H** is the applied field, α is the mean field parameter representing the interdomain coupling and a is a material parameter given by:

$$a = \frac{k_B T}{\mu_0 m} \tag{2.21}$$

where T is temperature, k_B is Boltzmann constant, μ_0 is permeability of free space and **m** is the magnetic moment of a typical domain.

In the Equation 2.20 the product of α and **M** represents the Weiss mean field and is added to applied field **H** to give the total effective field **H**$_e$.

Although the hysteresis free ferromagnetic materials don't exist in reality, the anhysteretic magnetisation curve can give a good approximation of real initial and hysteretic magnetisation curves in the following applied field regions:

- In the high field regions the initial magnetisation curve approaches the anhysteretic curve asymptotically therefore in those regions real magnetisation can be described fairly well by Equation 2.20

- For low coercivity materials the slope of hysteresis loops at the coercive point χ'_{Hc} is approximately equal to the slope of the anhysteretic curve at the origin χ'_{an} [5]. This can be written as:

$$\chi'_{Hc} \approx \chi'_{an} \qquad (2.22)$$

The above relation provides very useful information about the maximum differential hysteretic susceptibility, which corresponds to the slope of magnetisation curve at the coercive point, as the slope of the anhysteretic curve at the origin is quite linear and therefore both of these quantities can be expressed by:

$$\chi'_{Hc} \approx \chi'_{an} = \lim_{H,M \to 0} \left(\frac{d(M_{an}(H))}{dH} \right) = \frac{M_{sat}}{3a - \alpha M_{sat}} \qquad (2.23)$$

The above linear expression can be further developed to incorporate the effect of mechanical stress which will be shown in the following Section 2.5.

2.5 Domain structure and magnetisation under stress

Application of mechanical stress to ferromagnetic material affects the domain configuration through the mechanism called the magnetomechanical effect [10]. The resultant orientation of magnetic moments in a demagnetised stressed body is governed by combined influence of magnetocrystalline and magnetoelastic energies.

It was already discussed that in the demagnetised state of bcc structures, such as iron and steels, the magnetocrystalline anisotropy forces the magnetic moments within magnetic domains to be aligned along one of the energetically favourable cubic orthogonal directions with transition regions between domains being the 90° and 180° domain walls. When such a domain structure is subjected to stress it gains additional magnetoelastic energy. The previously given Equation 2.12 describing the magnetoelastic energy E_λ is rewritten below to provide a general instructive formula for describing the effect of applied stress on the energy of a ferromagnetic material:

$$E_\lambda = -\frac{3}{2} \lambda \sigma \cos^2 \theta \qquad (2.24)$$

where λ is the isotropic magnetostriction, σ is the uniaxial applied stress and θ is the angle between direction of stress and domain magnetisation **Ms**.

According to Equation 2.24 the response of the domain structure in the demagnetised state depends on the sign of product of magnetostriction and stress ($\lambda\sigma$) and therefore two types of situations can be considered:

- Type I: the sign of $\lambda\sigma$ is positive which is true for ferromagnetic materials with positive magnetostriction subjected to tensile stress or materials with negative magnetostriction subjected to compressive stress. In such cases domains magnetised along the stress axis are energetically favoured and will grow in volume on the expense of other domains
- Type II: the sign of $\lambda\sigma$ is negative which is valid when compressive stress is applied to material with positive magnetostriction or tensile stress is applied to material with negative magnetostriction. In such a situation domains magnetised at 90 degrees to stress direction are energetically favoured and expand on applications of stress at the expense of other domains

The above two types of magnetomechanical behaviour can be demonstrated by analysing the effect of unidirectional elastic stress applied to the simplified four domain structure of demagnetised ferromagnetic material with positive isotropic magnetostriction (λ>0) as shown in Fig. 2.10a. This structure is typical for bcc ferromagnetic materials and comprises:

- two antiparallel domains (α and α')magnetised along y-direction and separated by a 180° domain wall
- two closure domains (β and β') magnetised along x-direction and separated from the antiparallel domains by 90° domain walls.

The magnetomechanical effect for this structure can be explained as following:

- when tensile stress (σ>0) is applied along the y-direction (as shown in Fig. 2.10b) then the magnetic domains α and α' are energetically favoured by having their magnetisation along stress axis (λσ>0 & $\cos^2\theta=1$ thus E_λ is minimum). This causes a growth in volume of these two domains at the expense of domains β

and β' by means of 90° domain wall motion (as shown in Fig. 2.10b when comparing with initial structure in Fig. 2.10a)
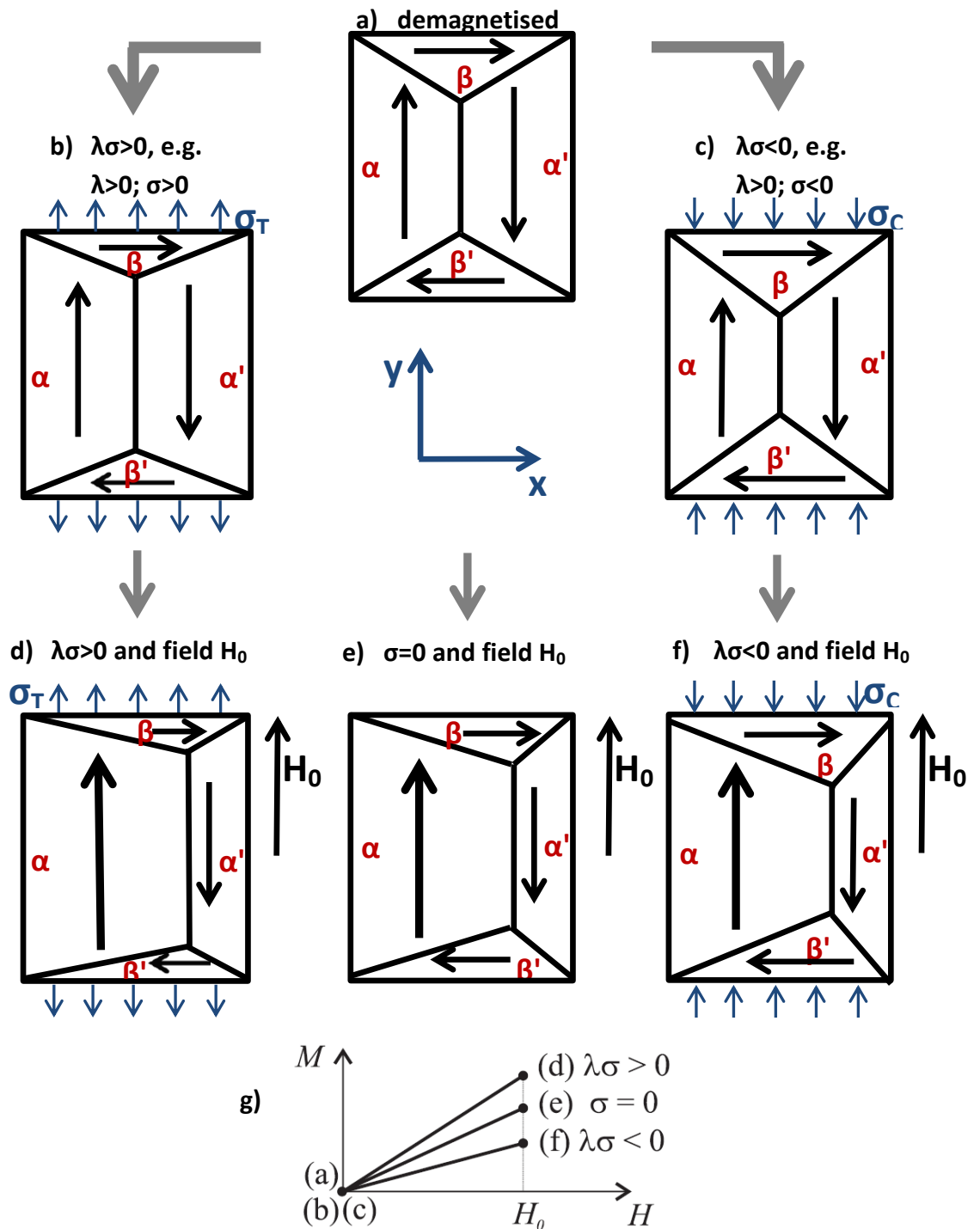

Fig. 2.10 a) to c) Schematic domain structures in unstressed and stressed bcc ferromagnetic material with no external field, d) to f) Schematic domain structures in unstressed and stressed bcc ferromagnetic material subjected to external field H_0, g) Illustrative plot of changes in magnetisation **M** with applied field H_0 in unstressed and stressed bcc ferromagnetic material.

- when compressive stress ($\sigma<0$) is applied along the y-direction (as shown in Fig. 2.10c) then the closure domains β and β' are energetically favoured by having their magnetisation at right angles to stress axis ($\lambda\sigma<0$ & $\cos^2\theta=0$ thus E_λ is minimised). This leads to expansion of these domains accompanied by shrinkage of domains α and α' through motion of 90° domain walls, which can be observed by comparing Figs. 2.10a and 2.10c.

The application of stress to bcc ferromagnetic structures leads only to motion of 90° domain walls, since the magnetoelastic energy of antiparallel domains separated by a 180° wall is equal (same value of $\cos^2\theta$), which is true even in cases where the stress axis is at non-zero angles to their magnetisation direction. Although the application of elastic stress causes a rearrangement of domain structure in a demagnetised ferromagnetic body, it does not change its total net magnetisation which remains zero (Fig. 2.10g).

The macro magnetic effect of elastic stress becomes visible when the stressed ferromagnet is subjected to external magnetic field **H**. The simplified domain structures in materials with both $\lambda\sigma>0$ and $\lambda\sigma<0$, subjected to magnetic field **H$_0$** which is coaxial with applied stress along the y-direction, are shown in Figs.2.10d and 2.10f. Additionally, the domain structure of stress-free material under the influence of magnetic field of the same strength is presented in Fig. 2.10e. In all three cases the antiparallel domains α which are magnetised along the field direction expand at the expense of other domains in order to minimise the magnetostatic energy. However the field modified effective areas of these domains can be seen to be different due to previously stress induced domain reconfigurations. This in consequence makes the net magnetisations of these structures to be also different where the highest value of **M** is obtained in material under tensile stress (for which $\lambda\sigma>0$) , moderate **M** is found for stress-free material and lowest **M** is achieved in material under compression (for which $\lambda\sigma<0$). This has been shown in the illustrative plot in Fig. 2.10g. The difference in magnetisation at a given field **H$_0$** for the studied domain structures can be accounted for the additional stress related component which is negative for $\lambda\sigma<0$ and positive for $\lambda\sigma>0$. The concept of this additional stress component, called the stress equivalent

field, was described by Sablik et al. in [11] where the following analytic formula was proposed:

$$H_\sigma = \frac{3}{2} \frac{\sigma}{\mu_0} \left(\frac{d\lambda}{dM}\right)_{\sigma,T} (cos^2\theta - v sin^2\theta) \tag{2.25}$$

where H_σ is the "stress equivalent field", σ is the mechanical stress, μ_0 is the permeability of free space, $\frac{d\lambda}{dM}$ is the slope of magnetostriction curve as function of magnetisation which also depends on stress and temperature, θ is the angle between direction of applied field H and stress axis, and v is Poisson's ratio.

Therefore the total effective field for stressed ferromagnetic material subjected to external field can be expressed by:

$$H_e = H + \alpha M + H_\sigma \tag{2.26}$$

where H is the applied field, αM the mean field and H_σ is the stress equivalent field.

The above expression for total effective field can be incorporated into equation 2.20 describing anhysteretic magnetisation as following:

$$M_{an} = M_{sat} \left[\coth\left(\frac{H + \alpha M + H_\sigma}{a}\right) - \frac{a}{H + \alpha M + H_\sigma}\right] \tag{2.27}$$

An example plot of anhysteretic magnetisations for ferromagnetic material with positive magnetostriction slope $\frac{d\lambda}{dM}$ at zero stress and under applied stresses of -/+200MPa is shown in Fig. 2.11.
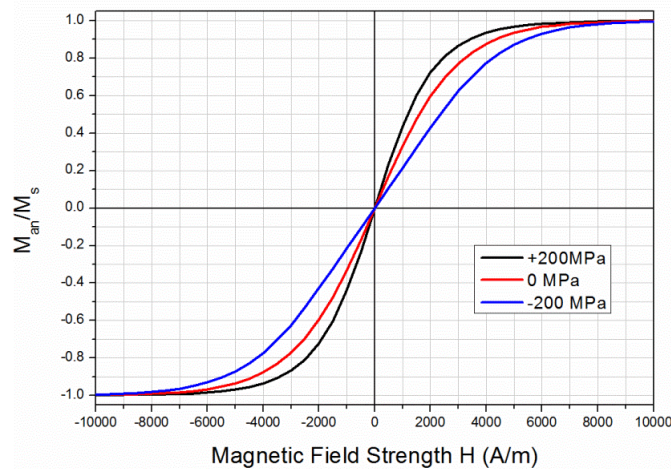

Fig. 2.11 Anhysteretic magnetisation curves for ferromagnetic material with positive magnetostriction at zero stress and under applied stresses of -/+200MPa.

The analytic Equation 2.25 for stress equivalent field can be further simplified by determining the derivative $\frac{d\lambda}{d\boldsymbol{M}}$. In a low magnetisation region this can be done by making some assumptions concerning the behaviour of λ with $\boldsymbol{M}$ proposed by Garikepati et al in [12]. In their work they suggested that magnetostriction at low magnetisation can be approximated by a single valued parabolic function of $\boldsymbol{M}$ which can be written as:

$$\lambda = b\boldsymbol{M}^2 \tag{2.28}$$

where λ is the average magnetostriction, $\boldsymbol{M}$ is magnetisation and b is the magnetostriction coefficient.

This in consequence leads to the following expression for the derivative at low magnetisation to be:

$$\frac{d\lambda}{d\boldsymbol{M}} = 2b\boldsymbol{M} \tag{2.29}$$

where the value of coefficient b can be obtained from the parabolic approximation of experimental values of averaged magnetostriction, as shown for 2% Mn pipeline steel in Fig.2.12b [13].

A similar approach of using a symmetrical parabolic function for representing the approximate dependence of magnetostriction on magnetisation in polycrystalline iron cobalt (FeCo+2%V) was made by Lorenz and Graham [14]. Their data is shown in Fig 2.13. Elsewhere the parabolic expression for $\lambda(\boldsymbol{M})$ has also been successfully used in modelling magnetic sensors [15,16].

The exact formula for the derivative $\frac{d\lambda}{d\boldsymbol{M}}$ from equation 2.29 can be incorporated into expression 2.25 for the stress equivalent field giving:

$$\boldsymbol{H_\sigma} = \frac{3b\sigma}{\mu_0}\boldsymbol{M}\left(cos^2\theta - vsin^2\theta\right) \tag{2.30}$$

In the case of coaxial stress and applied magnetic field this can be further reduced to:

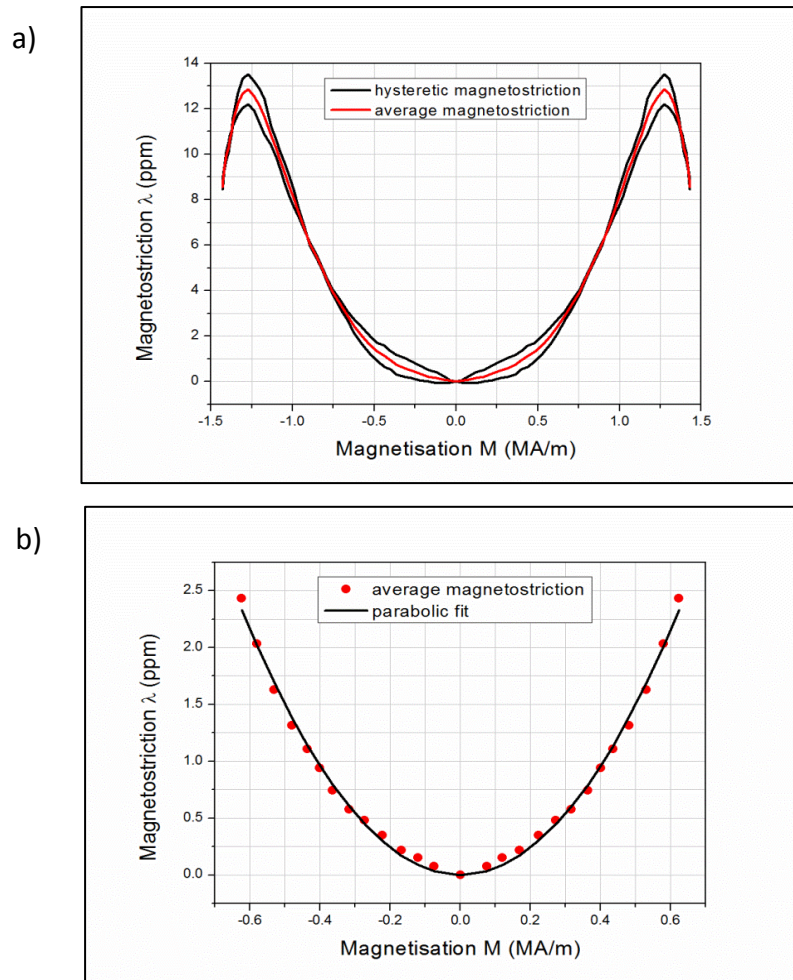$$\boldsymbol{H_\sigma} = \frac{3b\sigma}{\mu_0}\boldsymbol{M} \tag{2.31}$$

Fig. 2.12 a) Magnetostriction as function of magnetisation **M** in 2% Mn pipeline steel [13]; b) Average magnetostriction as function of **M** with parabolic approximation in low magnetisation region in 2% Mn pipeline steel.
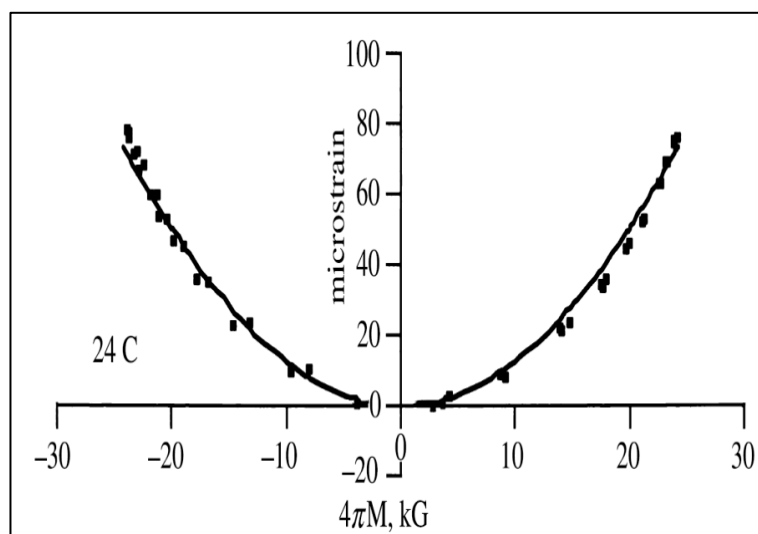

Fig. 2.13 Magnetostriction as function of magnetisation with parabolic approximation in polycrystalline iron cobalt (FeCo+2%V) [14].

The stress dependent anhysteretic magnetisation at low magnetisation regions can be therefore represented by:

$$M_{an} = M_{sat}\left[\coth\left(\frac{H+(\alpha+\frac{3b\sigma}{\mu_0})M}{a}\right) - \frac{a}{H+(\alpha+\frac{3b\sigma}{\mu_0})M}\right]$$ (2.32)

Finally the formula for differential anhysteretic susceptibility at origin χ'_{an} as function of mechanical stress σ applied along the magnetic field direction **H** can be written as:

$$\chi'_{an} = \frac{M_{sat}}{3a-(\alpha+\frac{3b\sigma}{\mu_0})\,M_{sat}}$$ (2.33)

The above expression provides useful information on the dependence of χ'_{an} on stress. Moreover, due to the previously introduced approximation in Equation 2.23, it indicates the relation between mechanical stress σ and maximum differential susceptibility χ'_{Hc} and differential permeability μ'_{Hc} corresponding to the slope of the hysteresis curve at the coercive point. Therefore it makes it possible to predict, describe and effectively evaluate the effects of mechanical stress by knowing the values of above mentioned measurable magnetic properties, i.e. χ'_{an}, χ'_{Hc} and μ'_{Hc}.

2.6   Magnetic Barkhausen Effect

The phenomenon known as the Barkhausen Effect was first observed and published by Barkhausen in 1919 [17]. In his work a piece of iron wound with a secondary coil connected to amplifier and loudspeaker was magnetised by a smoothly varying magnetic field, and as the magnetisation increased a series of clicks were heard over the loudspeaker due to small induced voltage pulses.

These voltage pulses were generated through the electromagnetic induction caused by discontinuous changes in magnetisation **M** (and consequently in the flux density **B**) of the iron specimen. Initially these discontinuities in induction were ascribed to rotation of domain magnetisation vectors but it is now known that the most significant factor contributing to Barkhausen emission is actually the discontinuous domain wall motion [18]. This experiment was one of the first confirmations for the theory of the existence of domains in ferromagnetic materials originally proposed by Weiss [2]. The

discontinuous changes in magnetisation can be seen under sufficient magnification of the magnetisation curve as shown in Fig. 2.14.
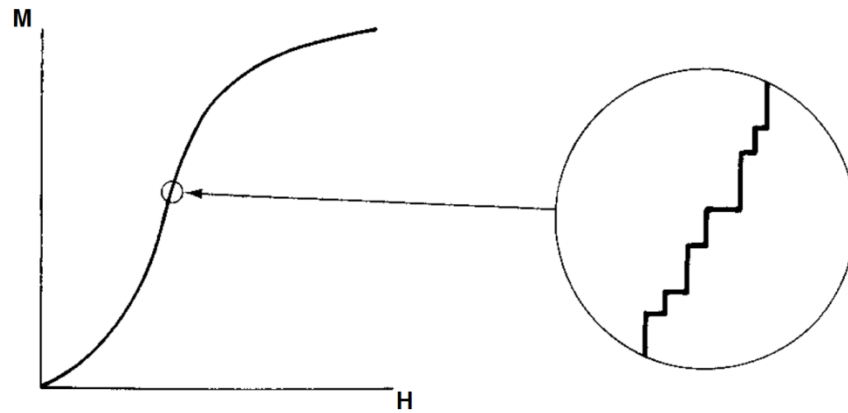

Fig. 2.14 Illustration of discontinuous changes in magnetisation obtained by magnifying a portion of magnetisation curve by factor of 10^9 [1].

2.6.1 Origin of Magnetic Barkhausen Effect

Subsequently it was found that there are three main domain processes which contribute to generation of Magnetic Barkhausen Noise (MBN), namely:

    I.   Irreversible discontinuous domain wall bowing

    II.   Irreversible discontinuous domain wall translation

    III.   Irreversible discontinuous domain rotation

Detailed description of these processes is given below:

I.   *Irreversible domain wall bowing*. At low fields domain wall bowing is a reversible process in which the wall expands like an elastic membrane under action of field. However this process becomes irreversible once the domain wall is sufficiently deformed that the expansion continues without further increase in field.

Irreversible domain wall bowing can take place if during this process the wall encounters pinning sites which prevent it relaxing once the field is removed [5]. This irreversible domain wall bowing can cause sudden changes in magnetisation and therefore generate Barkhausen Noise.

II.   *Irreversible domain wall motion.* This is the mechanism which contributes most to the generation of Barkhausen jumps. It takes place when domain walls break away from the pinning sites under sufficiently high magnetic field. In ferromagnetic materials the pinning sites are related to the presence of inclusions and localised residual microstresses resulting from crystal imperfections.

Inclusions can take many forms. They can be particles of a second phase in an alloy, carbide oxide or sulphide particles existing as impurities in a metal or they can be simply cracks or holes. From the magnetic point of view an "inclusion" in a domain is a region which has different spontaneous magnetisation from the surrounding material or no magnetisation at all [1]. Inclusions impede domain wall motion by reducing the local domain wall and magnetostatic energies which results in creation of local minimum in the energy potential. This takes place for example when domain wall bisects the inclusion as shown in Figs. 2.15b and Fig. 2.15d. When domain wall bisects the inclusion it redistributes the free poles associated with its presence (Figs. 2.15c and 2.15d) and the initial local magnetostatic energy is approximately halved, just as it is when a single domain crystal is divided into two oppositely magnetised domains [19].
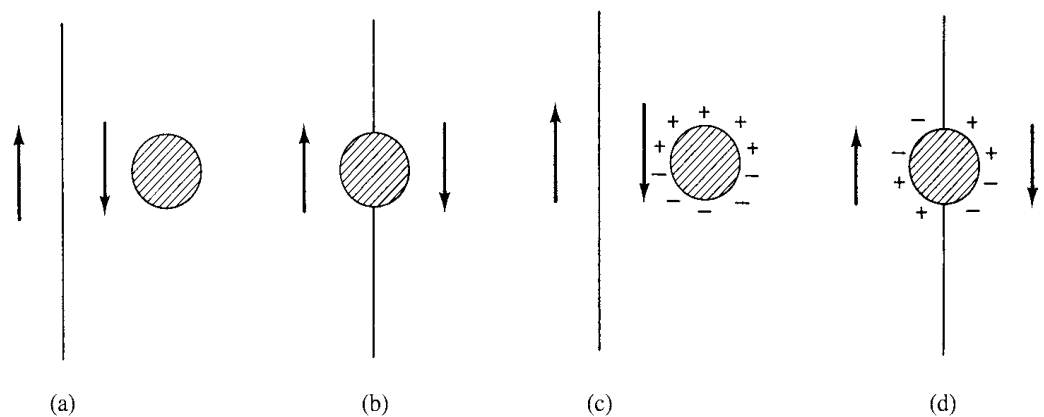

Fig. 2.15 Interaction of domain walls with inclusions [1].

The other effect of crystal imperfections is the generation of highly inhomogeneous regions of microstress within material [20]. These microstresses are caused by the presence of displacement fields in the vicinity of defects distorting the crystal lattice. The types of point and linear lattice defects giving rise to displacement fields can be described as follows:

a) interstitial impurity atoms (extra atoms within the lattice from an impurity element, for example carbon atoms in steel)

b) edge dislocations (which can be envisaged as extra crystallographic half planes along dislocation lines)

c) self-interstitial atoms (additional atoms within lattice)

d) vacancies (missing atoms in the lattice)

e) precipitate of impurity atoms (which for example in steels are related to alloying elements in steels, such as manganese, molybdenum, titanium, nickel, etc.)

f) vacancy type dislocation loop

g) interstitial type dislocations loop

h) substitutional impurity atom

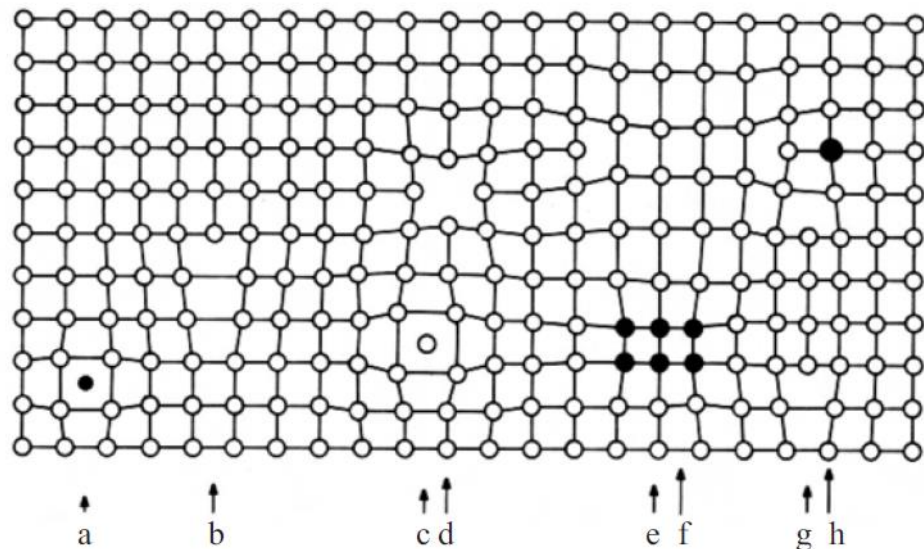All the above introduced types of point and linear lattice defects are shown in Fig. 2.16.

Fig. 2.16 Schematic overview of several types of crystal lattice defects [20].

An example illustration of the micro-stress distribution around an edge dislocation is presented in Fig. 2.17.
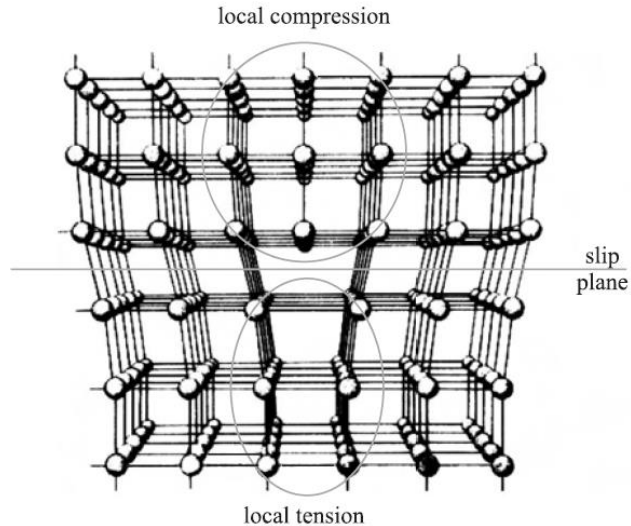
Fig. 2.17 Illustration of the micro-stress distribution around an edge dislocation [20].

In the polycrystalline materials microstresses can be also generated by planar defects such as grain and phase boundaries. Both of them occur at the interfaces between homogenous regions of material and can be characterised as follows:

- Grain boundaries separate neighbouring regions of different crystal lattice orientation. They can be considered as arrays of dislocations where the discontinuous change in lattice orientation takes place.

- Phase boundaries are the interfaces between regions of second phases and parent phase of the material. In phase boundaries the discontinuous change in both the crystal lattice itself as well as its orientation can occur. A typical example of phase boundaries can be observed between the austenite or/and martensite (secondary phases) and ferrite (parent phase) in steels.

The residual microstresses associated with crystal imperfections hinder the domain wall motion mostly because of their interactions with magnetostriction leading to fluctuations in magnetoelastic energy. Therefore the influence of local stress fields on behaviour of 90° walls (non-180° walls) and 180° wall is quite different. Motion of 90° walls changes the magnetisation direction in the volume swept out by the wall displacement. This in return creates a local magnetostrictive strain causing an elastic distortion within affected volume. This distortion interacts

with local microstress in such a manner that impedes the motion of domain walls as this would cause local increase in magnetoelastic energy [1]. The motion of 180° domain walls, on the other hand, alters the sense of magnetisation but not its direction and therefore no magnetostrictive strain occurs. Therefore in the case of 180° walls the effect of local microstress is the alteration in domain wall energy by adding to crystal anisotropy K_1 the local stress induced anisotropy K_σ given by:

$$K_\sigma = \frac{3}{2}\lambda_0\sigma_m \qquad (2.34)$$

where λ_0 is the spontaneous magnetostriction associated with the magnetic moments within domain wall and σ_m is the local microstress.

In summary, the presence of crystal lattice imperfections, in the form of inclusions and defect induced microstresses, gives rise to short-range fluctuations in magnetic energy. The resulting non-uniform energy distribution within the material can be represented by a magnetic energy E which fluctuates as a random function of position *x* as shown in Fig. 2.18a. The gradient of this energy dE/dx is plotted in Fig. 2.18b and represents the restoring force **F** on domain walls which arises when the wall position is not at the local energy minimum. This restoring force, if due to inclusion, arises from the change in magnetostatic energy. If caused by microstress, the restoring force is due to an increase in wall and magnetoelastic energy.

In the absence of an external magnetic field the domain wall occupies position 1 corresponding to local energy minimum thus no net force is imposed on the wall. In order to allow the domain wall to move reversibly to position 2 a magnetic field **H** of strength sufficient to counterbalance the restoring force **F₂** has to be applied. If the field was removed while in this range the wall would be restored to its initial position 1. But if instead the field strength is increased to exert force equal to **F₃** then domain will further propagate and make an irreversible jump to position 3. This is a Barkhausen jump. If the field is then reduced to zero, the wall will go back to point 4 which is the nearest local energy minimum. The wall motion thus causes hysteresis and remanence. When applying subsequently a reverse field **-H** of

corresponding force F_5 the wall moves to point 5 and further increase of **−H**, which applies force equal to F_6, causes another Barkhausen jump from position 5 to 6.
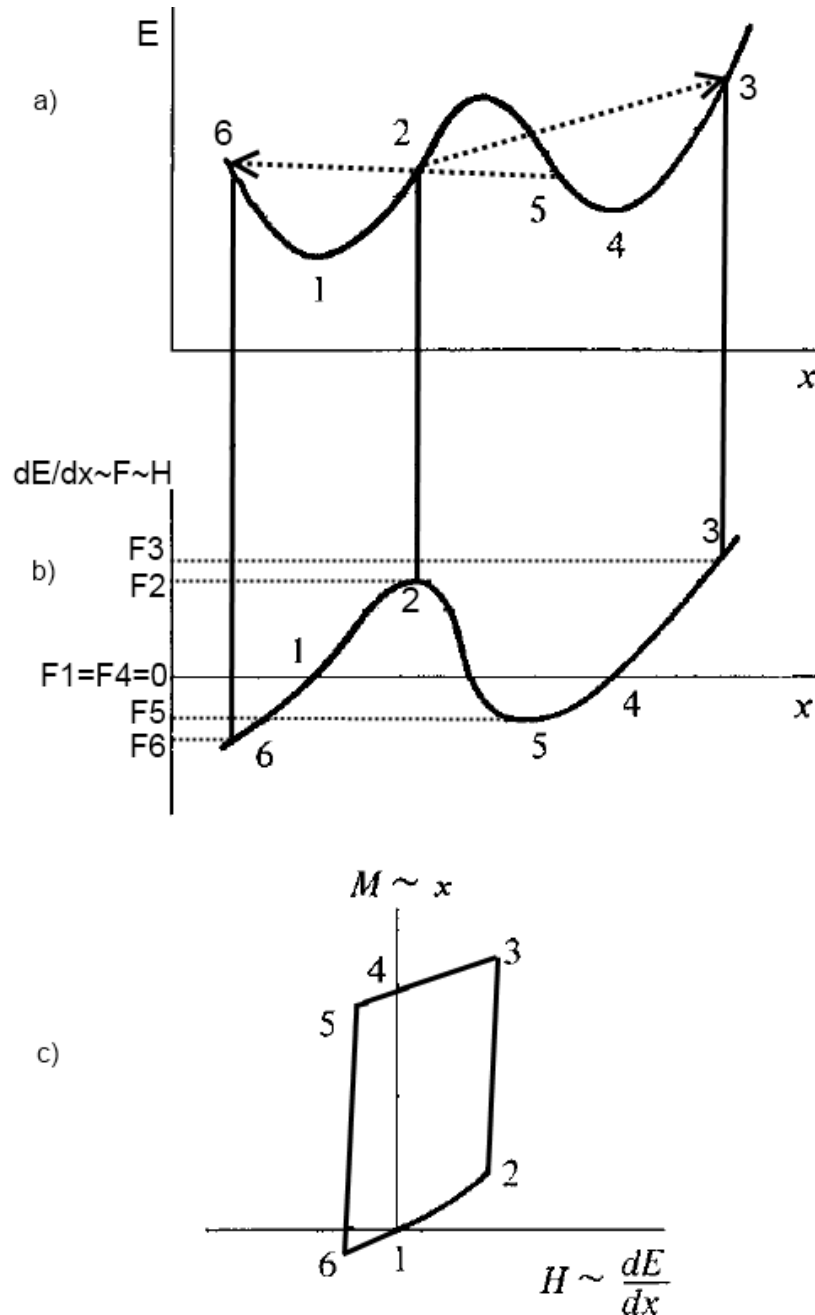

Fig. 2.18 Reversible and irreversible domain wall motion [1].

The mechanism of reversible and irreversible switching of domain wall position results in changes in magnetisation as each particular position x can be treated as representative of a level of **M**. The force required to drive domain walls to reach this magnetisation level is equal to the corresponding restoring force (dE/dx

gradient) and dependent on the external field **H**. Therefore the plot of position x (representing **M**) versus gradient dE/dx (representing **H**) takes the form of an elemental hysteresis loop as shown in Fig. 2.18c which refers only to one small region of a specimen and to a restricted range of **H**.

The macro hysteresis loop for the whole specimen is the sum of these elemental loops, of various shapes and sizes, summed over the total volume of the specimen [1]. Nevertheless this microscale example of **MH** loop in Fig. 2.18c illustrates the contribution of Barkhausen jumps, caused by irreversible domain wall motion, to bulk magnetisation under the influence of external field or any other stimulus able to exert sufficient unpinning force on domain walls (for example mechanical stress).

III. *Irreversible domain rotation.* At moderate to high magnetic field the magnetic moments within a domain rotate from their original easy axis to another easy crystallographic axis closest to the field direction. This occurs when energy associated with magnetic field overcomes the anisotropy energy. In such a case when field is removed the moments do not reverse to their initial orientation but remain aligned along the most recent easy axis they have been occupying. The switching of moments from one easy axis to another causes a sudden change in magnetisation and therefore generates a Barkhausen Noise emission.

The extent to which each of the irreversible domain processes contributes to total Barkhausen Noise emission depends on the rate of change of magnetisation d**M**/d**H** that it causes. In soft magnetic materials, such as iron and most steels, which have weak pinning sites the highest contribution to MBN comes from irreversible domain wall motion. In these types of materials the critical strength of field required to cause the walls to break away from pinning sites is relatively low. Therefore within a narrow range of low and moderate **H** the domain walls move with high velocity and can travel over long distance in a short time. The corresponding derivative d**M**/d**H** is relatively high and the strongest Barkhausen Effect can be observed at the highest slope of magnetisation curve which is located at the coercive point. The other contributing process of domain rotation takes place in relatively less frequent steps as each

requires quite high field strength. Thus in this stage of magnetisation process the average rate of change in **M** with **H** is lower and consequently less MBN is being generated when comparing with MBN due to domain wall motion. The relation between the magnitude of MBN and the magnetisation dynamics of the irreversible processes can be clearly demonstrated by plotting the typical Barkhausen emission in form of voltage bursts with the corresponding magnetisation hysteresis loop and differential permeability d**M**/d**H** as a function of applied field **H** as shown in Fig. 2.19.
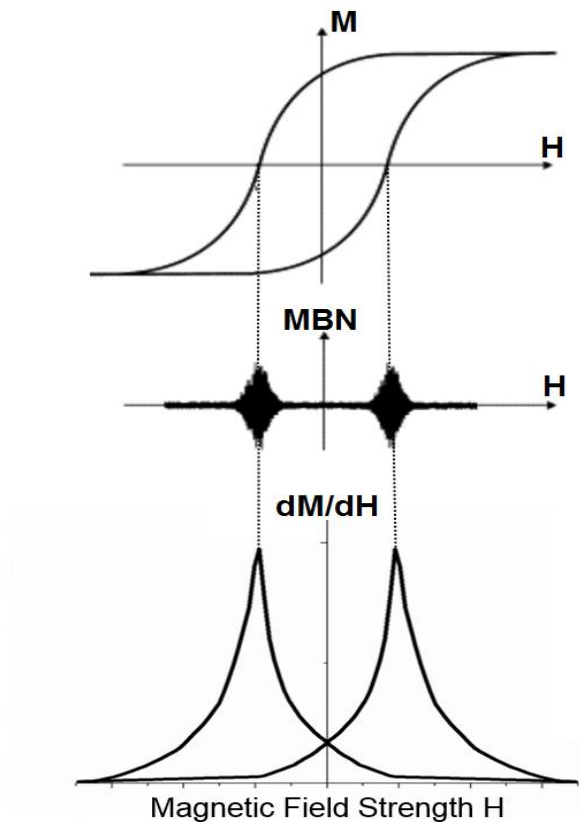

Fig. 2.19 Relation between the magnitude of Barkhausen Noise and magnetisation dynamics [21].

In Fig. 2.19 it can be clearly seen that the high MBN is generated at the steep part of **MH** curve with high d**M**/d**H** rates where the magnetisation takes place predominantly by irreversible domain wall motion, whereas the MBN emission, due to irreversible domain rotation which occurs at the higher levels of magnetic field, is shown to be relatively low. The existing link between the hysteresis parameters, such as coercivity and differential permeability, and Barkhausen Noise amplitude and peak position can provide useful information when evaluating the bulk mechanical properties of ferromagnetic steels.

2.6.2 Modelling of the Magnetic Barkhausen Effect

Due to complexity of domain wall interactions with randomly distributed pinning sites and their stochastic nature the modelling of Magnetic Barkhausen Noise is not a trivial task. The first serious attempt to mathematically describe the MBN emission was made in the work of Alessandro, Beatrice, Bertotti and Montorsi (ABBM) [22] where they proposed a model of planar domain wall motion interacting with random local imperfections characterised by local pinning field $\mathbf{H_p}$. In this model they proposed that the effective rate of change in flux $\dot{\boldsymbol{\phi}}$ (i.e. d$\boldsymbol{\phi}$/dt) caused by Barkhausen jump can be expressed as:

$$\sigma_e G \dot{\boldsymbol{\phi}} = \boldsymbol{H} - \boldsymbol{H_p} \qquad (2.35)$$

Where σ_e is the electrical conductivity, G is a dimensionless coefficient, $\mathbf{H}$ is the local magnetic field experienced by the wall and $\mathbf{H_p}$ is the local pinning field impeding its motion. The product σ_eG represents here the eddy current damping.

The fluctuations of $\mathbf{H_p}$ were modelled as a random function of domain wall position x and therefore of magnetic flux $\boldsymbol{\phi}$ using the following expression:

$$\frac{dH_p}{d\boldsymbol{\phi}} + \frac{H_p - <H_p>}{\xi} = \frac{dW}{d\boldsymbol{\phi}} \qquad (2.36)$$

where ξ represents the range of interaction of domain wall with pinning site and the function W(ϕ) is a white noise function which has zero mean but a finite variance proportional to intensity of local pinning field A, i.e.

$$< dW >= 0, < |dW|^2 >= 2Ad\boldsymbol{\Phi} \qquad (2.37)$$

If the local field is considered as the difference between the applied field $\mathbf{H_a}$ and demagnetising field $N_d\mathbf{M}$ then the Barkhausen emission dynamics contributing to changes in magnetic flux with time can be described by:

$$\frac{d\dot{\boldsymbol{\phi}}}{dt} = \frac{1}{\sigma_e G} \left(\frac{dH_a}{dt} - N_d \frac{dM}{dt} - \frac{dH_p}{dt} \right) \qquad (2.38)$$

In order to get the direct relation between the Barkhausen emission generated with time ($\frac{d\dot{\phi}}{dt}$) and the pinning field time fluctuations ($\frac{dH_p}{dt}$) Alessandro et al. must have restricted the rates of changes of applied magnetic field $\frac{dH_a}{dt}$ and magnetisation $\frac{dM}{dt}$ to have constant values. This allowed them to obtain analytical solutions of both the power spectrum and probability distributions in many regimes [22].

Despite the physical appeal of ABBM model the requirements which need to be met (constant d**H**/dt and d**M**/dt rates) seriously limit its application in typical magnetisation cases to a small region of hysteresis loop near the coercive point where the differential permeability is almost constant. This limitation was later overcome in the stochastic process model of Barkhausen Noise proposed by Jiles, Sipahi and Williams (JSW) [23]. In their work they made an assumption that the amplitude of MBN caused by irreversible domain processes in a given time period Δt is proportional to the total change in magnetisation Δ**M** in that period which can be written as follows:

$$MBN = \gamma \Delta M = \gamma \left(\frac{dM}{dt}\right)\Delta t = \gamma \left(\frac{dM}{dH}\right)\left(\frac{dH}{dt}\right)\Delta t = \gamma \chi' \dot{H}(\Delta t) \qquad (2.39)$$

Where γ is a coefficient of proportionality (0 ≤ γ ≤ 1) which represents the ratio of irreversible magnetisation to total magnetisation change, χ′ is the differential susceptibility and $\dot{H}$ is the rate of change of magnetic field.

In order to simulate the MBN emission as a function of magnetisation time and corresponding instantaneous values of applied field they introduced an additional concept of Barkhausen activity. This concept assumes that the number of Barkhausen emissions in a given period $N(t_n)$ follows a Poisson distribution and is related to Barkhausen emission count in the immediately preceding period $N(t_{n-1})$ where the difference in number of Barkhausen jumps between t_n and t_{n-1} is random and proportional to $N(t_{n-1})$ which can be described by the following expression:

$$N(t_n) = N(t_{n-1}) + \delta\sqrt{N(t_{n-1})} \qquad (2.40)$$

Where δ is a random number in a range -1≤ δ ≤ 1,

Finally the rate of change of MBN with time can be expressed by:

$$\frac{dMBN(t_n)}{dt} = < MBN > \chi' \dot{H}\left[N(t_{n-1}) + \delta\sqrt{N(t_{n-1})}\right] \qquad (2.41)$$

where <MBN> is an average amplitude of Barkhausen emission and <MBN>N(t) is the total amount of Barkhausen activity.

By using Equation 2.41 it is possible to simulate the MBN emission as function of time by performing successive iterations with fixed time step *dt*. An example of output from such a simulation with corresponding applied field waveform and experimental MBN data for iron specimen with 0.05%C is shown in Fig. 2.20.
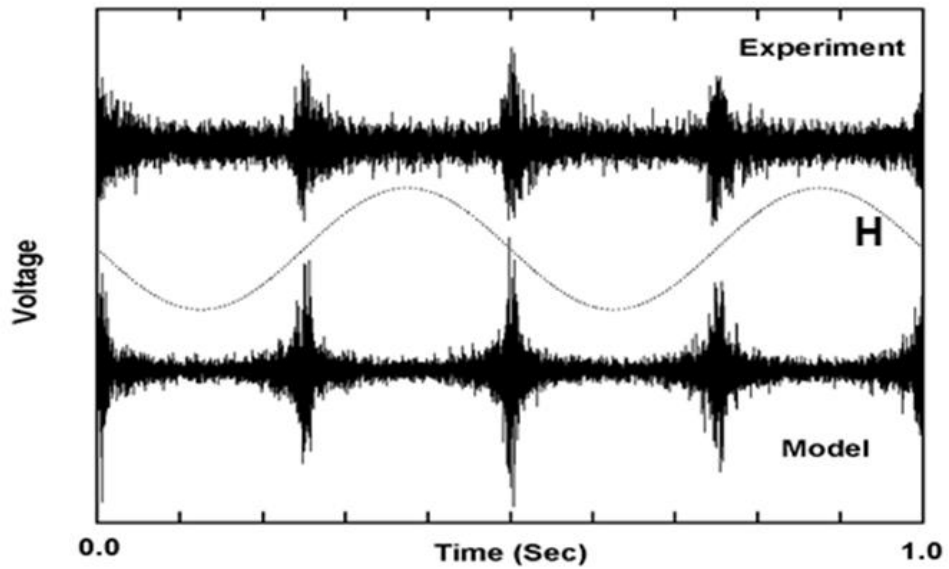

Fig. 2.20 Comparison of experimental and modelled Barkhausen signals obtained for iron specimen with 0.05%C [24].

The significance of JSW model is the fact that by utilising the proportional relation between the differential susceptibility d**M**/d**H** and MBN it describes the Barkhausen emission at all points of hysteresis curve for the complete magnetisation cycle under the action of variable rate of change of magnetic field. Moreover the established relation between the d**M**/d**H** and MBN makes it possible to predict the effect of stress on amplitude of Barkhausen emission when knowing the stress dependence of differential permeability. This analogy will be further used in development of the MBN model for quantitative evaluation of mechanical stress presented in Section 4.2.

2.7 Finite element modelling of electromagnetic circuits comprising ferromagnetic materials

Engineering analysis of electromagnetic systems can be performed by deriving and solving the differential equations relating the basic physical principles such as equilibrium, conservation of energy, conservation of electric charge and Maxwell's equations. However in the case of non-linear partial differential equations formulated for complicated geometries and material properties, the analytical solutions of derived mathematical models cannot be easily obtained. Therefore in mathematical analysis of such complex systems the continuum needs to be discretised allowing its global solution to be approximated by finite number of local solutions of elemental equations for system subdomains. The most widely used numerical technique for finding such an approximate solution is the Finite Element Method which will be discussed in detail in the following sections 2.7.1 to 2.7.3.

2.7.1 Introduction to Finite Element Modelling

The finite element method is based on the concept of dividing the original problem domain into an equivalent system (mesh) of numerous smaller subdomains called finite elements and applying a numerical formulation based on interpolation theory to these elements [25]. The steps of the solution procedure of finite element method can be described as follows:

1. **Discretization of the continuous problem domain.** The first step is to divide the solution domain into system of smaller finite elements called the mesh. These finite elements can have different shapes such as triangular, rectangular or other polygonal shapes in 2D mesh or tetrahedral shapes in 3D mesh. The primary points within and on the edges of the mesh elements are called nodes and their number specifies the total number of solutions for field governing equations meeting the boundary conditions in the original problem domain.

2. **Selection of interpolation functions.** The defined interpolation functions are used to interpolate the field variables over the elements (in between the

nodes). Typically these functions are chosen to be polynomials of which degree depends on number of nodes assigned to the element.

3. **Creation of matrix equations for elements.** The matrix equation for the elements need to established to relate the nodal values of the unknown original function with the coefficients of the corresponding interpolation function approximation. This correlation process is usually performed using the Galerkin method of weighted residuals.

4. **Global matrix assembly.** The global system of equations is assembled from the matrix equations for all the mesh elements. The boundary conditions are imposed into the solution equation system.

5. **Solving.** The solution of the matrix system is found and provides the values of fields at all the mesh nodes.

6. **Post-processing.** The solution is analysed from the calculated global quantities and field plots.

In FEM electromagnetic analysis the governing equations for which the nodal solutions need to be acquired are Maxwell's differential equations of the electromagnetic field that arise from field theory. These equations are described in the next section 2.7.2.

2.7.2 Finite Element Modelling of electromagnetic fields

The analysis of electromagnetic fields can be performed by means of five vector quantities and one scalar quantity, i.e. electric field **E** (V/m), magnetic field **H** (A/m), electric flux density **D** (C/m^2), magnetic flux density **B** (T), current density **J** (A/m^2) and the electric charge density ρ (C/m^3). These quantities are correlated with each other through the partial differential Maxwell's equations [26] as follows:

$$curl\ \boldsymbol{H} = \boldsymbol{J} + \frac{\partial \boldsymbol{D}}{\partial t} \quad \text{(Ampere's law)} \tag{2.42}$$

$$curl\ \boldsymbol{E} = -\frac{\partial \boldsymbol{B}}{\partial t} \quad \text{(Faraday's law)} \tag{2.43}$$

$$div\ \boldsymbol{D} = \rho \quad \text{(Gauss's law for electrostatics)} \tag{2.44}$$

$$div\ \boldsymbol{B} = 0 \quad \text{(Gauss's law for magnetism)} \tag{2.45}$$

The supporting constitutive equations involving material properties can be written as:

$$\boldsymbol{D} = \varepsilon_0 \boldsymbol{E} + \boldsymbol{P} \tag{2.46}$$

$$\boldsymbol{B} = \mu_0(\boldsymbol{H} + \boldsymbol{M}) \tag{2.47}$$

$$\boldsymbol{J} = \sigma_e \boldsymbol{E} \tag{2.48}$$

where $\boldsymbol{P}$ is the polarisation of electric poles and ε_0 is the permittivity of free space.

In modelling of static fields with no time variation the time derivatives in Equations 2.42 and 2.43 are neglected which gives:

$$curl\ \boldsymbol{H} = \boldsymbol{J} \tag{2.49}$$

$$curl\ \boldsymbol{E} = \boldsymbol{0} \tag{2.50}$$

In such a case the electrostatic field is determined using the Equations 2.46, 2.48 and 2.50 whereas the magnetostatic field can be obtained using Equations 2.47 and 2.49. When the field varies with time the electric and magnetic field are coupled through the time derivatives in Equations 2.42 and 2.43. Therefore the induced electric field $\boldsymbol{E}$ associated with time varying flux density $\boldsymbol{B}$ gives rise to induced current density $\boldsymbol{J}$ in conductive materials and this has to be taken into account.

2.7.3 FEM software processes

In the research work presented in this thesis the finite element modelling was performed using the *Magnet* FEM software package released by Infolytica [27]. The subsequent phases of the modelling process using this software can be characterised as follows:

1. **Pre-processing.** This initial phase involves the following steps:
   - geometrical construction of model components using CAD drawing tools
   - characterisation of physical properties of component materials, such as: initial magnetisation curve reflecting the magnetic properties of ferromagnetic materials, electrical conductivity and permittivity, mass density and thermal properties

- creation of system mesh based on the mesh size assigned to particular model components
- specification of boundary conditions
- specification of current sources in a form of energised coils or/and flux sources in systems comprising permanent magnets
- setting of convergence parameter and maximum number of iterations in calculation step

2. **Solving.** This phase is transparent to the user where the real time update of the subsequent solution steps is displayed on the screen. Depending on the type of problem specified and solver chosen, the type of solution algorithm can either be magnetostatic (no time variation), time harmonic (linear materials with sinusoidal excitation) or time transient (non-linear time varying systems).

3. **Post-processing.** The field solutions can be visualized in the form of contour, shaded or arrow plots. Moreover the numerical values of calculated fields and quantities can be probed within any specified region of the solution.

The main reasons for selecting the *Magnet* package to perform the electromagnetic field simulations in this study were:
- high calculation efficiency obtained by utilizing the multicore mesh-generators, solvers and post-processors
- user friendly interface allowing to rapidly define and edit the system properties and features

The FEM railway model created using the *Magnet* software together with the output from the electromagnetic field simulations for the modelled cases of flawed and unflawed railway rails will be presented in Sections 5.3 and 5.4 respectively.

2.8   Summary

This chapter introduced the principal micromagnetic energies determining domain configuration in ferromagnetic materials. It subsequently discussed the hysteretic and anhysteretic magnetisation processes, as well as the Magnetic Barkhausen Effect phenomenon. The quantitative relation between mechanical stress and magnetisation was analysed via the concept of stress equivalent field, and the link between Barkhausen amplitude and differential susceptibility was established using the JSW model. These relations will be later used in the development of the MBN model for stress evaluation in Chapter 4.

Additionally the underlying principles of the finite element method for numerical modelling of electromagnetic fields have been presented. This method will be used for calculating distributions of magnetic flux leakage profiles above various cases of unflawed and flawed rails in Chapter 5.

3. Non-destructive evaluation of structural integrity of steel components

3.1 Introduction

In general, the structural integrity of steel components can be defined as their ability to reliably withstand service conditions. In order to assure this ability the following aspects need to be considered:

- control and verification of the desired pre-service mechanical and microstructural properties determined by the quality of their manufacturing processes
- successive periodic monitoring of these properties under normal and severe operating conditions

Due to the significance of structural integrity of steel components in their failure mode it is considered as one of the main concerns in the design and operating performance of railway and building systems, gears and transmissions, reactor pressure vessels and power plants, or any other types of systems which are subjected to load during their service life [28,29,30]. In all those applications the structural integrity governs the total component life, called fatigue life, which can be defined as the total number of stress cycles required for initiation or/and propagation of cracks leading to mechanical failure. The main mechanical factors affecting the structural integrity of steel components are discussed in Section 3.2

Non-destructive evaluation (NDE) is a broad, interdisciplinary field aimed at assessing the condition of interrogated components and systems in a manner which does not cause any further damage or permanent deterioration of their properties, and therefore it does not affect their future applicability. In NDE the inspected material is appropriately impacted with a certain type of input energy and its response (energy output) is thoroughly captured and studied. The relationship between the input and output provides the information about the state of the material. Depending on the type of energy used for obtaining required information the non-destructive evaluation

methods can be mechanical, acoustic, thermal, optical, electrical, magnetic or radiative. The common non-magnetic, macromagnetic and micromagnetic NDE methods used for stress and flaw detection are described in Sections 3.3, 3.4 and 3.5.

3.2 Factors determining structural integrity of steel components

Hardness, residual stresses, applied stresses and presence of defects are some of the main mechanical factors affecting the structural integrity of steel components. The detailed description of these factors with reference to their effective influence on the behaviour of steel structure under load is given in the following sub-sections.

I. Hardness

Hardness can be defined as resistance of a material to localised deformation from indentation, scratching, cutting or bending. Hardness of steels is a function of their carbon content (as shown in Fig. 3.1) and generally is directly proportional to their strength (Fig. 3.2) and inversely proportional to ductility and toughness, i.e. resistance to cracking [31].
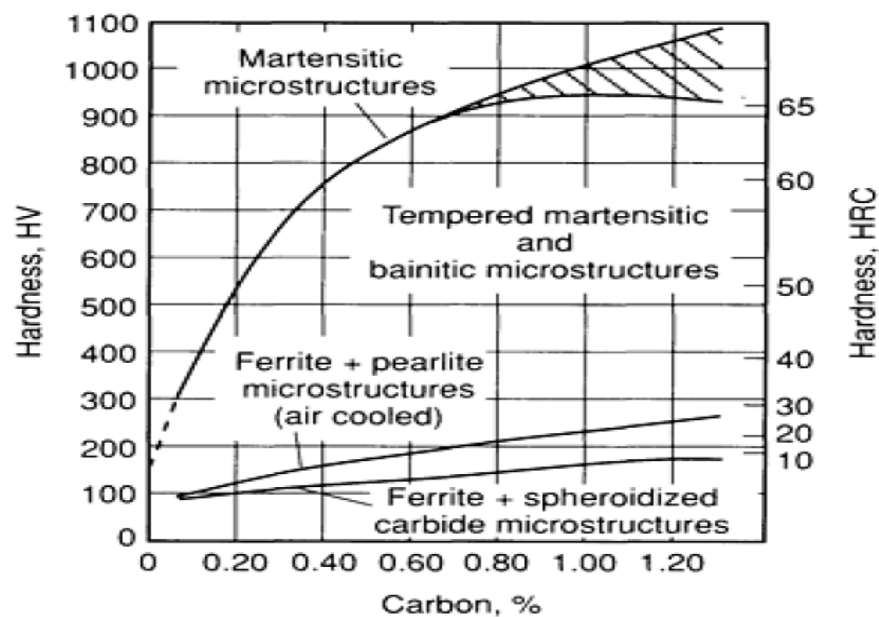
Fig. 3.1 Hardness as a function of carbon content for various microstructures in steels [31].
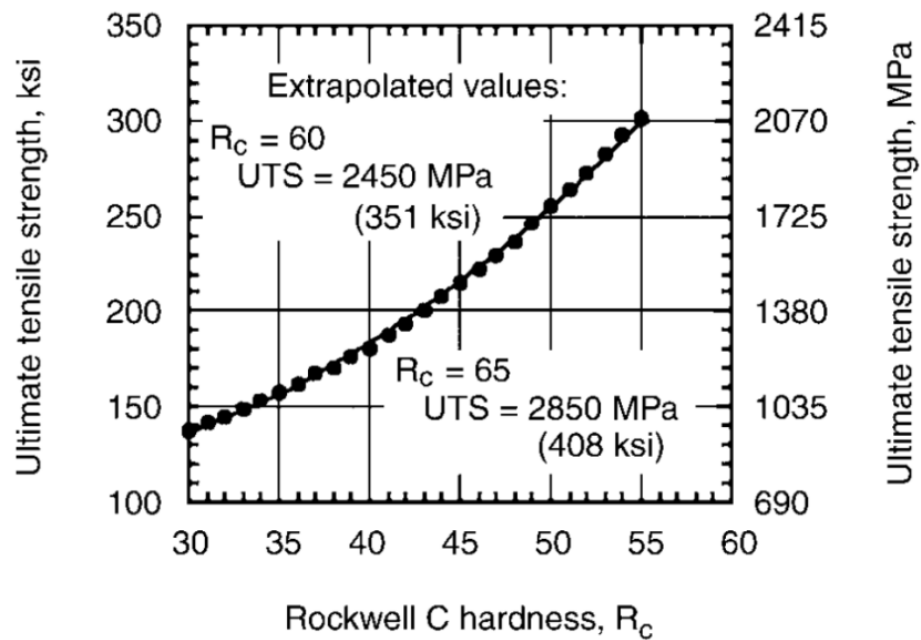
Fig. 3.2 Ultimate tensile stress of quenched and tempered steels as a function of hardness [32].

Heavy-duty steel components, such as gears and transmission elements, which are subjected to certain types of stresses, are typically only surface (case) hardened as this allows optimising their bulk mechanical properties. In surface hardened steels the hard outer case provides high wear resistance whereas the soft core ensures toughness enabling the component to withstand load without risk of cracking. Furthermore, the surface hardening of steel has an advantage over *through hardening* because the less expensive low-carbon and medium-carbon steels can be case hardened without the problems of distortion and fracturing associated with the bulk hardening of thick sections [33]. The industrial methods used for surface hardening of steels can be described as follows:

- **Carburizing** is the addition of carbon to the surface of low carbon steels (approx. 0.2%C) at typical temperatures of 850 to 950°C at which the austenite with high carbon solubility is the stable crystal structure. The carbon can be introduced to steel from the carbon bearing surrounding environments such as: gas (atmospheric gas, plasma and vacuum carburizing), liquids (salt bath carburizing) or solid compounds (pack carburizing). The hardening process is completed by quenching the high-carbon surface layer (typically in oil) to form

martensite with carbon content of 0.8 to 1%C. The case depth of carburized steel is proportional to carburizing time and available carbon at the surface. The case depth obtained through carburization is typically limited to 0.6mm. An example of microhardness depth profile for gas-carburized SAE 8620 steel is shown in Fig. 3.3.
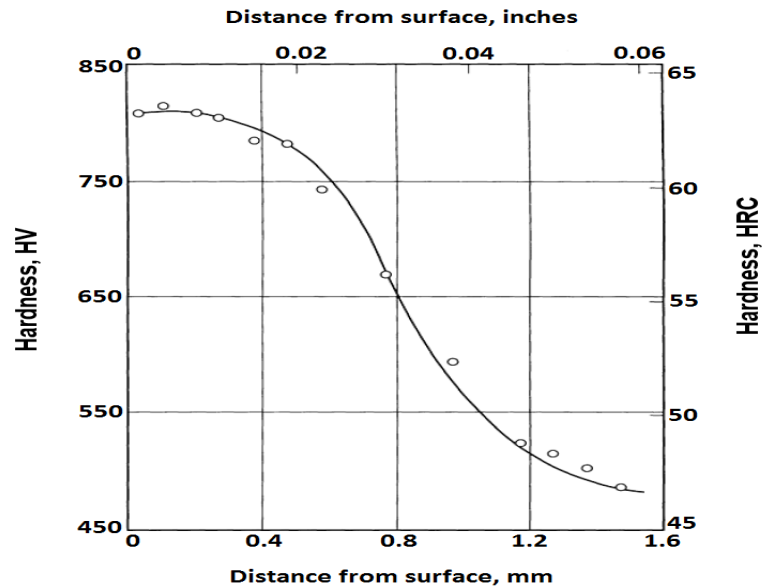

Fig. 3.3 Microhardness depth profile of SAE 8620 steel test bar after gas carburization [33].

- **Nitriding** is a heat treatment process which introduces nitrogen into the surface of medium-carbon steels (0.3 to 0.59% C) that contain strong nitride-forming elements such as aluminium, chromium, vanadium and molybdenum. The typical temperature range of this process is 500 to 550°C in which the nitrogen is added into ferrite and therefore no subsequent quenching is required. The nitrogen rich environments from which the nitrogen is absorbed and diffused in steel surface typically include gas (box furnace, fluidized bed and plasma nitriding) or liquid (salt bath). The final case hardness and depth depend on the alloy elements content as shown in Figs. 3.4a and 3.4b.
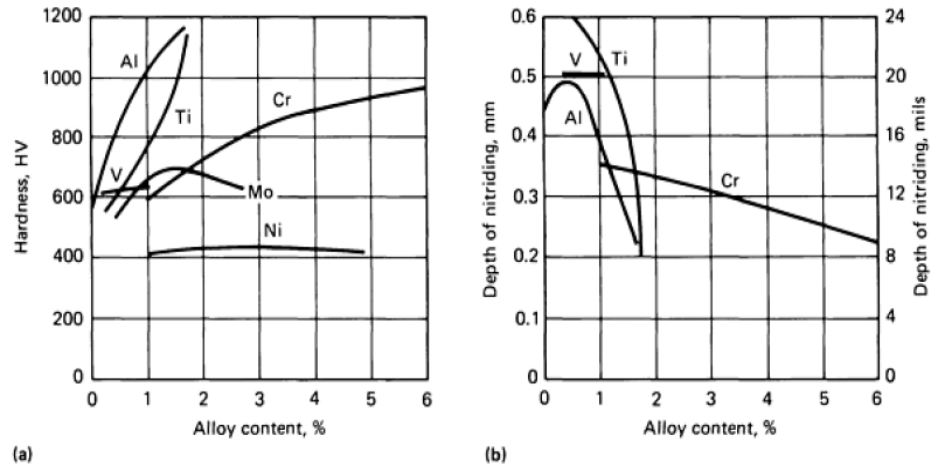
Fig. 3.4 Influence of alloying elements on: a) hardness after nitriding (base alloy, 0.35% C, 0.30% Si, 0.70%Mn) and b) depth of nitriding measured at 400 HV (nitriding for 8 h at 520 °C) [33].

- ▪ Other surface hardening methods include **flame hardening, induction heating, laser surface heat treatment and electron beam hardening**. In all these methods the case hardening is achieved by localized heating followed by quenching to produce hard outer martensitic layer, without any chemical modification of the surface.

Case hardening improves the fatigue strength of steel components and produces beneficial residual compressive stress in their surface. However in many cases those components are subjected to further finishing processes such as tempering, grinding and turning which can significantly alter the final residual stress condition and consequently affect their endurance, which is discussed in the following sub-section.

II. Residual stress

Residual stress is the type of stress which remains in the material after its original cause has been removed. This can be external forces, thermal gradients and surface constraints. The residual stresses are self-equilibrated, which means that the regions with compressive stress are always counterbalanced by areas having tensile stress, thus resulting in zero net stress for the bulk material [34]. The characteristic length scales over which they self-equilibrate is used as criterion according to which the following three types can be distinguished:

- **Type I** residual stresses are balanced over considerable fraction of component (several grains) and therefore are categorised as macro-stresses. This kind of stresses is produced during most of the manufacturing processes where their origins can be divided into three types, i.e. mechanical, thermal and metallurgical, as specified in Table 3.1.

Process type	Origin		
	Mechanical	Thermal	Metallurgical
Smelting, Casting	-	Temperature gradient during cooling	Change of phase
Shot-peening, Bending, Rolling, Forging, Straightening, Extrusion	Heterogeneous plastic deformation between the core and surface of the component	-	-
Grinding, Turning, Milling, Drilling, Boring	Plastic deformation due to removal of chips	Temperature gradients due to localised heating during machining	Change of phase during machining if the temperature reaches the phase transition threshold
Welding	-	Temperature gradient	Microstructural change (HAZ)

Table 3.1. Main origins of residual stress resulting from different manufacturing processes [35].

The **Type I** residual macro-stresses which extend over several grains induce local stress magnetic anisotropy and influence the magnetic properties, such as magnetic permeability and MBN amplitude, in a similar manner to applied stresses and therefore can be successfully evaluated using magnetic non-destructive techniques.

- **Type II** residual stresses vary over a grain scale and therefore are typically referred to as "intergranular stresses". Low level type II stresses are present within most of the polycrystalline materials due to the fact that the elastic and thermal properties of differently oriented grains create a local misfit resulting in micro-strain distortion. More significant intergranular stresses occur in

microstructures containing several phases or those which have undergone phase transformation [34]. These microscale stresses are difficult to evaluate using magnetic methods as their spatial order is typically beyond the resolution of standard magnetic non-destructive techniques.

- **Type III** residual stresses are short range stresses which exist on the range of several atoms and originate from the presence of crystal defects, such as dislocations, point defects, impurities and inclusions which have been previously introduced in Section 2.6.1 and shown in Fig. 2.16. The resulting incompatible permanent strains have a characteristic order of several crystal lattice parameters, which is considerably smaller than size of typical grain in steel. Due to very small spatial scale the individual characterisation of these sub-micro residual stresses exceeds the capabilities of standard macroscopic magnetic non-destructive testing techniques.

The final surface macro-residual stresses (Type I) play an important role in the fatigue and wear resistance of the component. Their relation with mechanical properties can be described as following:

a) Surface compression is the desired type of stress as it tends to enhance fatigue strength, slow crack growth and improve resistance to environmentally assisted cracking due to stress corrosion;

b) Tensile residual stress in the surface of the component is generally undesirable as it reduces fatigue strength, increases crack propagation and lowers fracture resistance.

The above characteristics clearly indicate how essential is the control and evaluation of ultimate surface stress condition produced during final manufacturing processes of critical steel components such as gears, crankshafts, bearings which are subjected to various loads throughout their operational lifetime.

The properties of case hardened steel specimens which were studied in this research work resemble those of heavy-duty parts as they have undergone surface finishing processes such as grinding and shot-peening typical to these types of components. An

introduction to these surface treatments with emphasis on the surface macro-residual stresses they can produce is given below:

- **Grinding** is an abrasive, chip forming machining process for producing flat surfaces of high precision. In grinding there are three main factors which contribute to creation of residual stresses [35] :

1. Plastic deformation involving smearing of the material in the plane of the surface which tends to produce compressive residual stress

2. Thermal expansion of the surface layer constrained by the bulk material which leads to generation of thermal stresses. When this stresses exceed the yield stress of material the subsequent cooling will create a surface tensile residual stresses

3. Surface re-hardening which occurs during grinding of workpieces made of hardenable steel where the rapid heating and cooling can form a surface layer of hard and brittle martensite with compressive residual stress

The total effective surface residual stress σ_r is governed by the balance between these three factors as shown in Fig. 3.5, where σ_r is given as function of grinding power with four distinguishable regions in which:

    a. Only elastic deformation occurs

    b. Thermoplastic deformation takes place

    c. Thermoplastic and thermomechanical deformations appear

    d. Martensitic re-hardening occurs
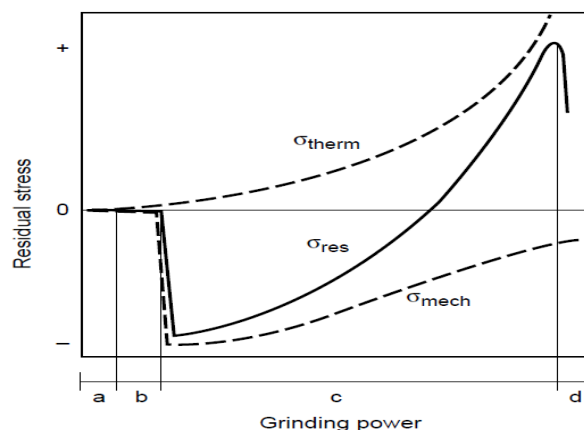
Fig. 3.5 Contributions of the thermal and mechanical components to the effective residual stress after grinding [35]

The primary parameters affecting the grinding operating conditions and resulting residual stresses are the cutting speed, the depth of cut and feed rate, the coolant rate, as well as the mechanical properties and heat conductivity of the workpiece and grinding wheel.

- **Shot-peening** is a material strengthening process in which the shots which are particles made of steel, ceramics or glass are launched against surface at high velocity by an air jet or centrifugal forces. It results in plastic deformation by means of vertical forces exerted on the workpiece surface by the impacts of spherical shots, which gives rise to compressive residual stress. The depth of the affected layer and magnitude of the induced stress depend on the radius and speed of shot balls as shown in Figs. 3.6a and 3.6b. The highest compressive residual stresses can be achieved by strain shot-peening when the workpiece is strained in tension during the process.
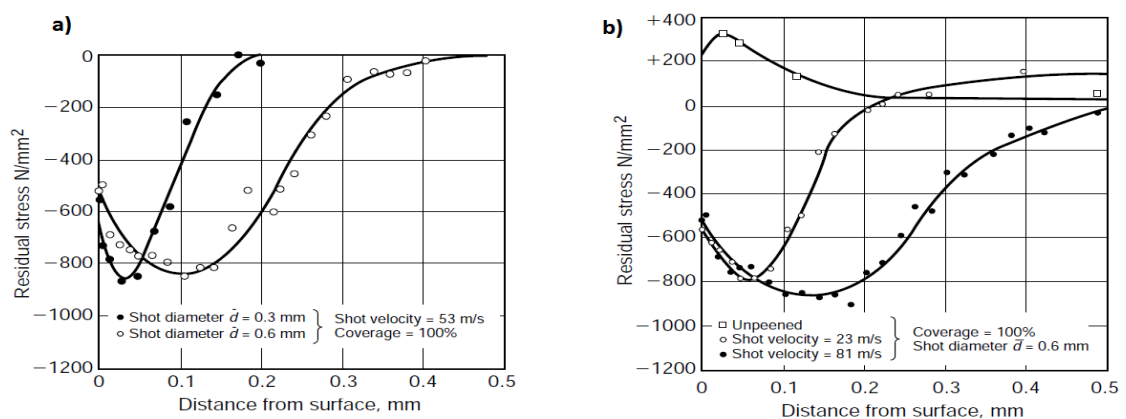
Fig. 3.6 Influence of shot-peening parameters on residual stress depth distributions: a) shot diameter, b) shot velocity [35].

III. Fatigue defects

High number of cyclic mechanical loadings applied to steel components leads to initiation and propagation of fatigue cracks. The level of repetitive stress required to trigger the defect formation is in many cases below the macroscopic yield stress limit but sufficient to cause microscopic plastic deformation in the vicinity of inherent material imperfections such as inclusions, scratches, voids, etc. The main reason for this occurrence is the existence of tensile micro-residual stresses associated with these imperfections which reduce the local micro-yield strength and therefore lower the

amplitude of effective applied stress needed to cause localised micro-plastic deformation within individual grains.

The **Stage I** of crack growth due to micro-plastic deformation is manifested by an increase of dislocation density, creation of dislocation tangles, dislocation walls and persistent slip bands along which the micro-sized cracks tend to nucleate. Once the micro-crack is initiated within particular grain the subsequent application of load will cause its propagation towards the grain boundaries and further into the neighbouring grains. In general, the subsequent **Stages II** and **III** of crack growth process can be described as follows:

- **Stage II.** In this stage the high number of cyclic loading causes the crack to propagate along the grain's slip plane being coaxial with the shear stress. When it reaches the boundary with the neighbouring grain of different lattice orientation it reorients and continues to grow along the new particular slip direction of the adjacent grain. As a result in this stage the micro-crack can reach a length of typically a few grain diameters [36], as shown in Fig. 3.7.

- **Stage III.** When a crack reaches a certain length its further growth becomes insensitive to grain boundary obstacles and orientation of crystallographic slip planes. The subsequent propagation takes place along the non-crystallographic planes perpendicular to axis of applied tensile stress, as depicted in Fig. 3.7. In this stage the crack growth rate is much higher than in Stage II.
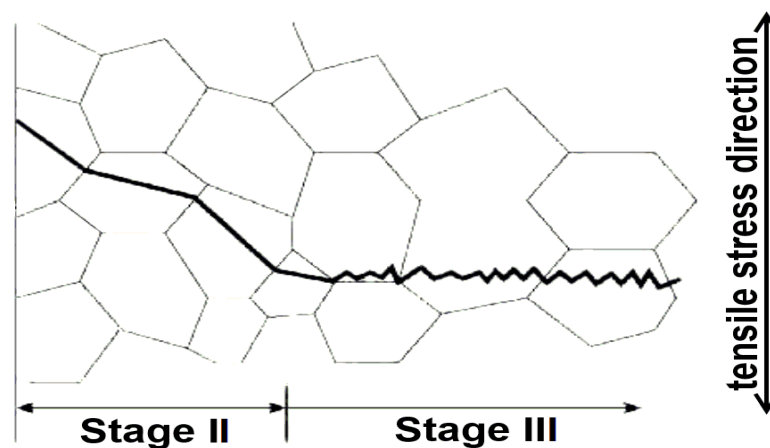
Fig. 3.7 Illustration of fatigue crack growth stages II and III in crystalline material.

The quantitative relationship between crack size and critical stress required to cause the crack growth is described by material property known as fracture toughness which can be defined as follows [37]:

$$\sigma_c = \frac{K_t}{\sqrt{\pi a}}$$

(3.1)

where σ_c is the amplitude of critical stress, a is the crack length and K_t is the fracture toughness.

Equation 3.1 clearly indicates that with increasing length of crack in a given material of particular fracture toughness the critical value of stress needed to cause its further propagation decreases. Hence the detection of crack in its early growth stages is of great importance in preventing failure of the components subjected to various load conditions.

A typical example of fatigue defect is the transverse defect (TD) which is commonly found in railway steel. Transverse defect is characterised as a progressive crosswise fracture which nucleates around the steel imperfections (usually in a form of diffused hydrogen and oxide atoms or voids) and under action of rail bending stress and wheel impact develops outward as smooth, round or oval surface in a plane transverse to the cross-section of the rail head as shown in Fig. 3.8 [38].
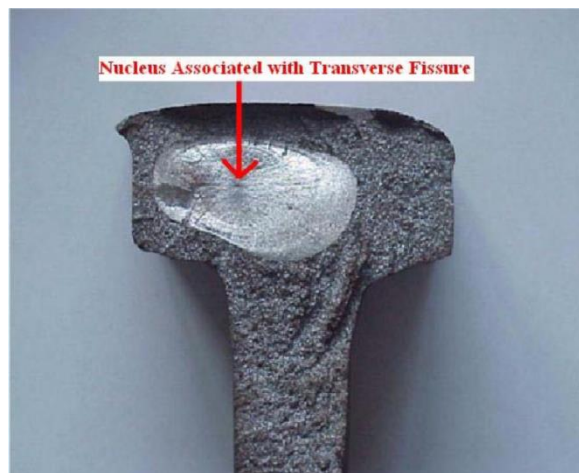
Fig. 3.8 Illustration of transverse defect which nucleated around steel imperfection in rail cross-section [38].

The microstructural imperfections around which the transverse defects originate are inherent in the manufacturing process and occur predominantly in railway steels produced with non-controlled cooling prior to the mid-1930s. The modern railway

steel making methods involve controlled cooling which considerably reduces the number of gas molecules absorbed by the liquid steel during heating and solidification but does not completely eliminate the hydrogen from the rail [39].

In the initial growth stage the development rate of small transverse defects is relatively low which allows the affected rail section to remain in service for a certain amount of time. When the size of a transverse flaw reaches 20% to 25% of the rail heads cross-section its further stress-induced development is significantly accelerated and can ultimately lead to sudden failure of the rail. The detailed fracture patterns of subsequent growth stages of transverse fissure are shown in Fig. 3.9 [38].
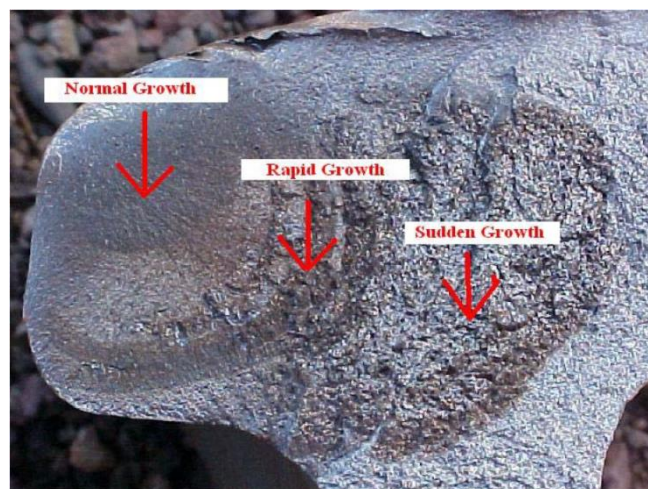
Fig. 3.9 Illustration of the subsequent growth stages of transverse rail defect [38].

According to American Federal Railroad Administration data, transverse defects have accounted for 43% of all derailments in the USA in years 2000-2009 with an average failure cost of $730 000 [40]. Therefore the improvement in early detection of transverse defects in rail steel has become a primary objective in service failure reduction in the railway industry.

3.3 Non-magnetic non-destructive evaluation methods

3.3.1 Ultrasonic technique

Ultrasonic technique is the oldest and therefore one of the most widespread NDE methods employed in materials evaluation [41, 42]. The general concept of this technique is based on propagation of sound waves which are launched in a form of

mechanical vibration into the inspected material and their reflections containing data on structural properties are registered and analysed. The mechanical vibrations are launched in the tested specimen using transducers which convert the electrical impulses into mechanical impulses and are typically made of piezoelectric materials (such as quartz, lithium niobate and lead zirconate titanate) responding to an applied voltage of a given frequency by straining at the same frequency [43].

The most popular methods for inspecting a material for flaws using ultrasound are the pulse-echo mode, in which the same transducer is used to launch the ultrasonic wave and to detect the echo, and the pitch-catch mode where two transducers are used - one to launch the pulse and the other to detect echo. The latter method has been implemented by Sperry Rail Ltd in their non-destructive in-situ rail flaw inspection using the X-fire detection system shown in Figs. 3.10a and 3.10b [40].
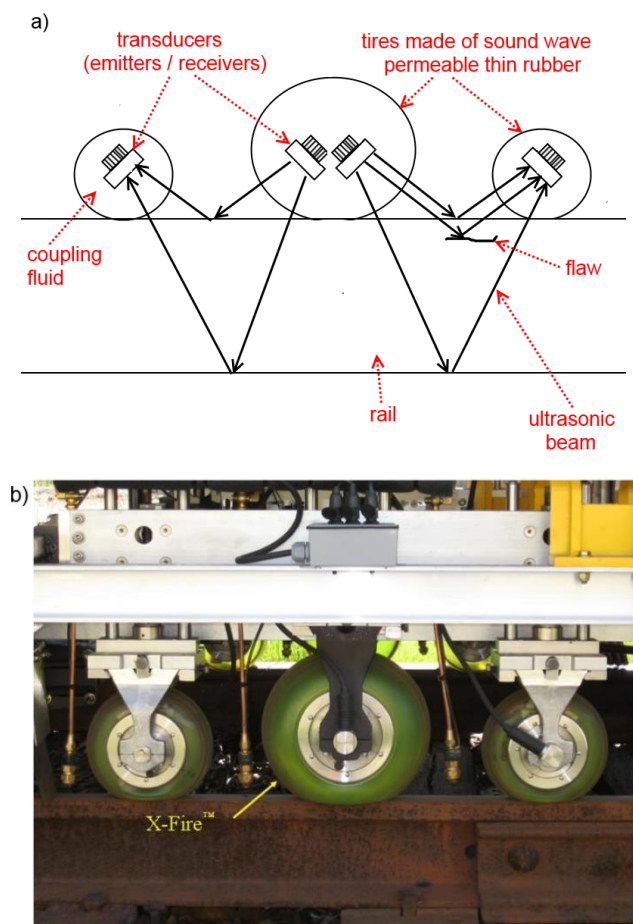
Fig. 3.10 a) Schematic diagram of the principal of ultrasonic rail inspection with Sperry X-fire system (refraction of ultrasonic beams has been neglected), b) photography of the X-fire set-up taken during the in-situ rail testing [40].

During the dynamic rail flaw inspection with the X-fire system the ultrasonic pulses are emitted by the transducers within the central wheel which subsequently propagate through the coupling fluid, sound wave permeable tires into the rail. If no flaw is present the applied ultrasonic pulses are reflected from the surface and bottom of the rail and the generated front and rear wall echoes are detected by the side-wheel transducers as shown in the left side of Fig. 3.10a. The pulse-echo diagram of signal intensity vs time for unflawed rail is depicted in Fig. 3.11a. In the case where flaw is present within rail structure the associated with it internal surfaces reflect the propagating waves (as illustrated on the right side of Fig. 3.10a) and generate an additional intermediate pulse-echo which arrives at the receiving transducer before the background wave as shown in Fig. 3.11b.
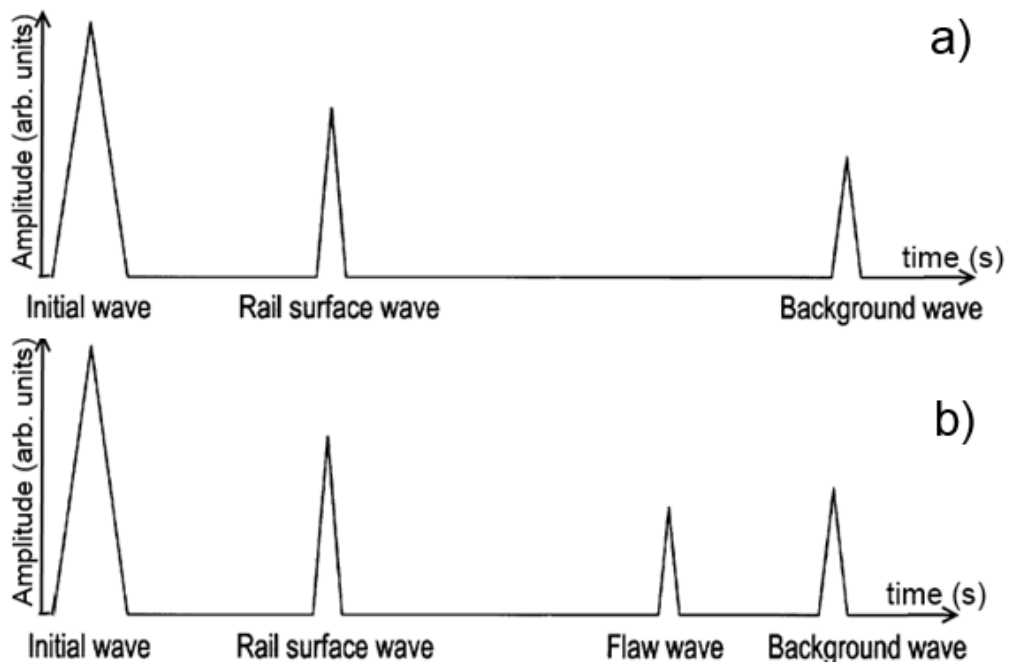
Fig. 3.11 The schematic pulse echo-diagram of signal intensity vs time for a) unflawed rail; b) rail with internal flaw generating an additional intermediate reflection echo.

The passage of sound waves in a material is subject to attenuation with distance and time due to such factors as scattering of the wave energy, absorption of some of the energy by the material and divergence [44]. Therefore the amplitude of echoes indicating the presence of flaw is a function of distance between the top surface of rail and the reflecting flaw surface and with known velocity of sound in rail the flaw location can be determined.

Although the ultrasonic technique is well established as an effective method in rail flaw detection it has some limitations which can considerably reduce its sensitivity and applicability. These limitations are related to surface anomalies in the form of grease, corrosion or rolling fatigue induced head checking (shown in Fig. 3.12) which alter the intended path of ultrasonic beams introduced into the rail and substantially lower the chance of detecting the internal flaws.
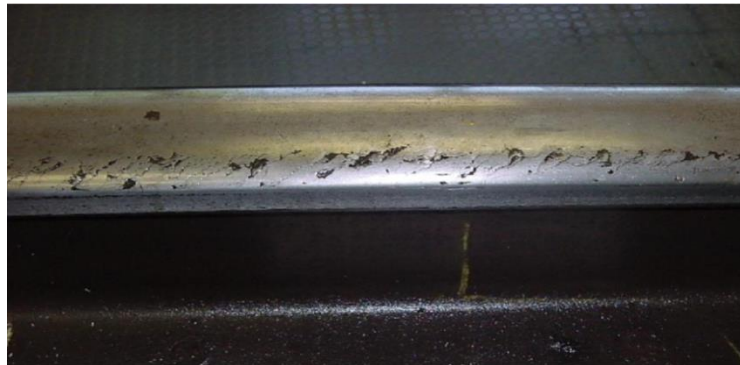

Fig. 3.12 Illustration of the fatigue induced rail head checking [40].

Moreover the ultrasonic technique has been proven to be inefficient in detecting smooth and shallow (approx. 0.1mm) transverse flaws oriented at 90 degrees to longitudinal planes of rail [40]. This is caused by the fact that the ultrasonic beams introduced into rail are reflected from this type of flaws towards the bottom of the rail first and then subsequently reflected back and redirected to surface. In the relatively long return time required for the beams to travel along the reflection path their intensity is greatly attenuated which in most of the cases makes this type of transverse flaws undetectable [40]. This type of situation is illustrated in Fig. 3.13.
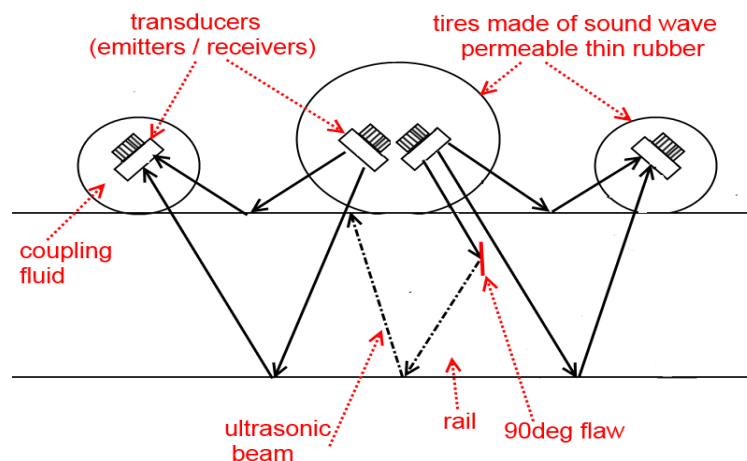
Fig. 3.13 Schematic diagram of the ultrasonic beam reflection from the 90° transverse rail flaw.

The above mentioned limitations of ultrasonic technique in rail flaw detection emphasize the requirement of using other complimentary non-destructive methods, such as eddy currents and magnetic flux leakage, which will be discussed in Sections 3.3.2 and 3.4.1 respectively.

3.3.2 Eddy current method

The principle of eddy current (EC) non-destructive method is based on Faraday's law of induction according to which the time-varying magnetic flux ϕ will cause a circulating electric field **E** which induces a current flow in a conducting material.

In eddy current flaw inspection the source of alternating magnetic flux, typically in a form of coil supplied with time varying voltage, is placed in the vicinity of a test material in which the induced circulating currents generate a magnetic flux opposing the one coming from the coil. The signal measured is the impedance of the coil Z which depends on the effective linking flux φ_l being the difference between the coil and eddy current fluxes. The presence of a flaw in the material affects the conducting path of eddy currents leading to distortion in their flow and variation in both Z and φ_l.

The common practice in EC flaw detection is to use the differential probe setup comprising two nominally identical coils wound in opposition [45]. When such a pair of coils is located above the unflawed homogenous material (Fig. 3.14a) the signals from the two coils cancel out each other giving zero output. When the differential probe is used to scan a region over a flawed material (Fig. 3.14b) the defect induced variations in eddy current flow and linking fluxes are detected in the form of changes in the real and imaginary parts of impedance as shown in Figs. 3.14c and 3.14d.

The critical factor in flaw inspection using eddy currents is their penetration depth in the interrogated material. The eddy current density decreases approximately exponentially with distance from the surface with an attenuation rate depending on the test frequency, electrical conductivity and magnetic permeability of the tested material.
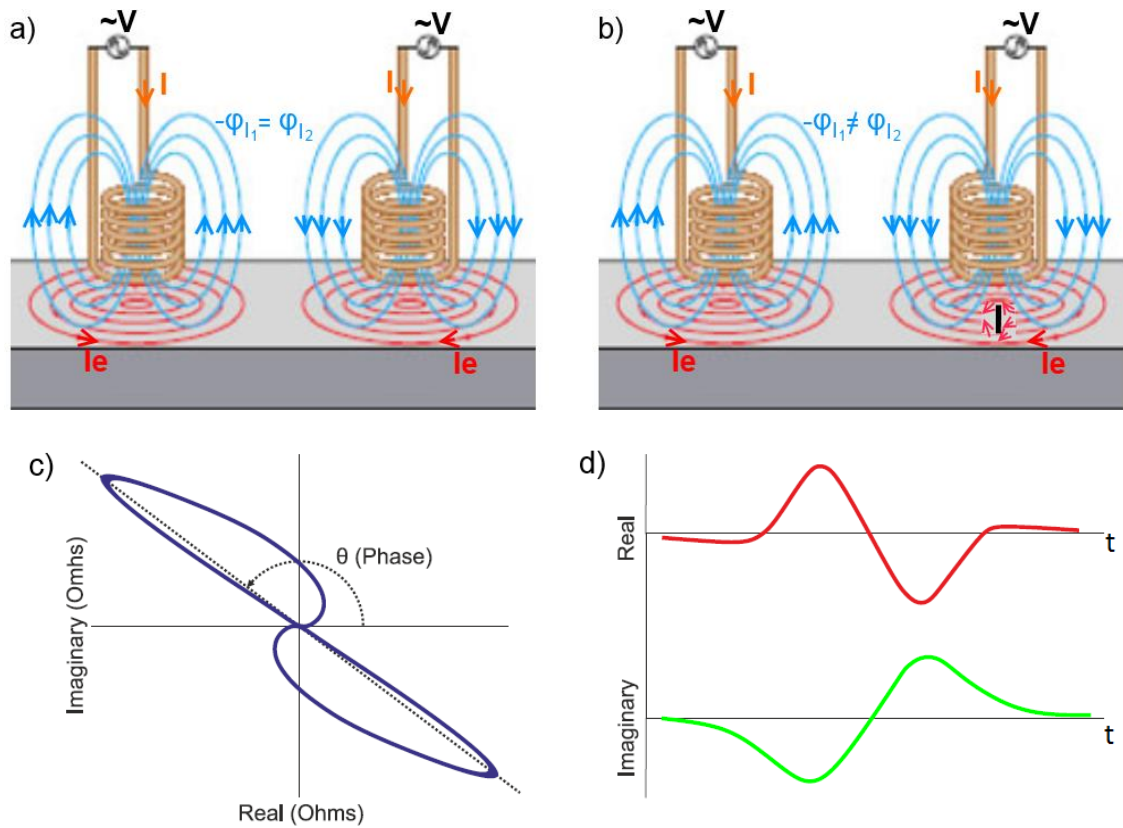
Fig. 3.14 Schematic diagram of EC differential probe positioned above a) unflawed material; b) flawed material with depicted distortion in eddy current flow. A typical output signal from EC differential probe indicating the presence of flaw plotted as c) loop on complex impedance plane; d) real and imaginary parts of impedance vs time [46].

The standard penetration depth of eddy currents in materials is generally taken to be the skin depth δ at which their density drops to value of approximately 37% (1/e) of the density at the surface of the material [45] and can be calculated from the following equation:

$$\delta = \sqrt{\frac{1}{\pi f \sigma_e \mu_0 \mu_r}} \qquad (3.2)$$

where δ is the skin depth and f is the test frequency.

For typical EC flaw test frequencies of 1kHz-2MHz [45] the corresponding skin depth values in pearlitic rail steel R260 having relative permeability μ_r of 150 and electric conductivity of 4.45×10^6 S/m [47] are within range of 0.01-0.62mm. This clearly implies that in the railway inspection the application of eddy current method is limited to surface and near surface flaw detection.

Another application of the eddy current non-destructive method is stress evaluation in ferromagnetic materials. A typical measurement set-up used in this type of testing is shown in Fig. 3.15 where a U-shape ferrite core wound with pair of coils connected in series is placed on steel rod to create a complete magnetic circuit [48]. A direct contact between the probe and sample must be maintained to avoid alterations in the effective permeability of the complete magnetic circuit caused by a possible lift-off.
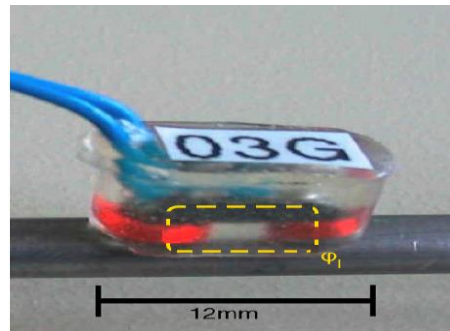

Fig. 3.15 EC stress measurement probe positioned at the surface of tested sample rod with indicated linking flux path [48].

During the test both coils are energised with an AC current to generate a time dependent magnetic flux in the ferrite core which is thoroughly enclosed via the investigated section of the specimen so that the values of coil linking fluxes φ_l and inductances L depend on the magnetic permeability μ in this magnetised region. When the magnetic permeability is altered by stress σ then both φ_l and L change adequately and demonstrate a rising trend with stress when $\frac{d\lambda}{dM}>0$, $\sigma>0$ or $\frac{d\lambda}{dM}<0$, $\sigma<0$ and descending trend with stress when $\frac{d\lambda}{dM}>0$, $\sigma<0$ or $\frac{d\lambda}{dM}<0$, $\sigma>0$ as shown in Figs. 3.16a and 3.16b for nickel, St37k and St1860 steels [48].
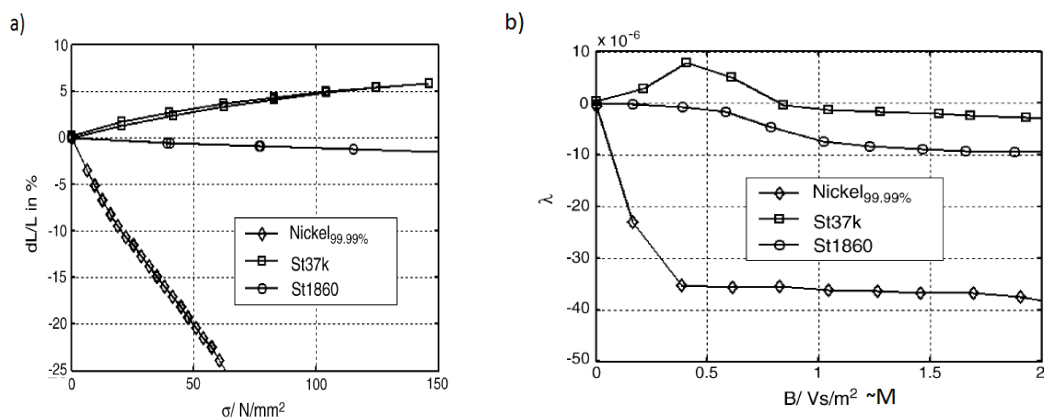

Fig. 3.16 a) Percentage changes in coil inductance with stress obtained from EC evaluation of nickel, St37k and St1860 steels; b) corresponding magnetostriction curves for tested samples of nickel, St37k and St1860 steels [48].

3.3.3 X-ray diffraction method

In the x-ray diffraction (XRD) method a collimated x-ray beam is focused onto the specimen and the intensity of x-rays diffracted from the crystal lattice, measured as the angle between the x-ray tube and x-ray detector, is changed. The conditions which are necessary for x-ray diffraction to occur via constructive interference (shown in Fig. 3.17) are governed by the Bragg's law [49] as follows:

$$n\lambda_x = 2dsin\theta_x \qquad (3.3)$$

where n is an integer, λ_x is the x-ray wavelength, d is the atomic lattice spacing and θ_x is the diffraction angle.
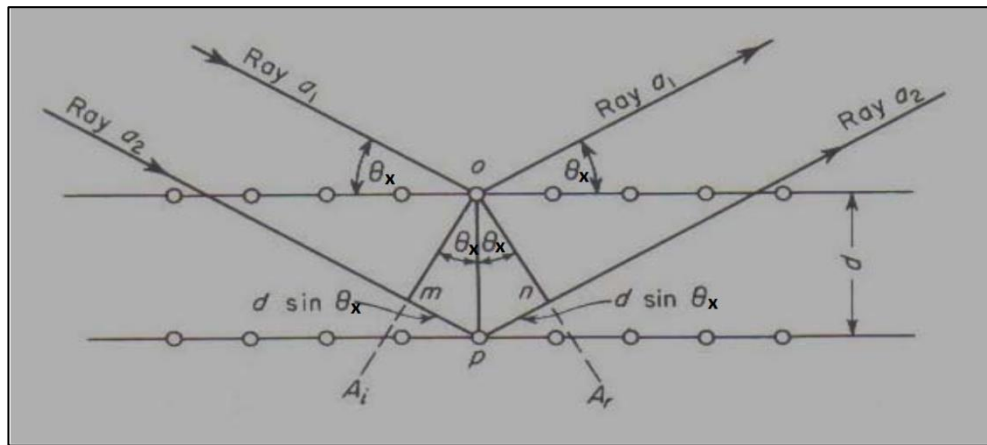
Fig. 3.17 Diffraction of X-rays by a crystal lattice satisfying the Bragg's law [49].

The presence of residual stresses in a crystalline material produces elastic strains which alter the atomic lattice spacing *d* in its crystal structure thereby causing a shift in diffraction angle. In general, tensile stress increases the lattice spacing for atomic planes perpendicular to the stress direction and decreases it for planes parallel to stress axis. In the case of compressive stress the elastic distortion in lattice spacing is opposite to the one observed for tension. If the lattice spacing d_0 for unstrained specimen is known then the elastic strain ε in the stressed specimen can be calculated from the following equation:

$$\epsilon = \frac{d_\sigma - d_0}{d_0} \qquad (3.4)$$

where d_σ is the lattice spacing in stressed specimen,

and with the assumption of linear elastic distortion the residual stress σ_r can be consequently determined from Hooke's law:

$$\sigma_r = E\epsilon \tag{3.5}$$

where E is the modulus of elasticity of the tested specimen.

The main drawback of the above stress evaluation approach is the requirement of the precise measurement of lattice spacing in the unstressed sample of the tested material. This inconvenience has been overcome in the '$\sin^2\psi$' x-ray diffraction technique in which the lattice spacing is measured at different tilt angles ψ between the normal of the sample and the normal of diffracting plane, as shown in Fig. 3.18.
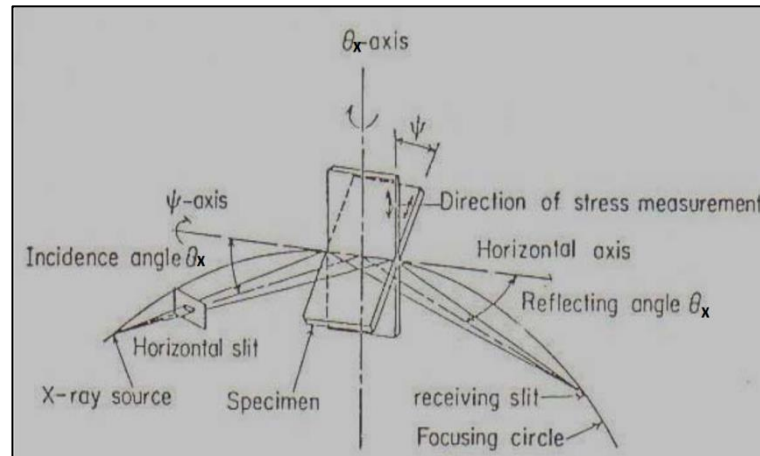
Fig. 3.18 Schematic diagram of residual stress measurement set-up using the $\sin^2\psi$ x-ray diffraction technique [49].

The recorded values of lattice spacing d are plotted against the corresponding $\sin^2\psi$ (as shown in Fig. 3.19) and the slope of this function is used to calculate the residual stress in the measured direction with the following equation:

$$\sigma_r = \left(\frac{E}{1+v}\right) m \tag{3.6}$$

where m is the slope of the $\sin^2\psi(d)$ function
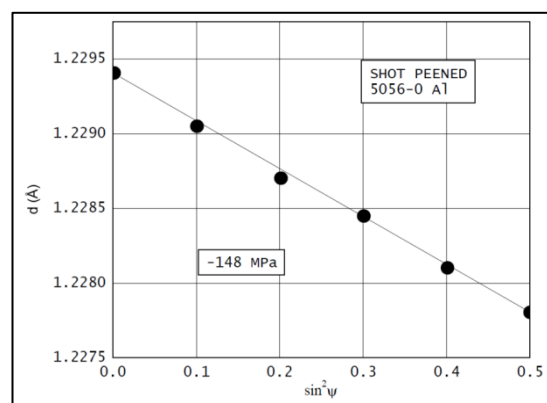
Fig. 3.19 Linear dependence of the measured lattice spacing with $\sin^2\psi$ for shot-peened 5056-0 aluminium [50].

The interception point of the $\sin^2\psi(d)$ curve with Y-axis provides the value of the unstressed lattice spacing d_0 and the inclination of this curve indicates the type of stress, which is positive for tension and negative for compression.

The useful penetration depth of x-ray in steel is typically below 10µm and therefore a condition of plane stress is assumed to exist in the diffracting surface layer [51]. The further subsurface stress measurements using x-ray diffraction require exposing the deeper layers of material which is commonly performed by electro-polishing. By using XRD in combination with electro-polishing and successive incremental material removal it is possible to obtain the variation of residual stress with depth in a form of a stress-depth profile. However, such an approach cannot be considered as non-destructive.

The primary disadvantages of XRD stress measurements are the errors related with sample properties, such as coarse grain size and severe texture, and instrumental difficulties, typically caused by the misalignment of the diffraction apparatus or displacement of the specimen. Moreover the small spatial resolution of XRD measurement makes the stress analysis of broad component areas time consuming. Nevertheless, XRD is industrially commonly accepted, time-proven and generally applicable non-destructive method for measuring residual stress.

3.3.4 Acoustic emission method

Acoustic Emission (AE) is defined as a transient elastic wave generated by the rapid release of energy within a material when subjected to an external stimulus such as change in pressure, load, or temperature [52]. This type of emission can be detected at the surface of material using transducers with a typical frequency range between 100kHz and 1MHz. The AE method is commonly applied in the monitoring of weld quality [53], detection of crack formation in the pressure vessels and pipelines transporting liquids under high pressures [54], as well as corrosion assessment in reinforced concrete structures [55]. As distinct from the previously characterised NDE techniques, the AE method is passive where instead of supplying energy to the interrogated component, the embedded transducers simply 'listen' for the energy released by the component due to internal crack initiation or propagation.

3.4 Macromagnetic non-destructive evaluation methods

3.4.1 Magnetic flux leakage method

Magnetic flux leakage (MFL) for detection of flaws is one of the most economical non-destructive methods used for in-service flaw monitoring of oil and gas pipelines, fuel storage tank floors and other industrial applications involving ferromagnetic components. The principle of this method relies on detection of the perturbation of magnetic flux around defects having different permeability than the surrounding magnetised ferromagnetic material. If the defect is located at the surface or near subsurface of the material then the diverted stray flux leaks into air (as shown in Fig. 3.20), where it can be detected by magnetic sensors such as a Hall probe or induction coil, or by magnetic particles which attach to the component in the vicinity of flaws.
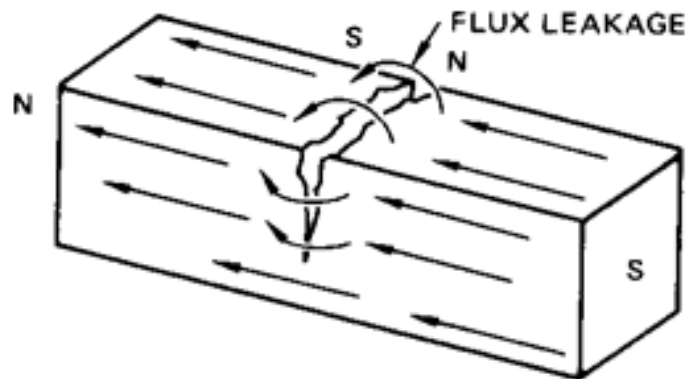
Fig. 3.20 Illustration of magnetic flux leakage in the vicinity of defect in ferromagnetic material.

In MFL there are a variety of ways used to produce the magnetic field across the test material. The typical MFL systems utilise permanent magnets, electromagnets or current injection to drive the magnetic flux and provide near-saturation magnetisation state within the investigated region.

The pattern of leakage field in the vicinity of a flaw depends on its geometry and orientation in respect to the magnetic flux in the material. A prediction of this pattern for the simplified case of a rectangular flaw can be made using the analytical description of the dipole model proposed by Zatsepin and Shcherbinin (Z-S model) [56].

The concept of this approach is illustrated in Fig. 3.21 where H_a is the applied field, H_d is the demagnetising field created by the magnetic charges at the end surfaces of the flaw (dipole south and north poles), b is the flaw depth and 2a is the flaw width.
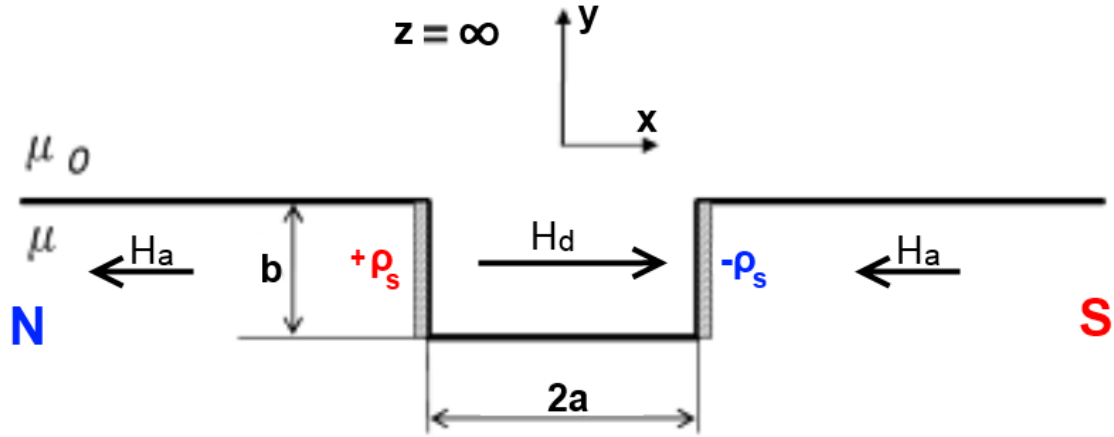

Fig. 3.21 Illustration of the principal of the leakage field dipole model for rectangular flaw proposed by Zatsepin and Shcherbinin [56].

For the above case the expressions for the tangential B_x and normal B_y components of the leakage flux density given by Zatsepin and Shcherbinin can be written as:

$$B_x = \frac{\mu_0 \rho_s}{2\pi} \left[tan^{-1}(\frac{b(x+a)}{(x+a)^2+y(y+b)}) - tan^{-1}(\frac{b(x-a)}{(x-a)^2+y(y+b)}) \right] \qquad (3.7)$$

$$B_y = \frac{\mu_0 \rho_s}{4\pi} \ln \left[\frac{((x+a)^2+(y+b)^2)((x-a)^2+y^2)}{((x-a)^2+(y+b)^2)((x+a)^2+y^2)} \right] \qquad (3.8)$$

where ρ_s is the magnetic charge density at the end surfaces of flaw, which can be determined from the following equation derived by Edwards and Palmer [57]:

$$\rho_s = H_a \frac{\pi n(\mu_r - 1)}{(n+\mu_r)tan^{-1}(n)} \qquad (3.9)$$

where n is the ratio of flaw depth and half-width, n=b/a.

The leakage flux distributions obtained using Equations 3.7, 3.8 and 3.9 have been validated and proved to be in reasonably good agreement with experimental results, which can be seen in Figs. 3.22a and 3.22b for the case of a rectangular flaw in steel plate in work of Abe et al. [58] and in Figs. 3.23a and 3.23b for corrosion pit flaw in

pipeline subjected to various hoop stresses in work of Mandal and Atherton [59]. Nevertheless these analytical formulas are limited to simple geometries (mostly rectangular flaws with their length much greater than their width (l>>w)) and therefore in more complicated situations, the leakage fields need to be calculated using the numerical methods, such as finite element modelling.
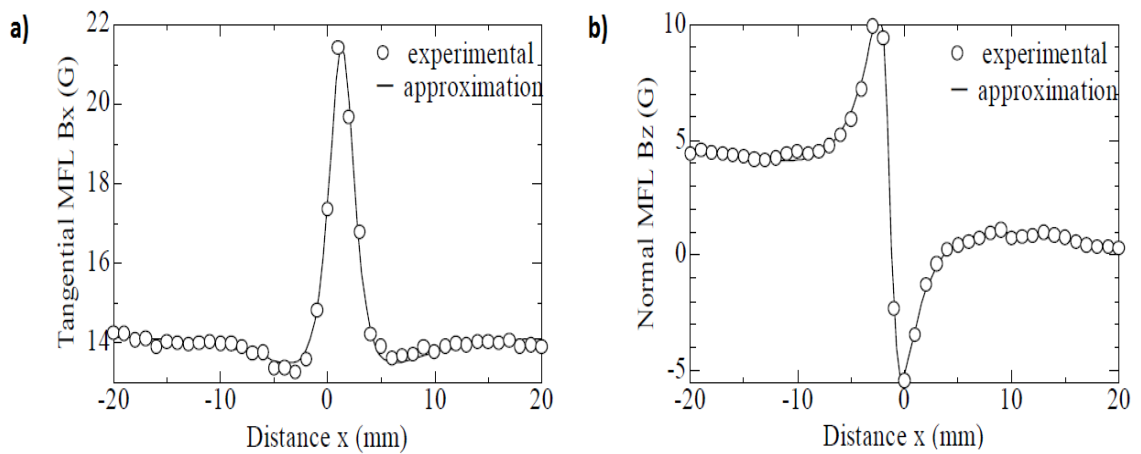

Fig. 3.22 Experimental profiles of tangential and normal components of MFL signals approximated with Z-S dipole model for case of rectangular flaw in steel plate [58].
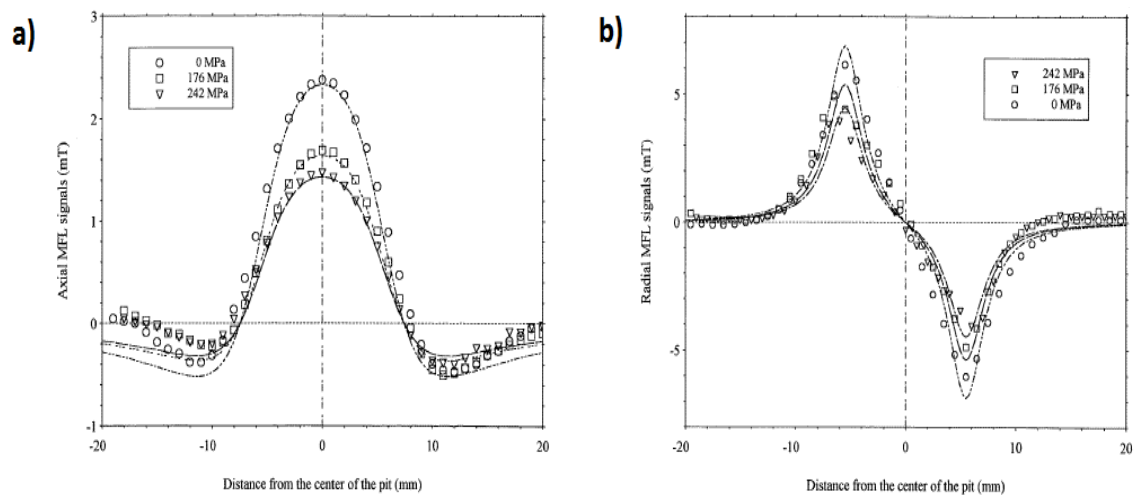
Fig. 3.23 Experimental profiles of tangential and normal components of MFL signals approximated with Z-S dipole model for case of corrosion flaw in steel pipeline subjected to various hoop stresses [59].

The main inspection parameters affecting the level of detected MFL signal are sensor lift-off and scanning velocity as shown in Figs. 3.24 and 3.25 respectively.
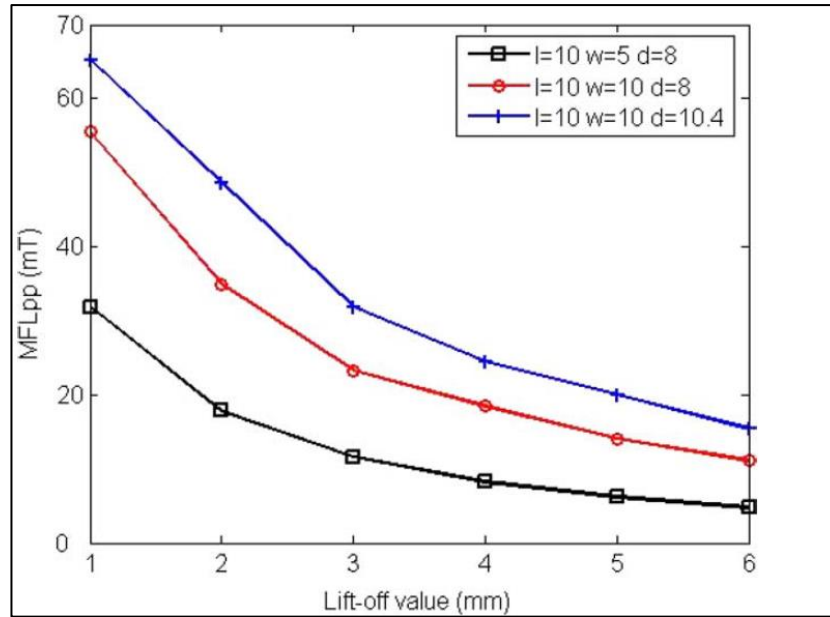
67

Fig. 3.24 Variation of the peak-to-peak MFL signal with sensor lift-off for three different cases of cuboid defect in steel plate (l-length, w-width, d-depth of the defect) [60].
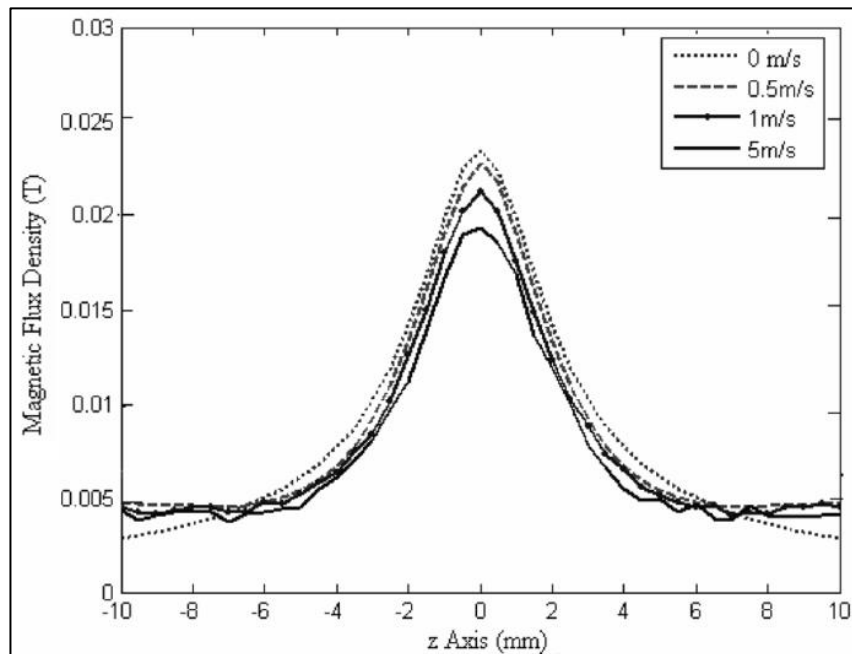

Fig. 3.25 Profiles of the tangential component of MFL density obtained at different inspection velocities for case of cuboid flaw in steel tube [61].

The decrease in MFL amplitude with increasing sensor lift-off is caused by the attenuation of leakage field with distance from the flaw, whereas the variation of MFL signal with testing velocity is due to eddy current effect, which becomes more pronounced with rising inspection speed resulting in a higher rate of change of applied magnetic field experienced by the test specimen.

The main limitation of the MFL method is the reduced sensitivity in detection of subsurface flaws located relatively far away from the surface, for which the induced flux variations are difficult to measure and identify, as shown in Figs. 3.26a and 3.26b.
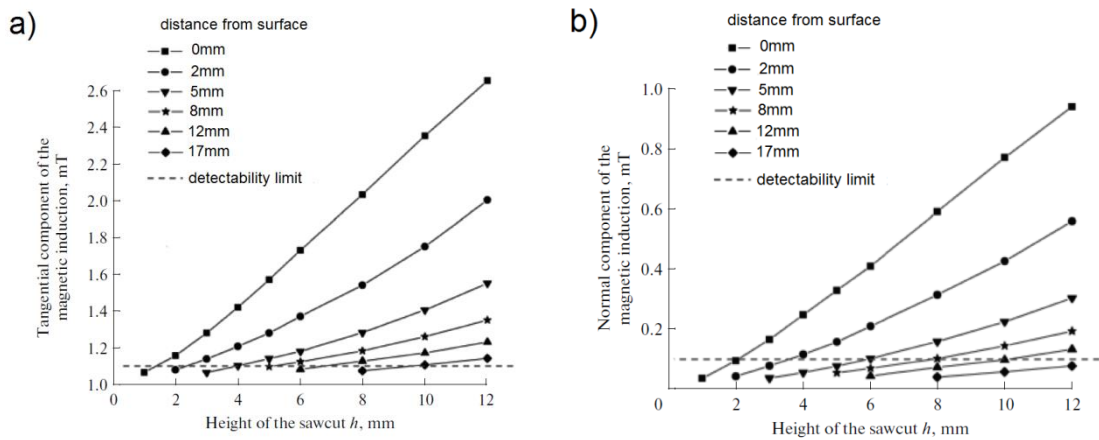

Fig. 3.26 Dependence of a) tangential and b) normal components of magnetic flux leakage on the height of flaw and its distance from rail surface [62].

Moreover the flux leakage effect is dependent on the angle between the flux (magnetic field) and the flaw. The MFL effect is greatest in those cases where flaw is perpendicular to the flux, and the effect decreases as the angle is reduced. When the flaw is parallel to the field it becomes undetectable with MFL method, as shown in Figs. 3.27a and 3.27b [37, 63].
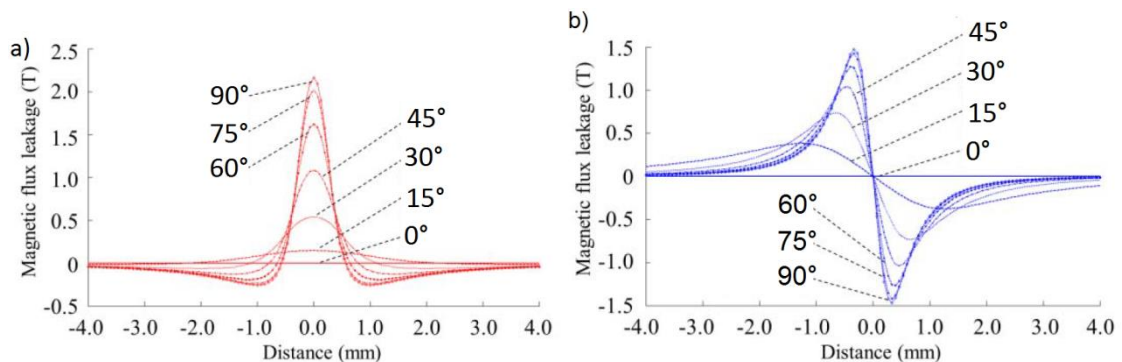

Fig. 3.27 Dependence of a) tangential and b) normal components of magnetic flux leakage on the angle between flaw and magnetic field direction [63].

Finally when considering disadvantages of the MFL method it must be noted that for the repetitive inspection the interrogated specimen requires complete demagnetisation to cancel out the effect of remanent magnetisation on the sensitivity of flaw detection.

In Chapter 5 the application of MFL method in detection of rail flaws will be discussed and analysed. The distributions of MFL signals above current carrying rails with surface

and subsurface flaws will be calculated using the developed FEM model and explained via the concept of current re-routing mechanism and effective re-orientation of magnetic field against the flaws. Subsequently, the correlation between modelled and real sensed signals will be validated. Finally, the comparative analysis of dynamic flaw inspections involving different current application techniques will be performed. The outcome will enable to identify the optimal inspection methodology which maximises the probability of transverse rail flaw detection involving current injection. The proposed testing methodology will be directly implementable in the currently performed structural integrity of rail.

3.4.2 Magnetic hysteresis method

In the magnetisation process of stressed ferromagnetic material the magnetomechanical stress equivalent field $\mathbf{H_\sigma}$ influences its anhysteretic and hysteretic behaviour, which leads to changes in the magnetic properties such as susceptibility, permeability, coercivity, remanence and hysteresis loss. The manner in which these properties change depends on the type, amplitude and direction of stress with respect to magnetisation, as well as the slope of magnetostriction with magnetisation $\frac{d\lambda}{dM}$ at the corresponding value of applied field $\mathbf{H}$, as already explained in Section 2.5.

The various effects of stress on anhysteretic and hysteretic parameters, such as differential susceptibilities at origin χ'_{an} and coercive point, χ'_{Hc} and permeabilities $\mu_r'_{Hc}$, μ'_{Hc}, coercivity H_c and remanence B_r, have been reported by numerous investigators, including Jiles and Atherton [64], Sablik [65, 66], Langman [67], Makar [68, 69] and Vandenbossche [70]. In general, based on their results it is possible to distinguish three types of magnetic properties behaviour under stress:

I. **Type I**. Consequent rising trend of χ'_{an}, $\mu_r'_{Hc}$, B_r and simultaneous drop in H_c with decreasing compressive stress σ_C and increasing tension σ_T in case where the sign of $\frac{d\lambda}{dM}$ remains positive and $\mathbf{H_\sigma}$ successively changes from maximum negative at lowest σ_C to maximum positive at highest σ_T, as shown in Figs. 3.28a, 3.28b and 3.28c for XC10 and M250 steels [65, 70].
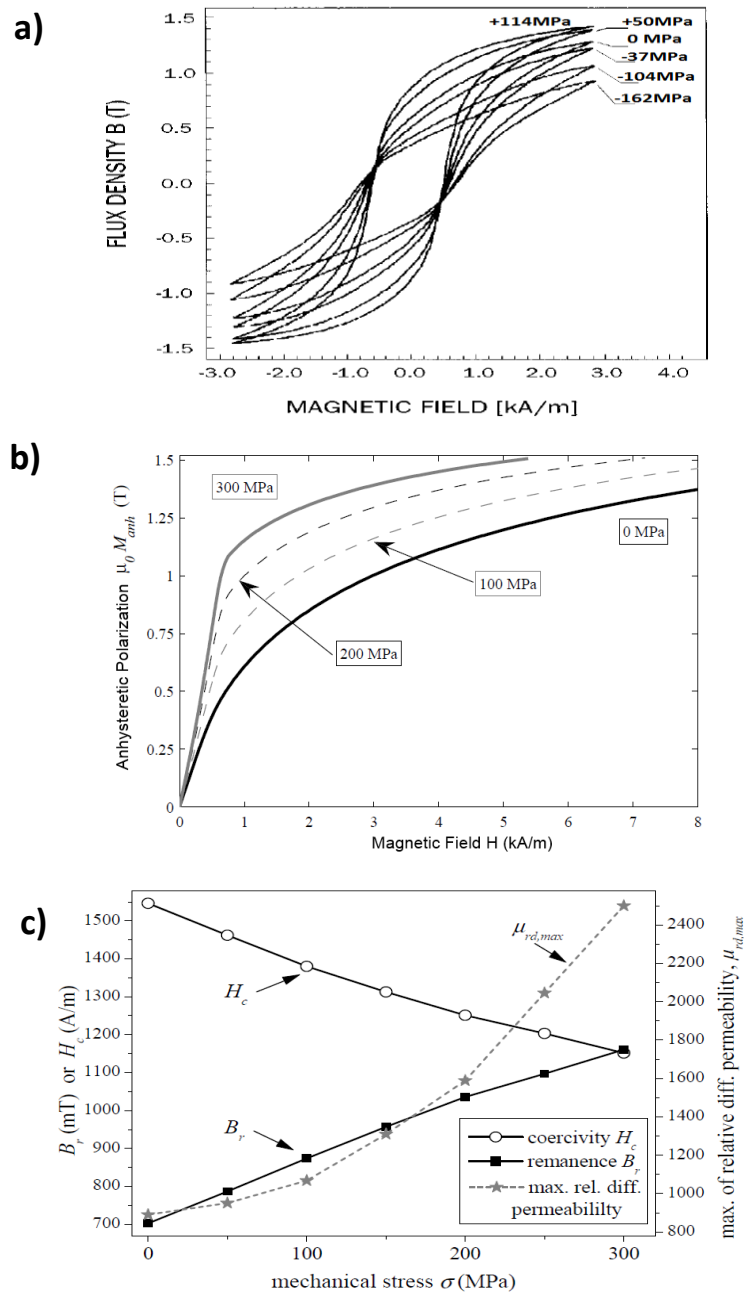
Fig. 3.28 a) Hysteresis loops for XC10 steel subjected to various applied stresses; b) Anhysteretic magnetisation curves obtained for M250 steel under different tensile loads; c) Variation of hysteretic parameters of M250 steel with tensile stress [65, 70].

II.   **Type II**. Successive declining trend of χ'_{an}, $\mu_r'_{Hc}$, B_r and simultaneous rise in H_c with decreasing compression σ_C and increasing tension σ_T in cases where the sign of $\frac{d\lambda}{d\mathbf{M}}$ remains negative and $\mathbf{H_\sigma}$ successively changes from maximum positive at lowest σ_C to maximum negative at highest σ_T , as shown in Figs. 3.29a and 3.29b for nickel (only tensile regime) [70].
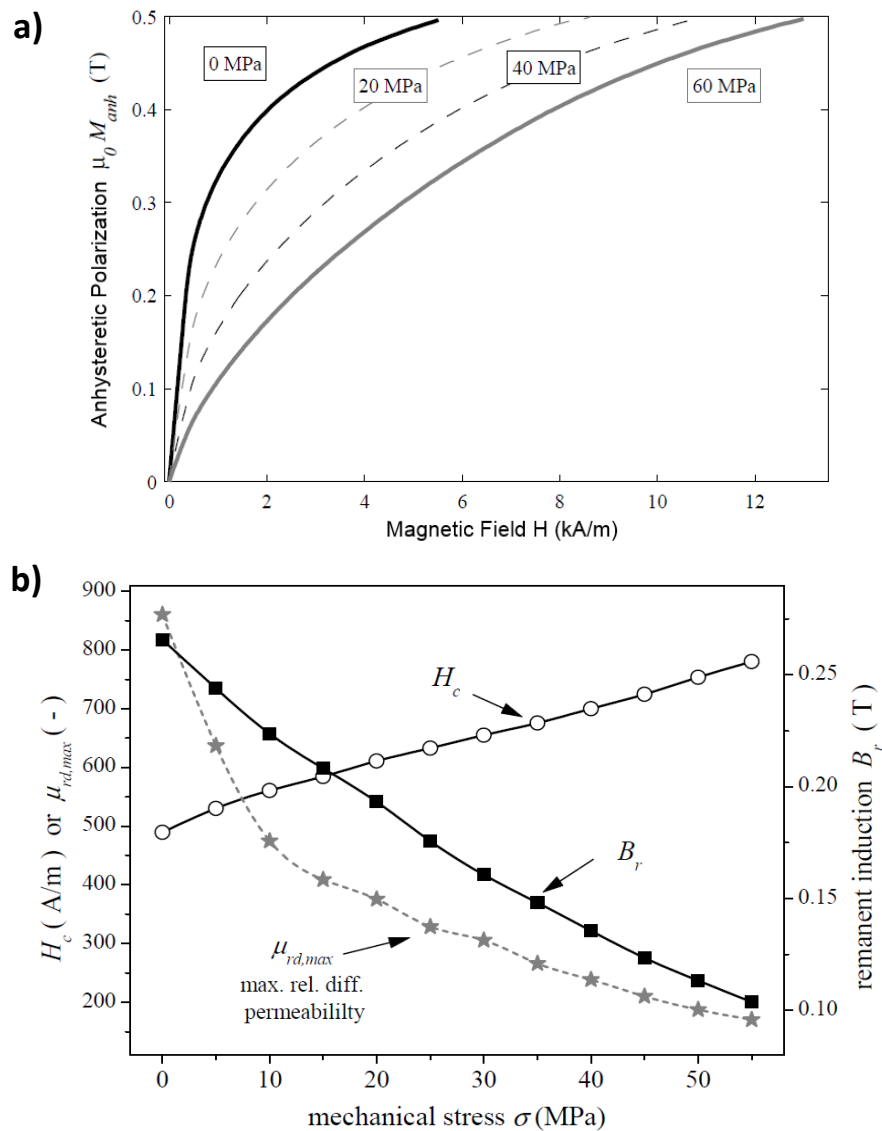
Fig. 3.29 a) Anhysteretic magnetisation curves for nickel under different tensile loads; b) Variation of hysteretic parameters of nickel with tensile stress [70].

III.   **Type III**. Non-monotonic behaviour of anhysteretic and hysteretic parameters with stress due to the occurrence of local extremum of H_σ at some critical intermediate value of tension σ_{Tc} at which the product of σ and $\frac{d\lambda}{dM}$ approaches maximum. As a result the χ'_{an}, $\mu_r'_{Hc}$, B_r reach their peak value at σ_{Tc} and then subsequently decrease with further increment in σ_T, as shown for low-carbon and 50D pearlitic steels in Figs. 3.30a, 3.30b and 3.30c [68,70].
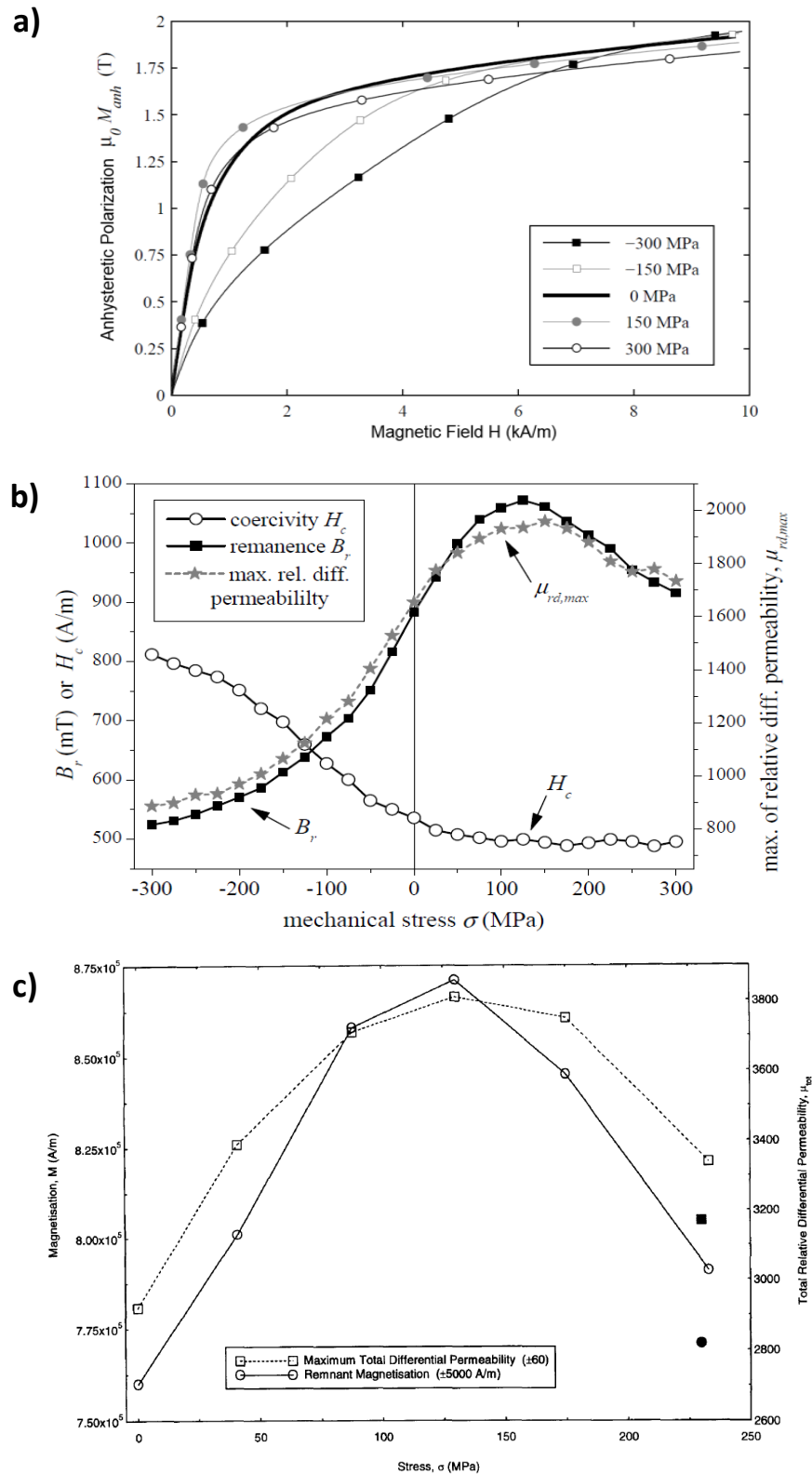
Fig. 3.30 a) Anhysteretic magnetisation curves for low carbon steel under different tensile loads; b) Variation of hysteretic parameters of low carbon steel with applied stress; c) Variation of maximum differential permeability and remanence of 50D pearlitic steel with tensile stress [68,70].

In cases where with increasing tension σ_T the $\frac{d\lambda}{dM}$ becomes negative within full range of magnetisation **M** , the stress equivalent field **H$_\sigma$** reduces the total magnetic field experienced by the material, which makes the values of susceptibility, permeability and remanence lower than those observed for an unstressed specimen, as shown for 0.85%C steel in Fig. 3.31a and 3.31b [69].
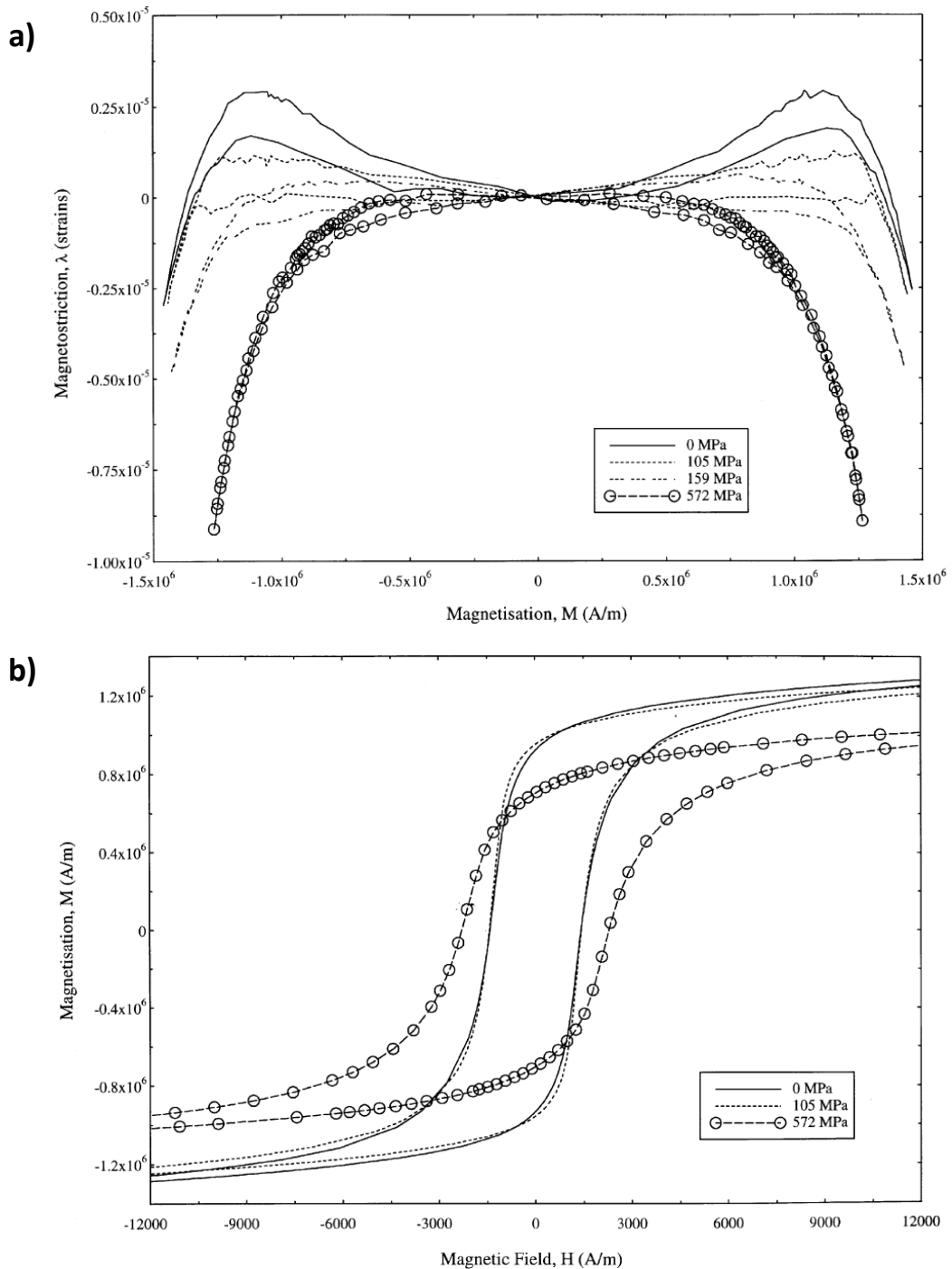

Fig. 3.31 a) Magnetostriction loops for 0.86%C steel subjected to various tensile stresses; b) Hysteresis loops for 0.86%C steel under different tensile loads [69].

In some magnetic materials the stress dependence of differential anhysteretic susceptibility at origin χ'_{an} and related χ'_{Hc}, μ'_{Hc} can be modelled using the previously introduced expression from work of Garikepati and Jiles (Equation 2.33) which was shown to be:

$$\chi'_{an} = \frac{M_{sat}}{3a - (\alpha + \frac{3b\sigma}{\mu_0})\, M_{sat}}$$

(3.10)

and can be further rewritten in a useful form for calculating stress:

$$\frac{1}{\chi'_{an}(\sigma)} = \frac{1}{\chi'_{an}(0)} - \frac{3b\sigma}{\mu_0}$$

(3.11)

which suggests a linear relationship of reciprocal susceptibility at origin $1/\chi'_{an}$ (and similarly $1/\chi'_{Hc}$, $1/\mu'_{Hc}$) with stress σ. This prediction was proven to be in good agreement with experimental data for AISI 4130 and 4140 steels subjected to various compressive and tensile loads, as shown in Figs. 3.32a and 3.32b [12, 71].
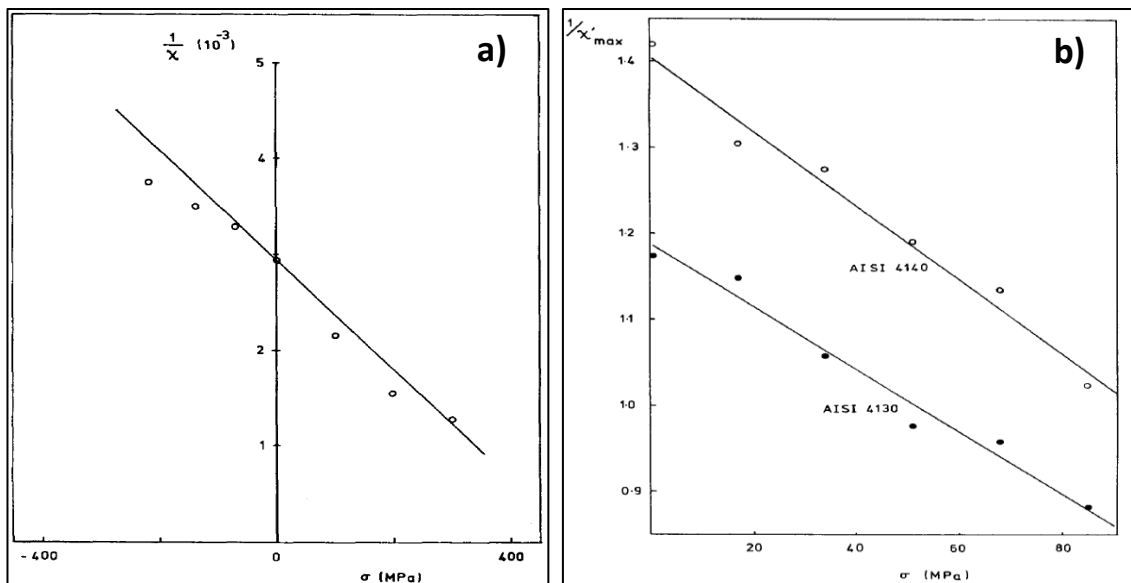

Fig. 3.32 Modelled linear approximation of: a) Reciprocal differential anhysteretic susceptibility at origin as function of stress in AISI 4130 steel; b) Variation of maximum reciprocal differential susceptibility of AISI 4130 and 4140 steels with stress [12, 71].

Although the above graphs confirmed that it is feasible to anticipate the changes of the reciprocal of χ'_{an} , χ'_{Hc} with stress using a convenient linear function, it must be noted that this approximation will be only accurate within range of stresses for which the slope $\frac{d\lambda}{dM}$ at low levels of **M** (represented by coefficient 'b' in Equation 3.11) does not significantly deviate from its value for unstressed condition. Therefore, in order to

make this model more generic the relation between the magnetostriction coefficient 'b' and stress needs to be included, which will be further discussed in Section 4.2.

The variation of hysteretic parameters with stress can be also modelled using the Jiles-Atherton or Preisach models of magnetic hysteresis, as reported in work of Jiles et al. [72], Lo et al. [73, 74], Sablik et al. [11, 75], Melikhov et al. [76] and Ktena et al. [77]. Detailed description of these models and their application to stress evaluation is beyond the scope of this thesis.

3.5 Micromagnetic non-destructive evaluation methods

3.5.1 Magnetoacoustic method

Magnetoacoustic emission (MAE) is an effect of generation of elastic waves in a ferromagnetic material due to changes of magnetostrictive strains via the creation, motion and annihilation of non-180° domain walls during magnetisation process. The magnetoacoustic emissions are typically detected by a piezoelectric transducer bonded onto a test specimen and the measured voltage signal is thoroughly amplified, filtered and smoothed. Owing to the fact that the stress affects the population and volume of non-180° domain walls, the amplitude of MAE of ferromagnetic materials is stress dependent, as shown in Figs. 3.33a and 3.33b for cases of low carbon steel and nickel [78]. The other factors influencing the MAE emissions are the magnetising frequency [79], microstructure [80] and sample geometry [81].
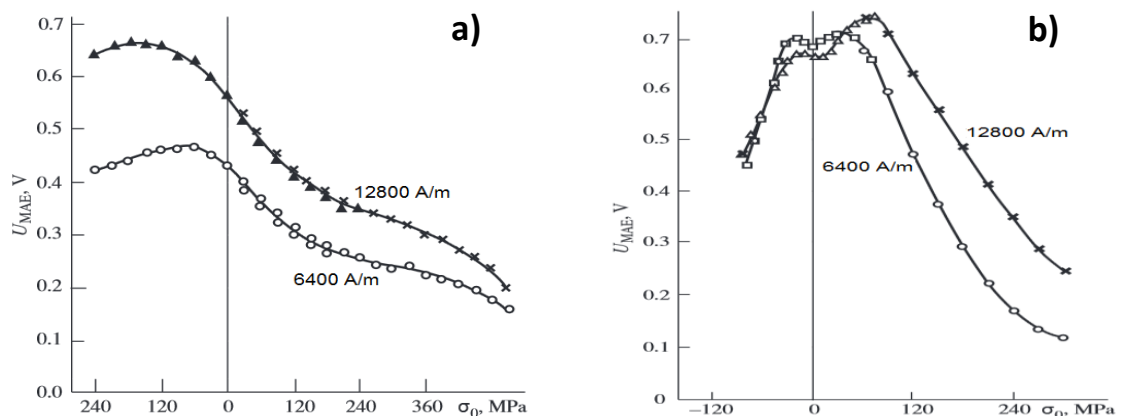

Fig. 3.33 Variation of mean-square values of MAE emissions with stress obtained for: a) low carbon steel and b) nickel, subjected to magnetic fields of 6400A/m and 12800A/m [78].

Since the MAE is closely related to the magnetic Barkhausen effect, these two methods can be used in conjunction for non-destructive evaluation of mechanical condition of ferromagnetic materials, as reported in work of Theiner and Willems [82] and Wilson et al. [83].

3.5.2 Magnetic Barkhausen Noise method

Due to high sensitivity of Barkhausen emission to stress and microstructural changes the MBN method has become one of the most popular NDE tools for investigating these intrinsic properties of magnetic materials such as steels. The following sub-sections will discuss the typical Barkhausen Noise testing methodology, dependence of MBN on bulk mechanical properties, as well as the previous work on applications of MBN method for stress evaluation.

I. Magnetic Barkhausen Noise measurement technique

The measurement systems used for detecting Barkhausen emission in ferromagnetic materials comprise two main units which are:

- The magnetising unit which is used to provide the magnetic field **H** and induce the change in magnetisation. This unit is typically an electromagnet which includes a U-shape core made of soft magnetic material (such as electrical steel, mild steel, soft ferrite or nickel iron) with a wound coil carrying the magnetising current supplied from a voltage source, as indicated in Fig. 3.34. The strength of generated magnetic field applied to electromagnet core can be calculated from Ampere's law equation [84] as follows:

$$H = \frac{NI}{l} \qquad (3.12)$$

where N is the number of coil turns, I is the amplitude of the magnetising current and l is the length of coil.

By placing the electromagnet directly on the specimen a closed magnetic circuit is created with magnetic flux passing through the section of material located in between the electromagnet poles.
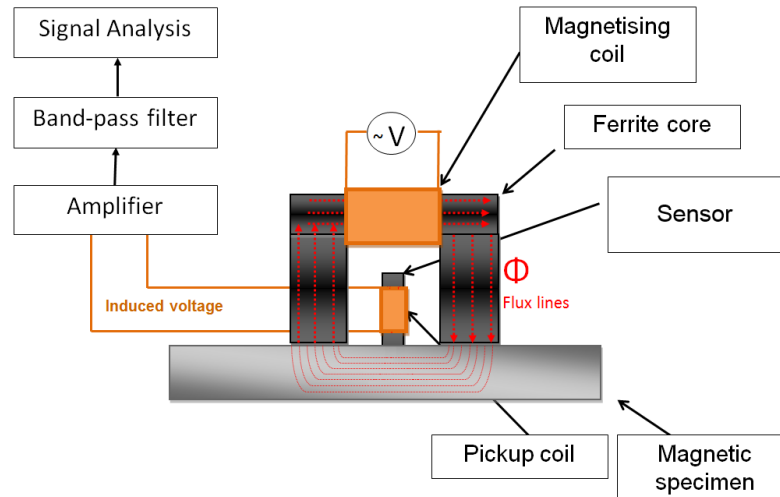
Fig. 3.34 Schematic diagram of typical Barkhausen Noise measurement set-up.

▪ The sensing unit which is used to detect Barkhausen emissions. The main component of this unit is the magnetic sensor which can pick-up the MBN signal generated by sudden ireversible changes in magnetisation within the specimen. This signal is typically recorded in a form of voltage pulses as a function of time. The most common type of magnetic sensor used for Barkhausen Noise measurements is the induction coil sensor [85] based on the principle of Faraday's law:

$$V = -N\frac{d\phi}{dt} \hspace{4cm} (3.13)$$

where V is the induced voltage, N is the number of turns, φ is the magnetic flux linking the coil.

The pick up coil used for MBN detection can be wound directly on the sample or enwrapped on a ferromagnetic core (typically ferrite) which is positioned between electromagnet legs at the surface of sample region under magnetisation (as shown in Fig. 3.34). In the latter case the ferrite core with wound coil acts as an antenna (receiver) capable of detecting electromagnetic pulses generated due to Barkhausen emissions. Moreover the high resistivity of ferrite materials prevents generation of eddy currents within the core, which could undesirably bias the sensed MBN signal.

The original voltage data obtained from the sensor output contains the low frequency component with superimposed MBN emission as shown in Fig. 3.35a. Therefore in order to obtain the MBN data only (shown in Fig. 3.35b) the aquired signal needs to be high-pass filtered with a typical cut-off frequency of a few kHz.
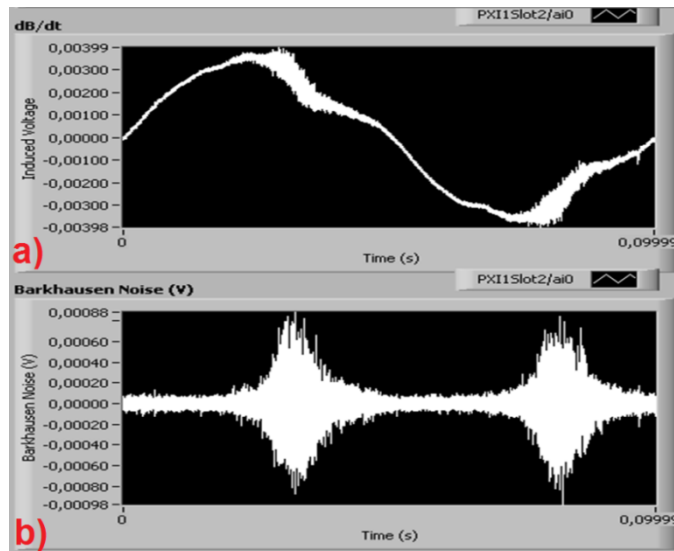
Fig. 3.35 a) Original voltage data obtained from the output of Barkhausen sensor; b) High-pass filtered Barkhausen signal.

The analysis of raw MBN signal is complex due to its stochastic nature and bipolarity. Hence in the post-processing phase the instantenous values of MBN RMS voltage bursts are averaged and smoothed using the moving average or Savitzky-Golay method [86, 87], as shown in Fig. 3.36a and 3.36b.
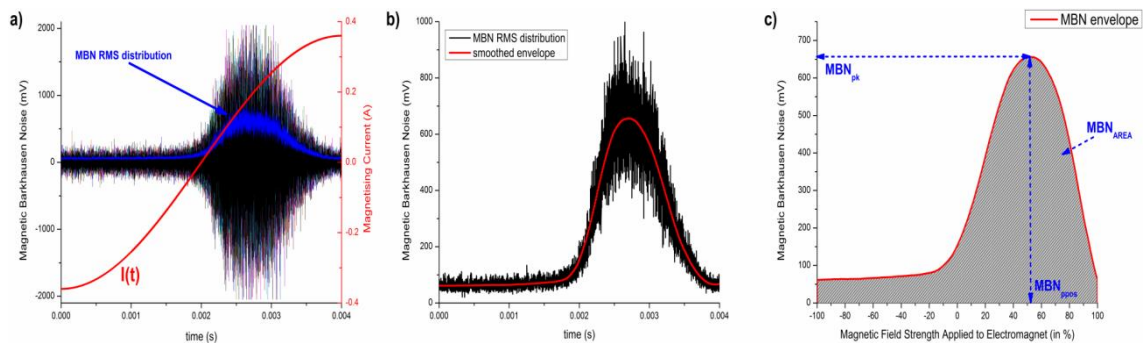

Fig. 3.36 a) Illustration of raw Barkhausen bursts and corresponding root mean square distribution of their instantaneous voltage pulses; b) Extraction of smoothed envelope of MBN RMS distribution; c) Smoothed MBN envelope with indicated analysis parameters.

The resulting rectified enevelope of the original MBN shown in Fig 3.36c allows a number of MBN parameters to be extracted such as: peak amplitude (MBN$_{pk}$), peak position (MBN$_{ppos}$) and area under the envelope (MBN$_{AREA}$) which can be thoroughly used for evaluation and modelling purposes.

II. Dependence of Magnetic Barkhausen Noise on bulk mechanical properties

When discussing the origin of Magnetic Barkhausen Noise the microscale hysteresis behaviour of domain walls was analysed (Fig. 2.18c). It was shown that by applying sufficient magnetic field a proportional force is exerted on a domain wall which allows it to overcome the local pinning sites such as inclusions, dislocations, and precipitates or other crystal imperfections and associated microstresses. The displacement of a domain wall in the form of Barkhausen jump was shown to correspond to changes in magnetisation whereas the particular wall position reflected the level of magnetisation. This elemental model of the local magnetisation process under influence of an applied field can be further extrapolated to describe the macroscale magnetic behaviour. In such a case the main pinning features affecting the bulk magnetic properties (such as permeability, coercivity, remanence and MBN parameters) will be the density and strength of all pinning sites present within the material.

In steel the character and distribution of pinning sites is governed by its microstructure which can contain single or multiple numbers of iron-carbon metallurgical phases. The common types of phases present in industrial steel at room temperature are: ferrite, cementite, martensite and austenite, where each of them can be differentiated in terms of their effective grain size, iron crystalline structure and amount of carbon atoms in the lattice [32]. The typical production processes which are used to induce a desirable phase in steel include heat treatment and both hot and cold working [86]. The description of microstructural (pinning) features determining mechanical and magnetic properties of all four mentioned phases and their combinations is given below:

▪ *Ferrite* is a metallurgical phase of steel comprising predominantly iron atoms organised in body centred crystalline (bcc) structures with maximum solubility of carbon at room temperature of only 0.005% [88]. The average size of ferrite grain depends mostly on the cooling rate used in the heat treatment process. The typical microstructure of very low carbon steel (0.002% C) which consists of only ferrite grains and grain boundaries is shown in Fig. 3.37.
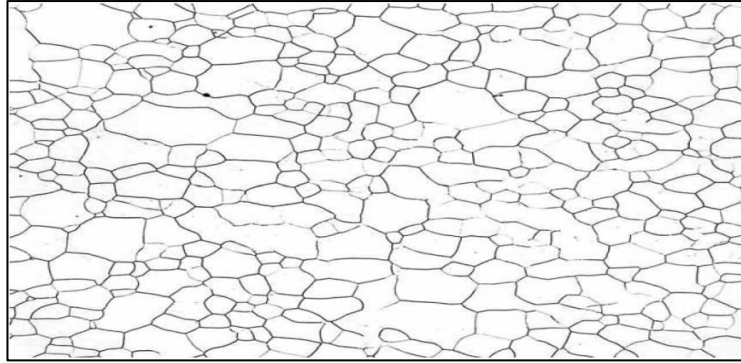
Fig. 3.37 Typical ferritic steel microstructure [88].

Because of very low carbon content and relatively low number of grain boundaries ferrite is considered as magnetically and mechanically soft with the hardness determined by its grain size. The low density and strength of pinning sites (grain boundaries, carbon atoms) in ferrite lead to high differential permeability values and small coercivity. In terms of MBN parameters ferrite exhibits high Barkhausen Noise amplitudes with peak position located at relatively low field strength as the domain walls can move over large distances with high velocity and require low depinning force to break away from the pinning sites.

- *Cementite* is an iron carbide compound which is formed by combination of iron and carbon in excess of the carbon solubility limit. This hard and brittle compound has the chemical formula Fe_3C and a carbon content of 6.7%. It can be observed in the form of particles at ferrite grain boundaries as shown in Fig. 3.38 or filaments dispersed in a ferrite matrix in microstructure known as bainite (Fig. 3.39). However most typically in the majority of steels it combines with ferrite and creates lamellar (parallel plates) microstructure called pearlite (Fig. 3.40) [88].
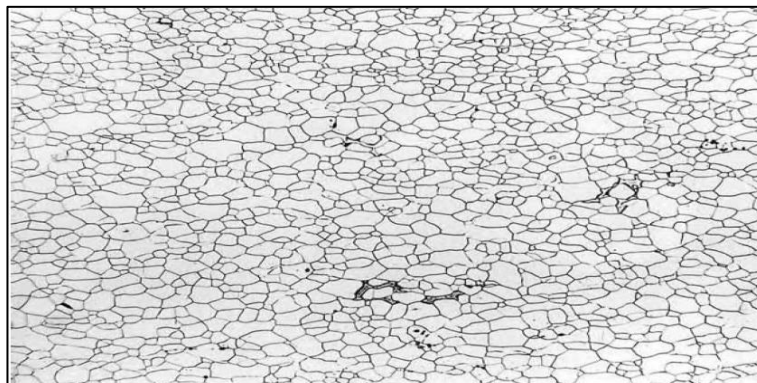

Fig. 3.38 Cementite (dark regions) in the form of particles at ferrite grain boundaries [88].
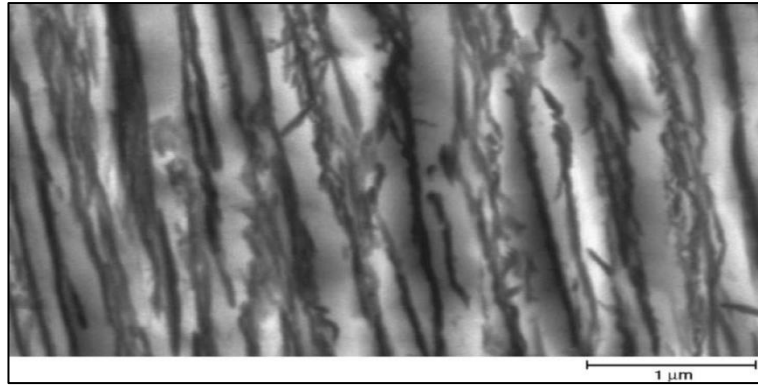
Fig. 3.39 Cementite (dark regions) in the form of filaments dispersed in a ferrite matrix in bainite microstructure [88].
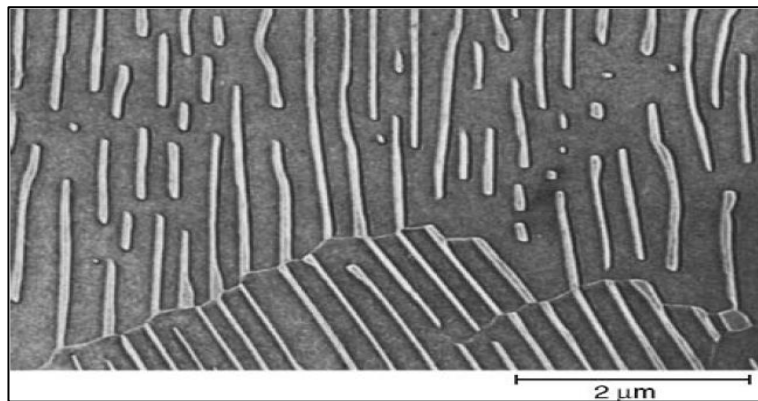

Fig. 3.40 Cementite (dark regions) and ferrite in the form of lamellar microstructure called pearlite [88].

All forms of cementite (particles, filaments and plates) improve the hardness and strength of steel but at the same time act as relatively strong pinning sites. Therefore the increase in the cementite volume results in higher coercivity and higher field strength corresponding to MBN peak position as well as in reduction in both differential permeability and MBN amplitude.

▪   *Martensite* is a form of ferrite which is supersaturated with carbon. It is produced in a process of quenching the steel where the very fast cooling doesn't give enough time for the carbon atoms to rearrange themselves, and some or all of them get trapped in the ferrite grains. Martensite is very hard and brittle thus it further undergoes an additional heating process, to temperatures between 350°C and 650°C, called tempering [88]. The tempering process allows some of the carbon to diffuse and form a carbide phase from the supersaturated iron lattice. This softens the steel and provides some ductility as well as allows the iron crystals to retrieve their bcc structure from the initial strained bct (body centre tetragonal) structure present in freshly

quenched martensite. A typical lath martensitic microstructure which is present in quenched steels with carbon content less than 0.6% is shown in Fig. 3.41 [88].
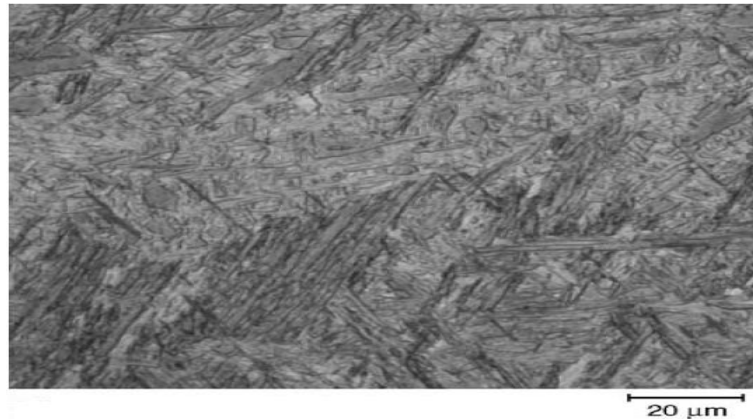

Fig. 3.41 Typical lath martensitic microstructure present in quenched steels with carbon content less than 0.6% [88].

The high density and strength of pinning sites in martensite in the form of carbon concentration, numerous grain boundaries and dislocations make it difficult to magnetise as the domain wall motion is strongly impeded. Therefore the average effective differential permeability and MBN amplitudes are very low whereas the coercivity and **H** location peak position are relatively high.

▪   *Austenite* is a paramagnetic iron phase with fcc (face-centred cubic) structure which occurs when the iron-based metal is heated above its eutectoid temperature. Typically if austenite is slowly cooled below this temperature level it decomposes into mixture of ferrite and cementite as the carbon diffuses. However in the case of rapidly cooled steels a considerable amount of austenite can be retained and form a combination with martensitic structure as shown in Fig. 3.42.
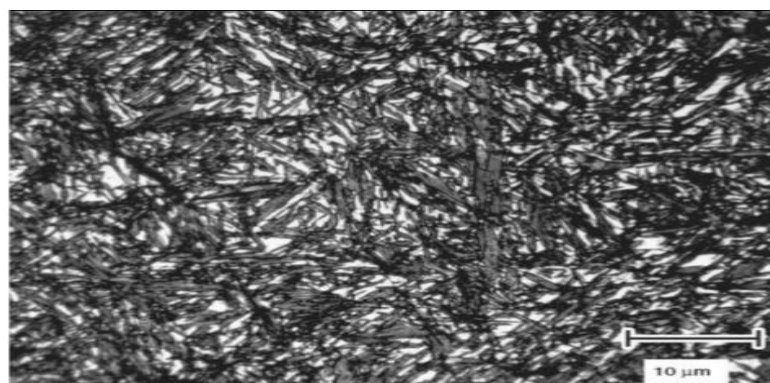

Fig. 3.42 Microstructure of water-quenched AISI 1080 steel showing plate martensite (dark regions) in combination with retained austenite (light regions) [88].

The amount of retained austenite in steel quenched to room temperature increases significantly with the carbon content and because it is softer than martensite it causes a decrease in hardness of steels with compositions above approximately 0.9%C [88]. As distinct from other microstructures the softening of steel, caused by the rise in paramagnetic austenite percentage and consequent reduction in amount of ferromagnetic martensite, results in a decrease in differential permeability, MBN amplitude and coercivity. This dependence of magnetic properties on the amount of retained austenite is often used for evaluation of stress-induced martensite in austenitic stainless steels [89].

A representative example of the microstructure dependence of MBN emission in SAE 1040 steel is shown in Fig. 3.43 [90] where:

a) hardest martensite (685HV) with strong and condensed pinning sites demonstrated lowest MBN amplitudes with peak position located at relatively highest level of applied field

b) tempered martensite, which was softened (310HV) by additional heating at 600°C allowing diffusion of carbon and consequently scattering of pinning sites, exhibited higher levels of MBN emission with MBN peak at lower **H** when comparing with initial as-quenched martensite

c) fine pearlite-ferrite with relatively moderate hardness (230HV) and pinning strength showed MBN amplitudes higher than those for martensitic phases with MBN_{ppos} at lower field

d) coarse pearlite ferrite with lowest hardness (178HV) and comparably weakest and dispersed pinning sites demonstrated highest MBN emission magnitudes and lowest field corresponding to MBN peak position
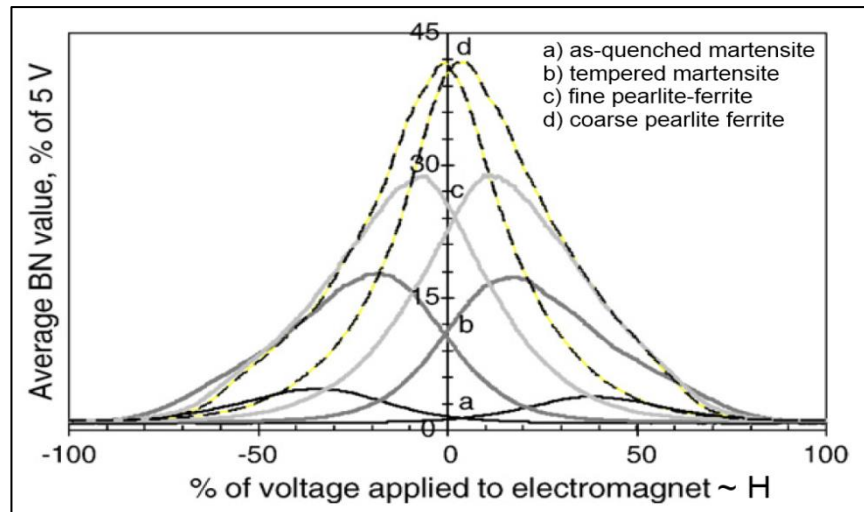
Fig. 3.43 MBN smoothed envelopes obtained for different SAE 1040 steel microstructures [90].

All microstructures studied for which the MBN envelopes are presented above can be seen in Figs. 3.44a to 3.44d.
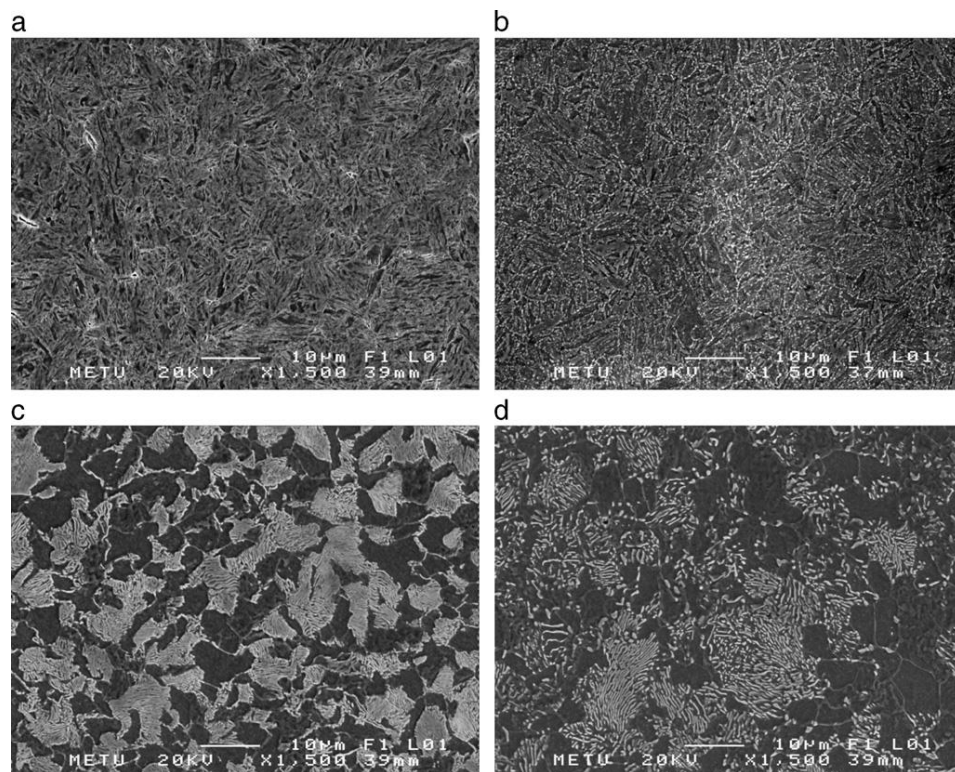

Fig. 3.44 SAE 1040 steel microstructures studied with Magnetic Barkhausen Noise: a) as-quenched martensite; b) tempered martensite; c) fine pearlite-ferrite, d) coarse pearlite-ferrite [90].

The relation between microstructural properties and pinning site features makes it possible to quantitatively evaluate mechanical hardness of steels using MBN method. However, when performing such an evaluation it is essential to know the stress

condition of the analysed material. This is caused by the fact that hysteretic and MBN properties of ferromagnets are also sensitive to type and amplitude of both applied and long-range residual stresses. The stress dependence of MBN is described in detail below.

It has been already discussed in Section 2.5 that mechanical stress can be treated as an equivalent field for which the sign depends on the type of stress (compressive or tensile) and slope of magnetostriction as function magnetisation $\frac{d\lambda}{dM}$ (Equation 2.25). Similar to an applied field, this stress-equivalent field can exert sufficient unpinning force, generated due to a change in the magnetoelastic energy, which induces non-180° domain wall motion to create a new optimal domain configuration of minimum total magnetic energy. Due to the presence of stress this new domain configuration will possess an additional form of anisotropy in which materials with a positive product of stress and magnetostriction ($\lambda\sigma>0$) the easy magnetisation plane lies along the stress direction whereas in materials with $\lambda\sigma<0$ the easy plane is at 90 degrees to stress direction. However it should be noted that in iron and steels the magnetocrystalline anisotropy is dominant since $K_1>>(3/2)\lambda_s\sigma$. Nevertheless, when analysing MBN emission under the action of applied field in an elastically stressed specimen the following cases can be considered:

- If $\frac{d\lambda}{dM}>0$, $\sigma>0$ or $\frac{d\lambda}{dM}<0$, $\sigma<0$ and **H** is applied along stress direction the stress equivalent field **H$_\sigma$** enhances the total effective field **H$_e$** and consequently increases the total depinning force exerted on domain walls allowing larger Barkhausen jumps generating higher MBN amplitudes than those which would be observed in stress-free specimen under the same **H**. In this case higher stress amplitude results in higher MBN amplitudes. This type of stress dependence of MBN can be observed in most of steels which have $\frac{d\lambda}{dM}>0$ within a wide range of loads and field values. Thus when subjected to progressively increased amplitude of tensile stress exhibit higher magnitude of MBN emission at the same applied field strength, as shown for high-strength carburised EN36 (SAE 3415) steel in Fig. 3.45a [91].

- If $\frac{d\lambda}{dM}>0$, σ<0 or $\frac{d\lambda}{dM}<0$, σ>0 and **H** is applied along the stress direction the stress equivalent field **H$_\sigma$** weakens the total effective field **H$_e$** and consequently reduces the total unpinning force exerted on domain walls. In this case the effective MBN emission will be lower than that observed for an unstressed specimen. Therefore in most steels the application of gradually increased compressive stress diminishes MBN amplitude within a wide range of **H,** as shown in Fig. 3.45b [91].
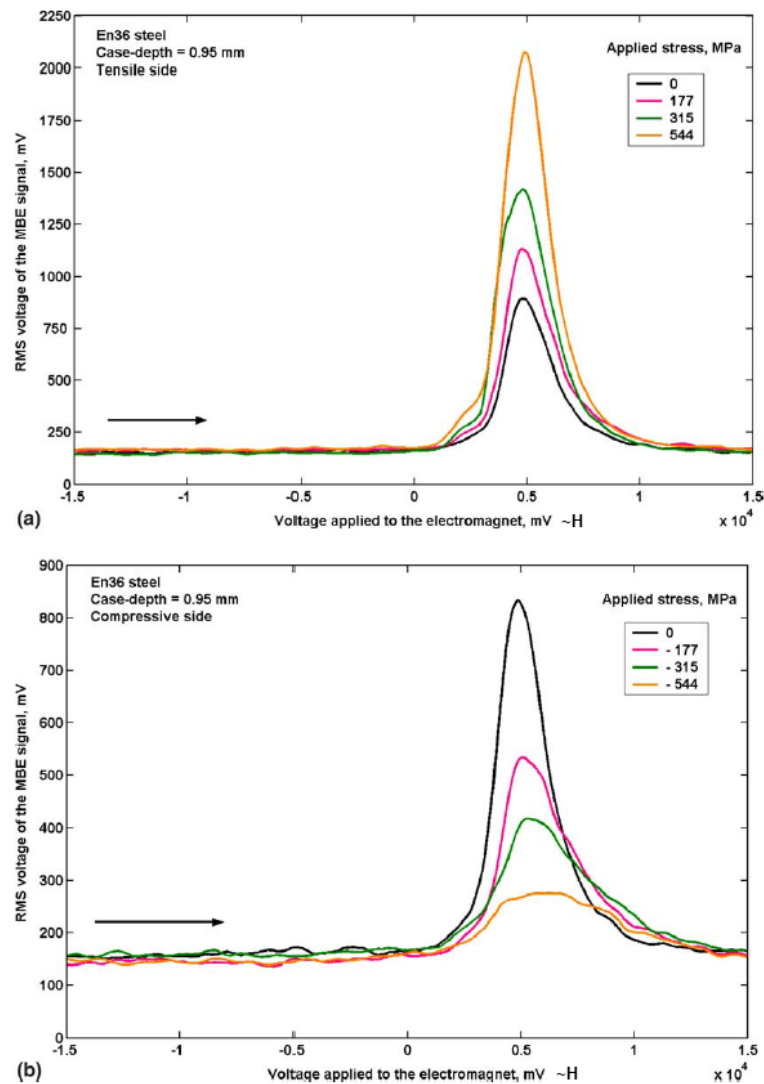

Fig. 3.45 Influence of a) tension and b) compression on Magnetic Barkhausen Noise in EN36 steel [91].

- In case of non-coaxial stress and applied field the resultant **H$_\sigma$** and its effect on total effective field and unpinning force can be calculated by incorporating the angular expression $(cos^2\theta - \nu sin^2\theta)$ where θ is the angle between direction of applied field **H** and stress axis, and ν is the Poisson's ratio (Equation 2.25).

Although, the stress dependence of MBN and differential permeability can be successfully explained by the concept of stress equivalent field, the practical implementation of this analytic expression in stress evaluation is more complex. This is mostly due to fact that in iron based polycrystalline materials the dependence of magnetostriction on magnetisation $\lambda(\mathbf{M})$ is not monotonic. In other words the magnetostriction slope $\frac{d\lambda}{d\mathbf{M}}$ can change its sign at some critical value of magnetisation $\mathbf{M_V}$ above which the effect of stress on both differential permeability and MBN amplitudes is reversed. This effect is known as Villari reversal [1]. An example for Villari reversal in pure iron is shown in Fig. 3.46.
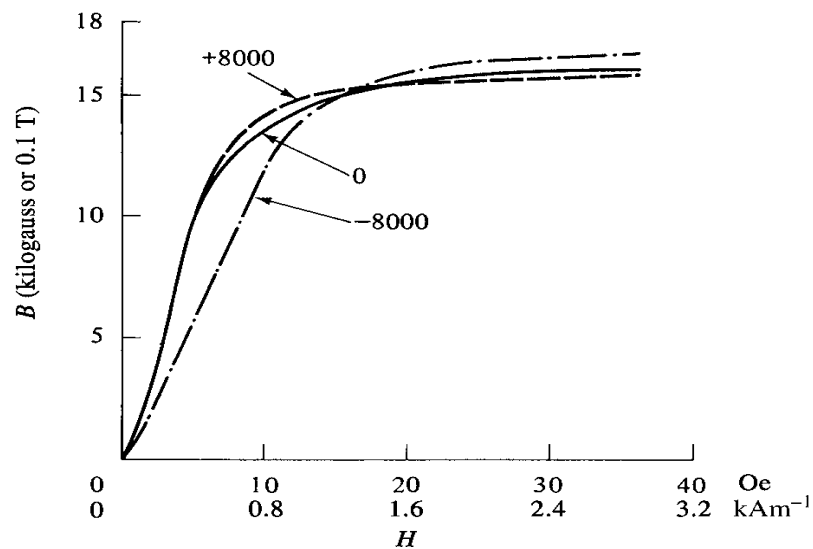

Fig. 3.46 Illustration of Villari reversal in pure iron [1].

In randomly oriented polycrystalline iron the trend of $\lambda(\mathbf{M})$ will depend on the combination of the magnetostrictive responses to given $\mathbf{H}$ of the individual grains as well as their relative orientation with respect to the direction of the applied field. Typical trends of $\lambda(\mathbf{M})$ and $\lambda(\mathbf{H})$ functions in unstressed iron have two distinguishable stages. In the first stage the magnetostriction keeps increasing under continuously ramped field as it is mostly generated by the motion of 90° domain walls and simultaneous expansion of 180° domains aligned along <100> direction and at non-right angles to field axis. The second stage begins when the field is high enough to cause rotation of moments away from <100> axes towards the <110> and <111> directions which causes the magnetostriction to decrease and slopes of $\lambda(\mathbf{M})$ and $\lambda(\mathbf{H})$

to be reversed. Typical λ(**H**) and λ(μ$_0$**M**) curves for unstressed iron are shown in Fig. 3.47a and 3.47b.
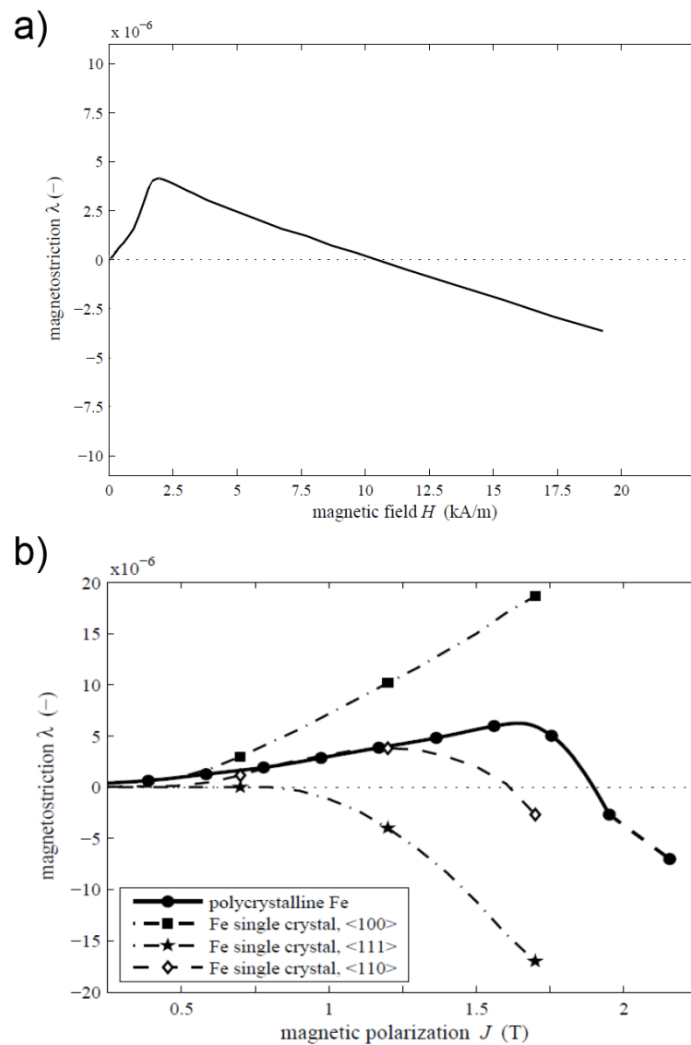

Fig. 3.47 a) Anhysteretic magnetostriction of iron as function of magnetic field; b) Magnetostrictive behaviour of polycrystalline and single crystal iron magnetised along principal directions [92] [93].

The presence of macrostress can considerably alter the domain structure in ferromagnetic materials (Fig. 2.10) and influence their λ(**M**) and λ(**H**) characteristics. Fig. 3.48 shows an example of such a stress influence on the anhysteretic function λ(**H**) of iron, where the effects of compressive and tensile stresses can be described as follows:

▪ Compressive stress in iron increases the total volume and population of closure domains which leads to higher positive magnetostriction under an applied field. Consequently the level of Villari critical field **H$_V$** is also higher and the second section of

λ(**H**) with negative slope shifts up towards the positive λ region. For higher compressive stresses the effect becomes more pronounced.

▪ Tensile stress reduces the overall volume and number of closure domains and stimulates expansion of 180° domains having magnetisation at non-right angles to the stress axis. Therefore under low and moderate tension the initial rising slope of magnetostriction with field (caused by 90° domain wall motion) is reduced and the level of **H$_V$** is reduced. The falling section of λ(**H**) function shifts downwards to the negative λ regime. With increasing tension this effect becomes stronger and high tensile stress can result in significant annihilation of closure domains in which case the values of λ(**H**) function will be predominantly negative (as shown in Fig. 3.48 for 70MPa).
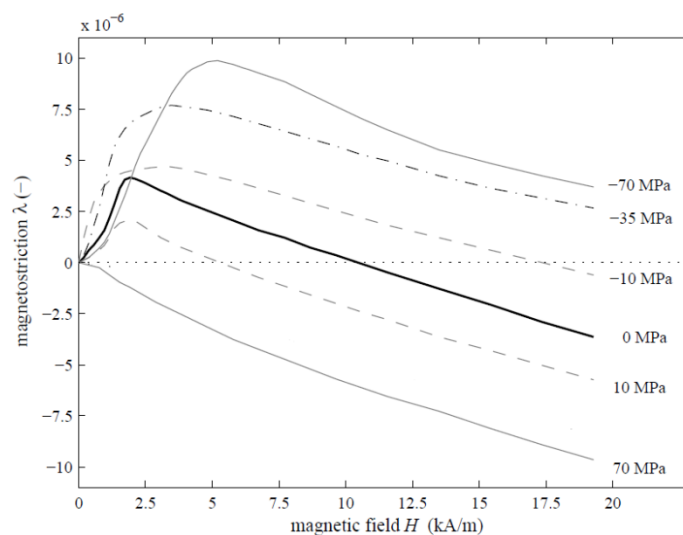

Fig. 3.48 Anhysteretic magnetostriction of iron obtained under different tensile and compressive stresses [92].

In steels the magnetostriction slopes $\frac{d\lambda}{d\boldsymbol{H}}$ and $\frac{d\lambda}{d\boldsymbol{M}}$ depend on microstructural features which govern the strength and density of pinning sites affecting the domain structure and domain wall motion. An example of this relation is shown in Fig. 3.49 where it can be seen that hard martensitic microstructure (Fig. 3.49b) has very low magnetostriction slope and therefore the stress-equivalent field and magnetomechanical effect are much weaker when comparing with those which can be observed in ferrite/pearlite (Fig. 3.49a).
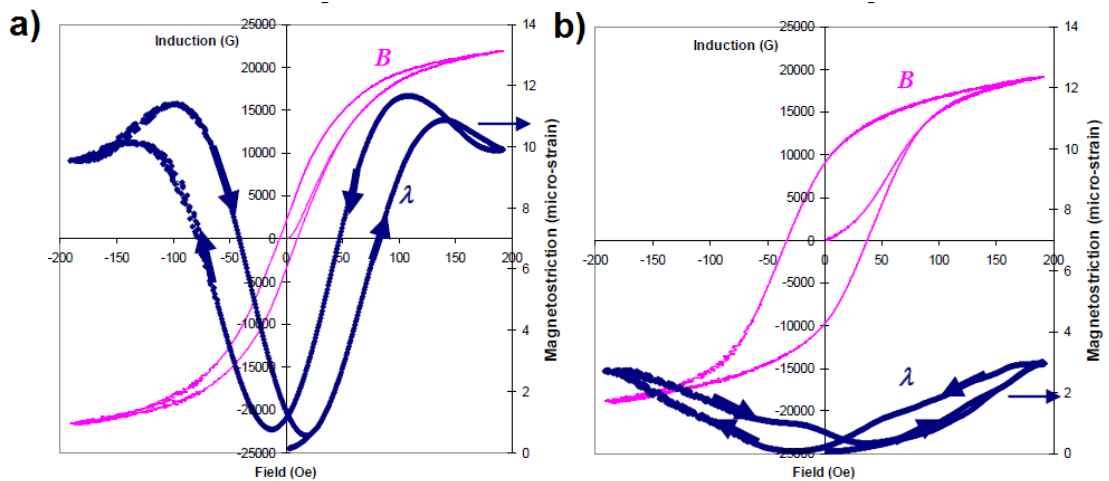
Fig. 3.49 Magnetostriction butterfly loops with corresponding hysteresis signatures obtained for a) ferrite/pearlite and b) martensitic steel microstructures [94].

Moreover the presence of pinning sites impedes the stress induced domain rearrangements (motion of 90° domain walls) and consequently modifies the effect of stress on λ(**M**) and λ(**H**) characteristics to a varying extent depending on the microstructural features. In low carbon steels having predominantly ferritic/pearlitic microstructure the stress influence on magnetostriction is quite similar to the one described for iron. However in fully pearlitic steels, having relatively higher density of pinning sites, the stress sensitivity of magnetostriction becomes less significant than that observed for iron, whereas in martensitic steels, exhibiting strong domain wall pinning, magnetostriction can be reasonably stress insensitive.

As a result it is expected that the response of magnetic parameters such as maximum differential susceptibility χ'_{Hc} and MBN peak amplitude to mechanical stress would vary in different grades of steels having various microstructures. The slopes of $\chi'_{Hc}(\sigma)$ and $MBN_{pk}(\sigma)$ functions are typically much higher for softer steels having ferritic/pearlitic phases and these functions can exhibit saturation or even reversal at some critical value of elastic tensile stress. Whereas in the case of steels with harder martensitic microstructures the slopes of $\chi'_{Hc}(\sigma)$ and $MBN_{pk}(\sigma)$ are less but should not vary much within the elastic stress regime. This emphasizes the fact that when performing stress evaluation in machined steel specimens of given grade using magnetic methods it should be assured that their microstructures do not vary significantly, i.e. no phase transformation has occurred during their manufacturing

process as this would additionally bias the trends of $\chi'_{Hc}(\sigma)$ and $MBN_{pk}(\sigma)$. More detailed discussion regarding the expected behaviour of maximum differential susceptibility and MBN peak amplitude in stressed steels having various microstructures will be given in Section 4.2. It will be shown that by taking into account the magnetostrictive properties of steels and their stress dependence, as well as the occurrence of Villari reversal the quantitative predictions of trends of $\chi'_{Hc}(\sigma)$ and $MBN_{pk}(\sigma)$ functions can be successfully made.

III. Previous work

The first attempts to use the Barkhausen effect to detect stress were reported in the late 1960s and 1970s by Leep [95], Pasley [96] and Titto [97]. Especially the work of Pasley helped the MBN method to gain acceptance as a viable stress measurement application, as he showed a distinct increase in MBN peak amplitude with increasing tension and an opposite trend in compression in the investigated steel specimens. Since the publication of their work a number of authors have identified a correlation between stress and various MBN parameters such as peak amplitude (MBN_{pk}) [98, 99, 100, 101], root-mean-square of Barkhausen noise (MBN_{RMS}) [102, 103], number of Barkhausen pulses (N_{MBN}) [104], Barkhausen Noise energy (MBN_{EN}) [105, 106], width (FWHM) and area (I_{MBN}) of MBN bursts [65, 107].

As the peak amplitude of MBN is directly proportional to differential susceptibility χ'_{Hc} and permeability μ'_{Hc} at the coercive point (Equation 2.39) the trends of changes of this Barkhausen parameter in transition from maximum compression to maximum tension are consistent with those already described for the bulk magnetic properties obtained from hysteresis measurements in Section 3.4.2, i.e. consequent rising (Fig. 3.50), successive declining (Figs. 3.51a to 3.51d) and non-monotonic (Figs. 3.52a and 3.52b).
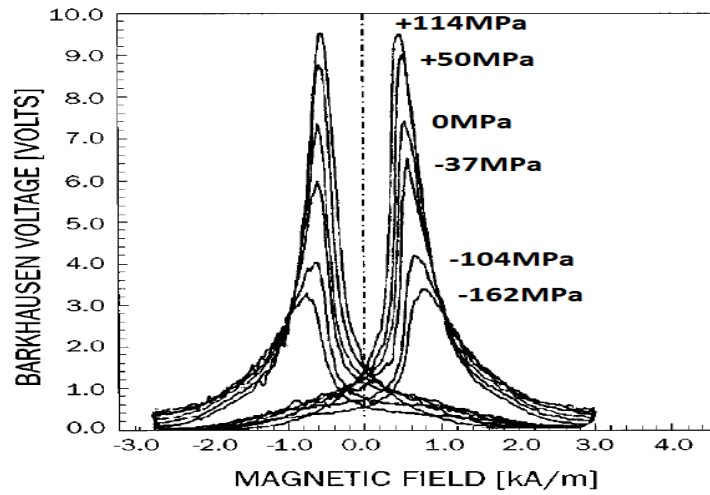
Fig. 3.50 MBN envelopes for XC10 steel subjected to different amplitudes of applied stress [65].
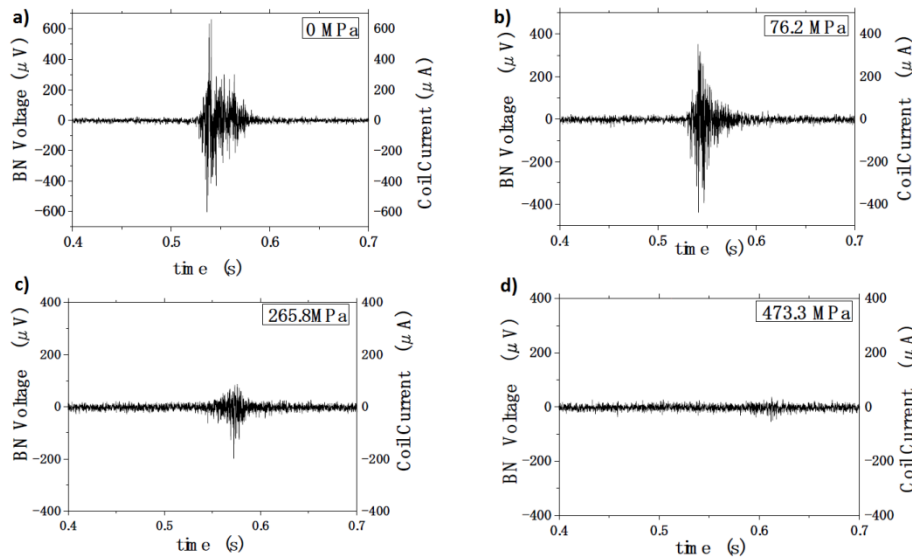

Fig. 3.51 MBN emissions obtained for rolled nickel plates under various magnitudes of tensile stress [109].
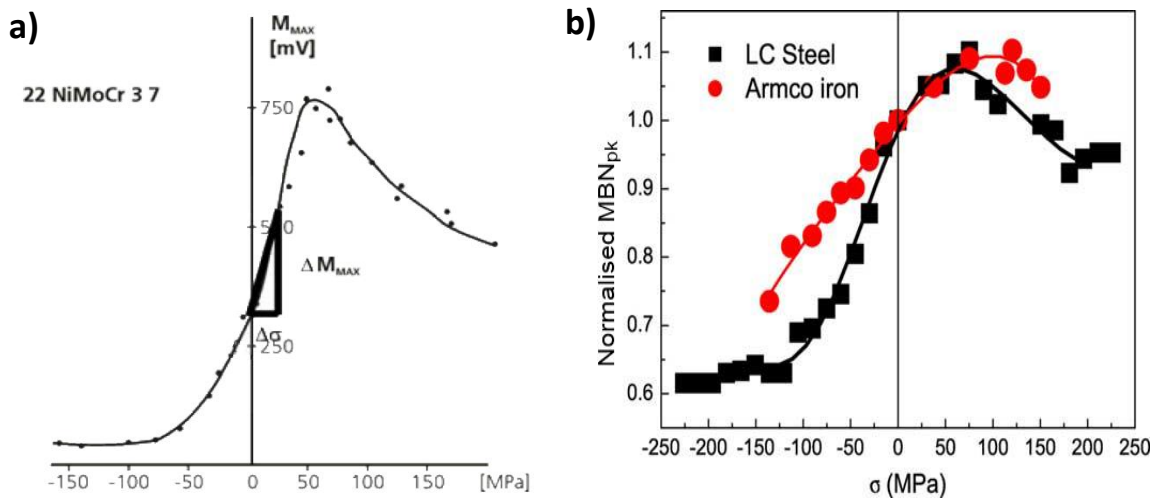

Fig. 3.52 Non-monotonic variation of MBN peak amplitude with applied stress for a) 22NiMoCr 37 pressure vessel steel; b) low carbon steel and Armco iron [100, 101].

In the case of the single-peak Barkhausen bursts the root-mean square of the signal (also referred to by some as the magnetoelastic parameter *mp* [108]) is proportional to peak amplitude and therefore trends of MBN$_{RMS}$(σ) are analogous to MBN$_{pk}$(σ), as shown in Fig. 3.53.
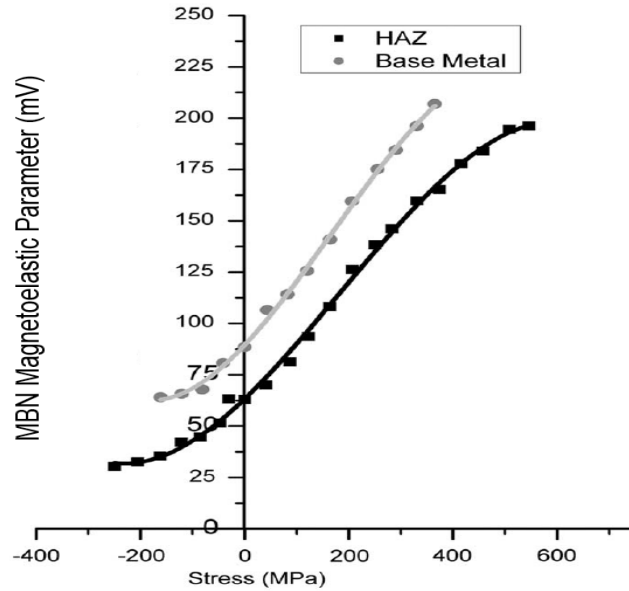

Fig. 3.53 MBN root-mean-square as function of applied stress for API 5L X70 steel before (base metal) and after welding process (HAZ – heat affected zone) [103].

The only experimentally validated approach of modelling the stress dependence of MBN amplitude was reported by Lo [73]. In his work the effect of applied stress was incorporated into the expression for differential irreversible susceptibility χ'_{irr} via the alterations of effective interdomain coupling parameter α_{eff} and the pinning coefficient k_{eff} being approximately equal to coercivity in soft magnetic materials. The mathematical formula used by Lo for computing χ'_{irr} was given as:

$$\chi'_{irr} = \frac{M_a - M_{irr}}{\left(\frac{k_{eff}\delta}{\mu_0}\right) - \left[\alpha_{eff} + \left(\frac{3\sigma}{2\mu_0}\right)\left(\frac{\partial^2\lambda}{\partial M^2}\right)\right](M_a - M_{irr})} \tag{3.14}$$

where the **M**$_a$ and **M**$_{irr}$ are the values of anhysteretic and irreversible magnetisations which were obtained using the modified Langevin equation and Jiles-Atherton hysteresis equation respectively. The k$_{eff}$ was determined from the measured hysteresis loops for different stress levels, δ was a directional parameter having a value of +1 for increasing **H** and -1 for decreasing **H**, the $\frac{\partial^2\lambda}{\partial M^2}$ was obtained from

94

measured magnetostriction data and the α_{eff} was calculated from the following expression:

$$\alpha_{\text{eff}} = \alpha + \frac{3b\sigma}{\mu_0} \qquad (3.15)$$

where α is the mean field coupling parameter and b is the magnetostriction coefficient from the parabolic approximation of the measured magnetostriction curves.

The computed values of χ'_{irr} were subsequently used to predict the Barkhausen emission as function of time using the modified ABBM model rewritten in terms of rate of irreversible changes in magnetisation M_{irr} governed by:

$$\frac{d(\mu_0\dot{M}_{irr})}{dt} = \frac{1}{\sigma_e GS}\left(\frac{dH_a}{dt} - \frac{dH_p}{dt}\right) - \frac{\mu_0\dot{M}_{irr}}{\sigma_e GS\chi'_{irr}} \qquad (3.16)$$

where $\frac{dH_a}{dt}$ is the rate of change of applied field, S is the cross-sectional area and H_p is the local pinning field analogous to the one from the original ABBM model but redefined in terms of M_{irr}.

The stress dependence of the RMS of both measured and simulated Barkhausen signals (normalised with respect to values at σ=0MPa) obtained by Lo for AISI 410 stainless steel are depicted in Fig. 3.54. It can be seen that a reasonable agreement was found within the stress range from approx. -200MPa to +200MPa.
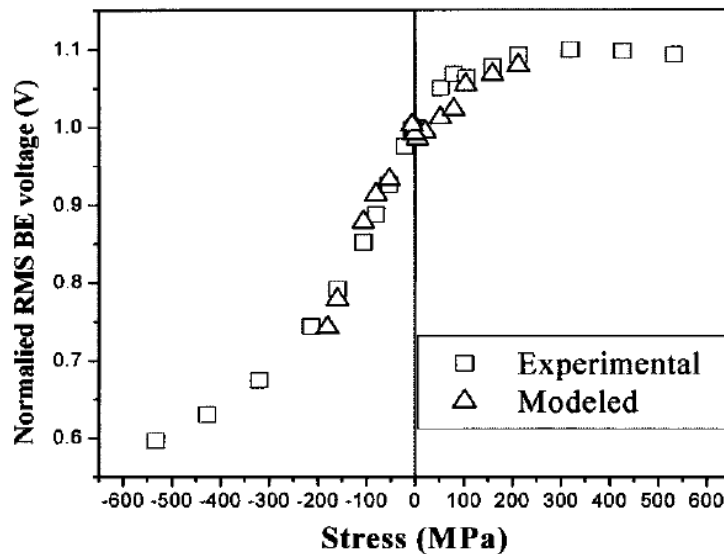

Fig. 3.54 Stress dependence of the normalised root-mean-square of measured and simulated Barkhausen signals obtained for AISI 410 stainless steel [73].

Despite achieving a good approximation of the experimental data of MBN $_{RMS}(\sigma)$ with modelled MBN $_{RMS}$ values, the procedure proposed by Lo relies mostly on the complex analysis of the measured, simulated and extracted hysteresis parameters rather than measured Barkhausen signal, and hence cannot be directly implemented into MBN non-destructive method. Therefore an alternative and much simpler method of stress evaluation using the correlation between directly measured Barkhausen parameters and hysteretic properties will be developed and presented in Chapter 4. This model will be shown to be able to describe the stress effects on MBN$_{pk}$ in a wide variety of magnetostrictive materials. The anticipated behaviour of 1/ MBN$_{pk}$ with stress based on the model will be validated by experimental results obtained for high-strength steels. The analogous magnetoelastic effect of both applied stress and long range Type I residual macro-stress on MBN emissions will be justified, and the model predictions will be validated for materials with both positive and negative magnetostrictions. Moreover, the generality of the proposed MBN model will be confirmed by its successful application in the quantitative stress evaluation in different types of steel.

Finally, a new comprehensive method for determining depth profiles of properties such as residual stress using Magnetic Barkhausen Noise measurements will be presented. This proposed novel methodology will show how to extract the Barkhausen emissions and related stress information from different points of origin using some simplifying assumptions.

3.6 Summary

This chapter provided the insight into industrial motivations for this research related to evaluation of integrity of steel components. It provided detailed background on the origin and significance of mechanical factors such as hardness, residual and applied stresses and structural defects in terms of their direct influence on the fatigue life of industrial steel components. Details of NDE measurement techniques, their advantages and disadvantages, as well as previous work on application of non-magnetic and magnetic NDE methods for flaw and stress detection were discussed.

4. Evaluation of stress using Magnetic Barkhausen Noise method

4.1 Introduction

In this chapter a new model relating the MBN peak amplitude and stress for materials having different magnetostrictive behaviour under load is proposed and validated. The derivation of underlying equations is presented in Section 4.2, followed by description and discussion on the verifying experimental procedure and results from MBN evaluation of surface hardened steel samples in Sections 4.3 to 4.5. In Section 4.6 the newly developed MBN model is applied to previously published results to demonstrate its generality. In Section 4.7 a new method for determining depth dependence of residual stress from measured magnetic Barkhausen signals is proposed. A complete set of equations is developed for describing the detected Barkhausen signals in terms of the actual emissions that are generated inside the material and how these appear when they propagate to the surface. A case study of depth profiling in a specimen that consists of multiple layers with different, but uniform, physical properties is presented. Finally, these latest findings and their relevance to non-destructive evaluation of stress are summarised in Section 4.8.

4.2 Development of MBN model for stress evaluation

It has been already discussed in Section 3.4.2 that for the case of coaxial stress and magnetisation the variation of the maximum differential anhysteretic susceptibility at origin χ'_{an} for materials which magnetostriction is relatively insensitive to stress can be modelled using the following expression:

$$\frac{1}{\chi'_{an}(\sigma)} = \frac{1}{\chi'_{an}(0)} - \frac{3b\sigma}{\mu_0} \tag{4.1}$$

It is also known from previous work that in soft magnetic materials the maximum anhysteretic differential susceptibility χ'_{an} is approximately equal to the maximum differential susceptibility at the coercive point χ'_{Hc} [5, 71, 72, 110] and therefore Equation 4.1 can be re-written in terms of χ'_{Hc} as:

$$\frac{1}{\chi'_{Hc}(\sigma)} = \frac{1}{\chi'_{Hc}(0)} - \frac{3b\sigma}{\mu_0} \tag{4.2}$$

According to the JSW stochastic model (Section 2.6.2) the amplitude of Magnetic Barkhausen Noise at any given point of a hysteresis curve is proportional to the differential susceptibility at that point, so for their maximum values at coercivity point can be written using the expression:

$$MBN_{pk} = \mu_0 \gamma_{Hc} \chi'_{Hc} \dot{H}_{Hc}(\Delta t) \tag{4.3}$$

which can then be used to modify the Equation 4.2 in terms of MBN_{pk} to give:

$$\frac{\mu_0 \gamma_{Hc(\sigma)} \dot{H}_{Hc(\sigma)}}{MBN_{pk}(\sigma)} = \frac{\mu_0 \gamma_{Hc(0)} \dot{H}_{Hc(0)}}{MBN_{pk}(0)} - \frac{3b\sigma}{\mu_0} \tag{4.4}$$

Finally by making the following assumptions that:

a) the ratio of irreversible magnetisation change to total magnetisation change at coercivity does not vary with stress, such that $\gamma_{Hc(0)} = \gamma_{Hc(\sigma)} = \gamma_{Hc}$, and

b) the rate of change of applied magnetic field with time $\dot{H}$ at the Barkhausen peak amplitude for stressed and unstressed material is constant (triangular **H** waveform) or both Barkhausen peaks lie within close proximity at the steepest part of sinusoidal field, such that $\dot{H}_{Hc(0)} = \dot{H}_{Hc(\sigma)} = \dot{H}_{Hc}$

the Equation 4.4 can be further simplified and becomes:

$$\frac{1}{MBN_{pk}(\sigma)} = \frac{1}{MBN_{pk}(0)} - \frac{3b'\sigma}{\mu_0} \tag{4.5}$$

where b' is a new coefficient directly proportional to the original coefficient b describing the slope $\frac{d\lambda}{d\mathbf{M}}$ at low levels of magnetisation **M**, as follows:

$$b' = \frac{b}{\mu_0 \gamma_{Hc} \dot{H}_{Hc}} \tag{4.6}$$

The newly derived Equation 4.5 suggests that for the case of ferromagnetic materials which magnetostriction is relatively insensitive to stress the variation of the reciprocal of Barkhausen peak amplitude $1/MBN_{pk}$ with stress σ is analogous to $1/\chi'_{Hc}(\sigma)$, and therefore can be approximated with a linear function due to the direct relation between the coefficients b and b'. An example of this analogy can be shown by plotting $\chi'_{Hc}(\sigma)$, $MBN_{pk}(\sigma)$, $1/MBN_{pk}(\sigma)$ and $1/\chi'_{Hc}(\sigma)$ normalised with respect to their values at zero stress for a hypothetical case of a soft ferromagnetic material having χ'_{Hc} =1000 at σ=0, and fixed value of $b(\sigma)=2\times10^{-18}$ $[1/(A/m)^2]$ within the stress range from -150MPa to + 150MPa, as presented in in Figs. 4.1a to 4.1d.
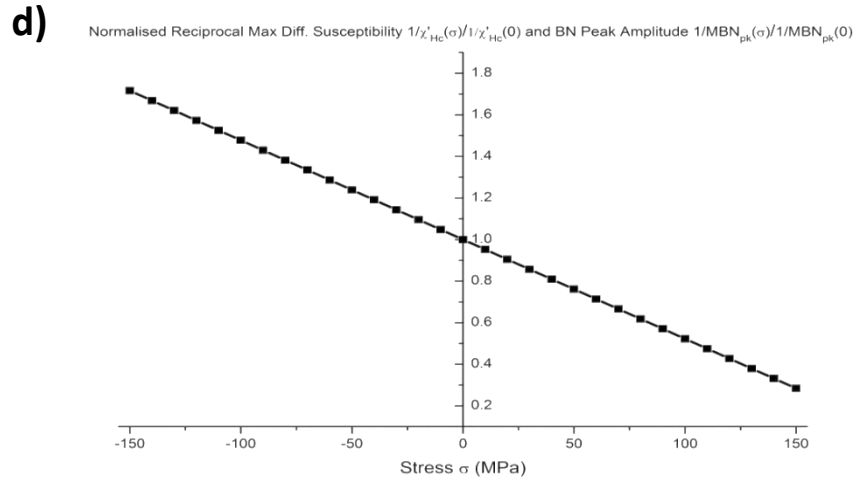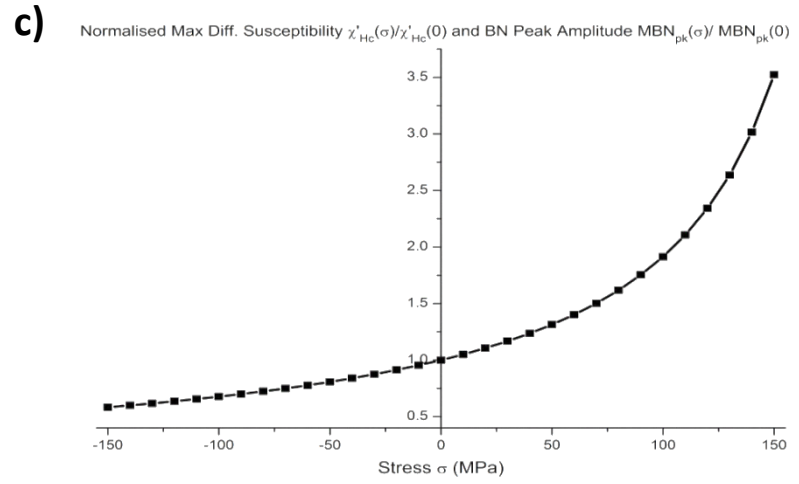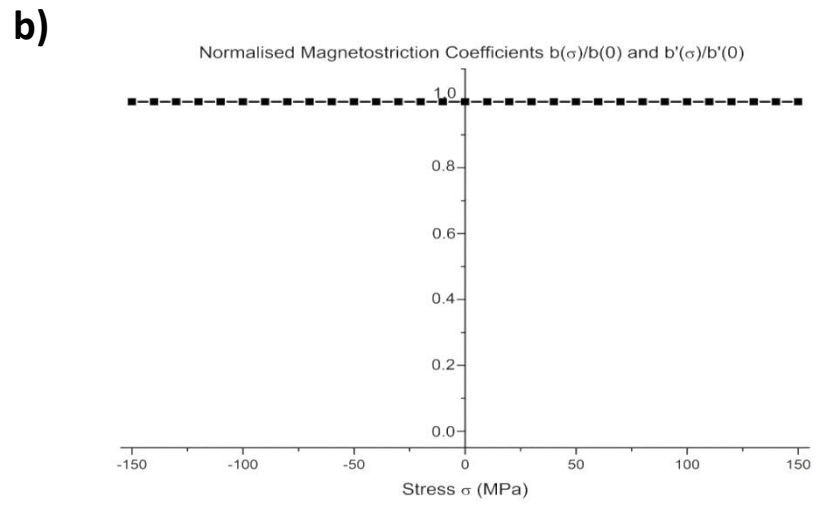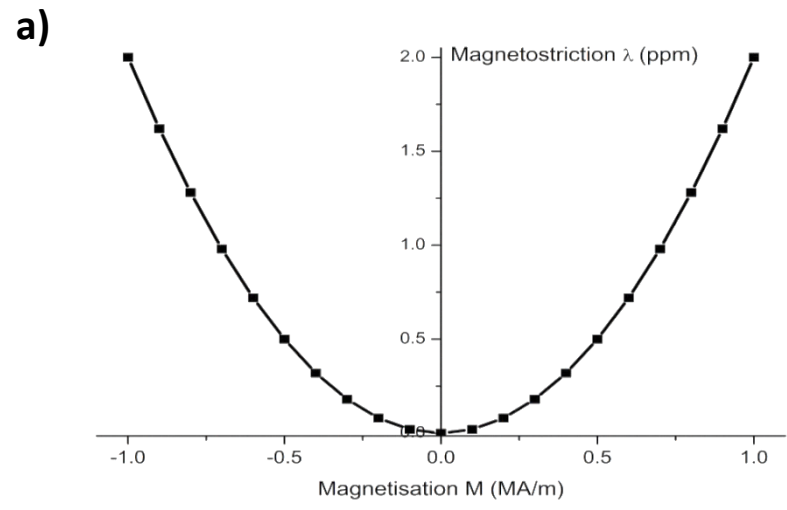
Fig. 4.1 a) Parabolic approximation of hysteresis-free magnetostriction curve with b=2×10⁻¹⁸; b) Normalised magnetostriction coefficients b and b' invariant with stress; c) Normalised maximum differential susceptibility χ'_{Hc} and MBN peak amplitude MBN_{pk} as functions of stress; d) Dependence of normalised reciprocal maximum differential susceptibility $1/\chi'_{Hc}$ and reciprocal MBN peak amplitude $1/MBN_{pk}$ on stress approximated with linear function.

For ferromagnetic materials with a magnetostriction slope at low **M** (and hence **B**) that are considerably altered by stress (as shown in Figs. 4.2a to 4.2c) both Equations 4.2 and 4.5 would need to be extended to account for the stress dependence of magnetostriction coefficients b and b', as follows:

$$\frac{1}{\chi'_{Hc}(\sigma)} = \frac{1}{\chi'_{Hc}(0)} - \frac{3b(\sigma)\sigma}{\mu_0} \tag{4.7}$$

$$\frac{1}{MBN_{pk}(\sigma)} = \frac{1}{MBN_{pk}(0)} - \frac{3b\prime(\sigma)\sigma}{\mu_0} \tag{4.8}$$
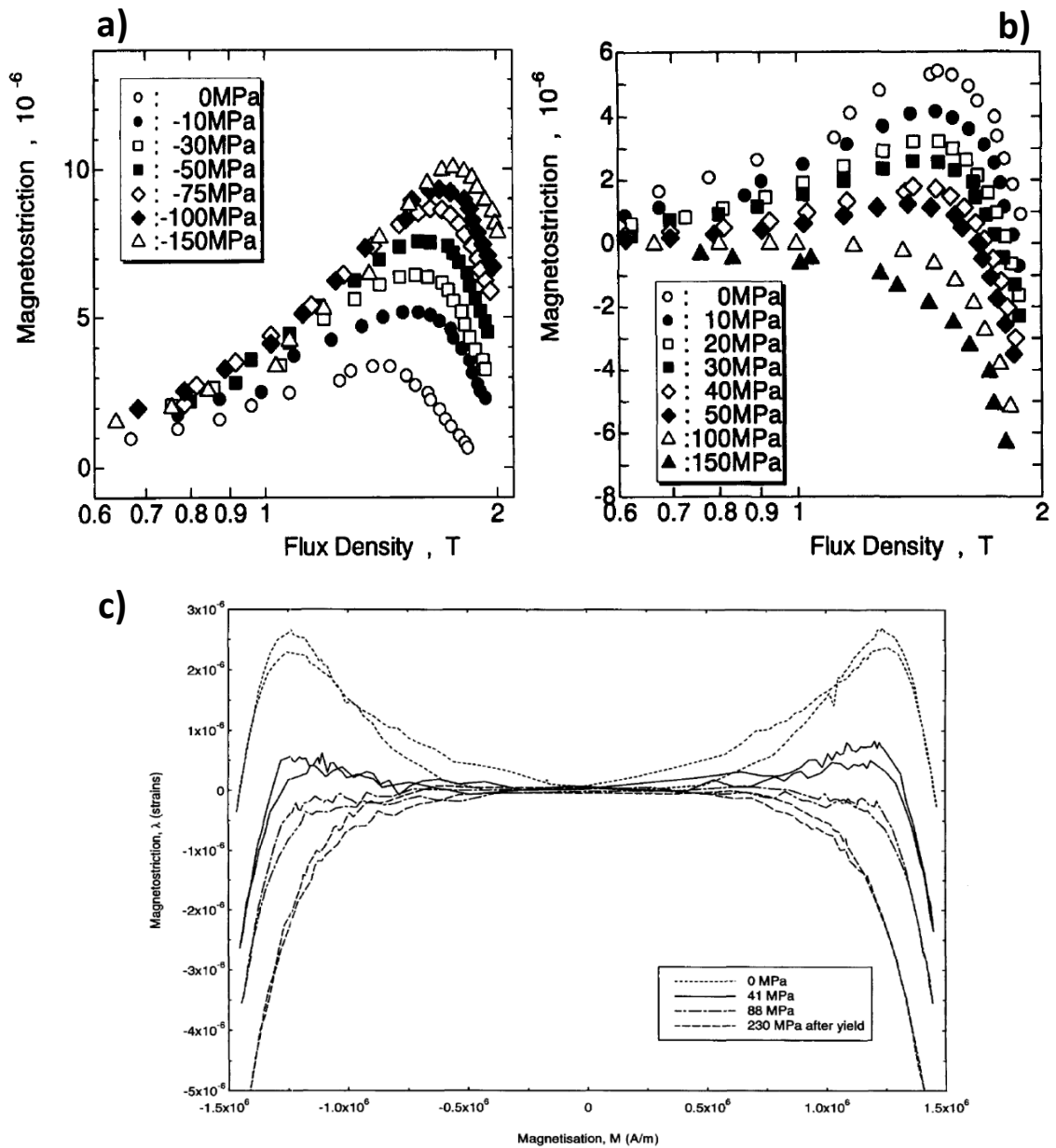

Fig. 4.2 a) & b) Effects of compressive and tensile stresses on magnetostriction curves in JIS-SS400 low carbon steel; c) Influence of tensile stress on magnetostriction butterfly loops in 50D pearlitic steel [69, 111].

The changes of coefficients b and b' with stress are difficult to predict theoretically but can be extracted from the measured values of $\chi'_{Hc}(\sigma)$ and $MBN_{pk}(\sigma)$ using the following equations:

$$b(\sigma) = \frac{\mu_0}{3\sigma}\left(\frac{1}{\chi'_{Hc}(0)} - \frac{1}{\chi'_{Hc}(\sigma)}\right) \qquad (4.9)$$

$$b'(\sigma) = \frac{\mu_0}{3\sigma}\left(\frac{1}{MBN_{pk}(0)} - \frac{1}{MBN_{pk}(\sigma)}\right) \qquad (4.10)$$

In general the trends reported for iron and low carbon steels showed that the slope of $\frac{d\lambda}{dM}_{M=0}$ is reduced and can become negative under the influence of increasing tension, whereas under increasing compression it initially rises and starts to decline, as depicted in Figs. 3.48 and 4.2.

Functions of $\chi'_{Hc}(\sigma)$ and $MBN_{pk}(\sigma)$ as well as $1/\chi'_{Hc}(\sigma)$ and $1/MBN_{pk}(\sigma)$ for materials with magnetostriction that is sensitive to stress can be modelled using Equations 4.7 and 4.8. An example of such a modelling was performed by incorporating the relative variations of $b(\sigma)$ with respect to $b(0)$ obtained from the best parabolic approximations of the experimental curves from Figs. 4.2a and 4.2b. The initial magnetic parameters used at σ=0 remained unchanged, i.e. χ'_{Hc} =1000, $b(0)=2\times10^{-18}$ [1/(A/m)^2] and the analysed stress range was kept from -150MPa to + 150MPa. The projected curves are shown in Figs. 4.3a to 4.3d.
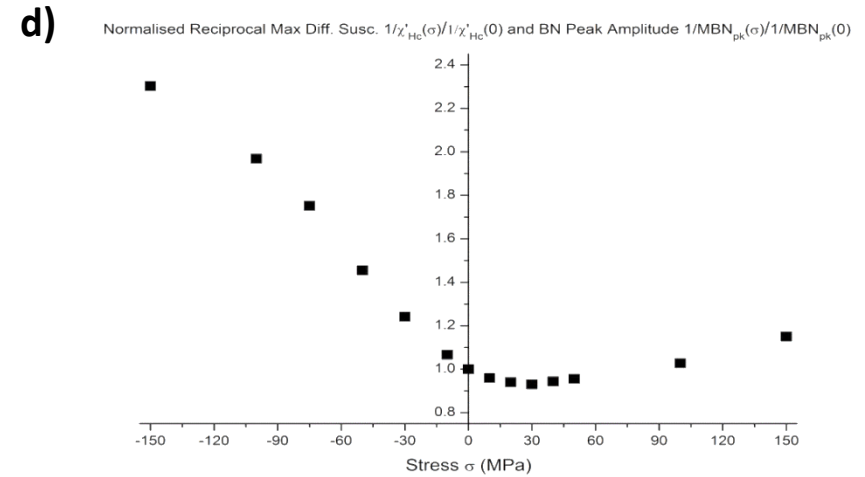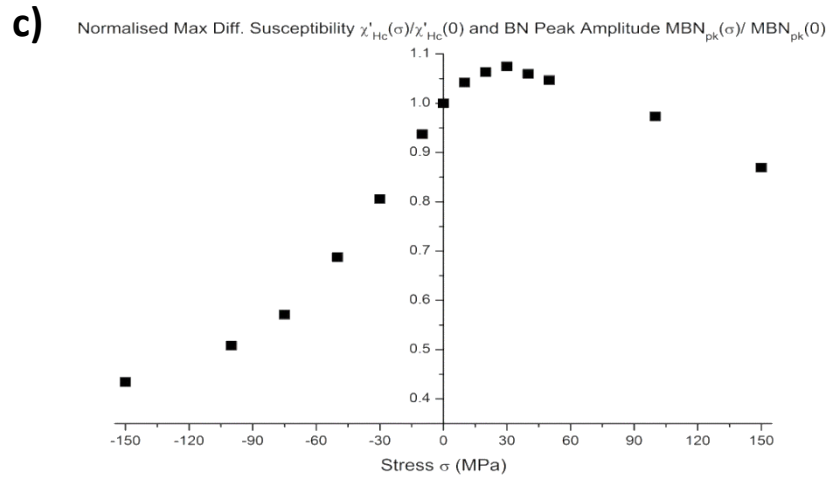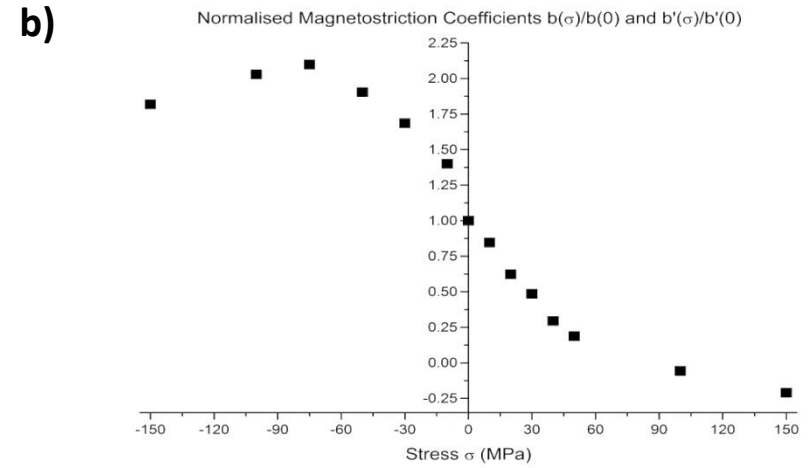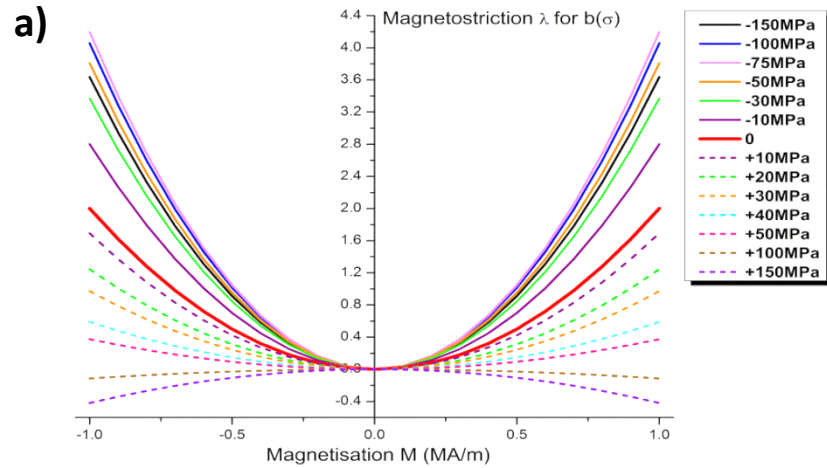
Fig. 4.3 a) Effects of stress on magnetostriction curves equivalent to that reported for low carbon steel and obtained via parabolic approximation of experimental data from [111]; b) Normalised magnetostriction coefficients b and b' as functions of stress; c) Normalised maximum differential susceptibility χ'_{Hc} and MBN peak amplitude MBN_{pk} as functions of stress; d) Non-linear dependence of normalised reciprocal maximum differential susceptibility $1/\chi'_{Hc}$ and reciprocal MBN peak amplitude $1/MBN_{pk}$ on stress.

The modelling output for the stress sensitive magnetostrictive material confirmed that after incorporating the stress dependence of coefficients b and b' both models of $\chi'_{Hc}(\sigma)$ and $MBN_{pk}(\sigma)$ produce non-monotonic trends, which resemble those previously reported and shown in Figs. 3.30b, 3.30c, 3.52a, 3.52b and 3.54. This implied that the extended versions of models have generic character and can be applied to describe the stress effects on $\chi'_{Hc}(\sigma)$ and $MBN_{pk}(\sigma)$ for a wide variety of ferromagnetic materials.

It will be shown in Section 4.5 that the newly developed model is capable of evaluating the magnetoelastic effect of both applied stress and long range Type I residual macro-stress on MBN emissions in high-strength steels, such as SAE9310 and SAE 6481. In order to quantitatively evaluate both types of stresses the slopes of anticipated linear behaviour of 1/ MBN_{pk} vs σ will be obtained by correlating the Barkhausen amplitude with known magnitudes of either applied load, or residual stress remaining in the interrogated components. The calibration procedures will be performed under controllable load using the Instron 8801 servo-hydraulic machine (for applied stress), and by linking the high-pass filtered MBN emissions with XRD residual stress measurements corresponding to similar depth of origin of approximately 10μm.

The differences in the origin and nature of applied and Type I residual macro-stresses will be revealed in the MBN results. In case of applied stress the MBN parameters will show clear trends as they will be acquired under ramped elastic tensile stress from a magnetised section of given microstructure, for which the density and strength of pinning sites can be assumed constant at all analysed stress levels. In case of residual stresses the trends in MBN will be more complex as their origins, related to various heating and cooling conditions, can be expected to alter the effective distribution and character of pinning sites within analysed surface regions.

4.3   Samples

The samples studied in this research were made of SAE 9310 and SAE 6481 steels which are commonly used in the automotive and aerospace industries for manufacturing gears, crankshafts, camshafts and other load-bearing parts. Their typical chemical compositions are given Table 4.1 [112, 113]. All samples were case hardened either by carburising (SAE 9310) or nitriding (SAE 6481) and had subsequently undergone different surface machining processes, such as grinding and shot-peening.

Depending on the type of test to be carried out the samples were divided into two groups. The first group comprised two tensile specimens made of each grade of steel which were designated for MBN evaluation under applied stress (TS samples). The second group contained eight SAE 9310 samples subjected to different levels of surface machining, which were used for MBN assessment of various produced residual stresses (RS samples). The details on the samples, geometries, heat treatments, machining parameters and residual stresses measured by 'sin$^2\psi$' x-ray diffraction technique are given in Table 4.2.

SAE 9310	C	Mn	Si	P	S	Cr	Ni	Mo	Cu
	0.07 - 0.13	0.4 - 0.7	0.15 - 0.35	0 - 0.015	0 - 0.015	1 - 1.4	3 - 3.5	0.08 - 0.15	0 - 0.35
SAE 6481	C	Mn	Si	P	S	Cr	Ni	Mo	V
	0.29 - 0.36	0.4 - 0.7	0 - 0.4	0 - 0.025	0 - 0.035	2.8 - 3.3	0.3	0.7 - 1	0.15 - 0.25

Table 4.1 Typical chemical compositions of SAE 9310 and SAE 6481 steels [112, 113].

	Steel grade	Type of geometry	Dimensions l – length, w – width, t – thickness, d –diameter (mm)	Case-hardening heat treatment	Estimated case-depth (mm)	Speed of grinding wheel (turn/min)	Machining Advancement – feed rate (mm/turn)	Lubrication (in %)	Shot-peening parameters	Residual stress from XRD (MPa)
TS sample 1	SAE 6481	"dog-bone"	gauge section: l: 17, w: 14.9, t:6.9	Gas nitriding at 545°C for 100 hours	0.5-0.6	20	0.5	100	-	-309
TS sample 2	SAE 9310	cylindrical dumbbell	gauge section: l: 50, d: 10	Gas carburising at 927°C for 8 hours	1.1 - 1.25	95	0.002	100	Shot peened using SAE 110 balls of HRC 55-60, with intensity 0.008 – 0.01 A	-805
RS sample 1		cuboid	l: 75.8, w: 18.9, t:8			95	0.002	100		-627
RS sample 2									-	-482
RS sample 3						38	0.004	50	-	-405
RS sample 4			l: 35 d :25			24	0.04	50	-	-339
RS sample 5		cylindrical				24	0.15	0	-	+256
RS sample 6						24	0.1	0	-	+292
RS sample 7						25	0.15	0	-	+339
RS sample 8						25	0.1	0	-	+393

Table 4.2 Details on the geometry, heat treatment, machining parameters and surface XRD residual stresses for the SAE 9310 and SAE 6481 samples.

4.4 Experimental procedure

I.   DC hysteresis loops measurements

The experimental set-up used for DC hysteresis loops measurements of SAE6481 and SAE9310 samples is shown in Fig. 4.4.
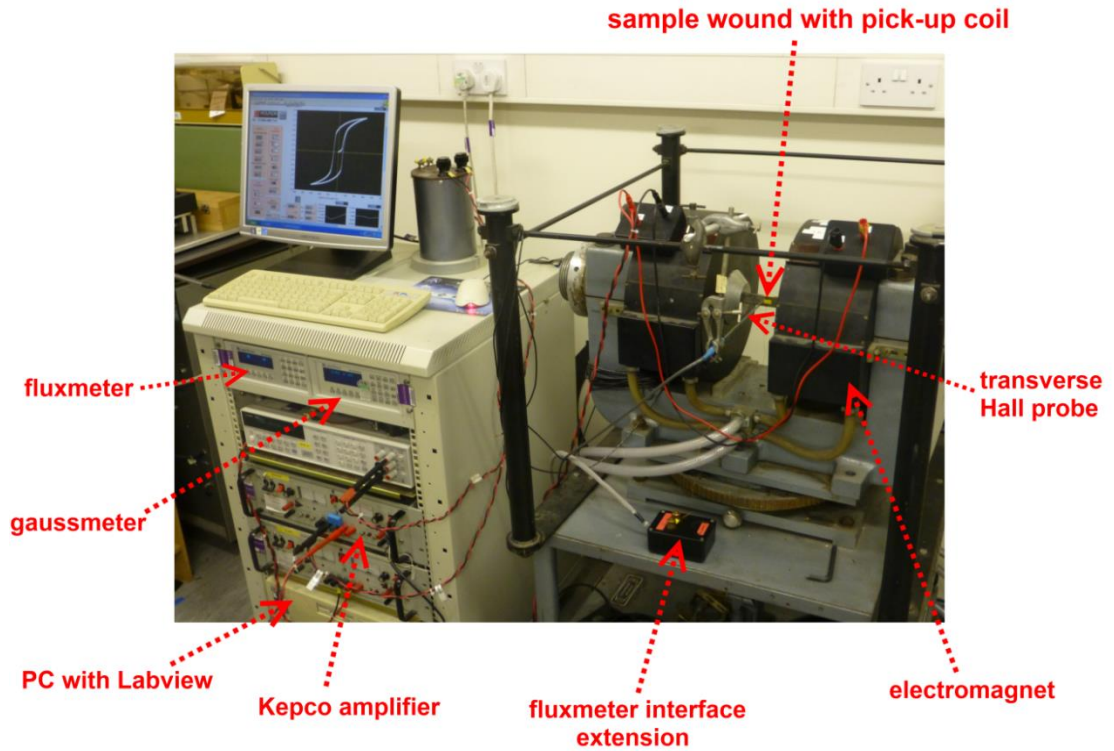
Fig. 4.4 Image of the DC hysteresis loop measurement set-up.

During testing the sample was magnetised using an electromagnet driven by quasi-DC current (0.01Hz) supplied from a National Instruments data acquisition card (NI DAQ) and subsequently amplified using a Kepco amplifier. The resulting strength of applied magnetic field **H** was measured at the surface of the sample with a transverse Lakeshore Hall probe [114] connected to a gaussmeter coupled with a PC via GPIB link. Simultaneously the values of magnetic flux density **B** were probed by GPIB linked Lakeshore fluxmeter integrating the voltage of 20 turns pick-up coil wound around the mid-section of the sample, using the following equation:

$$B = \frac{1}{NA} \int V(t) dt \qquad (4.11)$$

where N was the number of pick-up coil turns and A was the cross-sectional area of the specimen.

The complete test procedure was controlled using NI Labview software code. At the end of the measurement the resulting DC hysteresis loop was displayed on the monitor screen and the acquired **BH** data was saved on hard disk storage for further analysis. The resulting mean **BH** loops for SAE6481 and SAE9310 samples are shown in Section 4.5.

II.   Magnetostriction measurements

The magnetostrictive properties of both types of investigated steels were characterised via measurements of reference flat samples TS1 and RS1. The schematic diagram of testing system used in those measurements is shown in Fig. 4.5.

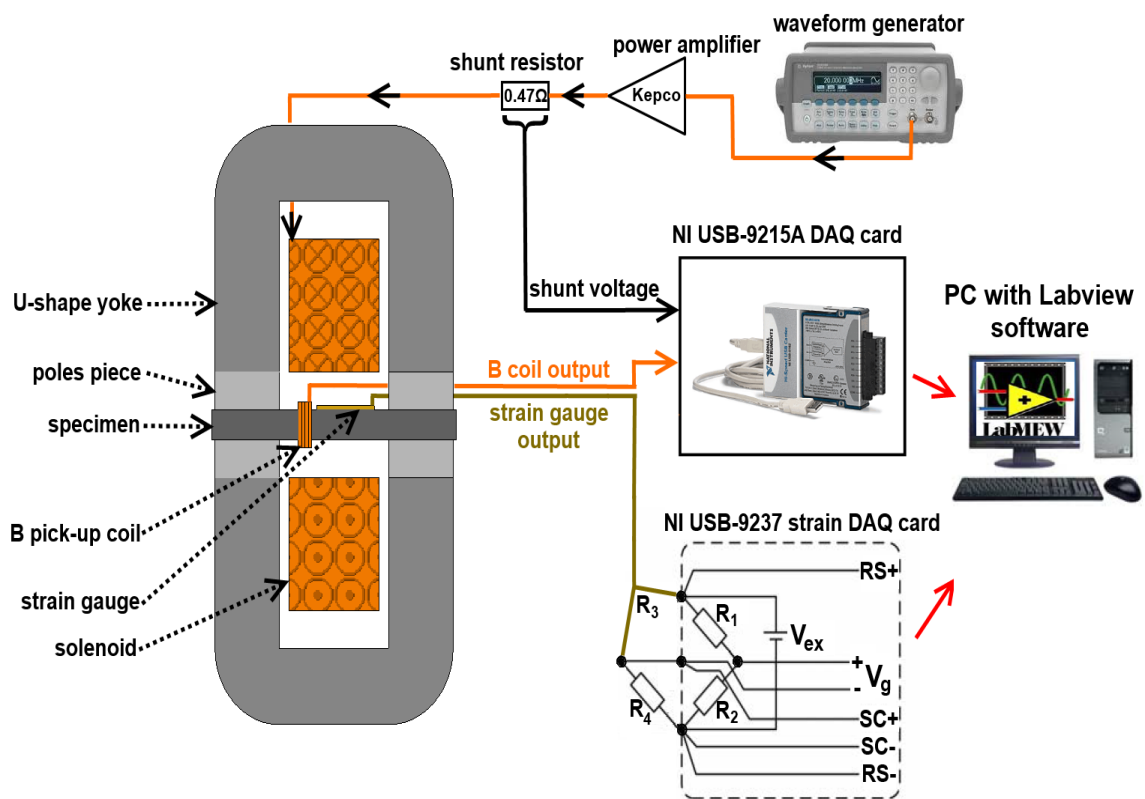Fig. 4.5 Schematic diagram of the AC magnetostriction measurement set-up.

During tests the specimen was magnetised using a 28mm long solenoid of 687 turns driven by 125Hz current supplied from an Agilent sinusoidal waveform generator and amplified with a Kepco power amplifier. The amplitude of magnetising current was determined from the voltage signal on the 0.47Ω shunt resistor using Ohm's law:

$$I = \frac{V}{R} \qquad (4.12)$$

The peak value of current was set to approx. 0.21A to achieve peak magnetic field of 5.15kA/m in the centre of solenoid (estimated using Equation 3.12), which corresponds approximately to that measured for MBN sensor. The magnetic flux path was enclosed via mild steel pole pieces and U-shapes yokes made of electrical steel. The flux density and consequently magnetisation values were obtained from the voltage induced in 20 turns pick-up coil wound near the centre section of the sample. Both voltage signals, from the shunt resistor and pick-up coil, were acquired with the NI USB-9215A DAQ card with simultaneous sampling at a rate of 100kHz.

The magnetostriction of tested samples were measured using foil strain gauges of the following specifications:

Resistance (R_g) [Ω]	Gauge factor (K_g)	Gauge length [mm]	Gauge width [mm]	Package length × width [mm]
120	2 ± 3.5%	11	5	18 × 8

Table 4.3 Technical specifications of the foil strain gauges used in magnetostriction measurements. [115]

Each strain gauge was glued in the middle section of specimen and its leads were connected to Wheatstone bridge comprising external dummy 120Ω resistor R4 and built-in circuit of NI USB-9237 DAQ card, as shown in the bottom right corner of Fig. 4.5. The DAQ card circuit contained two 120Ω resistors R_1 and R_2 for bridge completion, excitation voltage source V_{ex} which was set to 2.5V, shunt calibration (SC+ and SC-) and remote sensing (*RS*+ and *RS*−) for correcting errors due to lead wire resistance. Prior to the measurement the bridge was balanced giving zero output voltage, V_g =0.

During the measurement the magnetostriction λ induced alterations in strain gauge resistance R_3 led to changes in bridge output voltage V_g according to the following relation:

$$V_g = \frac{1}{4} K_g V_{ex} \lambda \qquad (4.13)$$

where K_g is the strain gauge factor.

Therefore by modifying Equation 4.15 it was possible to determine magnetostriction from measured bridge output voltage V_g as follows:

$$\lambda = \frac{4V_g}{K_g V_{ex}}$$
(4.14)

In each measurement the magnetostriction signal vs time was averaged over 100 sinusoidal cycles and plotted against the corresponding magnetisation values to obtain the "butterfly loop" of λ vs **M**. The total number of measurements performed for any particular sample was set to five. The acquired minor magnetostriction butterfly loops are presented in Section 4.5.

III.   Magnetic Barkhausen Noise measurements

In this study the Barkhausen noise measurements were carried out using the Microscan 600 system supplied by Stresstech [116]. The main components of this system include:

- the central unit, comprising the power supply and data acquisition card, which is connected to the PC via LAN port using the cross-over Ethernet cable
- the Barkhausen sensor, containing the magnetising and probing circuits, which is coupled to the central unit via LEMO multi-pin interface

The schematic diagram of the experimental set-up with detailed cross-sectional diagram of the Barkhausen sensor used in the measurements is presented in Fig. 4.6.
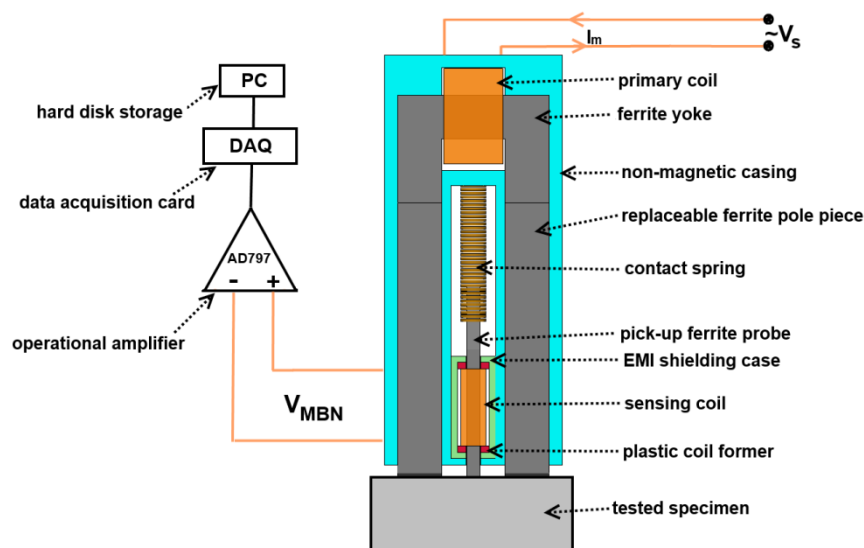

Fig. 4.6 Schematic diagram of the Barkhausen Noise measurement set-up.

During measurement the sinusoidal current I_m flowing in the primary coil generated a magnetic flux in the ferrite yoke, which was enclosed via ferrite pole pieces and the magnetised volume of the tested specimen underneath the sensor. The cross-sectional area of the sensor ferrite poles was 24mm^2 (8mm×3mm) and the distance between them was 5mm. The Barkhausen emissions from the magnetised section of tested sample were detected in a form of voltage pulses induced in the pick-up coil wound on a plastic former with inserted spring loaded ferrite probe of 3mm^2 cross-sectional area (3mm×1mm). The output voltage from the pick-up coil was subsequently amplified with the low noise AD797 operational amplifier [117] and digitised by data acquisition card with sampling frequency of 2.5MHz. The acquired data was stored on the hard disk drive for post-processing.

The measurement parameters, such as magnetising frequency and voltage, number of bursts, analysis and sampling frequencies, were controlled using the Microscan software interface, as depicted in Fig. 4.7.
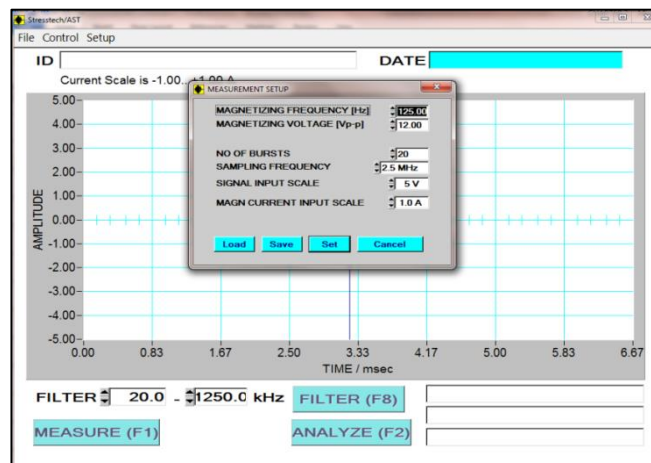
Fig. 4.7 Screen capture of the Microscan 600 software interface.

The magnetising frequency used in the measurements was set to 125Hz and the corresponding magnetising voltage was 6.5V. This combination of parameters was made based on the following criteria:

1. avoidance of ferrite yoke saturation and distortion in sinusoidal waveform of magnetising current

2. assurance of reproducibility and confidence of measurement by limiting the triple relative standard deviation of MBN amplitude to less than 10% for the reference sample TS2, which generated lowest Barkhausen emissions and therefore showed worst signal-to-noise ratio

3. identification of the relatively lowest frequency and highest voltage meeting the above requirements, which allowed optimisation of the penetration depth and uniformity of applied field in the surface and sub-surface regions of interest

The resulting peak value of magnetising current used in measurements was 0.36A and the corresponding maximum magnetic field strength, measured under the centre of sensor poles with transverse Hall probe of Lakeshore 455 gaussmeter, was 4.95kA/m. The number of Barkhausen bursts acquired in each measurement was set to 20 with total number of 10000 data points in each burst. An example of the first few bursts with incident current waveform displayed after completing the measurement can be seen in Fig. 4.8.
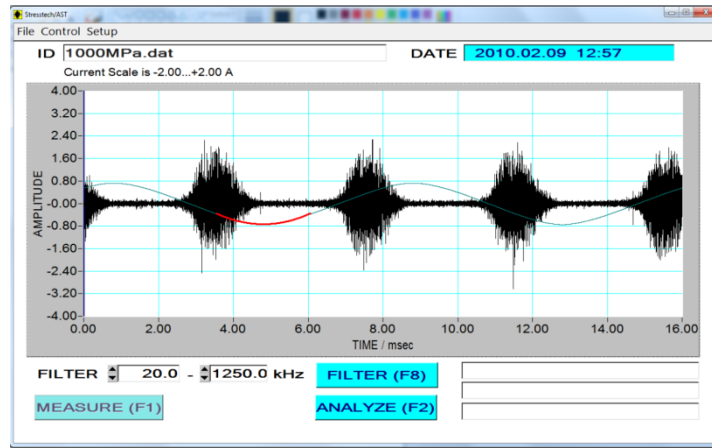

Fig. 4.8 Illustration of Barkhausen voltage bursts acquired with Microscan 600.

The measured Barkhausen voltage bursts (Fig. 4.9a) were exported to PC workstation and underwent subsequent stages of post-processing. Firstly, the time distribution of root mean square values of instantaneous voltage pulses in Barkhausen bursts $MBN_{RMS}(t)$ was determined (Fig. 4.9b) using the following equation:

$$MBN_{RMS}(t) = \sqrt{\frac{\sum_{i=1}^{N_b} MBN^2(t)}{N_b}} \qquad (4.15)$$

where N_b is the number of acquired Barkhausen bursts and MBN(t) is the instantaneous value of voltage in the given Barkhausen burst.

Secondly, the resulting RMS MBN time distribution was smoothed using moving average method with 1000 consecutive data points to attain signal envelope, as depicted in Fig. 4.9c. Finally, the signal envelope was plotted against the field applied to electromagnet for extraction of analysis parameters, such as peak amplitude MBN_{pk},

peak position MBN$_{ppos}$ and sum of RMS Barkhausen emissions MBN$_{AREA}$, as presented in Fig. 4.9d.
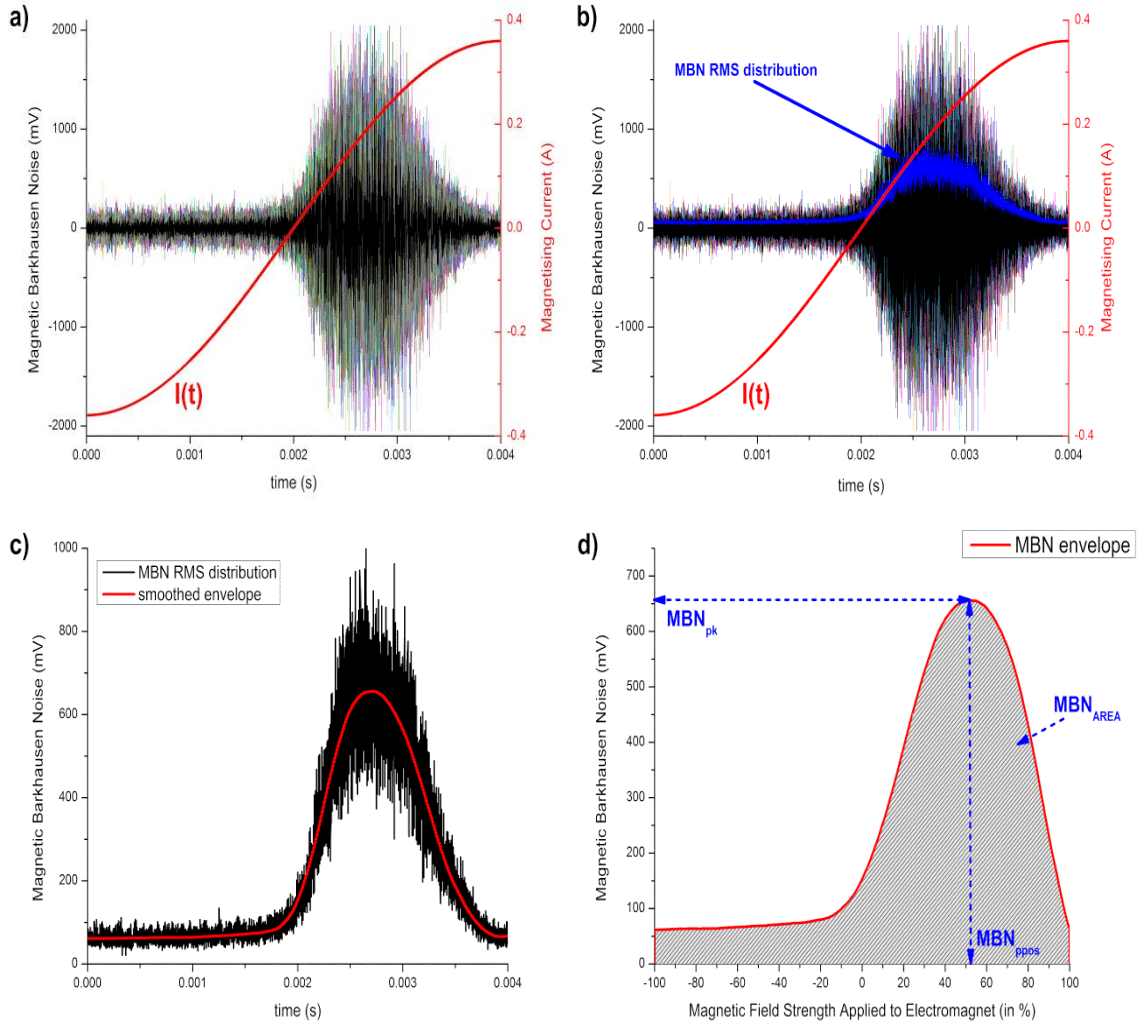
Fig. 4.9 a) Super-imposed Barkhausen voltage bursts with corresponding magnetising current I; b) Illustration of time distribution of root mean square values of instantaneous voltage pulses in Barkhausen bursts; c) Extraction of smoothed envelope of MBN RMS distribution; d) Smoothed MBN envelope with indicated analysis parameters.

The MBN parameters, determined using the above described post-processing methodology, were found to be repeatable due to elimination of the stochastic fluctuation of the Barkhausen emissions.

The other parameter used in the analysis was the root mean square of the complete acquired raw MBN signal calculated with the following expression:

$$MBN_{RMS} = \sqrt{\frac{\sum_{i=1}^{N_p} MBN^2}{N_p}}$$

(4.16)

where N$_p$ is the total number of detected Barkhausen voltage pulses.

IV.   Magnetic Barkhausen Noise measurements under applied stress

In the investigation of Barkhausen Noise under applied stress the specimens TS1 and TS2 were loaded using the Instron 8801 servo-hydraulic machine shown in Fig. 4.10a.
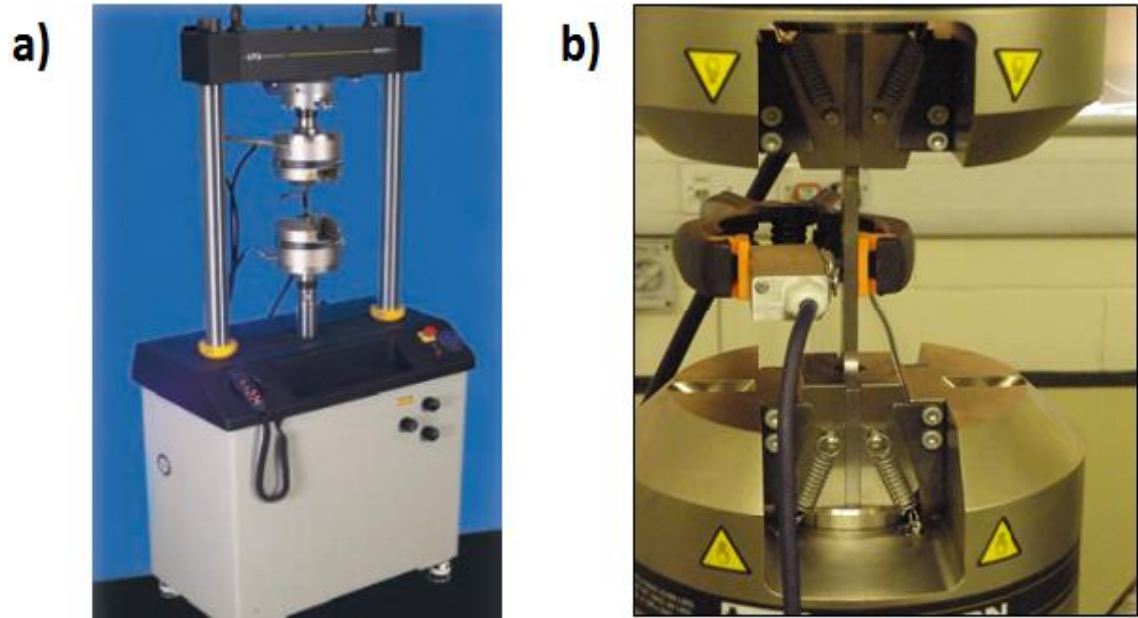
Fig. 4.10 a) Image of Instron 8801 servo-hydraulic system [118]; b) Illustration of the MBN sensor clamped at the centre of gauge section of specimen subjected to tensile stress.

Prior to the tensile tests the MBN sensor was positioned and clamped in the centre of sample gauge section as shown in Fig. 4.10b.

During the experiments the MBN data was recorded under monotonically increased tensile stress with increments of 50MPa calculated using the following expression:

$$\sigma = \frac{F}{A} \hspace{3cm} (4.17)$$

where **F** is the applied load and A is the nominal cross-sectional area of specimen.

4.5   Measurements results and discussion

I.   DC hysteresis loops

The DC hysteresis loops obtained for carburised SAE9310 samples are shown in Figs. 4.11a to 4.11i.
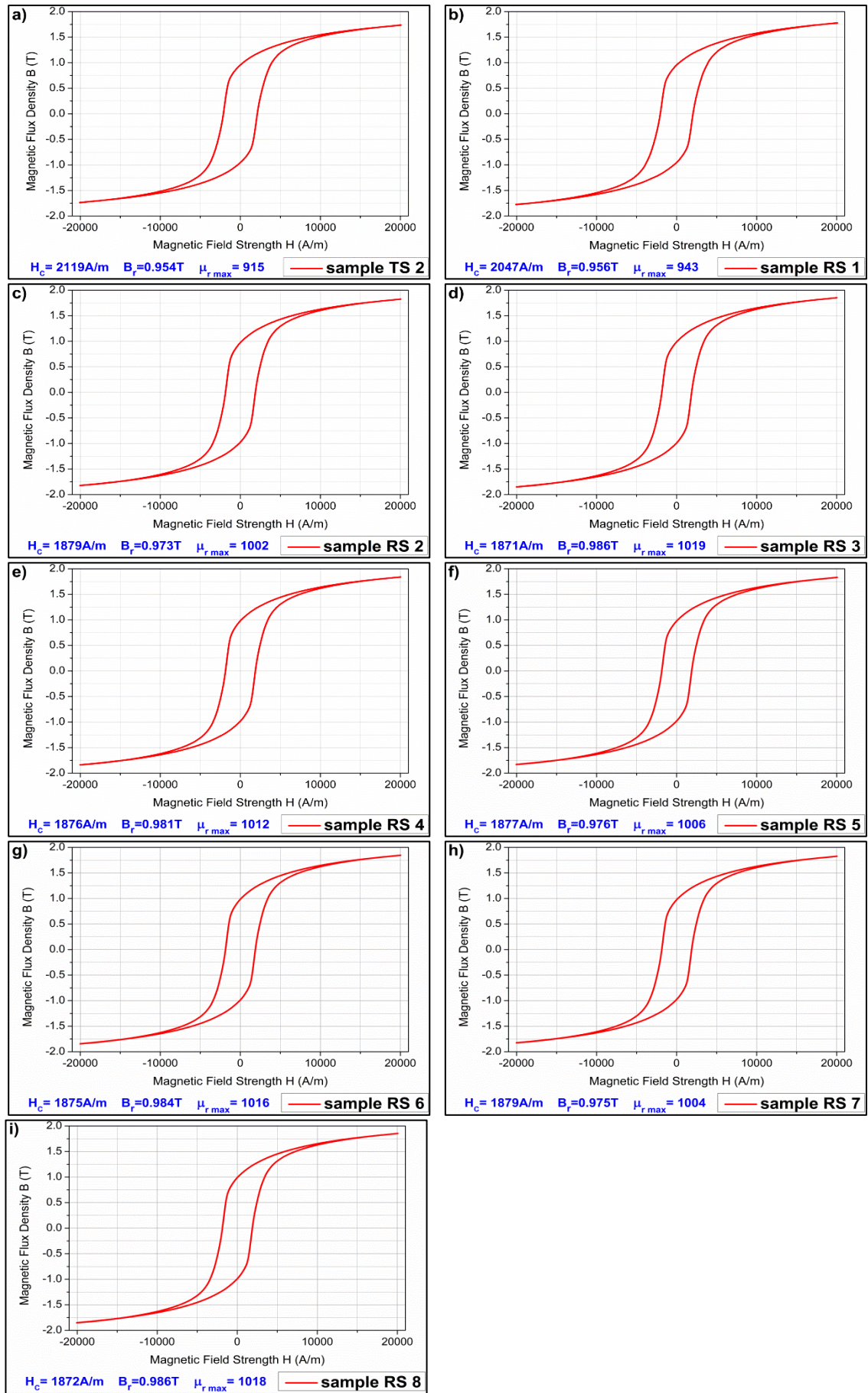
Fig. 4.11 DC hysteresis loops obtained for carburised SAE9310 samples.

The main hysteresis parameters, such as remanence B_r, coercivity H_c and maximum differential relative permeability $\mu_{r\,max}$, of all measured carburised samples are plotted against their surface residual stresses in Figs. 4.12a to 4.12c respectively.
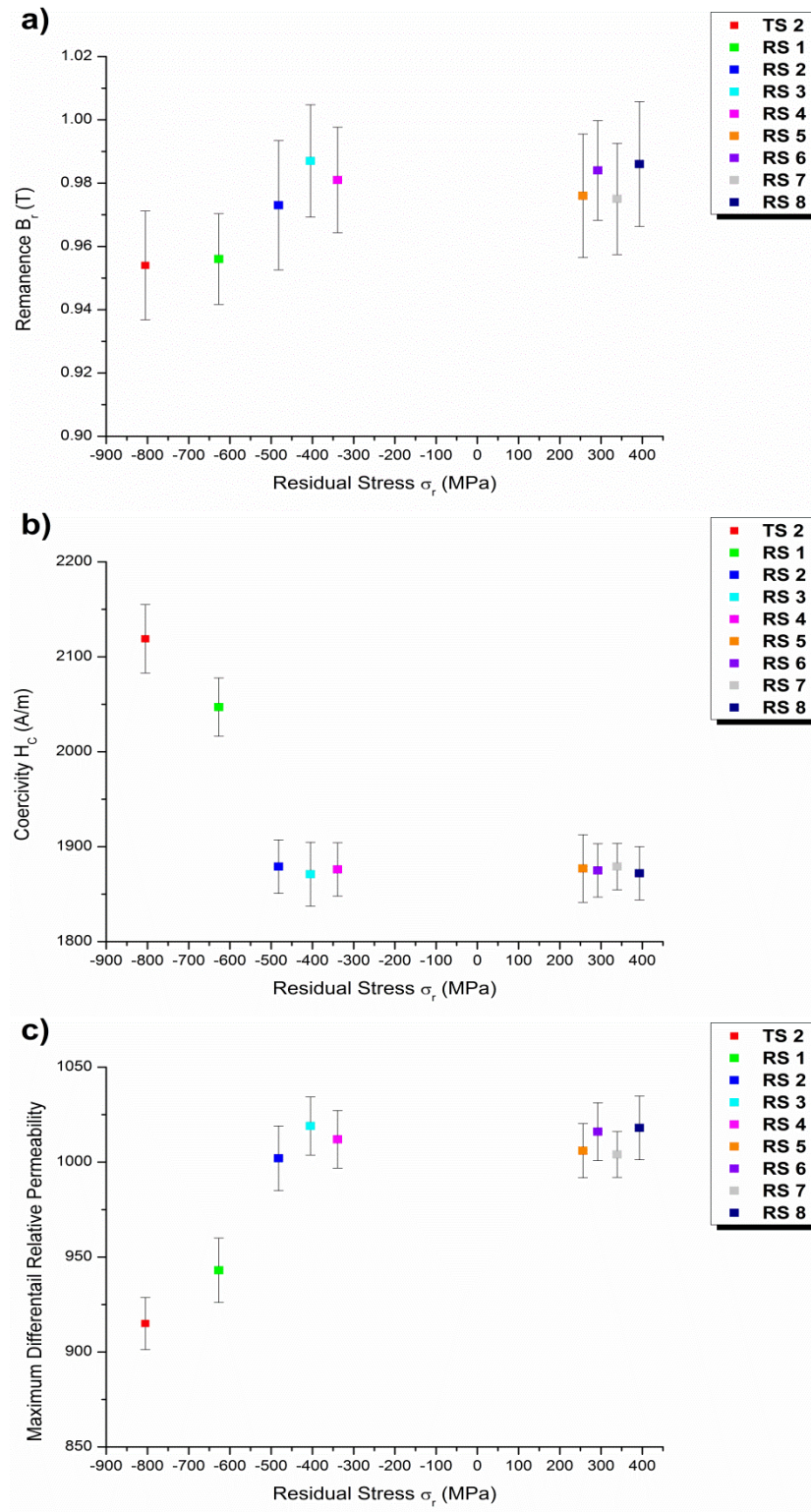

Fig. 4.12 Main DC hysteresis parameters of carburised SAE9310 samples as function of their surface residual stress.

In order to analyse the individual effect of residual stress on hysteresis parameters and exclude the influence of microstructural variation within the magnetised volume, only samples with similar hard outer case to total volume ratio R_C should be considered. Therefore in this study the direct comparison of residual stress effects on bulk remanence, coercivity and maximum differential relative permeability could be made only for samples RS2 to RS8 for which the ratio R_C was within approximate range from 0.17 to 0.19 for estimated case depths of 1.1 to 1.25mm. As can be seen in Figs. 4.12a to 4.12c for this particular group of samples (RS2 to RS8) no apparent trends of **B_r**, **H_c**, $\mu_{r\,max}$ with varying residual stresses were observed. This confirmed their self-equilibrating nature, where within the whole material volume the regions with compression were counterbalanced with adjacent regions of tension and vice versa, which made the bulk magnetic properties insensitive to local variations in residual stress.

In case of samples TS2 and RS1 the higher **H_c**, and lower **B_r** and $\mu_{r\,max}$ values depicted in Figs. 4.12a and 4.12c, can be assigned to their greater R_C ratios of approximately 0.39-0.44 and 0.36-0.4 respectively. Their greater relative volumes of hard martensitic layer with high density of strong pinning sites in the form of carbon precipitates, numerous grain boundaries and dislocations impeding the domain wall motion, reduced their net magnetisation response to applied field and consequently their hysteresis signature.

The DC hysteresis loop obtained for nitrided sample TS1 made of SAE6481 steel is shown in Fig. 4.13.
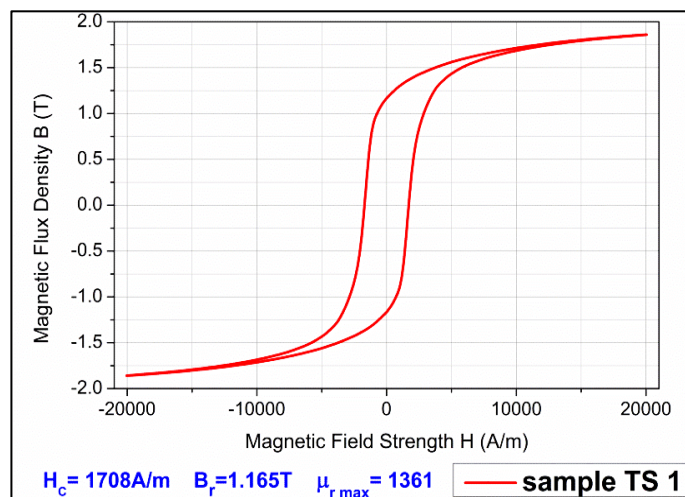

Fig. 4.13 DC hysteresis loop of nitrided SAE6481 sample.

The effective ratio R_C for TS1 sample was within range from 0.2 to 0.24 for estimated case depth within range from 0.5-0.6mm. The main hysteresis parameters extracted from measured BH loop had values of **H_c**=1708A/m, **B_r**=1.165T and $\mu_{r\,max}$=1361. When comparing with SAE9310 samples RS2 to RS8 which had similar R_C ratio it can be seen that the nitrided TS1 specimen is magnetically softer and therefore would be expected to generate more MBN emission over the same range of applied magnetic field.

II. Magnetostriction butterfly loops

The magnetostriction λ vs magnetisation **M** butterfly loops obtained for reference samples TS1 (SAE6481) and RS1 (SAE9310) are shown in Figs. 4.14a to 4.14d. Due to low input signal level and high harmonic distortion only fundamental components of measured magnetostriction data is presented.
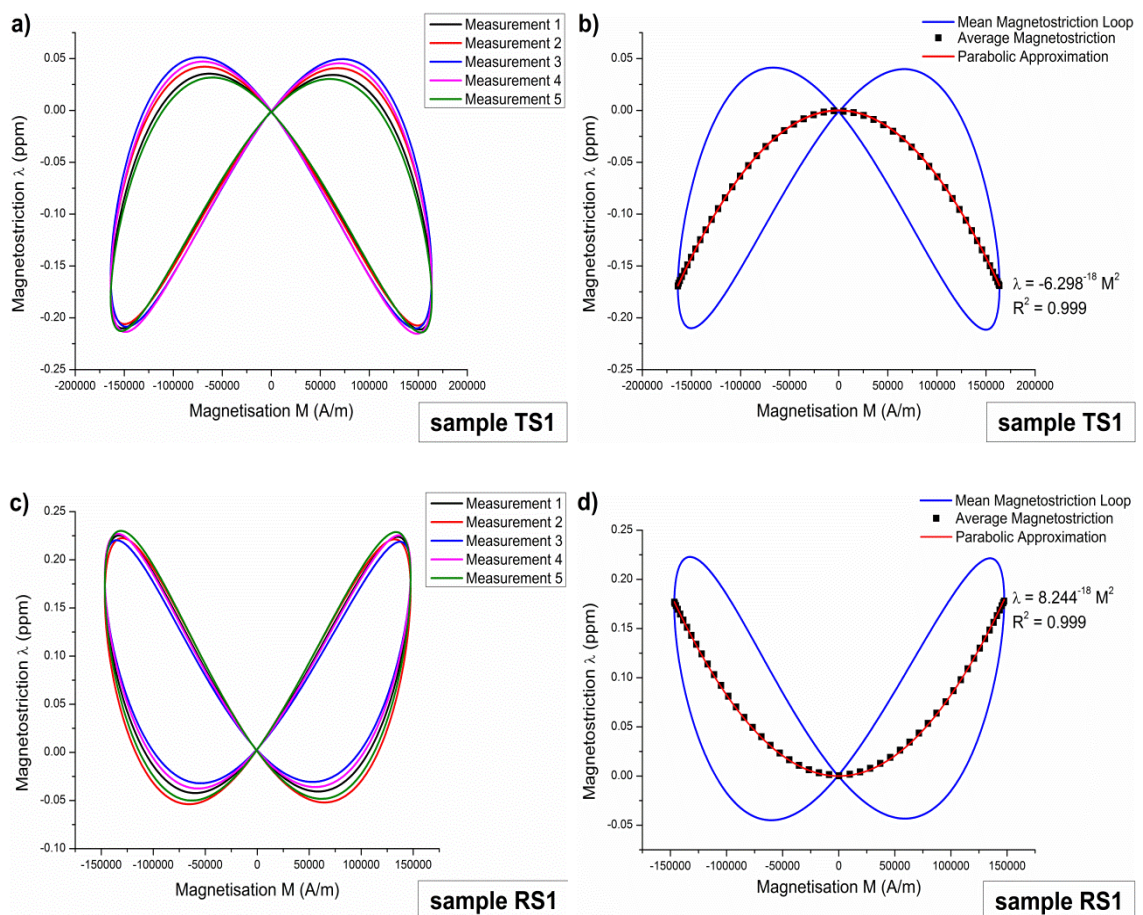

Fig. 4.14 a) & c) Minor AC magnetostriction butterfly loops measured for nitrided SAE6481 and carburised SAE9310 samples, respectively; b) & d) Mean AC magnetostriction butterfly loops for nitrided SAE6481 and carburised SAE9310 samples with corresponding average values of λ vs **M** approximated by parabolic function.

The minor λ vs **M** butterfly loops measured for nitrided sample TS1 (shown in Fig. 4.14a) indicated a negative magnetostriction in the low field region. The resulting slope dλ/d**M** of the parabolic approximation of average non-hysteretic magnetostriction for this sample (Fig. 4.14b) was equal to b=-6.298^{-18}(A/m)$^{-2}$. This implied that the stress equivalent field **H**$_\sigma$ would be negative under applied tensile stress and therefore the total effective magnetic field **H**$_e$ experienced by the specimen would decrease under increasing tension leading to consequent reduction in MBN amplitude.

In the case of the carburised sample RS1 the recorded minor butterfly loops (Fig 4.14c) showed positive magnetostrictive response to applied field. The effective slope dλ/d**M** of parabolic function fitted to average λ vs **M** values (Fig. 4.14d) was steeper than that for TS1 sample with determined value of b=8.244^{-18}(A/m)$^{-2}$. This suggested that the stress equivalent field **H**$_\sigma$ would be positive under applied tension leading to increase in total effective field **H**$_e$ and MBN amplitude under ramped tensile stress, with higher rate of changes with stress than that expected for nitrided specimen.

III. Magnetic Barkhausen Noise measurements under applied stress.

III.I SAE9310 TS2 carburised sample

The representative raw MBN bursts for SAE9310 TS2 sample, obtained under magnetic field applied coaxially with monotonically increasing tensile stress within range from 0MPa to 1000MPa, are shown in Fig. 4.15. These acquired bursts clearly indicated the effect of elevated tension on the magnetisation dynamics of this specimen. The additional positive field **H**$_\sigma$ of increasing amplitude, arising from motion of 90° domain walls and reconfiguration of magnetic moments towards the energetically favoured easy axes closest to the stress direction, enhanced the total magnetic field **H**$_e$ and corresponding depinning force exerted on domain walls, allowing larger Barkhausen jumps generating higher MBN emissions. Moreover it can be seen that with increasing tension, and hence of effective field **H**$_e$, the Barkhausen emissions were triggered at a lower level of applied magnetic field **H** leading to gradual increase in width of MBN bursts.
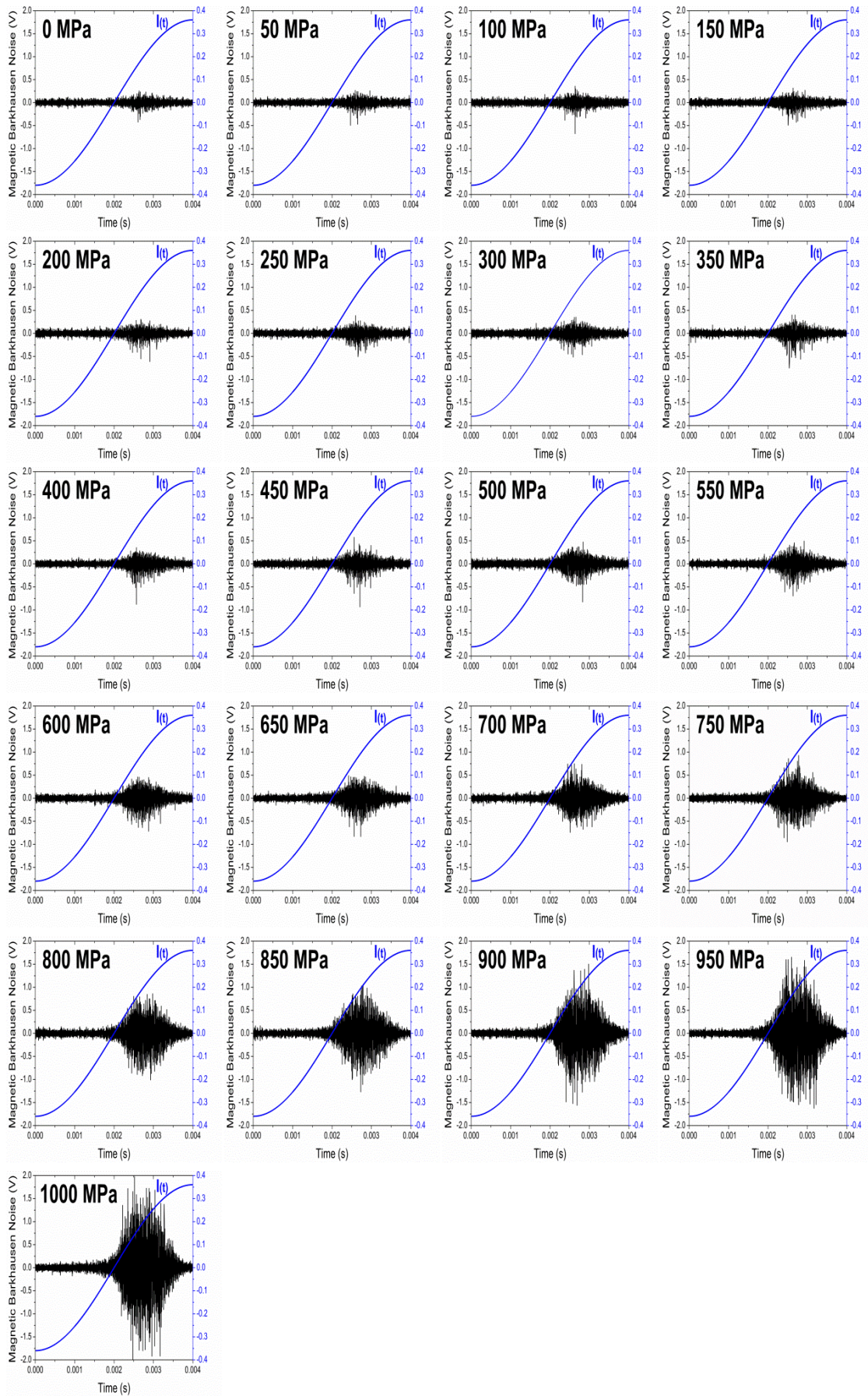
Fig. 4.15 Barkhausen voltage bursts acquired for SAE9310 TS2 sample under various applied tension.

The quantitative effect of stress on MBN emissions in SAE TS2 sample was evaluated via analysis of the smoothed MBN signal envelopes shown in Fig. 4.16. These envelopes clearly demonstrated the progressive broadening of the MBN bursts under ramped tensile stress due to increase in the amplitudes of Barkhausen emissions and range of magnetic field within which they occurred.
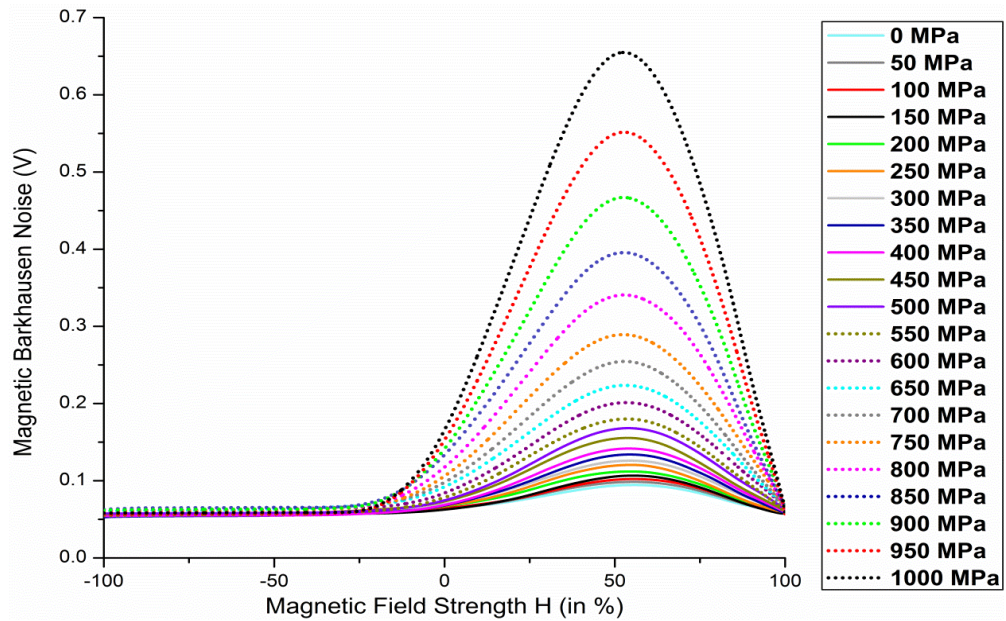
Fig. 4.16 Magnetic Barkhausen Noise signal envelopes obtained for TS2 sample under various applied tensile stress.

The primary parameter which was extracted from each of the above envelopes was the peak amplitude MBN_{pk}. The dependence of this parameter on applied tensile stress is depicted in Fig. 4.17a.
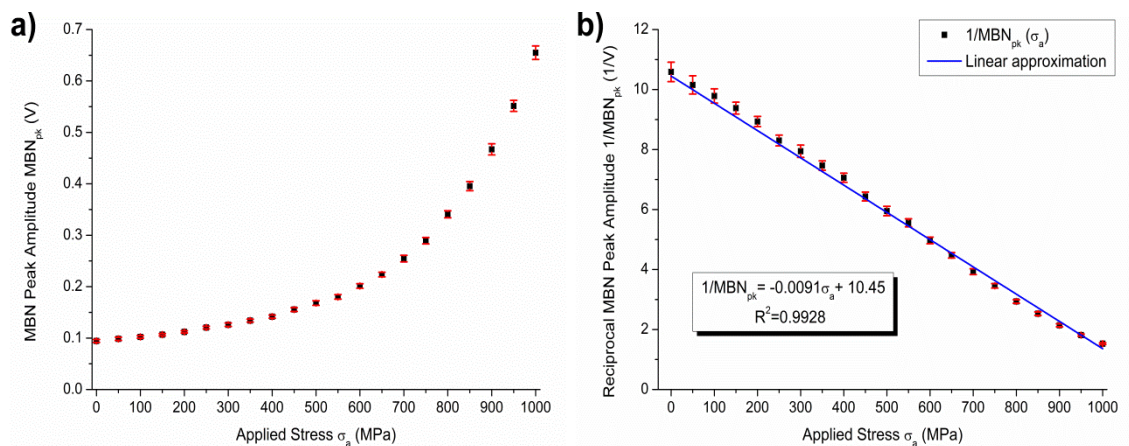
Fig. 4.17 a) MBN peak amplitude as a function of applied stress for SAE9310 TS2 sample; b) Dependence of reciprocal MBN peak amplitude on applied stress approximated with linear function. Red bars reflect the standard deviation from the mean data values.

It can be seen that the MBN_{pk} for TS2 specimen exhibited a clear rising trend for increasing applied tension. This type of stress dependence resembled that previously observed for anhysteretic susceptibility at the origin χ'_{an} for AISI 4130 steel in work of Garikepati et al [12], as well as the trends of maximum differential susceptibility χ'_{Hc} and MBN_{pk} projected for material of stress insensitive magnetostriction analysed in Section 4.2. Therefore this suggested that by analogy the plot of reciprocal MBN_{pk} obtained for SAE TS2 sample could also be represented by linear function of applied stress σ_a, as shown in Fig. 4.17b. The best linear fit to the data was shown to approximate the dependence of $1/MBN_{pk}$ on σ_a with relatively high 99.28% "goodness of fit" (coefficient of determination $R^2=0.9928$). The magnetostriction coefficient b' (Section 4.2) calculated using the slope of this function was determined as $b'=3.81\times10^{-15}$ $(msA^{-1}N^{-1})$. The minor discrepancies between the values of modelled linear function and measured data points implied that the fluctuations of the magnetostriction coefficient b' with stress were almost negligible. This can be attributed to the following reasons:

- Firstly, the outer martensitic layer of specimen TS2, from which the acquired MBN emissions originated, is characterised by high density and strength of pinning sites impeding the domain wall motion. Hence the stress induced reduction in volume and population of 90° closure domains in hard martensite, responsible for magnetostrictive properties of steel, can be expected to be much less significant than those observed in the soft iron and ferritic steels. As a result, in the martensitic steel the magnetostriction coefficient b, which is directly proportional to b', exhibits relatively lower dependence on tensile stress than those observed in softer steels.

- Secondly, the presence of residual compressive stress favoured the closure domains to be aligned away from the axis of applied tension and field in order to minimise their magnetoelastic energy. This in return reduced the unpinning force exerted on the 90° domain walls by the total effective field and restrained their motion and related magnetostrictive changes. Therefore it could be envisaged that the MBN emissions were generated with no meaningful dimensional variations occurring.

The next parameter which was analysed in terms of its stress dependence was the root-mean square MBN_{RMS} of raw Barkhausen signal, as shown in Fig. 4.18a.
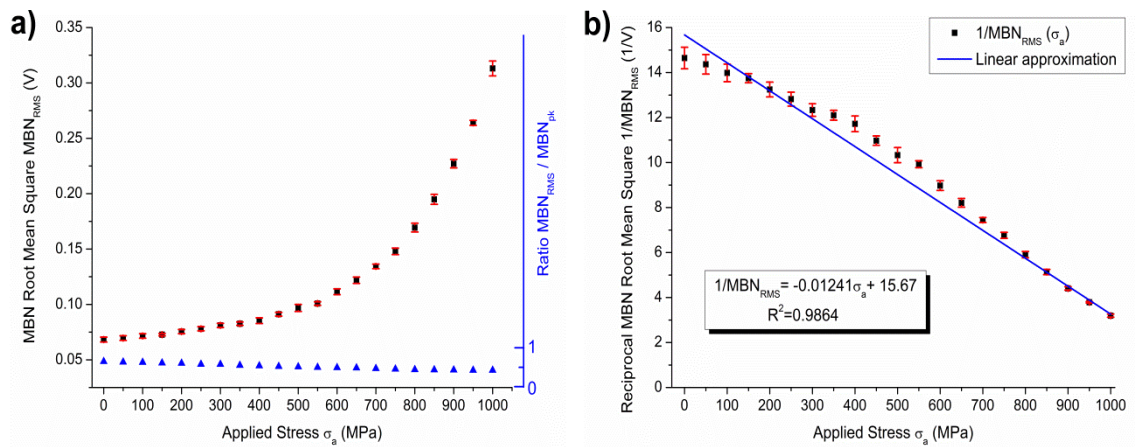

Fig. 4.18 a) MBN root-mean-square amplitude as a function of applied stress for SAE9310 TS2 sample; b) Dependence of reciprocal MBN root-mean-square on applied stress approximated with linear function. Red bars reflect the standard deviation from the mean data values.

It can be seen that the function of MBN_{RMS} vs σ_a is comparable to MBN_{pk} (σ_a) exhibiting positive inclination with increasing tensile stress. The resulting steeper linear approximation plot of reciprocal $1/MBN_{RMS}$ vs σ_a (Fig. 4.18b) could be treated as non-parallel translation of linear function $1/MBN_{pk}$ (σ_a). The high value of R^2=0.9864 of this linear approximation suggested that the MBN_{RMS} and its reciprocal $1/MBN_{RMS}$ could be useful quantities for evaluation of stress in SAE9310 steel.

The final parameters used in this analysis were the MBN peak position (MBN_{ppos}) and area of smoothed distributions of Barkhausen emissions (MBN_{AREA}) which were obtained from the MBN signal envelopes (Fig. 4.16). The stress dependencies of these parameters are shown in Figs. 4.19a and 4.19b.

In Fig. 4.19a it can be observed that from 0-750MPa the MBN_{pk} shifted gradually towards the lower values of applied field which indicated a decrease in coercivity of the corresponding hysteresis loops. This can be explained by considering the energy required to allow domain walls to break away from the pinning sites in stressed ferromagnetic materials.
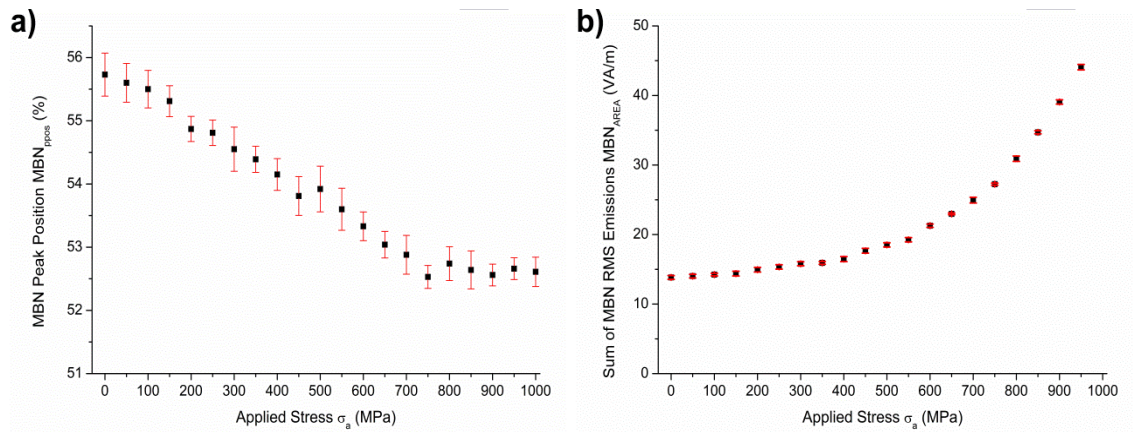
Fig. 4.19 a) MBN envelopes peak positions obtained for SAE9310 TS2 sample under various tension; b) Variation in area of MBN signal envelopes for TS2 sample subjected to different levels of tension. Red bars reflect the standard deviation from the mean data values.

As already explained in Section 2.5 the application of constant stress affects the energetically unfavourable 90° domains and induces the motion of 90° domain walls in order to minimise the magnetoelastic energy. If the depinning force supplied by stress equivalent field H_σ is sufficient to overcome the pinning force then irreversible Barkhausen jumps and changes in magnetisation occur. At the same time for those domain walls of energetically unfavourable domains which remain pinned after application of stress, the force needed to overcome pinning sites is altered by the presence of H_σ and depends on stress amplitude. Therefore the coercivity of soft magnetic materials that is predominantly determined by overall pinning strength, also changes with stress with the rate governed by stress amplitude. As the TS2 sample exhibited positive magnetostriction under applied field the increasing coaxial tensile stress within range 0-750MPa progressively reduced the pinning force which led to a decrease in coercivity and a shift of MBN_{ppos} to lower values of H.

At higher values of applied tension (beyond 750MPa) a plateau of $dMBN_{ppos}/d\sigma_a$ trend was observed. A possible explanation could be that beyond this level the effect of stress induced changes in 90° domain wall pinning on coercivity became insignificant.

The rising trend of MBN_{AREA} with increasing tension (Fig. 4.19b) demonstrated the positive addition of the stress equivalent field to effective magnetic field sensed by domains. The larger domain wall translations under gradually enhanced depinning force generated higher Barkhausen emissions resulting in higher sum of detected voltage pulses.

124

III.II SAE6481 TS1 nitrided sample

The raw MBN bursts measured for SAE6481 TS1 under coaxial field and monotonically increased tensile stress within range from 0MPa to 700MPa are shown in Fig. 4.20. Since the measured λ vs **M** butterfly loops revealed negative magnetostriction of this nitrided specimen (Fig. 4.14) the effect of applied tension was opposite to that observed for SAE9310 TS2 sample. The negative contribution of H_σ to total effective field H_e reduced the amplitude of MBN emissions and narrowed the range of amplitudes of applied field **H** capable of inducing the unpinning processes.
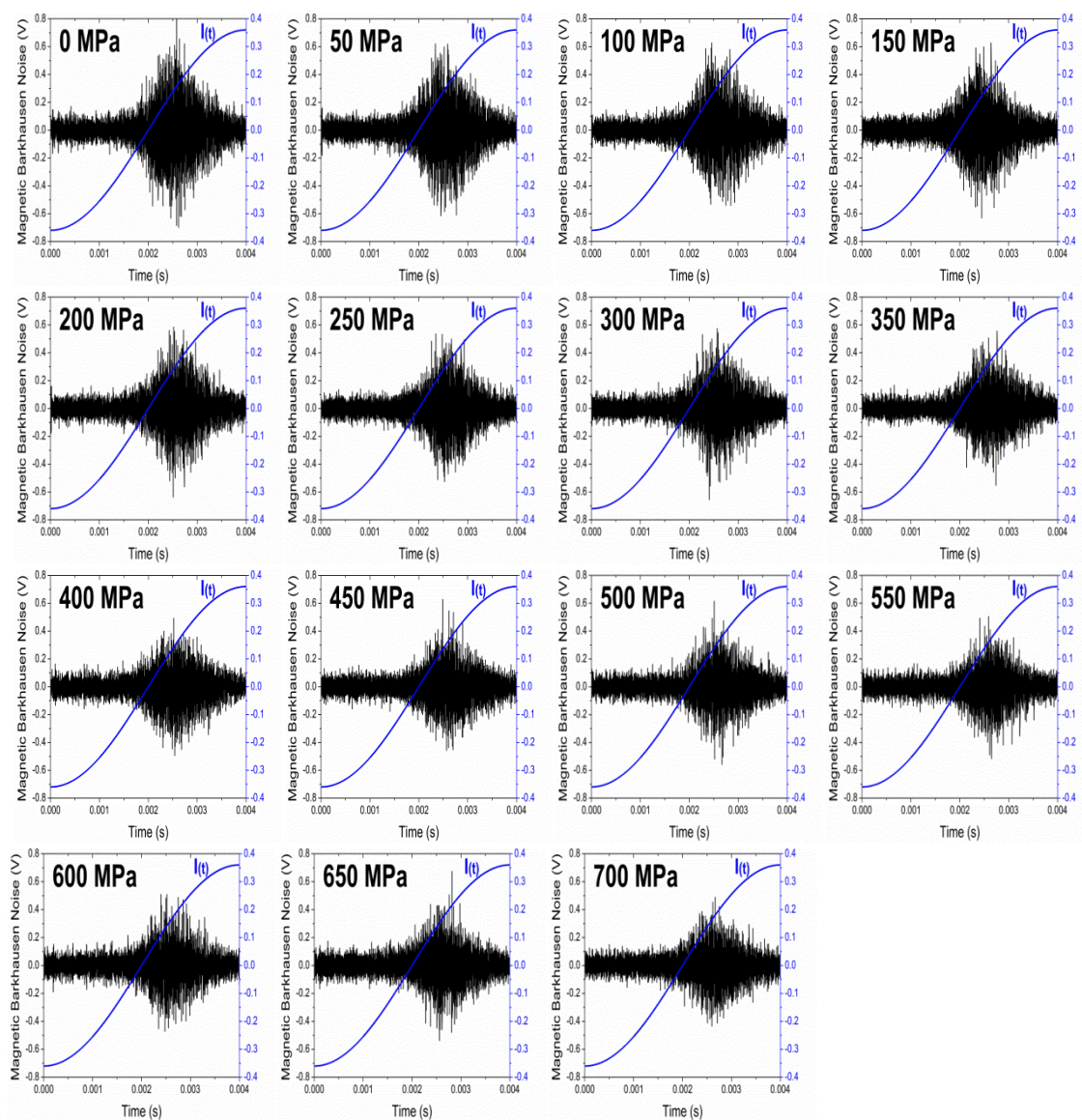
Fig. 4.20 Barkhausen voltage bursts acquired for SAE6481 TS1 sample under various applied tension.

The narrowing of the field range and reduction of amplitude of MBN bursts, caused by increase in volume of closure domains at non-right angles to stress axis, was evidently revealed in analysis of smoothed signal envelopes shown in Fig. 4.21. However it was noticed that the dynamics of these mechanisms was lower than for the inverse case of SAE9310 TS2 sample.
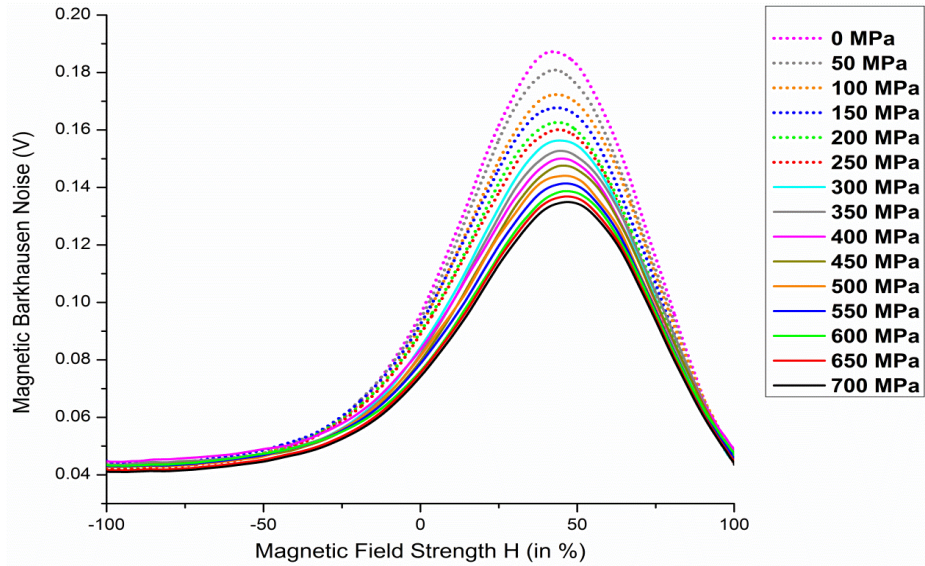
Fig. 4.21 Magnetic Barkhausen Noise signal envelopes obtained for TS2 sample under various applied tensile stress.

The lower rate of changes of MBN_{pk} under ramped tension is depicted in Fig. 4.22a. It can be seen that the peak amplitude gradually decreased with rising stress but less rapidly than in case of SAE9310 carburised specimen. This was confirmed by the positive slope of linear function (s=0.00289) well approximating (R^2=0.9884) the relation of reciprocal peak amplitude and applied stress, as shown in Fig. 4.22b.
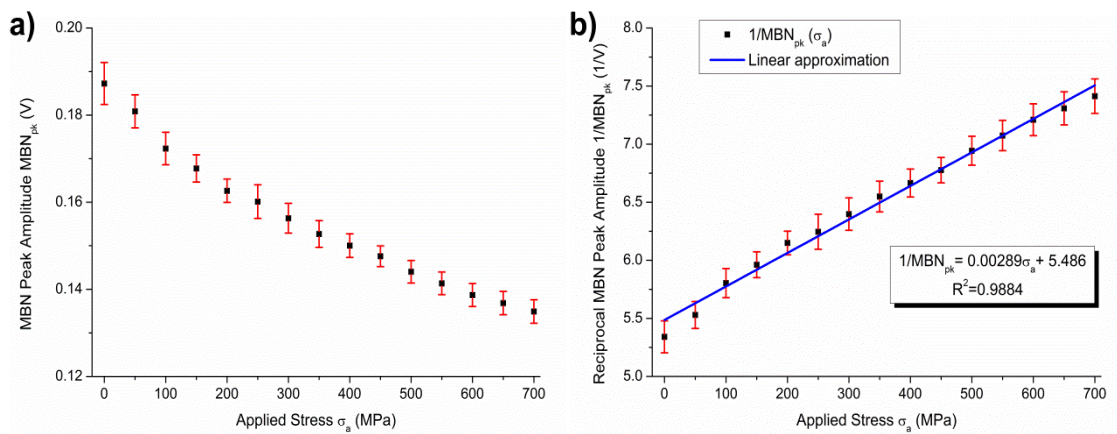
Fig. 4.22 a) MBN peak amplitude as a function of applied stress for SAE6481 TS1 sample; b) Dependence of reciprocal MBN peak amplitude on applied stress approximated with linear function. Red bars reflect the standard deviation from the mean data values.

The calculated value of the coefficient b' for TS1 nitrided sample was b'=-1.21×10^{-15} when the corresponding b' for TS2 was 3.81×10^{-15}. The difference in value of b' for TS1 specimen could be attributed to lower magnetostriction slope b and compressive residual stress favouring the orientation of closure domains close to direction of applied tension and field.

The small variations in b' coefficient at elevated levels of tension could be assigned to strong domain wall pinning by the nitride particles weakening potential stress induced domain reconfiguration as well as reduction of total effective field by residual compression.

The stress dependence of the root-mean square MBN_{RMS} of raw Barkhausen signal measured for nitrided TS1 sample is shown in Fig. 4.23a. The observed trend was similar to that for MBN_{pk}. However the distinctive feature in this case was the lower slope of the linear function approximating the variation of 1/ MBN_{RMS} with stress, as shown in Fig. 4.23b.
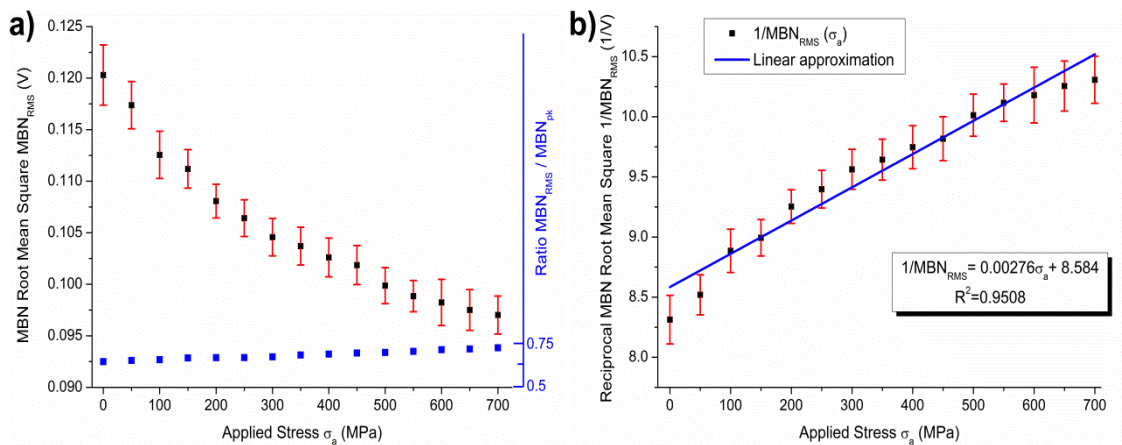
Fig. 4.23 a) MBN root-mean-square amplitude as a function of applied stress for SAE6481 TS1 sample; b) Dependence of reciprocal MBN root-mean-square on applied stress approximated with linear function. Red bars reflect the standard deviation from the mean data values.

The effects of progressively increased tension on MBN_{ppos} and MBN_{AREA} for nitrided TS1 sample are shown in Figs. 4.24a and 4.24b respectively.

The ascending trend of MBN_{ppos} vs σ_a indicated the gradual increase in additional stress induced pinning force on impeded 90° domain walls. This type of behaviour was expected for this negatively magnetostrictive specimen for which the applied tension favoured the closure domains to be oriented away from their common axis with

applied field **H**. The resulting increase of coercivity with stress was demonstrated by higher values of **H** at corresponding peak locations.
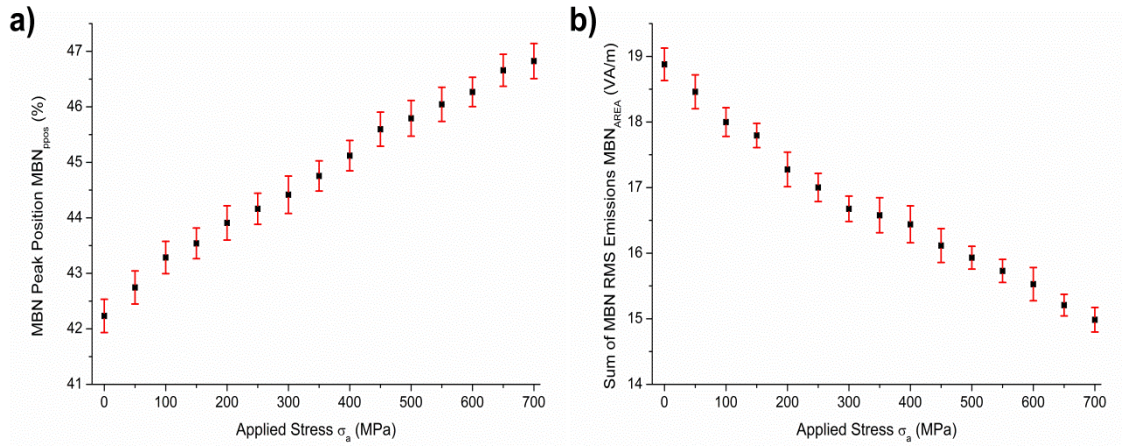
Fig. 4.24 a) MBN envelopes peak positions obtained for SAE6481 TS1 sample under various tension; b) Variation in area of MBN signal envelopes for TS1 sample subjected to different levels of tension. Red bars reflect the standard deviation from the mean data values.

The reduction in area under smoothed envelopes of MBN bursts with elevated tension (Fig. 4.24b) was caused by the negative contribution of stress equivalent field to total effective magnetic field sensed by domains. Consequently the progressively lowered effective depinning force with stress exerted on domain walls led to diminished Barkhausen jumps and gradual decrease in the sum of detected voltage pulses.

IV. Magnetic Barkhausen Noise measurements under residual stress.

The representative MBN bursts obtained for RS samples [Table 4.2] having different levels of surface residual stress are shown in Fig. 4.25. In order to correlate the depth range of XRD stress measurements (10µm) with the depth of origin of acquired MBN emissions the Barkhausen voltage signal was high-pass filtered with the lower frequency limit determined using the following re-written skin depth equation:

$$f = \frac{1}{\pi \sigma_e \mu_0 \mu_r \delta^2} \qquad (4.18)$$

The value of conductivity used in the calculations was $\sigma_e = 4.57 \times 10^6$ S/m [110] and that of relative permeability was $\mu_r = 915$ measured previously for sample TS2, which due to a relatively high martensitic case to soft core ratio was chosen as the best

permeability reference for the surface stress evaluation. The resulting MBN frequency range used in the analysis was 605.7kHz - 1250kHz.
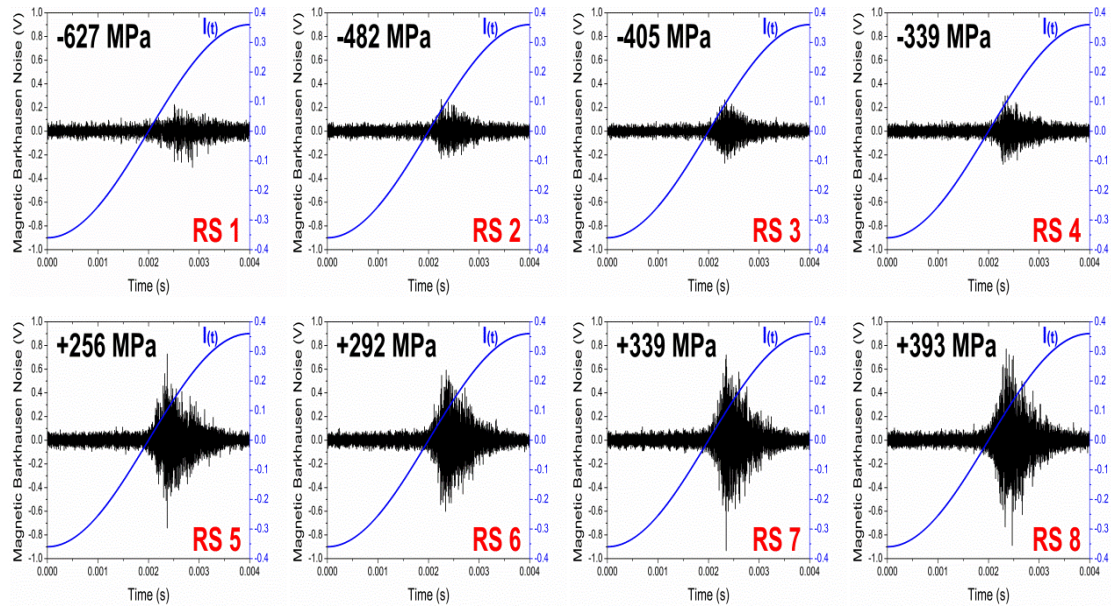
Fig. 4.25 Barkhausen voltage bursts acquired for SAE9310 RS samples with various levels of surface residual stress.

As it can be seen in Fig. 4.25 the magnetoelastic effect of residual stress on MBN emissions in SAE9310 samples was analogous to that observed for applied stress in Fig. 4.15. The highest compressive stress in sample RS1 and the corresponding strongest negative stress equivalent field H_σ led to weakest total effective field H_e and depinning force experienced by domains and their boundaries. As a result the induced domain wall motion processes were least dynamic which was exhibited by the lowest MBN emissions observed within a narrow range of applied field H.

The following cases of samples RS2, RS3 and RS4 confirmed that the negative contribution of H_σ to H_e decreased respectively with reduction in amplitude of compressive stress which was indicated by simultaneous rise in levels of MBN emissions and range of their occurrence.

The presence of tensile stress in surface regions of samples RS5, RS6, RS7 and RS8 was evidently pronounced by their MBN bursts. The additional positive field H_σ, increasing with tension amplitude, favoured the realignment of magnetic moments towards the coaxial stress and field direction giving rise to larger magnetisation changes via Barkhausen jumps, and thus generating higher MBN emissions within successively wider bands of applied magnetic field.

129

All the above stress effects on MBN bursts were also demonstrated by their smoothed envelopes shown in Fig. 4.26.
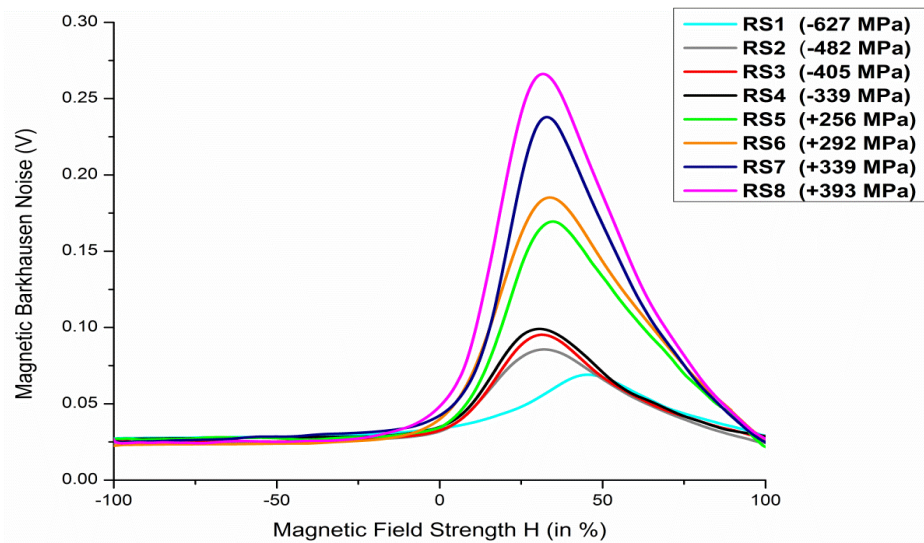
Fig. 4.26 Magnetic Barkhausen Noise signal envelopes obtained for SAE9310 RS samples with various levels of surface residual stress.

The broadening and increasing amplitudes of the MBN envelopes obtained for RS samples adequately indicated the different residual stress levels within both, tensile and compressive regimes. However, as distinct from those acquired for tensile specimen TS2 (Fig. 4.16) under applied load, there was no clear trend in shift of peak location with stress. This implied the difference between these two studies in terms of the potential additional microstructural effect on MBN emission of stressed steel specimens. In case of TS2 specimen the MBN bursts were acquired under ramped elastic tensile stress from a magnetised section of given microstructure, for which the density and strength of pinning sites could be assumed constant at all analysed stress levels. In case of RS samples the analysed residual stresses were produced via surface grinding under different heating and cooling conditions, and therefore the effective distribution and character of pinning sites would be expected to differ. In the extreme cases the thermo-plastic deformation during the abusive grinding could have induced microstructural alterations, such as:

- over-tempering of martensite leading to mechanical and magnetic softening of surface layer,

- conversion of retained austenite to martensite increasing relative volume of ferromagnetic phases in near-surface layers,

- creation of hard martensitic regions via re-hardening process

The net effect of the above metallurgical transformations would govern the microstructural properties of surface and sub-surface regions of RS samples, leading to local alterations in the density and strength of pinning sites, and thus variations in the their local coercivity and corresponding MBN peak position, as can be seen in Fig. 4.26.

Despite the varation of peak locations, the peak values of MBN envelopes showed a clear rising trend in transition from highest compressive to highest tensile residual stress, as depicted in Fig. 4.27a. This type of stress induced changes in MBN_{pk} was similar to that observed for applied stress previously shown in Fig. 4.17a. In fact the negative slope of the linear function approximating variation of the reciprocal peak amplitude $1/MBN_{pk}$ with residual stress σ_r was calculated as s=-0.00915 (Fig. 4.27b) and corresponded very well to that determined for applied stress which had value of s=-0.0091 (Fig. 4.17b). The main difference was the lower value of coefficient of determination R^2=0.9644 for residual stress case (R^2=0.9928 for applied stress) most likely caused by the previously explained microstructural variations. Nevertheless, this close correlation confirmed the analogous magnetoelastic effect of both applied stress and long range Type I residual macro-stress on MBN emissions.

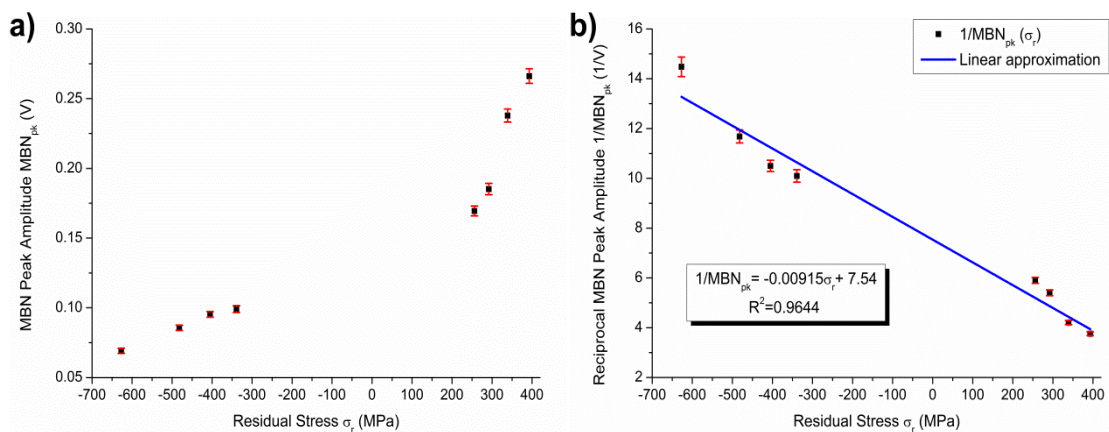
Fig. 4.27 a) MBN peak amplitude as a function of residual stress for SAE9310 RS samples; b) Dependence of reciprocal MBN peak amplitude on residual stress approximated with linear function. Red bars reflect the standard deviation from the mean data values.

The residual stress dependence of the root-mean square MBN_{RMS} of raw Barkhausen signal for SAE9310 RS samples is shown in Fig. 4.28a.
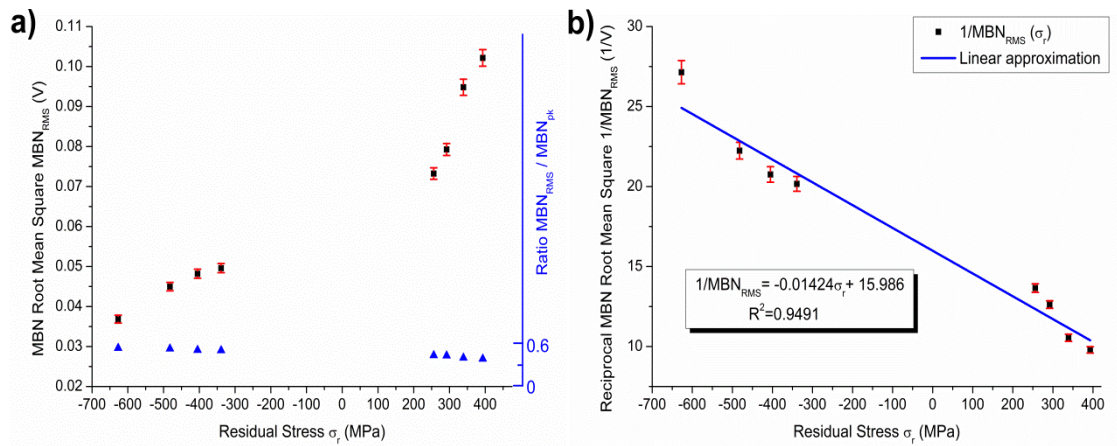
Fig. 4.28 a) MBN root-mean-square amplitude as a function of residual stress of SAE9310 RS samples; b) Dependence of reciprocal MBN root-mean-square on residual stress approximated with linear function. Red bars reflect the standard deviation from the mean data values.

It can be seen that the function of MBN_{RMS} vs σ_r is comparable to MBN_{RMS} vs σ_a (Fig. 4.18a) with similarly descending ratio of MBN_{RMS}/ MBN_{pk}, as shown in lower section of Fig. 4.28a. This analogous steeper linear approximation plot of reciprocal $1/MBN_{RMS}$ vs σ_r (Fig. 4.28b) had lower fit goodness of R^2=0.9491.

The scatter in the MBN_{ppos} vs σ_r results shown in Fig. 4.29a confirmed the expected local alterations in the density and strength of pinning sites caused by the different degrees of heat induced thermo-plastic deformation. This consequently suggested that the MBN_{ppos} would not be a reliable parameter for residual stress analysis.
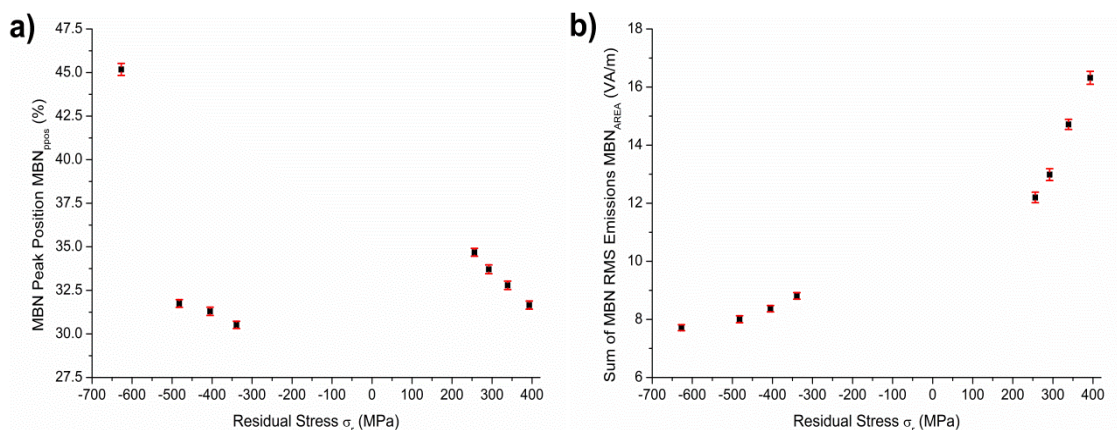
Fig. 4.29 a) MBN envelopes peak positions obtained for SAE9310 RS samples; b) Variation in area of MBN signal envelopes acquired for SAE9310 RS samples. Red bars reflect the standard deviation from the mean data values.

Unlike the MBN_{ppos} the sum of detected Barkhausen voltage pulses, represented by MBN_{AREA}, showed a systematic trend with residual stress amplitude, as depicted in Fig.

4.29b. This type of behaviour could also be assigned to effect of stress equivalent field, which eventually had either reduced (compressive stress) or enhanced (tensile stress) depinning force experienced by domains, and therefore effectively influenced the amplitude and field range of Barkhausen emissions.

4.6   Application of Magnetic Barkhausen Noise stress model to previously published results

The newly developed MBN stress model (Section 4.2), validated with results for both applied and residual stresses, has been summarised and published in IEEE Transactions on Magnetics [119] and World Intellectual Property Organization Patent [120] in 2011. Prior to these publications other researchers had reported a similar trend in MBN peak amplitude vs stress for different steel grades but without providing the quantitative explanation of their results. Therefore in this section the linear dependence of reciprocal peak MBN amplitude on stress predicted by the model for the previously published data of others will be explored and explained. Additionally some more recent examples of application of the MBN stress model in analysis of loaded high strength steels will be presented.

In 1989 C. Jagadish et al. published results from their investigation on the influence of stress on surface Barkhausen Noise generation in pipeline steels [121]. In their study the section of half-pipe sample made of hot rolled ferritic-pearlitic steel was subjected to bending stress calibrated using strain gauges.
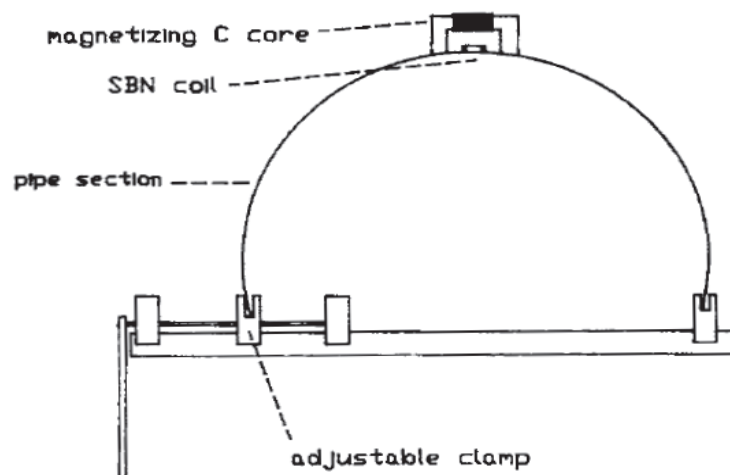
Fig. 4.30 MBN measurement set-up used in work of Jagadish et al [121].

The MBN measurements were taken using a standard set-up comprising C-shaped ferrite electromagnet driven by 1Hz triangular current and induction probe placed in between the electromagnets poles, as shown in Fig. 4.30.

In order to examine the results quantitatively, the peak-to-peak amplitude of surface Barkhausen Noise (SBN) was recorded and plotted as a function of ascending and descending tension and compression applied to the pipe, as depicted in Fig. 4.31.
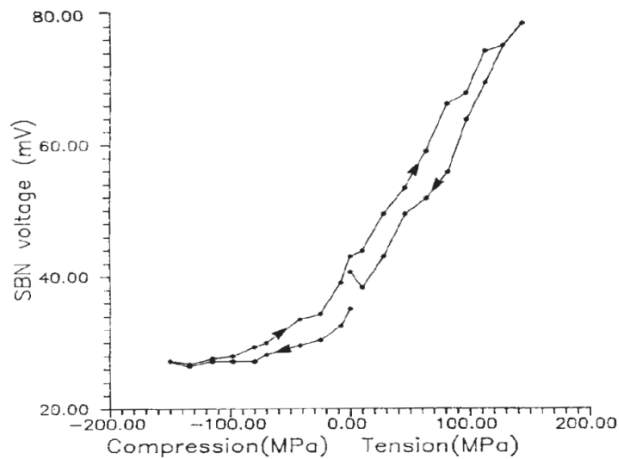
Fig. 4.31 Peak-to-peak amplitude of surface Barkhausen Noise (SBN) obtained by Jagadish for pipeline steel sample under various applied stress [121].

As it can be seen the trend of SBN vs σ obtained for pipeline steel was similar to that presented for SAE9310 steel in Fig. 4.17a. Therefore by analogy and with assumption of symmetry of MBN bursts against time axis, the reciprocal of half the value of SBN should also exhibit a linear dependence on stress, which is validated in Figs. 4.32a and 4.32b for results of Jagadish et al [121].
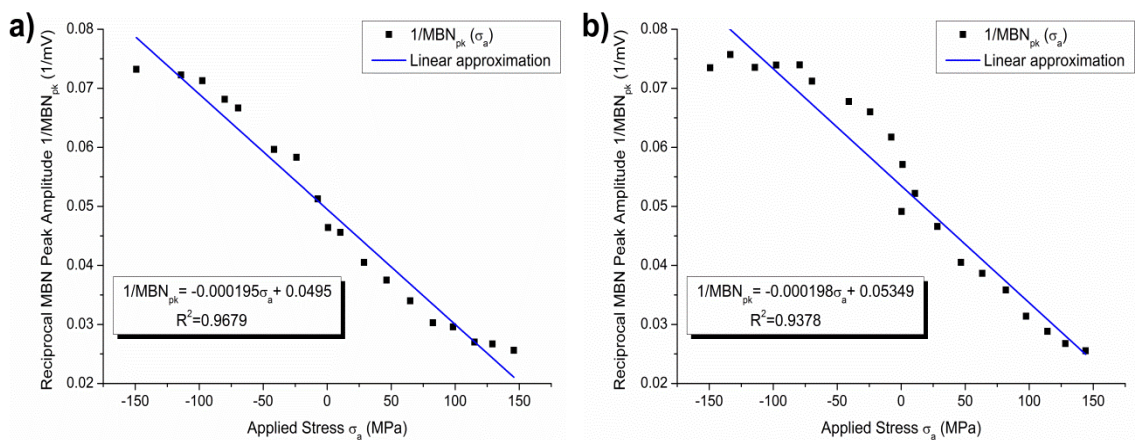
Fig. 4.32 a) & b) Linear approximations of the relations between the reciprocal MBN peak amplitude with ascending and descending stresses applied to pipeline steel sample. Based on the results of Jagadish et al [121].

The relatively high values of coefficient of determination for both ascending (R^2=0.9679) and descending (R^2=0.9378) load applied to pipeline sample confirmed a successful application of the MBN stress model for this type of ferromagnetic steel.

In 2004 another group of researchers led by Moorthy conducted a study on the MBN evaluation of applied stress in case-carburised EN36 steel [91] which similarly to SAE9310, is also widely used in manufacturing of heavy-duty components, such as gears. In their study the investigated ground samples of two different case depths, i.e. 0.65mm and 0.95mm, were loaded in a cantilever beam set-up to specific bending stress levels. The MBE measurements were made on both tensile and compressive sides of specimens using the system shown in Fig. 4.33.
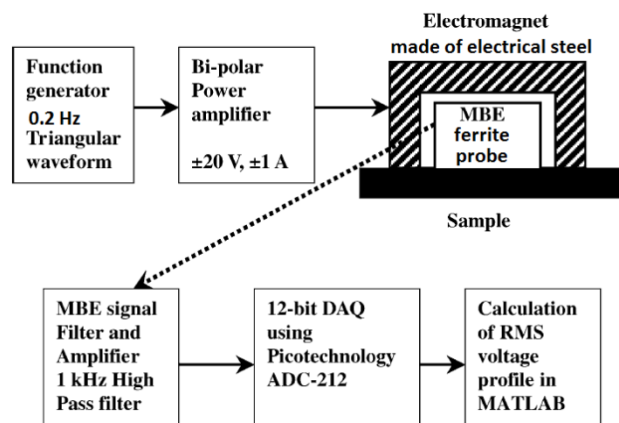
Fig. 4.33 MBN measurement set-up used in work of Moorthy et al [91].

The smoothed MBN envelopes obtained by Moorthy et al. for the EN36 specimen with carburised case-depth of 0.65mm, under different amplitudes of compression and tension are shown in Figs. 4.34a and 4.34b respectively.
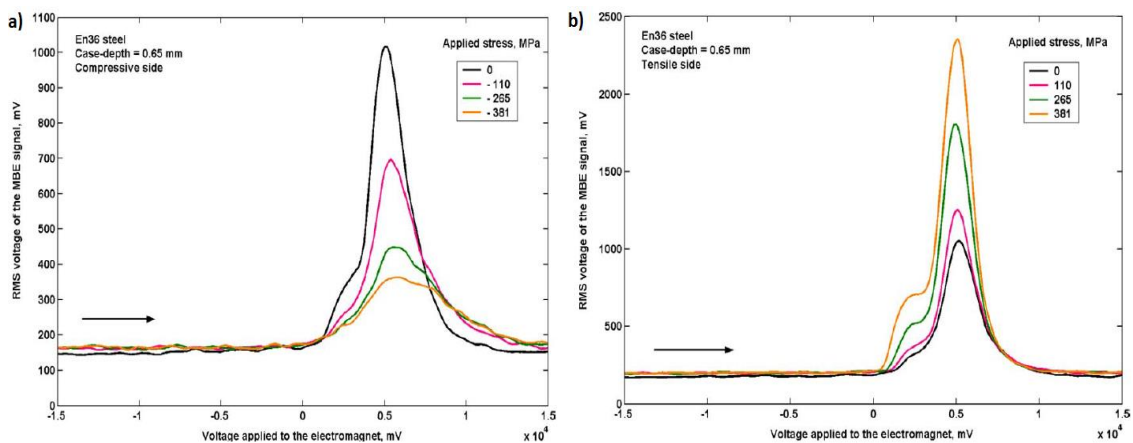
Fig. 4.34 MBN envelopes obtained by Moorthy for the EN36 specimen with carburised case-depth of 0.65mm subjected to various applied stress [91].

As can be seen with the low magnetisation frequency (0.2Hz) and shallower case depth the MBN envelopes demonstrated a double peak profile. The first peak recorded at lower field **H** corresponded to the softer ferritic-pearlitic core and the second peak at higher **H** represented the outer harder martensitic layer. The amplitudes of both of these peaks showed a visible rising trend in transition from highest compressive to highest tensile stress applied. The dependencies of the second peak amplitude and its reciprocal on the applied stress are shown in Figs. 4.35a and 4.35b respectively.
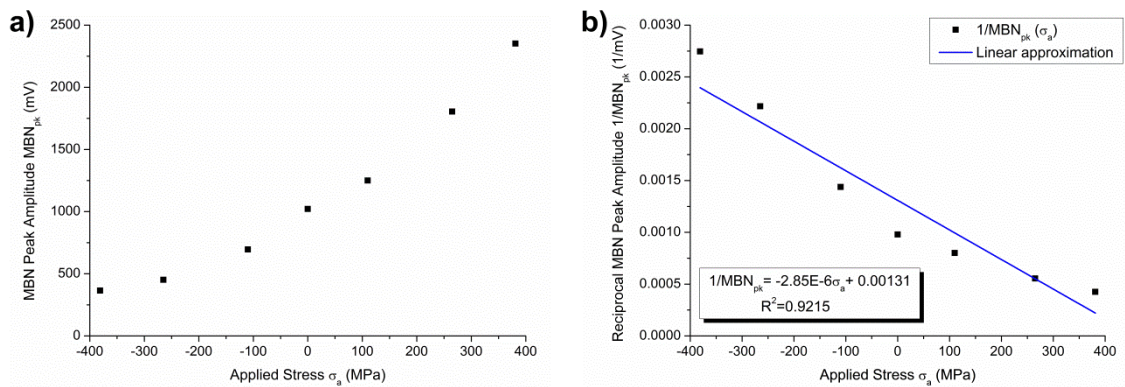
Fig. 4.35 a) MBN peak amplitude as a function of applied stress for EN36 sample with 0.65mm case-depth [91]; b) Dependence of reciprocal MBN peak amplitude on applied stress approximated with linear function.

The high goodness of fit of the linear approximation of $1/MBN_{pk}$ vs σ_a indicated by $R^2=0.9215$ confirmed a good agreement between the theoretical predictions and measured data for the above specimen.

The MBN envelopes reported by Moorthy for the EN36 specimen with carburised case-depth of 0.95mm under various compressions and tensions are presented in Figs. 4.36a and 4.36b, respectively.
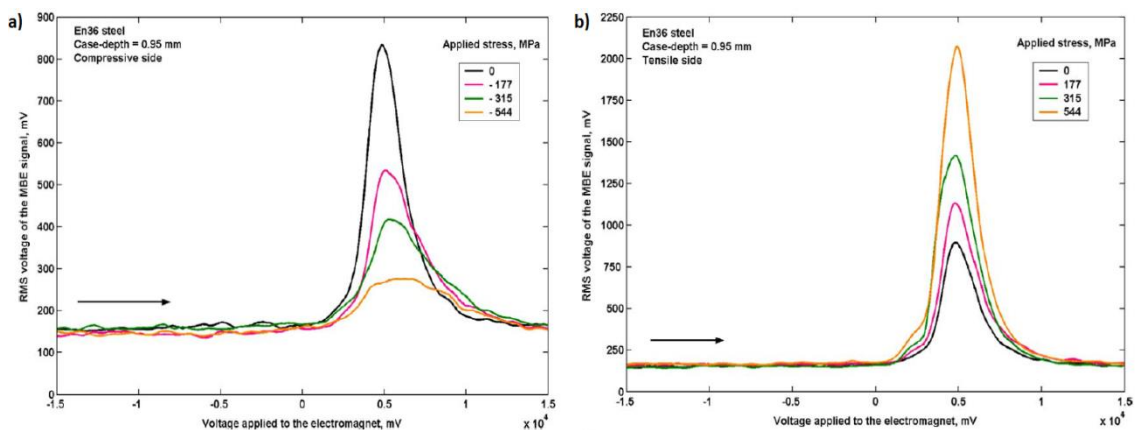
Fig. 4.36 MBN envelopes obtained by Moorthy for the EN36 specimen with carburised case-depth of 0.95mm subjected to various applied stress [91].

The plots of MBN_{pk} vs σ_a and $1/MBN_{pk}$ vs σ_a for this specimen are shown in Figs. 4.37a and 4.37b.
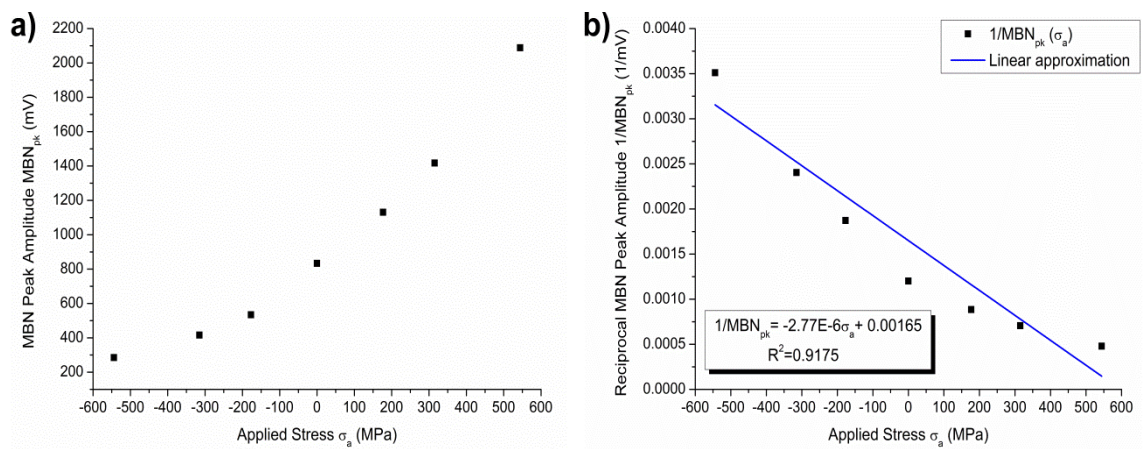
Fig. 4.37 a) MBN peak amplitude as a function of applied stress for EN36 sample with 0.95mm case-depth [91]; b) Dependence of reciprocal MBN peak amplitude on applied stress approximated with linear function.

As in the previous sample with shallower case depth, the dependence of $1/MBN_{pk}$ vs σ_a for specimen with thicker carburised layer of 0.95mm was closely approximated by linear function (R^2=0.9175). Moreover the slopes of best linear fits from both cases corresponded well with each other, i.e. s=-2.85E-6 and s=-2.77E-6. This therefore implied an analogous magnetoelastic effect of stress on MBN emissions from the two EN36 specimens, despite the fact of their different carburised case depths. In both these cases the linear behaviour anticipated by the model effectively described the variation in $1/MBN_{pk}$ within analysed range of applied stresses.

In 2005 Moorthy reported on another study of influence of residual stress on MBN emissions in case-carburised EN36 steel [122]. In that research a set of ground specimens with various surface residual stresses (identified via X-ray diffraction method) was evaluated with MBN method using Microscan 500-2 (former version of Stresstech Microscan 600) and an in-house built measurement set-up presented previously in Fig. 4.33. The main difference in application of those two measurement systems was the magnetising frequency used in analysis, i.e. 125Hz with Microscan 500-2 and 0.2Hz with the in-house unit.

The correlation of the residual stress and MBN peak amplitude obtained with the Microscan 500-2 is shown in Fig. 4.38a. The scatter in the results corresponding to

stress levels of -34MPa and -14MPa was attributed by the authors to additional microstructural variations induced during grinding and therefore these data points were neglected in calculation of $1/MBN_{pk}$ vs σ_r presented in Fig. 4.38b.
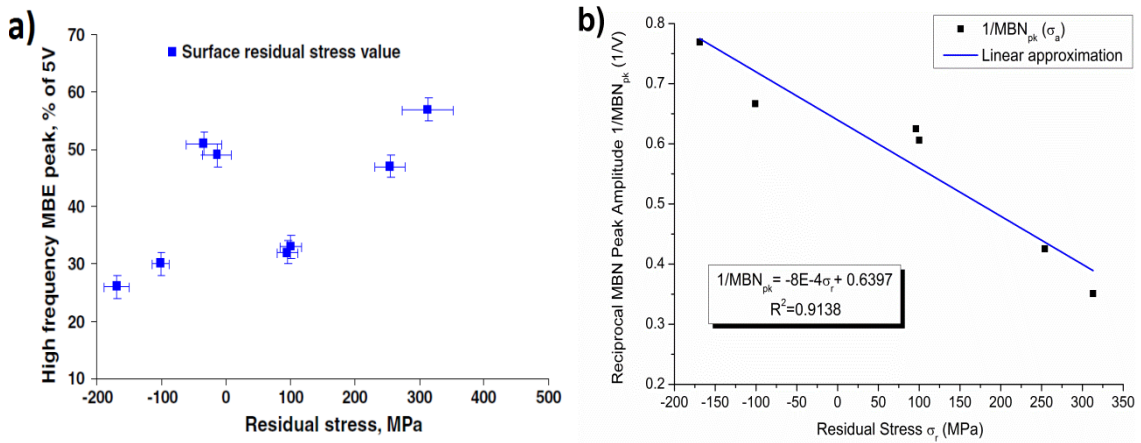
Fig. 4.38 a) High-frequency MBN peak amplitude as a function of surface residual stress in EN36 samples [120]; b) Dependence of reciprocal high-frequency MBN peak amplitude on residual stress approximated with linear function, after Moorthy et al. [122].

The residual stress dependencies of the low frequency MBN_{pk} and $1/MBN_{pk}$ are shown in Fig. 4.39a and 4.39b respectively. Consequently the scattered data assigned by Moorthy et al. to considerable microstructural variations was ignored.
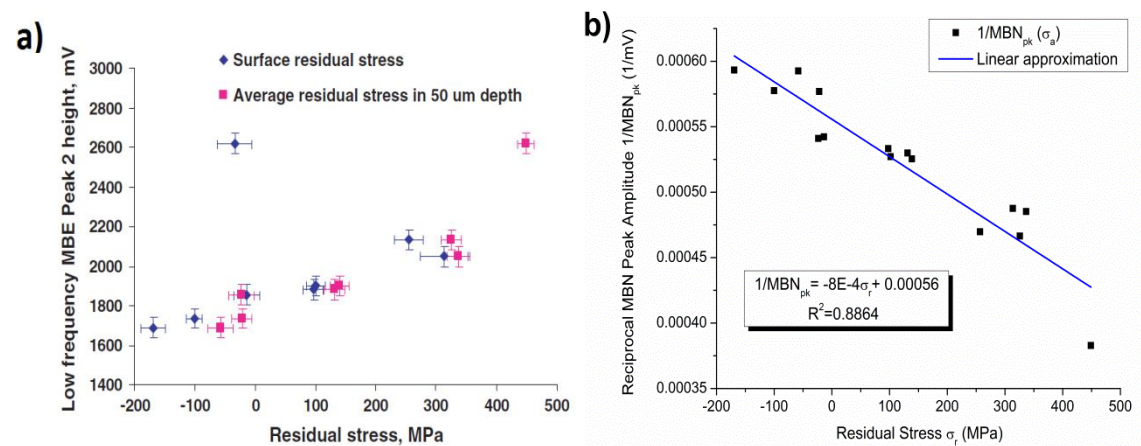
Fig. 4.39 a) Low-frequency MBN peak amplitude as a function of surface residual stress in EN36 samples [122]; b) Dependence of reciprocal low-frequency MBN peak amplitude on residual stress approximated with linear function, after Moorthy et al. [122].

As it can be seen in Figs. 4.38b and 4.39b the linear functions closely approximated the variation in low and high frequency reciprocal MBN amplitudes with residual stress in EN36 steel. This confirmed that the developed MBN stress model was capable of describing the residual stress effect on Barkhausen emissions in this type of steel.

After publication of the newly developed MBN stress model other researchers, who referred to that work, reported on its successful application to other types of heavy-duty steels [123, 124, 125].

In 2012 Santa-aho confirmed a close correlation between the predicted by model linear behaviour and measured RMS values of Barkhausen emissions from case-carburised RAEX400 and EN10084 steels [123, 124]. In her work the Barkhausen measurements were carried out using the Microscan 600 system with magnetising frequency of 125Hz. An example of the dependence of MBN RMS on applied stress reported by Santa-aho for EN10084 tempered specimens of various surface hardness are shown in Fig. 4.40a. The plots of 1/MBN$_{RMS}$ vs σ_a for these specimens approximated with linear functions are presented in Figs. 4.40b and 4.40c.
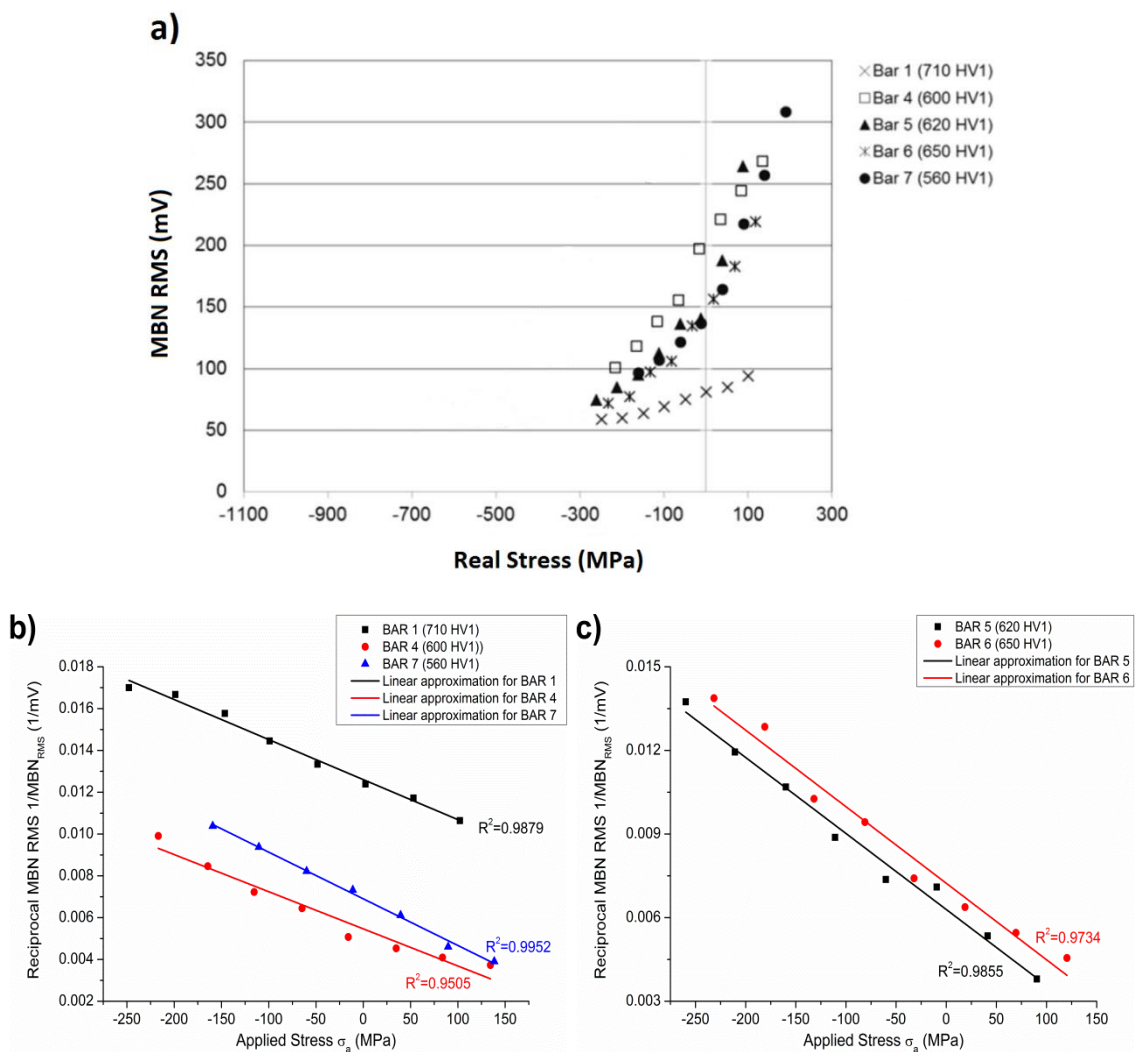
Fig. 4.40 a) a) MBN root-mean-square amplitude as a function of stress applied to EN10084 samples of various surface hardness; b) & c) Dependencies of reciprocal MBN root-mean-square on applied stress for EN10084 samples approximated with linear functions, after Santa-aho [123].

As depicted in Figs. 4.40b and 4.40c the best fitted linear functions accurately corresponded to the trends of changes in reciprocal MBN RMS with variable applied stress. This implied that despite differences in surface hardness the influence of stress induced magnetoelastic effect on Barkhausen emissions was effectively described by the MBN stress model.

The most recent application of the MBN stress model was reported in 2013 by Kypris et al. in their investigation on ASTM A36 steel, commonly used for load bearing parts [125]. The measurement system used in that study was the Microscan 600 with magnetising frequency of 100Hz. The plots of $1/MBN_{pk}$ vs σ_a and $1/MBN_{RMS}$ vs σ_a obtained by Kypris et al. are shown in Figs. 4.41a and 4.41b.
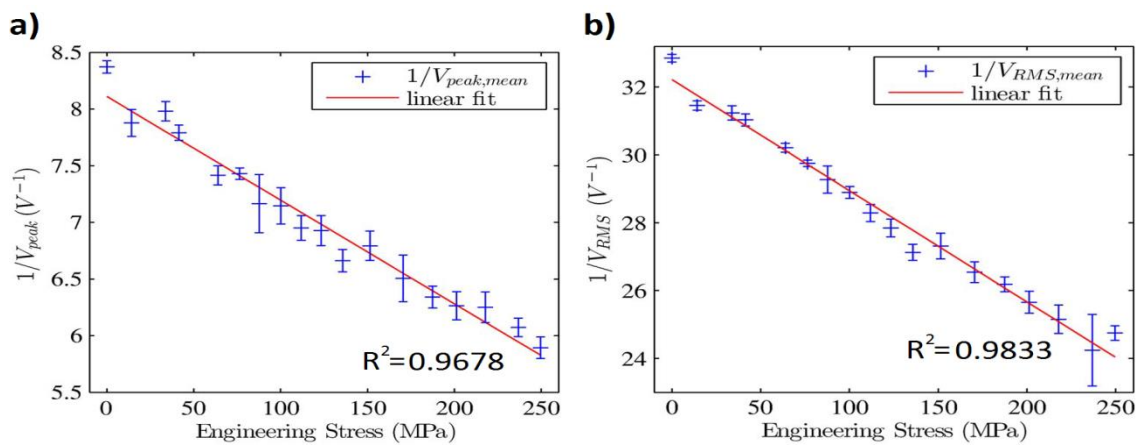
Fig. 4.41 a) & b) Linear approximations of stress dependencies of the reciprocal MBN peak amplitude and reciprocal MBN root-mean-square of ASTM A36 steel, after Kypris [125].

As can be seen in the above graphs the expected linear relations of reciprocal peak and RMS amplitudes with stress were proved to be in a very good agreement with the experimental data, which was indicated by $R^2=0.9678$ and $R^2=0.9833$, respectively. This further confirmed a potential of the MBN stress model in the quantitative evaluation of loaded heavy-duty steels using Barkhausen emissions.

4.7 Approach to stress depth profiling using Magnetic Barkhausen Noise method

In the ferromagnetic specimen that is subjected to alternating magnetic field Barkhausen emissions of various durations occur at different depths simultaneously. The resulting electromagnetic emissions diverge outwards from the origin of local magnetisation changes and can be measured at the surface in the form of voltage pulses using a pickup coil. The measured voltages are representative of, but not identical to, the emissions occurring inside the material. Attenuation of magnetic Barkhausen emissions in magnetic materials is frequency dependent and therefore information from different depths inside the material is contained in the frequency spectrum of the detected Barkhausen signal. The depth dependent information about material conditions, such as variations in microstructure and/or the presence of residual stress in steel components (e.g., load bearings, gears and camshafts), is of great technical interest. However this depth dependent information, although present in the Barkhausen emissions needs to be deconvolved from the measured MBN signal. In the previous sections the amplitude of measured Barkhausen signals was shown to depend on the state of stress due to additional magnetoelastic energy and related stress equivalent field influencing the unpinning and motion of domain walls. It can be therefore assumed that for a case of specimen with non-uniform stress depth distribution the Barkhausen emissions generated within given magnetised region is biased by the local stress magnitude determining the dynamics of domain wall processes. Providing that the amplitude of the original MBN emissions originating from a given depth within material can be extracted from measured MBN signal, the developed MBN model can be subsequently used to determine the level of stress locally at different depths.

I. Development of mathematical expressions for depth profiling using Magnetic Barkhausen Noise method

In this study the measured Magnetic Barkhausen Noise $V_{MBNmeas}$ is considered to arise as a result of the rate of change of magnetic flux density that emerges at the surface when a Barkhausen emission event occurs at a location at depth x inside the material. If we denote the surface as x = 0 then, assuming for simplicity that the signal is not diverging and that the passage of the Barkhausen signal does not change its frequency ω, even though it changes its amplitude, the signal $V_{MBNmeas}(x, ω)$ that is detected at the surface will be the original signal at depth x, $V_{MBNorigin}(x, ω)$ attenuated as it propagates to the surface. A simplifying assumption has been made that this attenuation is described by the exponential decay term as shown in Equation 4.19:

$$V_{MBNmeas}(x, \omega) = V_{MBNorigin}(x, \omega) * \exp\left(\frac{-x}{\sqrt{\frac{2\rho}{\omega\mu_0\mu_r}}}\right) \qquad (4.19)$$

where x is a depth at which $MBN_{origin}(x, ω)$ was emitted, ρ is the electrical resistivity, ω = 2πf is the MBN signal frequency and $μ_r$ is the relative permeability.

An example attenuation curves for MBN signals with original amplitudes of 1mV and frequencies of 20kHz, 100kHz and 500kHz propagating within a hypothetical ferromagnetic material with resistivity of $ρ=5*10^{-7}Ωm$ and relative permeability of $μ_r=100$ are shown in Fig. 4.42.
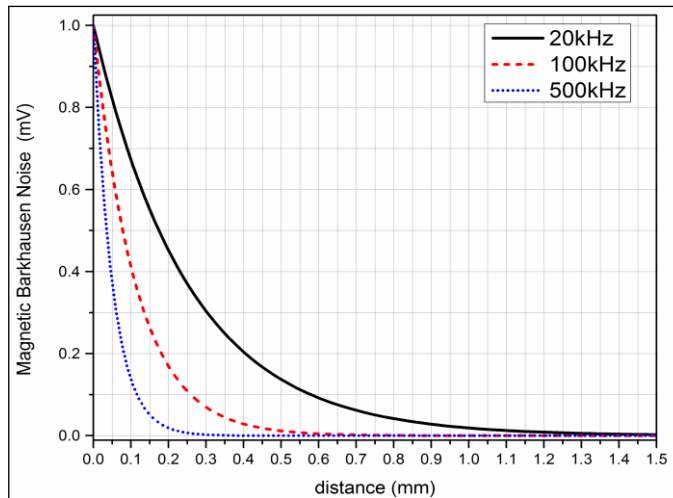
Fig. 4.42 Attenuation curves for MBN signals with frequencies of 20kHz, 100kHz and 500kHz propagating within hypothetical ferromagnetic material.

For a multiple number of Barkhausen events which occur throughout the volume of material, the detected signal at a given frequency ω will be the sum of all the detected signals of these events at different depths within the volume of inspection from x=0 to x=x_{max}, as shown in Equation 4.20.

$$V_{MBN\,meas}(0, x_{max}, \omega) = \sum_{x=0}^{x=x_{max}} V_{MBN\,origin}(x, \omega) * \exp(-\alpha x \sqrt{\omega}) \qquad (4.20)$$

where $\alpha = \sqrt{\dfrac{\mu_0 \mu_r}{2\rho}}$.

When treating the distribution of emissions as continuous Equation 4.20 can be expressed in the integral form as shown in Equation 4.21:

$$V_{MBN\,meas}(0, x_{max}, \omega) = \int_{0}^{x_{max}} V_{MBN\,origin}(x, \omega) * \exp(-\alpha x \sqrt{\omega}) dx \qquad (4.21)$$

The above expression deals only with one frequency, but Barkhausen emissions occur over a range of frequencies. If the frequency band of detection is from ω_L (lower) to ω_U (upper) then the expression for the measured Barkhausen noise will be:

$$V_{MBN\,meas}(0, x_{\omega_L}, \omega_L, \omega_U) = \int_{\omega_L}^{\omega_U} \int_{0}^{x_{\omega_L}} V_{MBN\,origin}(x, \omega) * \exp(-\alpha x \sqrt{\omega}) dx d\omega \qquad (4.22)$$

This is the basic model equation that has been developed in the present work for the non-divergent Barkhausen signal detected at the surface. The depth $x_{\omega L}$ from which MBN signal can be detected depends on the lower frequency limit ω_L. Control of this measurement parameter ω_L can therefore be used to preferentially sample Barkhausen emissions from different depths in the material. In particular a set of measurements with the same high frequency cut off but a series of different low frequency cut offs, allows differentiation of the measured signal with respect to the lower frequency and hence allows the Barkhausen emissions and related properties to be probed as a function of depth.

By way of example a test specimen which consists of two layers with different stress levels (shown in Fig. 4.43) will be considered. In this specimen the depths of x_1 and x_2

correspond to low frequency cut-offs of ω_1 and ω_2. The terms $V_{MBNorigin1}$ and $V_{MBNorigin2}$ are representative of the local Barkhausen emissions at the point of origin in the first and second layer before attenuation.
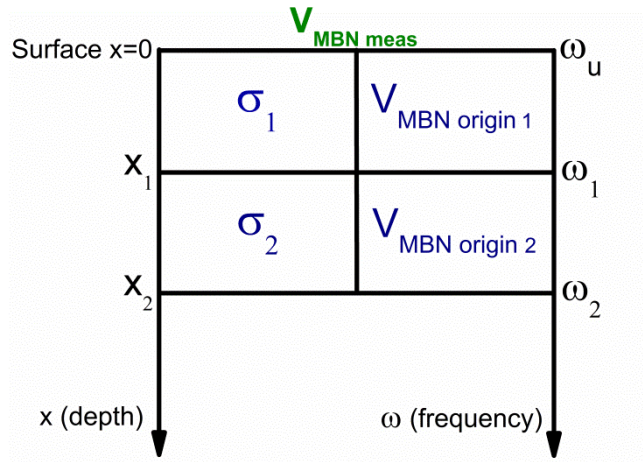
Fig. 4.43 Schematic diagram of layered specimen.

- **Analysis of the first layer**

In the case where the stress is uniform throughout, the amplitude of $V_{MBNorigin}$ will not change with depth x. Furthermore, for the purpose of simplification here we assume that in this particular case the amplitude of the emissions at their origin, $V_{MBNorigin}$, before they get attenuated is the same for all frequencies. This is the "white noise" assumption. Different frequency spectra such as "1/f" or other types of "pink noise" are also possible.

With the "white noise" assumption at the point of origin, the expression for the measured Barkhausen voltage $V_{MBNmeas}$ from the first layer becomes:

$$V_{MBNmeas}(0, x_1, \omega_1, \omega_U) = \int_{\omega_1}^{\omega_U} \int_0^{x_1} V_{MBNorigin_1} * \exp(-\alpha x \sqrt{\omega}) dx d\omega \qquad (4.23)$$

where x_1 is the depth of the first layer, and ω_1 and ω_u are the lower and upper bounds of the range of detection frequencies. The term $V_{MBNorigin1}$ is representative of the local Barkhausen emissions in the first layer before attenuation. The result of the integration is:

$$V_{\mathrm{MBNmeas}}(0,x_1,\omega_1,\omega_u) = \frac{2*V_{\mathrm{MBNorigin}_1}}{x_1\alpha^2}*(\exp(-x_1\alpha\sqrt{\omega_u})-\exp(-x_1\alpha\sqrt{\omega_1}) \quad (4.24)$$
$$+ x_1\alpha(\sqrt{\omega_u}-\sqrt{\omega_1}))$$

From Equation 4.24 it is possible to calculate $V_{\mathrm{MBNorigin1}}$, which is the unattenuated Barkhausen emission occurring inside the sample, in terms of the measurable Barkhausen emission voltage $V_{\mathrm{MBNmeas.}}$. So if the first layer in the layered specimen of Fig. 4.43 has a uniform stress σ_1 the expression for the Barkhausen emission voltage inside the material will be:

$$V_{\mathrm{MBNorigin}_1}(\sigma_1) = \frac{V_{\mathrm{MBNmeas}}(0,x_1,\omega_1,\omega_u)\dfrac{\alpha^2}{2}}{\dfrac{1}{x_1}\left(\exp(-x_1\alpha\sqrt{\omega_u})-\exp(-x_1\alpha\sqrt{\omega_1})+x_1\alpha(\sqrt{\omega_u}-\sqrt{\omega_1})\right)} \quad (4.25)$$

and therefore

$$\frac{1}{V_{\mathrm{MBNorigin}_1}(\sigma_1)} = \frac{\dfrac{1}{x_1}\left(\exp(-x_1\alpha\sqrt{\omega_u})-\exp(-x_1\alpha\sqrt{\omega_1})+x_1\alpha(\sqrt{\omega_u}-\sqrt{\omega_1})\right)}{V_{\mathrm{MBNmeas}}(0,x_1,\omega_1,\omega_u)\dfrac{\alpha^2}{2}} \quad (4.26)$$

It is important to note that this term $V_{\mathrm{MBNorigin}}$ needs to be determined for correct depth profiling of the condition of the material, not V_{MBNmeas}. This arises because it is $V_{\mathrm{MBNorigin}}$ that is primarily dependent on stress (V_{MBNmeas} is only secondarily dependent on stress through the stress dependence of $V_{\mathrm{MBNorigin}}$). Therefore $V_{\mathrm{MBNorigin}}$ can be used to determine the level of stress locally at different depths, provided it can be calculated from the measurements, because it contains information on the local condition at depths in the material.

- **Analysis of the combined first and second layer**

In order to take measurements from both layer 1 and layer 2, the lower cut off frequency needs to be reduced to allow detection of emissions from deeper inside the sample. Let this new lower cut off frequency be ω_2, such that $\omega_2 < \omega_1$ and let the corresponding depth of penetration be x_2 such that $x_2 > x_1$. Then the integral for combined emissions will be:

$$V_{\mathrm{MBNmeas}}(0,x_2,\omega_2,\omega_u) = \int_{\omega_2}^{\omega_u}\int_0^{x_2} V_{\mathrm{MBNorigin}}(x)*\exp(-\alpha x\sqrt{\omega})\,dx\,d\omega \quad (4.27)$$

Splitting this into two terms, the separate integrals which represent the detected emissions from each of the two layers are:

$$V_{MBNmeas}(0,x_2,\omega_2,\omega_u) = \int_{\omega_2}^{\omega_u}\int_0^{x_1} V_{MBNorigin_1} * \exp(-\alpha x\sqrt{\omega})dxd\omega$$

$$+ \int_{\omega_2}^{\omega_u}\int_{x_1}^{x_2} V_{MBNorigin_2} * \exp(-\alpha x\sqrt{\omega})dxd\omega$$

(4.28)

In this case the properties of the two layers are different so that the unattenuated Barkhausen emissions, $V_{MBNorigin1}$ and $V_{MBNorigin2}$ will be different and will represent conditions at the point of origin.

- **Analysis of the second layer alone**

To a first approximation emissions from the second layer at frequencies between ω_1 and ω_u will not reach the surface because emissions at these frequencies will be highly attenuated. So only emissions from that layer with frequencies between ω_2 and ω_1 are of interest. Therefore for the second layer, for which the frequency bounds are ω_2 ($<\omega_1$) and ω_u, the expression for the measured Barkhausen emission is:

$$V_{MBNmeas}(x_1,x_2,\omega_2,\omega_1) = \int_{\omega_2 x1}^{\omega_1 x_2} V_{MBNorigin_2} * \exp(-\alpha x\sqrt{\omega})dxd\omega$$

(4.29)

and Equation 4.28 must be modified to:

$$V_{MBNmeas}(0,x_2,\omega_2,\omega_u) = \int_{\omega_2}^{\omega_u}\int_0^{x_1} V_{MBNorigin_1} * \exp(-\alpha x\sqrt{\omega})dxd\omega$$

$$+ \int_{\omega_2}^{\omega_1}\int_{x_1}^{x_2} V_{MBNorigin_2} * \exp(-\alpha x\sqrt{\omega})dxd\omega$$

(4.30)

where the values of $V_{MBN\ origin1}$ and $V_{MBN\ origin2}$ are assumed constant within each layer but different from layer to layer.

The first integral on the RHS of Equation 4.30 represents the emissions from the first layer. This can also be split into two parts. The integral from ω_1 to ω_u represents the measurement $V_{MBNmeas}$ in Equation 4.23, while the integral from ω_2 to ω_1 represents additional emissions measured from the first layer that arise because of the

increased bandwidth from ω_1 to ω_2 in the second measurement. This can be written as follows:

$$V_{MBN_{meas}}(0, x_2, \omega_2, \omega_u) = \int_{\omega_1}^{\omega_u} \int_0^{x_1} V_{MBNorigin_1} \exp(-\alpha x \sqrt{\omega}) dx d\omega$$
$$+ \int_{\omega_2}^{\omega_1} \int_0^{x_1} V_{MBNorigin_1} \exp(-\alpha x \sqrt{\omega}) dx d\omega + \int_{\omega_2}^{\omega_1} \int_{x_1}^{x_2} V_{MBNorigin_2} \exp(-\alpha x \sqrt{\omega}) dx d\omega \qquad (4.31)$$

and since the first term on the RHS of the above Equation 4.31 is equivalent to the first measurement $V_{MBNmeas}(0,x_1,\omega_1,\omega_U)$ given in Equation 4.23 the above formula can be rewritten:

$$V_{MBN_{meas}}(0, x_2, \omega_2, \omega_u) = V_{MBN_{meas}}(0, x_1, \omega_1, \omega_U)$$
$$+ \int_{\omega_2}^{\omega_1} \int_0^{x_1} V_{MBNorigin_1} \exp(-\alpha x \sqrt{\omega}) dx d\omega + \int_{\omega_2}^{\omega_1} \int_{x_1}^{x_2} V_{MBNorigin_2} \exp(-\alpha x \sqrt{\omega}) dx d\omega \qquad (4.32)$$

In order to determine $V_{MBNorigin2}$ the solution of the following integral in Equation 4.32 needs to be found:

$$\int_{\omega_2}^{\omega_1} \int_0^{x_1} V_{MBNorigin_1} \exp(-\alpha x \sqrt{\omega}) dx d\omega \qquad (4.33)$$

The white noise assumption provides that the amplitude spectrum of emissions in the range of frequencies of interest can be approximated by a constant function. This means that $V_{MBNorigin}$ is independent of frequency. Therefore the result of Equation 4.24 can be used to solve the integral in Equation 4.33 as follows:

$$\int_{\omega_2}^{\omega_1} \int_0^{x_1} V_{MBNorigin_1} * \exp(-\alpha x \sqrt{\omega}) dx d\omega = = \frac{2 * V_{MBNorigin_1}}{x_1 \alpha^2} * (\exp(-x_1 \alpha \sqrt{\omega_1})$$
$$- \exp(-x_1 \alpha \sqrt{\omega_2}) + x_1 \alpha (\sqrt{\omega_1} - \sqrt{\omega_2})) \qquad (4.34)$$

and substituting this into Equation 4.32 gives:

$$V_{MBN_{meas}}(0, x_2, \omega_2, \omega_u) = V_{MBN_{meas}}(0, x_1, \omega_1, \omega_U)$$
$$+ \frac{2 * V_{MBNorigin_1}}{x_1 \alpha^2} * (\exp(-x_1 \alpha \sqrt{\omega_1}) - \exp(-x_1 \alpha \sqrt{\omega_2}) + x_1 \alpha (\sqrt{\omega_1} - \sqrt{\omega_2})) \qquad (4.35)$$
$$+ \int_{\omega_2}^{\omega_1} \int_{x_1}^{x_2} V_{MBNorigin_2} \exp(-\alpha x \sqrt{\omega}) dx d\omega$$

It is also known from Equation 4.25 that:

$$V_{MBNorigin_1}(\sigma_1) = \frac{V_{MBNmeas}(0,x_1,\omega_1,\omega_u)\dfrac{\alpha^2}{2}}{\dfrac{1}{x_1}\left(\exp\left(-x_1\alpha\sqrt{\omega_u}\right)-\exp\left(-x_1\alpha\sqrt{\omega_1}\right)+x_1\alpha(\sqrt{\omega_u}-\sqrt{\omega_1})\right)} \tag{4.36}$$

which can be substituted into Equation 4.35 to give:

$$V_{MBNmeas}(0,x_2,\omega_2,\omega_U) = V_{MBNmeas}(0,x_1,\omega_1,\omega_U)$$
$$+V_{MBNmeas}(0,x_1,\omega_1,\omega_U)*\frac{\left(\exp\left(-x_1\alpha\sqrt{\omega_1}\right)-\exp\left(-x_1\alpha\sqrt{\omega_2}\right)+x_1\alpha(\sqrt{\omega_1}-\sqrt{\omega_2})\right)}{\left(\exp\left(-x_1\alpha\sqrt{\omega_u}\right)-\exp\left(-x_1\alpha\sqrt{\omega_1}\right)+x_1\alpha(\sqrt{\omega_u}-\sqrt{\omega_1})\right)}$$
$$+\int_{\omega_2}^{\omega_1}\int_{x_1}^{x_2}V_{MBNorigin_2}\exp(-\alpha x\sqrt{\omega})dxd\omega \tag{4.37}$$

Therefore from the two measurements $V_{MBNmeas}(0,x_1,\omega_1,\omega_U)$ and $V_{MBNmeas}(0,x_2,\omega_2,\omega_U)$ it should be possible in principle to calculate $V_{MBNorigin2}$ and thereby determine the condition of the material in the second layer from depth x_1 to x_2.

Next to evaluate is the double integral on the RHS of Equation 4.37:

$$\int_{\omega_2}^{\omega_1}\int_{x_1}^{x_2}V_{MBNorigin_2}\exp(-\alpha x\sqrt{\omega})dxd\omega = \frac{2V_{MBNorigin_2}}{\alpha^2}\left(\begin{array}{l}\dfrac{1}{x_2}(\exp(-\alpha x_2\sqrt{\omega_1})-\exp(-\alpha x_2\sqrt{\omega_2}))\\[2mm]-\dfrac{1}{x_1}\left(\exp(-\alpha x_1\sqrt{\omega_1})-\exp(-\alpha x_1\sqrt{\omega_2})\right)\end{array}\right) \tag{4.38}$$

Subsequently using Equations 4.37 and 4.38 an expression for $V_{MBNmeas}(0,x_2,\omega_2,\omega_U)$ representing the measurement from the second layer can be obtained:

$$V_{MBNmeas}(0,x_2,\omega_2,\omega_u) = V_{MBNmeas}(0,x_1,\omega_1,\omega_U)+$$
$$+V_{MBNmeas}(0,x_1,\omega_1,\omega_U)*\frac{\left(\exp\left(-x_1\alpha\sqrt{\omega_1}\right)-\exp\left(-x_1\alpha\sqrt{\omega_2}\right)+x_1\alpha(\sqrt{\omega_1}-\sqrt{\omega_2})\right)}{\left(\exp\left(-x_1\alpha\sqrt{\omega_u}\right)-\exp\left(-x_1\alpha\sqrt{\omega_1}\right)+x_1\alpha(\sqrt{\omega_u}-\sqrt{\omega_1})\right)}+$$
$$+\frac{2V_{MBNorigin_2}}{\alpha^2}\left(\frac{1}{x_2}(\exp(-\alpha x_2\sqrt{\omega_1})-\exp(-\alpha x_2\sqrt{\omega_2}))-\frac{1}{x_1}\left(\exp(-\alpha x_1\sqrt{\omega_1})-\exp(-\alpha x_1\sqrt{\omega_2})\right)\right) \tag{4.39}$$

and consequently the unattenuated Barkhausen emissions $V_{MBNorigin2}$ occurring inside layer 2 of the sample can be expressed in terms of the two Barkhausen noise voltages measured at the surface $V_{MBNmeas}(0,x_2,\omega_2,\omega_U)$ and $V_{MBNmeas}(0,x_1,\omega_1,\omega_U)$ as shown in Equation 4.40:

$$V_{MBN_{origin_2}} = \frac{\alpha^2}{2} \frac{V_{MBN_{meas}}(0,x_2,\omega_2,\omega_u) - V_{MBN_{meas}}(0,x_1,\omega_1,\omega_U)\left(1 + \frac{\left(\exp\left(-x_1\alpha\sqrt{\omega_1}\right) - \exp\left(-x_1\alpha\sqrt{\omega_2}\right) + x_1\alpha\left(\sqrt{\omega_1}-\sqrt{\omega_2}\right)\right)}{\left(\exp\left(-x_1\alpha\sqrt{\omega_u}\right) - \exp\left(-x_1\alpha\sqrt{\omega_1}\right) + x_1\alpha\left(\sqrt{\omega_u}-\sqrt{\omega_1}\right)\right)}\right)}{\left(\frac{1}{x_2}(\exp(-\alpha x_2\sqrt{\omega_1}) - \exp(-\alpha x_2\sqrt{\omega_2})) - \frac{1}{x_1}\left(\exp(-\alpha x_1\sqrt{\omega_1}) - \exp(-\alpha x_1\sqrt{\omega_2})\right)\right)}$$

(4.40)

The reciprocal of V$_{MBNorigin2}$ will then be:

$$\frac{1}{V_{MBN_{origin_2}}} = \frac{2}{\alpha^2} \frac{\left(\frac{1}{x_2}(\exp(-\alpha x_2\sqrt{\omega_1}) - \exp(-\alpha x_2\sqrt{\omega_2})) - \frac{1}{x_1}\left(\exp(-\alpha x_1\sqrt{\omega_1}) - \exp(-\alpha x_1\sqrt{\omega_2})\right)\right)}{V_{MBN_{meas}}(0,x_2,\omega_2,\omega_u) - V_{MBN_{meas}}(0,x_1,\omega_1,\omega_U)\left(1 + \frac{\left(\exp\left(-x_1\alpha\sqrt{\omega_1}\right) - \exp\left(-x_1\alpha\sqrt{\omega_2}\right) + x_1\alpha(\sqrt{\omega_1}-\sqrt{\omega_2})\right)}{\left(\exp\left(-x_1\alpha\sqrt{\omega_u}\right) - \exp\left(-x_1\alpha\sqrt{\omega_1}\right) + x_1\alpha(\sqrt{\omega_u}-\sqrt{\omega_1})\right)}\right)}$$

(4.41)

Providing that the stress dependence of unattenuated Barkhausen emissions V$_{MBNorigin}$ at the point of origin is analogous to that described for the MBN$_{pk}$ by the previously introduced MBN stress model, then we can write :

$$\frac{1}{\left[V_{MBN_{origin_2}}(\sigma_2)\right]} - \frac{1}{\left[V_{MBN_{origin_1}}(\sigma_1)\right]} = \frac{3\,b'(\sigma_1 - \sigma_2)}{\mu_0}$$

(4.42)

The difference in stress between the two layers can be calculated from the following equation:

$$\sigma_1 - \sigma_2 = \frac{\mu_0}{3b'}\frac{2}{\alpha^2}\left[\frac{\left(\frac{1}{x_2}(\exp(-\alpha x_2\sqrt{\omega_1}) - \exp(-\alpha x_2\sqrt{\omega_2})) - \frac{1}{x_1}\left(\exp(-\alpha x_1\sqrt{\omega_1}) - \exp(-\alpha x_1\sqrt{\omega_2})\right)\right)}{V_{MBN_{meas}}(0,x_2,\omega_2,\omega_u) - V_{MBN_{meas}}(0,x_1,\omega_1,\omega_U)*\left(1 + \frac{\left(\exp\left(-x_1\alpha\sqrt{\omega_1}\right) - \exp\left(-x_1\alpha\sqrt{\omega_2}\right) + x_1\alpha\left(\sqrt{\omega_1}-\sqrt{\omega_2}\right)\right)}{\left(\exp\left(-x_1\alpha\sqrt{\omega_u}\right) - \exp\left(-x_1\alpha\sqrt{\omega_1}\right) + x_1\alpha\left(\sqrt{\omega_u}-\sqrt{\omega_1}\right)\right)}\right)}\right]$$
$$-\frac{\mu_0}{3b'}\frac{2}{\alpha^2}\left[\frac{\frac{1}{x_1}\left(\exp\left(-x_1\alpha\sqrt{\omega_u}\right) - \exp\left(-x_1\alpha\sqrt{\omega_1}\right) + x_1\alpha(\sqrt{\omega_u}-\sqrt{\omega_1})\right)}{V_{MBN_{meas}}(0,x_1,\omega_1,\omega_u)}\right]$$

(4.43)

The above derived set of equations allows extracting stress depth information from the original Barkhausen emissions deconvolved from MBN signal detected at the surface. This methodology requires two measurements, one limited to the surface

layer 1, the other including emissions from both layers 1 and 2. The developed mathematical formalism enables the emissions from both layers to be separated.

An experimental procedure utilising these developed formulas is proposed in the next sub-section.

II. Experimental procedure

The schematic diagram of the MBN experimental set-up required for stress depth profiling is shown in Fig. 4. 44.
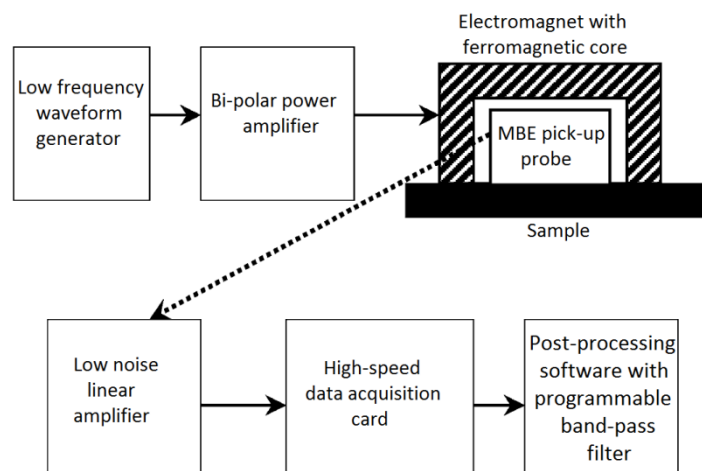
Fig. 4.44 Schematic diagram of MBN set-up for depth profiling analysis.

The depth profiling procedure involving the above set-up can be described as following:

- The interrogated sample is magnetised using an electromagnet comprising U-shape ferromagnetic yoke with wound coil energized by low frequency current to ensure uniform magnetization within the investigated depth range of the specimen

- The MBN emissions are sensed using a surface pick-up probe positioned symmetrically in-between the electromagnet poles. The pick-up probe should have a linear characteristic and could be an induction sensor, Hall probe or any other suitable type of magnetic sensor. When an induction sensor is used it should have its resonant frequency outside the analyzed MBN frequency range.

- The raw MBN signal can be amplified with a low noise amplifier having a linear characteristic in the full analysed frequency spectrum

- The MBN data is collected with a high resolution data acquisition card with high sampling frequency of at least 2MHz to provide sufficient frequency spectrum for multi-layer analysis

- The final calculations of MBN parameters used in the depth profiling formulas are performed with a post-processing software containing a filter for extracting MBN data within various ranges of frequency

In cases where the analysed material exhibits a linear dependence of reciprocal $V_{MBNorigin}$ on stress the function $1/V_{MBNorigin}(\sigma)$ can be obtained using only two reference specimens with known but different surface stress levels. If the stress dependence of Barkhausen emissions is more complex than a higher number of samples are required to obtain the calibration curve.

In both cases calibration can be performed by correlating the stress obtained from X-ray diffraction with the $V_{MBNorigin1}$ calculated from Equation 4.36 where the low frequency limit ω_1 (Fig. 4.43) should correspond to the XRD penetration depth. The established quantitative relation for the first layer can be further used to determine the stress in the second layer as the functions $1/V_{MBNorigin1}(\sigma_1)$ and $1/V_{MBNorigin2}(\sigma_2)$ are analogous.

4.8   Summary

- DC hysteresis measurements were performed for samples with different levels of residual stress. No apparent trends of bulk magnetic properties, such as coercivity, remanence and permeability, were observed due to self-equilibrating nature of Type I residual stresses. This justified the difference between macromagnetic (hysteresis) and micromagnetic (MBN) methods, where the bulk magnetic properties, unlike Barkhausen parameters, are insensitive to local variations in residual stress.

- A new model describing dependence of magnetic Barkhausen noise peak amplitude on stress has been developed. This model predicted a very useful linear relation between reciprocal of MBN_{pk} and stress σ for ferromagnetic materials in which magnetostriction is relatively insensitive to stress. Moreover, it was shown that after incorporating the stress dependence of magnetostriction coefficients b and b' the proposed MBN model could be further applied to describe the stress effects on MBN_{pk} in a wide variety of stress-sensitive magnetostrictive materials.

- The anticipated linear behaviour of $1/ MBN_{pk}$ with stress based on the model was validated by experimental results obtained for carburised SAE9310 and nitrided SAE6481 samples. The analogous magnetoelastic effect of both applied stress and long range Type I residual macro-stress on MBN emissions in SAE9310 steel was justified. Most significantly the model predictions were validated for materials with both positive and negative magnetostrictions.

- The generality of the proposed MBN model was confirmed by its successful application in the quantitative stress evaluation using Barkhausen emissions in other types of steel, such as pipeline and EN36 steels [91, 121, 122] and also in the recent results of other investigators for RAEX400, EN10084 and ASTM A36 steels [123, 124, 125].

- A new comprehensive method has been developed for determining depth profiles of properties such as residual stress using Magnetic Barkhausen Noise measurements. The developed underlying equations involve knowledge of the stress dependence of MBN amplitude and in addition knowledge of the attenuation of the original MBN signal. The proposed methodology shows how to extract the Barkhausen emissions and related stress information from different points of origin using some simplifying assumptions.

- The complete set of equations has been derived for the first time here in this work, and for the purposes of demonstration a particular case has been presented in which the stress is uniform in each of two layers, but different from one layer to the next.

- An experimental methodology for practical implementation of the developed equations was proposed. This methodology can be used for determining the variation of stress with depth in magnetic materials with the information being extracted from the frequency dependence of the detected Barkhausen signals.

5.   Finite Element Modelling of magnetic flux leakage in detection of transverse flaws in rail structure

5.1   Introduction

The main objectives of the work presented in this chapter include analysis and justification of the magnetic flux leakage distributions in vicinity of transverse flaws generated with currently applied rail inspection method, as well as modelling and validation of the voltage signals detected with Sperry Induction Sensing Unit. The outcome of this analysis provides a full understanding of the currently used inspection methodology and is consequently used for comparison with the alternative detection methods, involving different current injection techniques enabling generation of greater flux leakage effects. The proposed testing procedures are easily implementable in the commonly performed examination of structural integrity of rail.

In Section 5.2 the underlying principles of generation and distribution of magnetic field within and around a current carrying conductor is given. In Section 5.3 the flaw detection methodology of induction sensing unit (ISU) currently applied by Sperry Ltd. in railway inspection is presented. In Section 5.4 the details of developed FEM model used for magnetic flux leakage analysis are described. The calculated results on the currently obtained distributions of magnetic flux leakage above various cases of flawed rails, as well as types of voltage signals recorded by inductive sensors during rail inspection involving longitudinal current injection procedure are given. Subsequently alternative current injection techniques, i.e. diagonal and transverse, are proposed and evaluated. These techniques determine different current divergence and re-routing mechanisms within flawed rails, and produce more pronounced MFL signals, thus offering an improved effectiveness of the rail flaw inspection. The simulated voltage signatures which can be obtained from induction sensors during the inspections involving three analysed current application methodologies are compared and discussed in detail.

Finally, the outcome from the performed MFL rail analysis is summarised in Section 5.5.

5.2 Underlying principles of magnetic flux leakage method with current injection

The magnetic field profiles within and outside the current carrying conductor can be obtained using the Biot-Savart law. In case of infinitely long conductor this law is described by a simple expression:

$$H = \frac{I}{2\pi l} \tag{5.1}$$

where **H** is the magnetic field, I is the current in the conductor and l is the radial distance between the conductor and the point at which the field **H** is measured and calculated.

Using the basic Equation 5.1 analytic formulas for calculation of magnetic field profiles within and around a rectangular current carrying conductor of dimensions 70mm×40mm approximating the shape of typical rail head can be derived. The schematic diagram for this derivation is shown in Fig. 5.1 in which the indicated in-plane direction of current flow is shown as well as the components H_x and H_y of the clockwise circulating magnetic field **H** at some given distance l from the conductor.
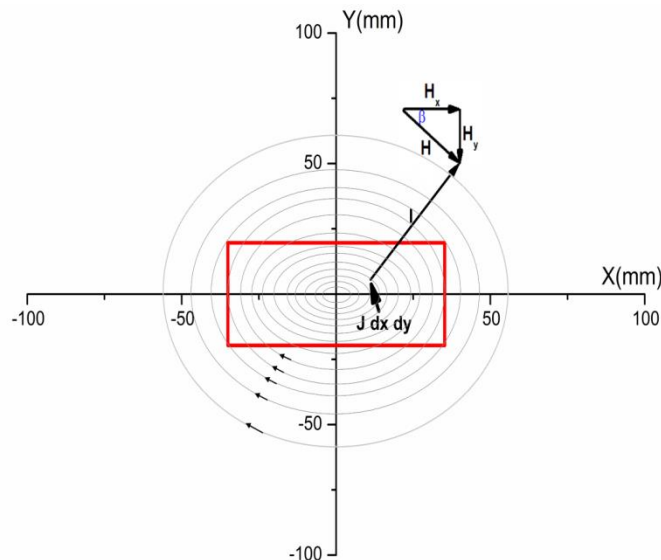

Fig 5.1 Schematic diagram of rectangular current carrying conductor and corresponding circulating magnetic field.

The general equation for magnetic field **H** in the above case can be written as follows:

$$H = \frac{I}{2\pi l} = \frac{I}{2\pi\sqrt{(x_H - x_J)^2 + (y_H - y_J)^2}} \qquad (5.2)$$

where x_H, y_H are the coordinates of the position P_H (x_H, y_H) at which **H** is calculated and x_J, y_J are the coordinates of the position P_J (x_J, y_J) of the current carrying conductor. The formulas for tangential H_x and normal H_y components of the magnetic field can be given as:

$$H_x = H \cos \beta \qquad (5.3)$$

$$H_y = H \sin \beta \qquad (5.4)$$

where β is the angle between the tangential component vector H_x and total field vector **H** (as depicted in Fig. 5.1) and can be described as:

$$\cos \beta = \sin(90 - \beta) = \frac{y_H - y_J}{\sqrt{(x_H - x_J)^2 + (y_H - y_j)^2)}} \qquad (5.5)$$

$$\sin \beta = \cos(90 - \beta) = \frac{x_H - x_J}{\sqrt{(x_H - x_J)^2 + (y_H - y_j)^2)}} \qquad (5.6)$$

In order to sum the contributions from all current elements within the conductor to give the total tangential and normal components of the generated magnetic field the following double integrals need to be solved:

- For the tangential component H_x:

$$H_x = \int_{-0.035}^{0.035} \int_{-0.02}^{0.02} \frac{i(y_H - y_J)}{2\pi[(x_H - x_J)^2 + (y_H - y_J)^2]} dx_J dy_J \qquad (5.7)$$

which after integration gives this analytical function:

$$H_x = \frac{1}{4\pi} \times J \times (2*(0.02 - y_H)*ArcTan(\frac{0.035 - x_H}{0.02 - y_H}) - 2*(0.02 + y_H)*$$

$$ArcTan(\frac{0.035 - x_H}{0.02 + y_H}) + (0.035 - x_H)*(Log[(0.035 - x_H)^2 + (0.02 - y_H)^2] -$$

$$Log[(0.035 - x_H)^2 + (0.02 + y_H)^2]) + 2*(0.02 - y_H)*ArcTan(\frac{0.035 + x_H}{0.02 - y_H}) -$$

$$2*(0.02 + y_H)*ArcTan(\frac{0.035 + x_H}{0.02 + y_H}) + (0.035 + x_H)*$$

$$(Log[(0.035 + x_H)^2 + (0.02 - y_H)^2] - Log[(0.035 + x_H)^2 + (0.02 + y_H)^2])$$

$$(5.8)$$

where **J** is now a current density.

- For the normal component H_y:

$$H_Y = \int_{-0.035}^{0.035}\int_{-0.02}^{0.02} \frac{i(x_H - x_J)}{2\pi\left[(x_H - x_J)^2 + (y_H - y_J)^2\right]}dx_J dy_J \quad (5.9)$$

which after solving gives:

$$H_Y = \frac{1}{4\pi}\times J \times (2*(0.035 - x_H)*ArcTan(\frac{0.02 - y_H}{0.035 - x_H}) - 2*(0.035 + x_H)*$$

$$ArcTan(\frac{0.02 - y_H}{0.035 + x_H}) + (0.02 - y_H)*(Log[(0.035 - x_H)^2 + (0.02 - y_H)^2] -$$

$$Log[(0.035 + x_H)^2 + (0.02 - y_H)^2]) + 2*(0.035 - x_H)*ArcTan(\frac{0.02 + y_H}{0.035 - x_H}) -$$

$$2*(0.035 + x_H)*ArcTan(\frac{0.02 + y_H}{0.035 + x_H}) + (0.02 + y_H)*$$

$$\left(Log[(0.035 - x_H)^2 + (0.02 + y_H)^2] - Log[(0.035 + x_H)^2 + (0.02 + y_H)^2]\right)$$

$$(5.10)$$

- The magnitude of the magnetic field strength **H** can then be calculated using equation:

$$H = \sqrt{H_X^2 + H_Y^2} \qquad (5.11)$$

The obtained analytical functions from Equations 5.8 and 5.10 can be used to calculate the profiles of magnetic field in and around the analysed rectangular conductor representing the rail head. In order to indicate the decay of magnetic field with distance from rail surface the profiles of tangential and normal components at distance of 1mm, 5mm and 10mm along the width of rail (Fig. 5.2a) carrying a current of 3000A were calculated, as shown in Figs. 5.2b and 5.2c.

a)
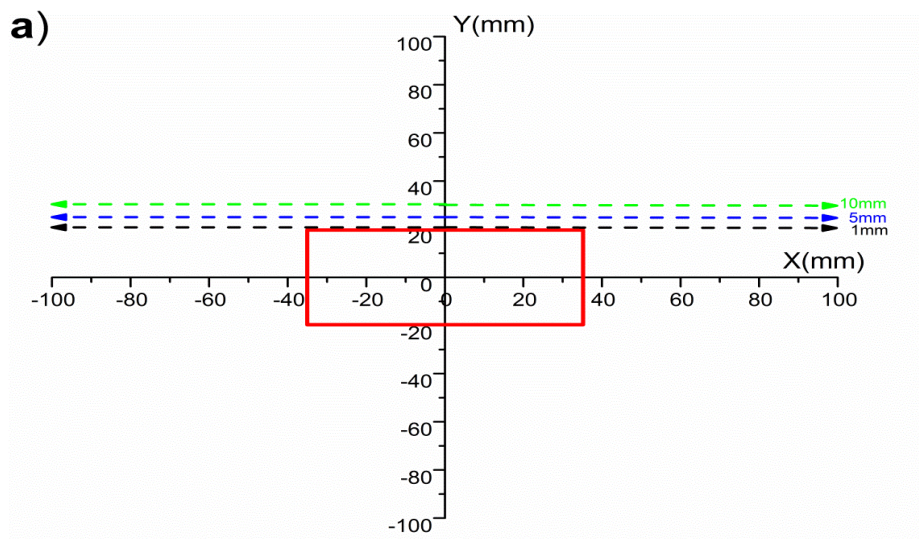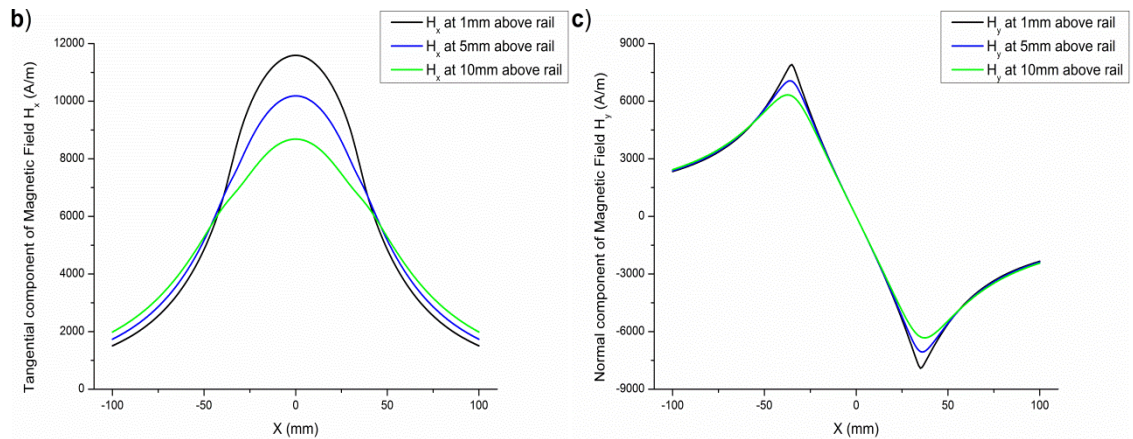
Fig. 5.2 a) Indication of the regions in which the profiles of tangential and normal components of magnetic field were simulated; b) & c) Distributions of tangential H_x and normal H_y components at different levels above a rectangular approximation of a rail head carrying current of 3000A.

As it can be seen in Fig. 5.2b the distributions of tangential component H_x exhibit a single peak profile with the maximum value located above the centre of the rectangular conductor. It can be also seen that the values of H_x in the region above rail decrease with increasing distance from the surface. In the case of the normal component H_y the distribution is represented by a bi-polar two-peak profile with the maximum and minimum values located above the side edges of the analysed rail head. The values of H_y in those regions decay with increasing gap.

Another characteristic of the magnetic field generated by a current carrying conductor is the **H** distribution from the conductor centre to its edges and outwards. This type of profile was simulated for H_x and H_y components along the normal direction in the mid-section of rectangular rail head carrying current of 3000A, as depicted in Figs. 5.3a and Fig 5.3b.
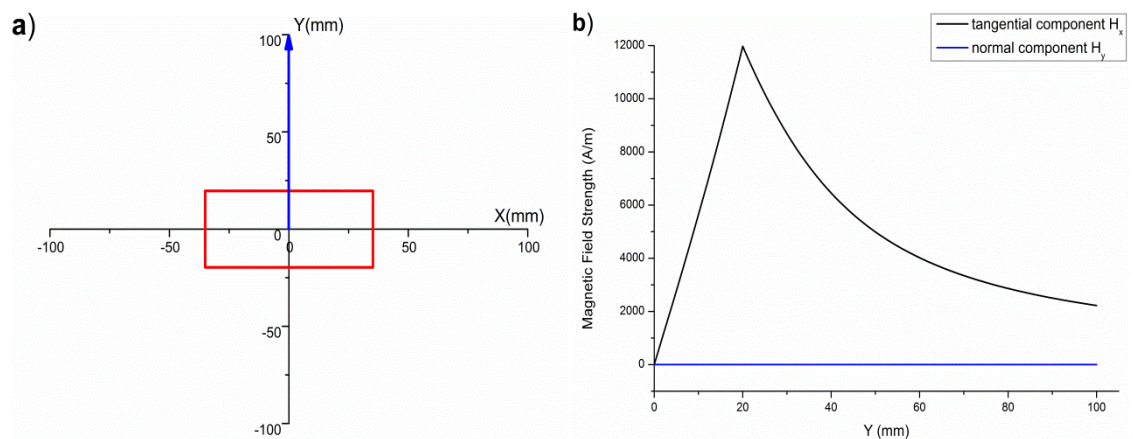
Fig. 5.3 a) Indication of the region in which the profiles of H_x and H_y were simulated; b) Values of H_x and H_y along the normal direction from centre of the rail head.

As shown in Fig. 5.3b in the calculations the tangential component H_x is equal to total magnetic field H as the normal component H_y is zero due to its profile symmetry against the centre axis of conductor. Both H_x and consequently H can be seen to increase linearly with distance from the centre of rectangular rail head to its boundary and subsequently decrease in inverse proportion to distance beyond that point. This is a typical magnetic field characteristic for current carrying conductor.

The other main factor governing the magnetic field strength inside and around the current carrying conductor is the amplitude of current I and consequently the current density J. This dependence is shown in Figs. 5.4a and 5.4b, where the profiles of H_x and H_y calculated along width at 1mm above the rectangular rail head carrying currents of 1000A, 2000A and 3000A are presented.
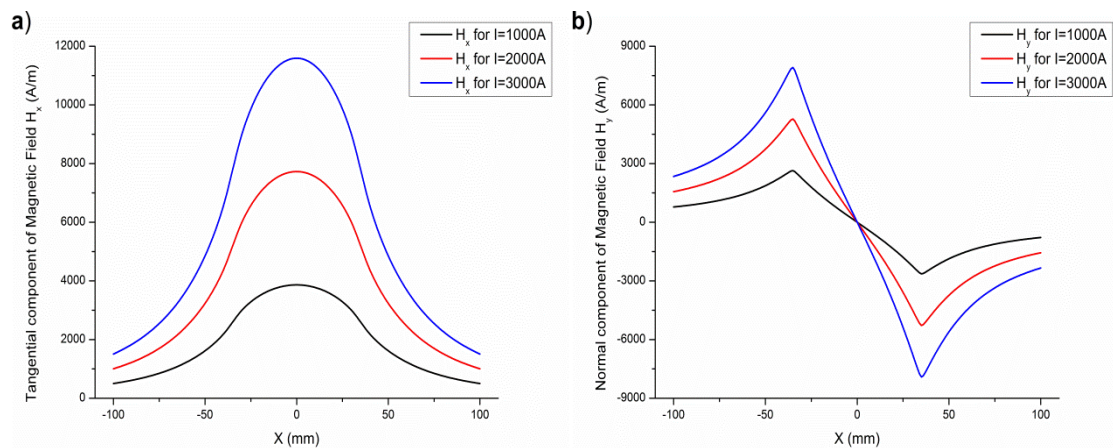
Fig. 5.4 a)&b) Distributions of tangential H_x and normal H_y components at 1mm above rectangular rail heads carrying currents of 1000A, 2000A and 3000A.

It can be seen in Figs. 5.2 to 5.4 that the analytic formulas derived for rectangular current carrying conductor can provide reliable basic information on the distribution of magnetic field within and around an energised unflawed rail head. In this particular case the flow of the current along the longitudinal direction of rail would generate only tangential and normal components, and can be treated as a simplified 2D model. In the case of a flawed rail the analysis becomes more complex. The presence of a flaw in the rail structure will force the currents in the affected region to re-route into an alternative path of lower resistance. The pattern of this current re-routing mechanism will therefore determine the effective perturbation in distribution of magnetic field components within and above the flawed section of rail. The main effects of the re-

routing of current will include an increase in the current density in the regions surrounding the flaw, as well as the alteration in direction of current flow within the affected rail volume leading to a variation in magnetic field profile above the rail.

5.3 Application of Sperry Induction Sensing Unit in detection of transverse defects

Sperry Rail Ltd performs a continuous rail inspection using their test vehicles with installed ultrasound and magnetic induction detection systems at speeds up to 60km/h. Due to limitations of ultrasonic inspection in detection of transverse rail flaws the complementary system used for their identification is the Induction Sensing Unit (ISU) comprising beryllium-copper electrodes and a sensor unit, as shown in Fig. 5.5.
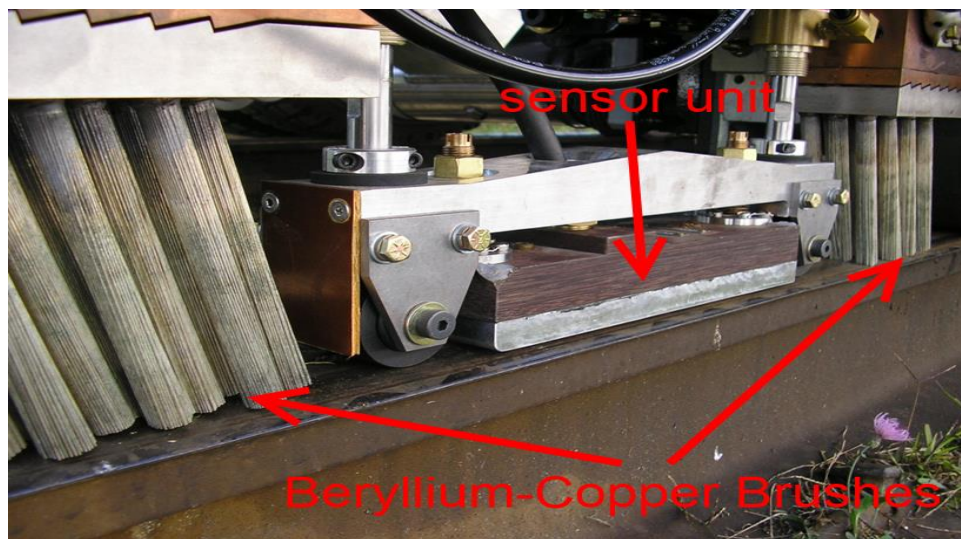
Fig. 5.5 Illustration of Sperry Induction Sensing Unit (ISU).

During the dynamic inspection a DC current with typical amplitude of 3000A is applied to the rail via the electrodes and the potential perturbation in magnetic field caused by re-routing of current in the vicinity of the flaw is detected with the induction sensors enclosed in the non-magnetic case positioned above the rail. The types of electrodes used in this type of inspection are typically forms of beryllium-copper brushes or long cylindrical beryllium-copper bars. The sensing unit comprises a set of induction sensors detecting variations in particular components of magnetic field, which are organised in a specific layout shown in Fig. 5.6.
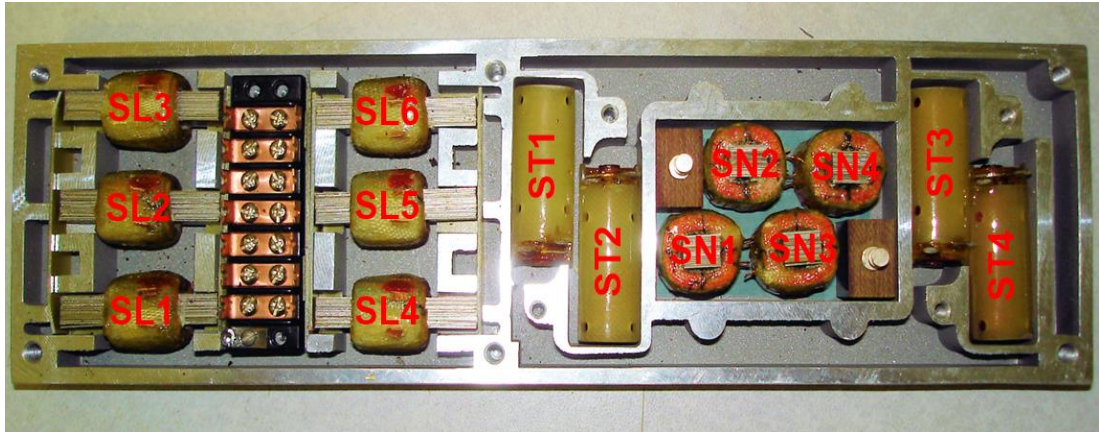
Fig. 5.6 Illustration of the Sperry induction sensors layout.

As it can be seen in the above image the arrangement of induction sensors, made of electrical steel cores wound with pick-up coils, includes three groups designated for sensing magnetic field perturbation in the longitudinal direction (labelled as SL sensors), normal direction (SN sensors) and tangential direction (ST sensors). The detected dynamic variations in magnetic flux φ and consequently magnetic flux density **B** appear as an induced voltage in the pick-up coils, according to Faraday's law of induction (Equation 2.36). The typical signatures of these induced voltage signals indicating the presence of transverse flaws are shown in Figs. 5.7a and 5.7b.

Fig. 5.7 Typical induced voltage signatures indicating the presence of transverse flaw probed with: a) longitudinal sensor SL (purple curve) and normal sensor SN (yellow curve); b) longitudinal sensor SL (purple curve) and tangential sensor ST (yellow curve).

The FEM results on the flaw related directional perturbations in magnetic field for the case of rail carrying current in the longitudinal direction (equivalent to ISU inspection procedure) will be presented and analysed in Section 5.4.1. These results explain the voltage signals picked-up during the rail testing (Figs. 5.7a and 5.7b), which will be justified and discussed in Section 5.4.2.

5.4 Finite Element Modelling of electromagnetic field distributions for various cases of unflawed and flawed rails

In this section the FEM models and calculation results for various cases of unflawed and flawed rails will be presented. The Section 5.4.1 provides an outcome from the static analysis on the MFL distributions above the rails with transverse defects, which were energised with current flowing in different directions relative to the flaws. Section 5.4.2 justifies the agreement between the modelled and real-case voltage signals recorded during the rail inspection with the Sperry ISU unit. Subsequently in Section 5.4.3 the output from the alternative inspection techniques involving different current injection procedures will be compared in order to evaluate their effectiveness in detection of transverse rail defects.

5.4.1 Distributions of magnetic flux leakage in vicinity of transverse rail defects

I. Development of FEM solid model.

An example of the solid model used for the static FEM analysis of energised unflawed and flawed rails is shown in Fig. 5.8.
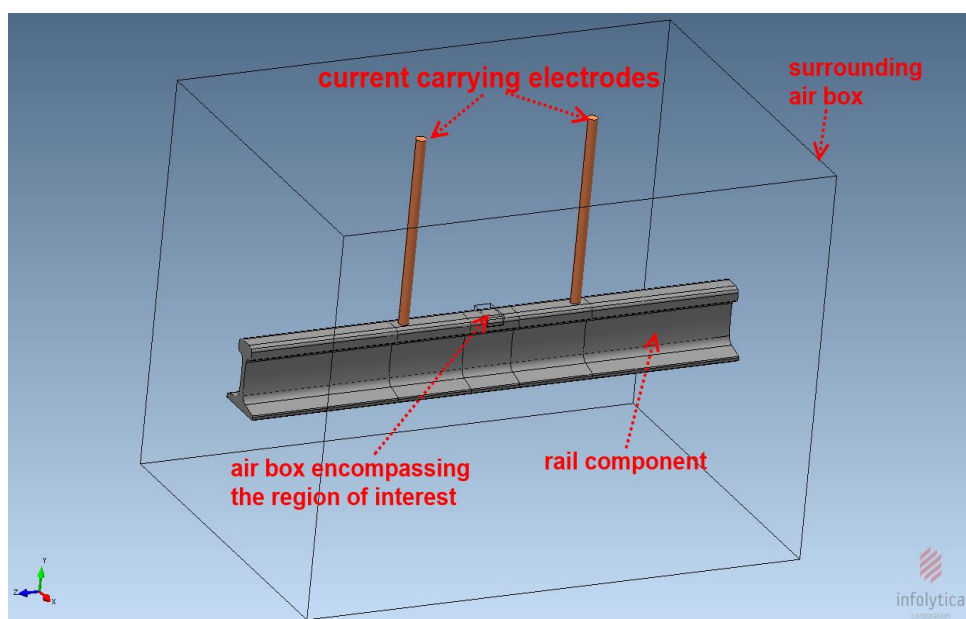
Fig. 5.8 FEM solid model used for static field analysis of energised flawed and unflawed rails.

The primary components of this FEM model were the following:

- Rail component made of pearlitic R260 steel having electric conductivity of σ_e= 4.45×10^6 S/m. The magnetic properties of this steel grade were defined by its initial magnetisation curve **B(H)** obtained experimentally using the hysteresis-graph previously described in Section 4.3. This initial **B(H)** curve is shown in Fig. 5.9.
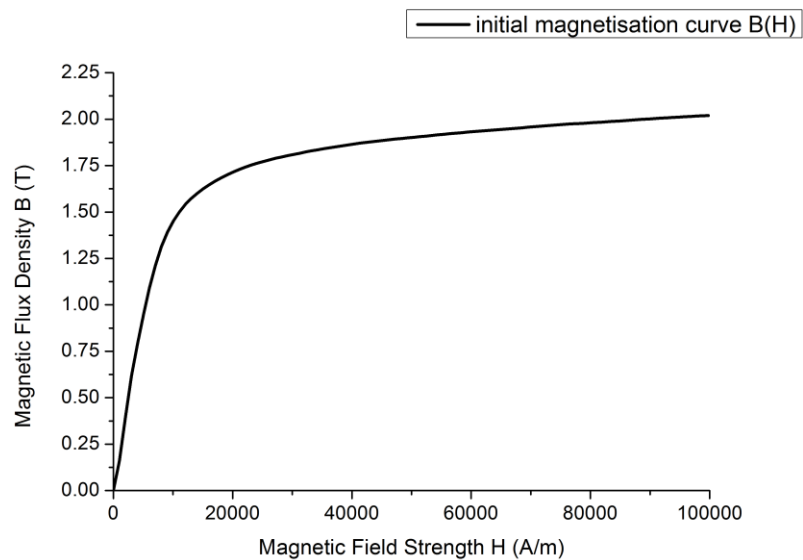
Fig. 5.9 Initial magnetisation curve of R260 rail steel.

Both electrical and magnetic properties of modelled rail were assumed to be isotropic. In reality some local variations in these properties can be expected due to factors such as residual stress, ageing or/and fatigue. Due to complexity in the implementation of this non-uniformity into FEM modelling of anisotropic 3D materials the evaluation of influence of those individual factors on MFL signals is beyond the scope of this thesis.

The total length of the analysed rail component was 1500 mm. Its cross-section with the main dimensions and indicated sub-sections is shown in Fig. 5.10.
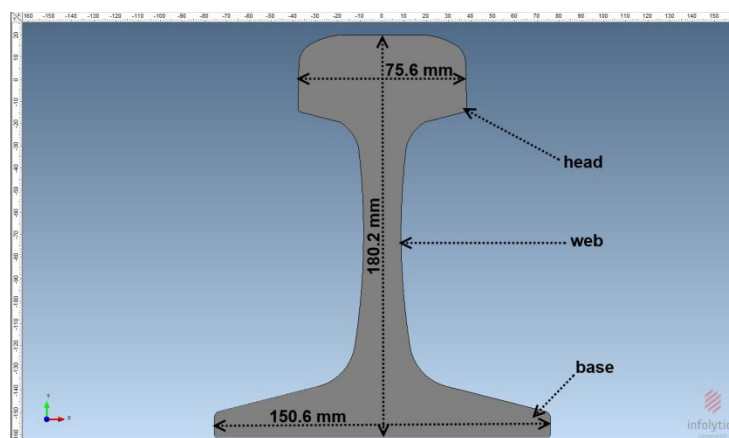
Fig. 5.10 Cross-section of analysed rail with indicated sub-sections and main dimensions.

The FEM mesh of this rail component was optimised in its particular sub-volumes in order to improve the accuracy of the calculations. The end sections of rail lying outside the current flow region had a relatively coarse mesh, whereas the mesh created for the inner sections carrying the magnetising current was progressively refined with the finest elements defined in the rail centre volume. The resulting global mesh is shown in Fig. 5.11.
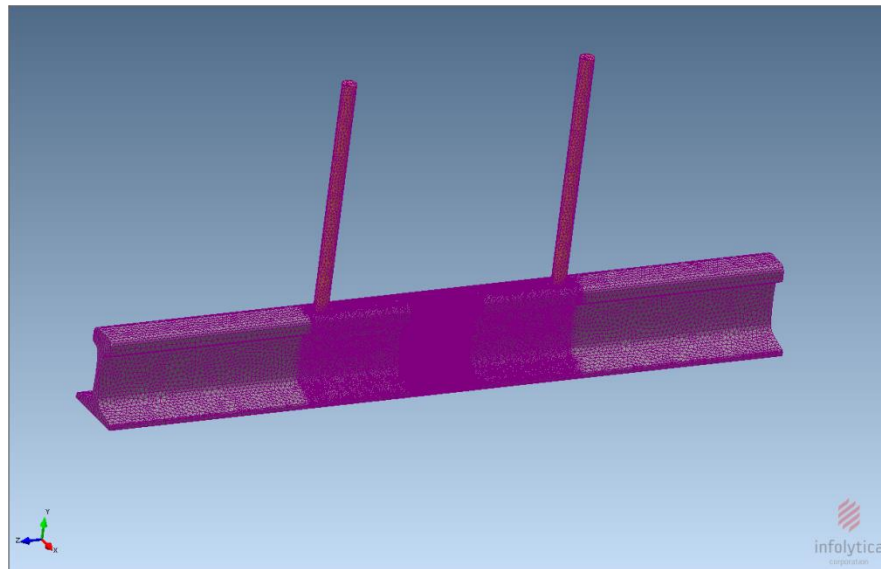
Fig. 5.11 Solution meshes for different model components.

▪ A set of beryllium-copper electrodes with σ_e= 3.7×10^7 S/m, injecting a DC current of 3000A into the rail. Three different sets of electrodes were used in order to study the MFL distributions for cases where the current was flowing in the longitudinal direction (Fig. 5.12a), tangential direction (5.12b) and at 45° to the longitudinal and transverse planes of rail (Fig. 5.12c).
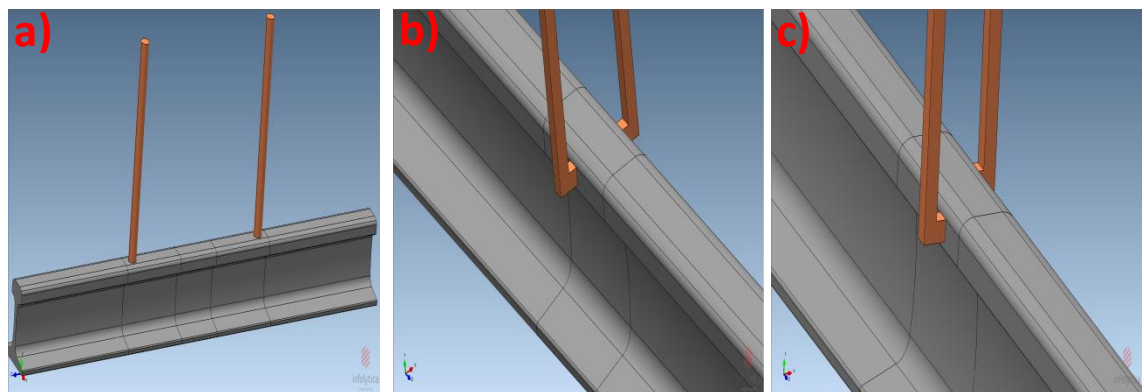
Fig. 5.12 Illustrations of modelled beryllium-copper electrodes applying current: a) in longitudinal direction; b) in transverse direction; c) at 45°to longitudinal and transverse planes of rail.

The electrodes which were used to apply current along the length of the rail (longitudinal direction) had a circular cross-section of 30mm diameter and were separated by distance of 500mm, which was equivalent to the original Sperry ISU system. The other two set-ups had electrodes of square cross-sections 15.4mm×15.4mm with their electrical contacts positioned symmetrically against the centre of the rail head.

▪ Transverse flaws of 15mm diameter and 0.1mm thickness were incorporated as air inclusions in the mid-volume of the rail head. The analysed flaws were positioned at the surface and at depths of 1mm, 3mm and 5mm in the centre and side regions of the rail cross-section, as shown in Figs. 5.13. The selected geometry of the flaw corresponded to the initial stage of its growth when the detection is most critical and most difficult, as shown in Fig. 3.9 (depicted as normal growth). The selected positions of investigated flaws within the rail head reflect the typical locations of transverse defects detected by Sperry during their dynamic rail inspection.
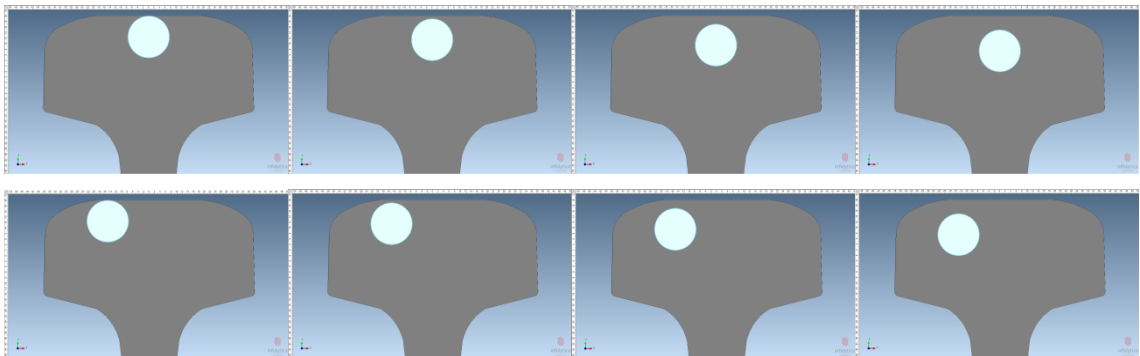
Fig. 5.13 Illustrations of analysed flaw positions within rail's cross-section.

▪ air box encompassing the region above the flawed rail volume shown in Fig. 5.14. This air component was assigned a very fine mesh which allowed accurate evaluation of the perturbation in magnetic field caused by the defect.
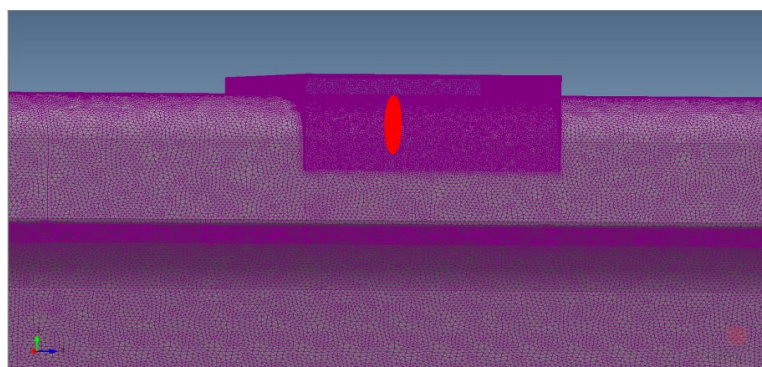
Fig. 5.14 Illustration of very fine mesh of air box encompassing the region above a flawed rail volume.

II. FEM results for rail with current flowing in the longitudinal direction.

The distributions of current density **J** and flux density **B** within and outside the unflawed rail energised along the longitudinal direction are shown in Figs. 5.15a and 5.15b.
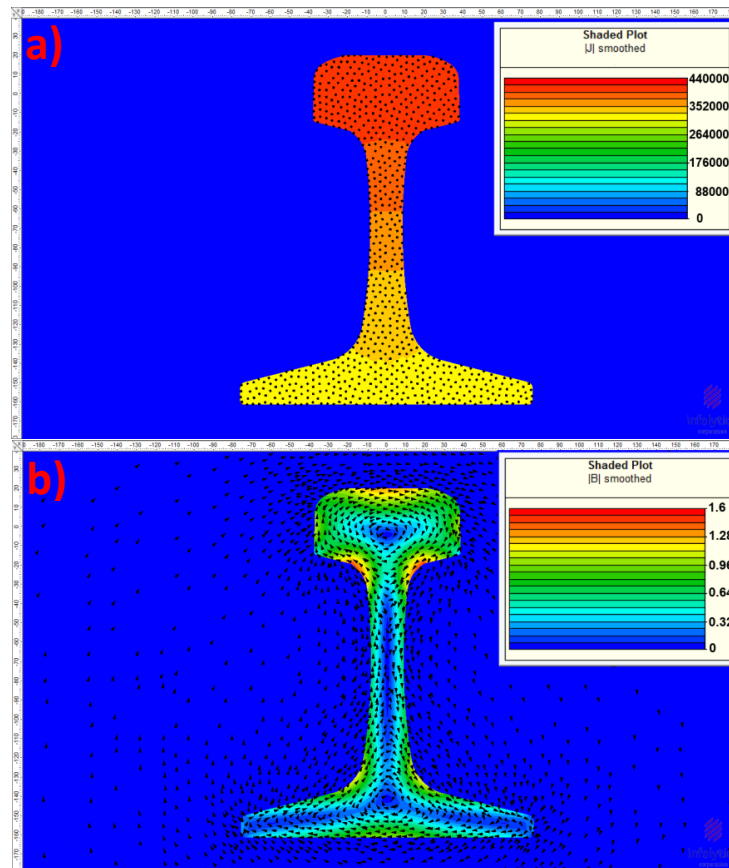
Fig. 5.15 Distributions of a) current density **J** and b) flux density **B** within and outside the unflawed rail energised along the longitudinal direction.

It can be seen in Fig. 5.15a that the current applied with the ISU electrodes was diverted within the energised volume and flowed within the whole cross-section of rail. In the mid-section of rail the highest current density was obtained in the rail head with uniform distribution within the range of **J**=420kA/m^2 to 440kA/m^2. The resulting circulating magnetic field **H** obeying the 'right-hand rule' shown in Fig. 5.15b produced a flux density **B** with highest levels at the top and bottom edges of rail head, and approximately zero levels in the centre regions of rail head, web and base due to cancellation effect of elementary fields generated by individual current elements. The corresponding levels of **B** components were studied at distance of 1mm from the surface of mid-section of rail in the area indicated in Fig. 5.16.

166
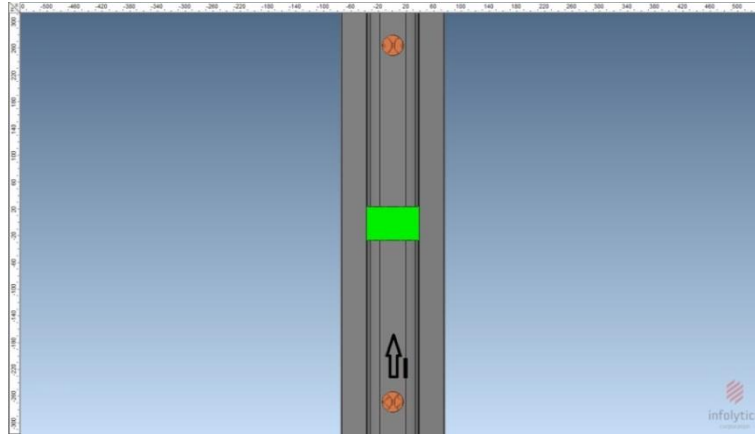
Fig. 5.16 Top view on analysed rail with indicated area (green) within which the magnetic field distributions for unflawed and flawed cases were studied.

The resulting distributions of tangential component B_T calculated along the width of the rail, normal component B_N calculated along the height of rail and longitudinal component B_L calculated along the length of the rail within the selected representative area of interest are shown in the form of shaded plots in Figs. 5.17a, 5.17b and 5.17c. Additionally the numerical line profiles of these distributions taken in the regions indicated by the arrows are shown in Fig. 5.17d.
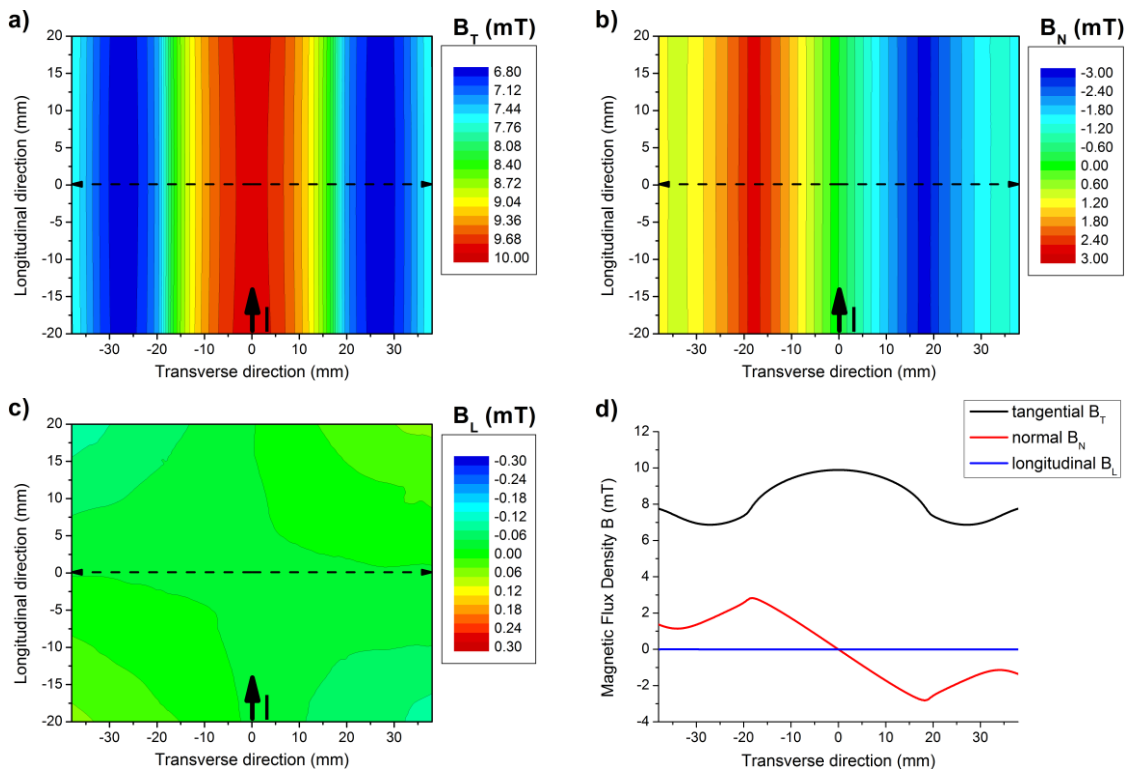
Fig. 5.17 Distributions of a) tangential component; b) normal component and c) longitudinal component of magnetic field at 1mm above central section of longitudinally energised unflawed rail; d) Numerical profiles of these magnetic field components probed in the regions indicated by the arrows.

As depicted in Fig. 5.17a the B_T distribution exhibited a dominant positive peak above the centre volume of rail. The numerical B_T profile probed above the top flat segment of the rail head (from -20mm to +20mm in Fig. 5.17d) showed a good agreement with the analytical solution presented previously in Section 5.2. The further apparent declinations in B_T profile corresponded to the side curved segments of the rail and resulted from the reduction in the current carrying volume.

In the case of the B_N component the calculated distribution showed a double peak profile with its extrema corresponding to the endpoints of the flat upper section of rail head. This type of profile also agreed well with the analytical analysis from Section 5.2. Consequently the deviation in the modelled B_N profile corresponded to regions above the side curved rail head segments.

Due to the fact that the current was applied along the length of the rail the calculated distribution of tangential component B_L exhibited as expected negligible levels. The only observable non-zero values of B_L in Fig. 5.17c were obtained due to contributions of magnetic fields generated by current flowing in the electrodes.

The presence of the transverse flaw in the rail forced some of the current to re-route into an alternative conducting paths in its vicinity. This effectively led to an increase in the local density J in regions adjacent to the flaw edges and a reduction in J directly in the front and rear of flaw faces, as shown in Figs. 5.18a and 5.18b.
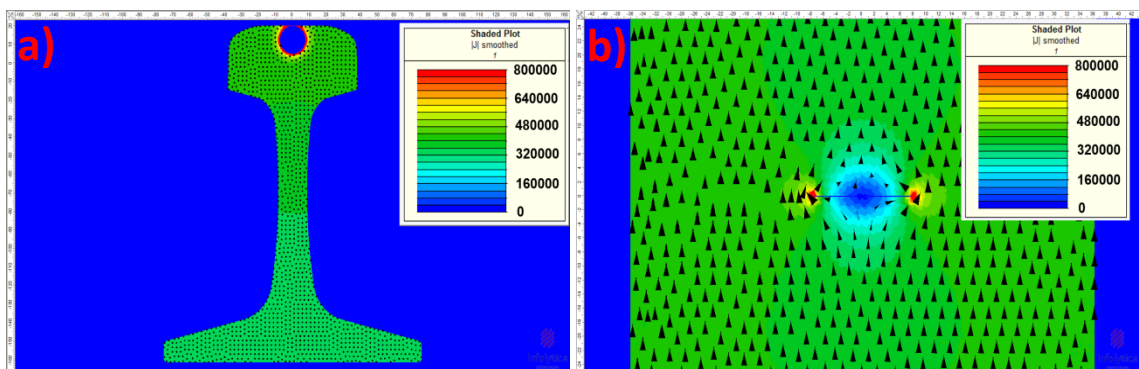
Fig. 5.18 Distributions of current density J within a) transverse cross-section and b) longitudinal cross-section of longitudinally energised flawed rail.

The manner in which the current re-routed around the flaw determined the character of magnetic field perturbation within and above the rail. The pattern of perturbation in the tangential component B_T above the rail can be observed by comparing the B_T distributions for unflawed and surface flawed cases shown in Figs. 5.19a and 5.19b. In order to demonstrate the effective variations in B_T the 2D matrix with values for the

flawed case was subtracted from the corresponding matrix for unflawed case providing a differential distribution ΔB_T caused by the flaw, as depicted in Fig. 5.19c.

Fig. 5.19 Distributions of tangential component of magnetic field at 1mm above longitudinally energised: a) unflawed rail and b) flawed rail; c) Differential distribution ΔB_T indicating effective perturbation in tangential component of magnetic field above surface flawed rail; d) Numerical profiles of differential perturbations in tangential component probed above longitudinally energised rails with surface and sub-surface flaws; e) Qualitative 2-D analysis of the current flow in the affected rail volume.

Based on the differential distribution ΔB_T it can be seen that due to the presence of a flaw the level of tangential component of flux density B_T was reduced above the mid-section of the rail (Fig. 5.19c). The maximum negative differences in B_T of approximately -1mT were calculated above the top of the surface transverse flaw and descended towards the flaw sides. It can be also seen that in the areas above rail sections neighbouring the surface flaw the tangential flux density levels increased within range up to 0.12mT. The scale of both negative and positive perturbations in ΔB_T decreased with distance between the flaw and rail surface which was evaluated by the numerical profiles taken along the width of the rail (indicated with arrow in Fig.

5.19c) presented in Fig. 5.19d. The resulting character of variations in B_T could be explained by a simplified qualitative 2-D analysis of the current flow in the affected rail volume, as demonstrated in Fig. 5.19e. In the centre regions located in front and rear of the flaw the re-routing of current resulted in reduction in J and therefore lower B_T generated directly above this rail section. The re-routed current which spread to the sides of the flaw increased the current density in the adjacent regions which consequently raised the level of B_T.

The distributions of normal component B_N above the unflawed and surface flawed rails energised along longitudinal direction are shown in Fig. 5.20a and 5.20b.
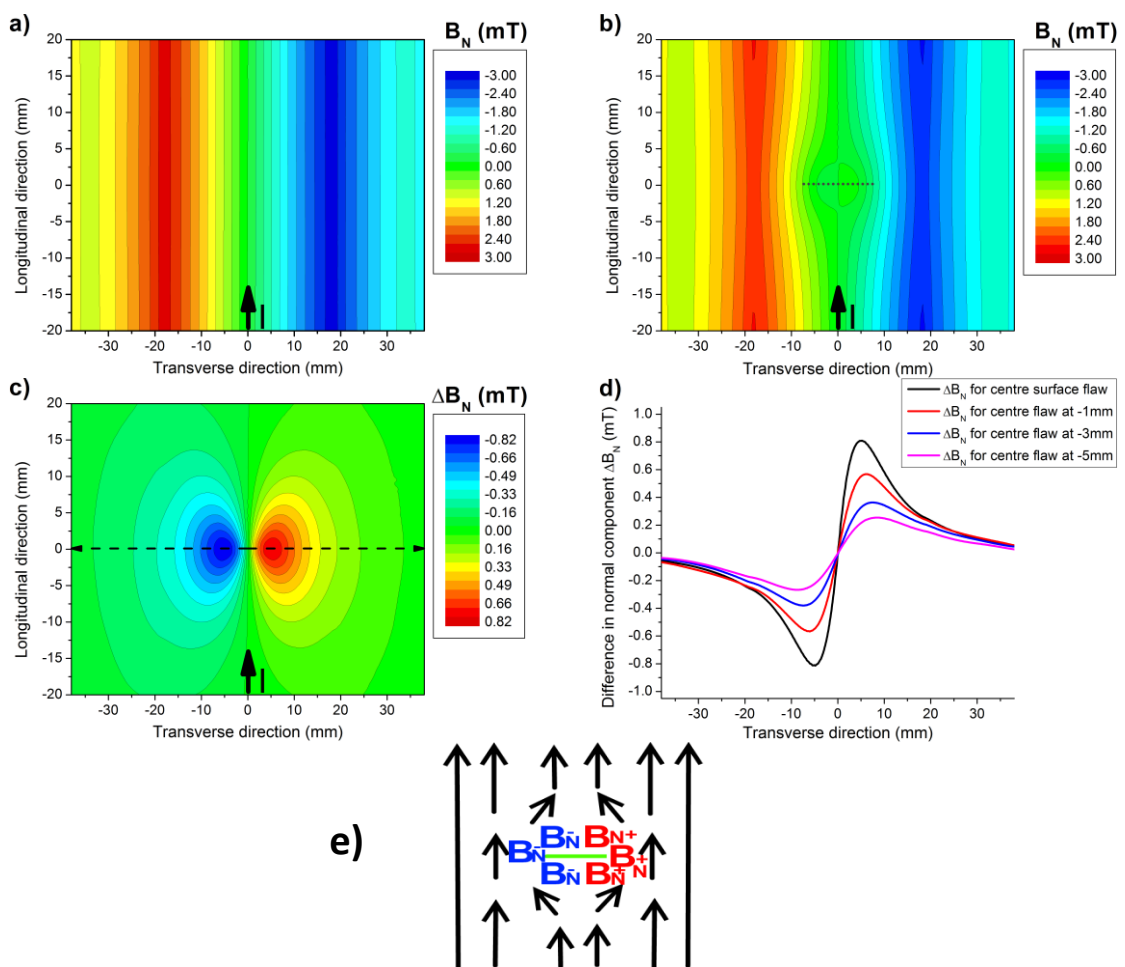
Fig. 5.20 Distributions of normal component of magnetic field at 1mm above longitudinally energised: a) unflawed rail and b) flawed rail; c) Differential distribution ΔB_N indicating effective perturbation in normal component of magnetic field above surface flawed rail; d) Numerical profiles of differential perturbations in normal component probed above longitudinally energised rails with surface and sub-surface flaws; e) Qualitative 2-D analysis of the current flow in the affected rail volume.

When comparing these two distributions it can be noticed that the alteration in current flow caused by the defect broke the symmetry in B_N above centre rail section.

The resulting changes $\Delta\mathbf{B_N}$ presented in Fig. 5.20c revealed a symmetrical bi-polar pattern of alterations with peak values of approximately +/- 0.8mT. This representative bi-polar pattern of $\Delta\mathbf{B_N}$ with corresponding divergence of current around the flaw is also shown in Fig. 5.20e. It can be seen that the current which re-routed towards the right-side of flaw generated positive $\Delta\mathbf{B_N}$ whereas that which re-routed to the left side produced negative $\Delta\mathbf{B_N}$. The numerical profiles taken along the transverse direction shown in Fig. 5.20d demonstrated the attenuation in the local peak values of these variations with increasing depth at which the flaw was located.

The distributions of longitudinal component $\mathbf{B_L}$ above the unflawed and surface flawed rails are presented in Figs. 5.21a and 5.21b.
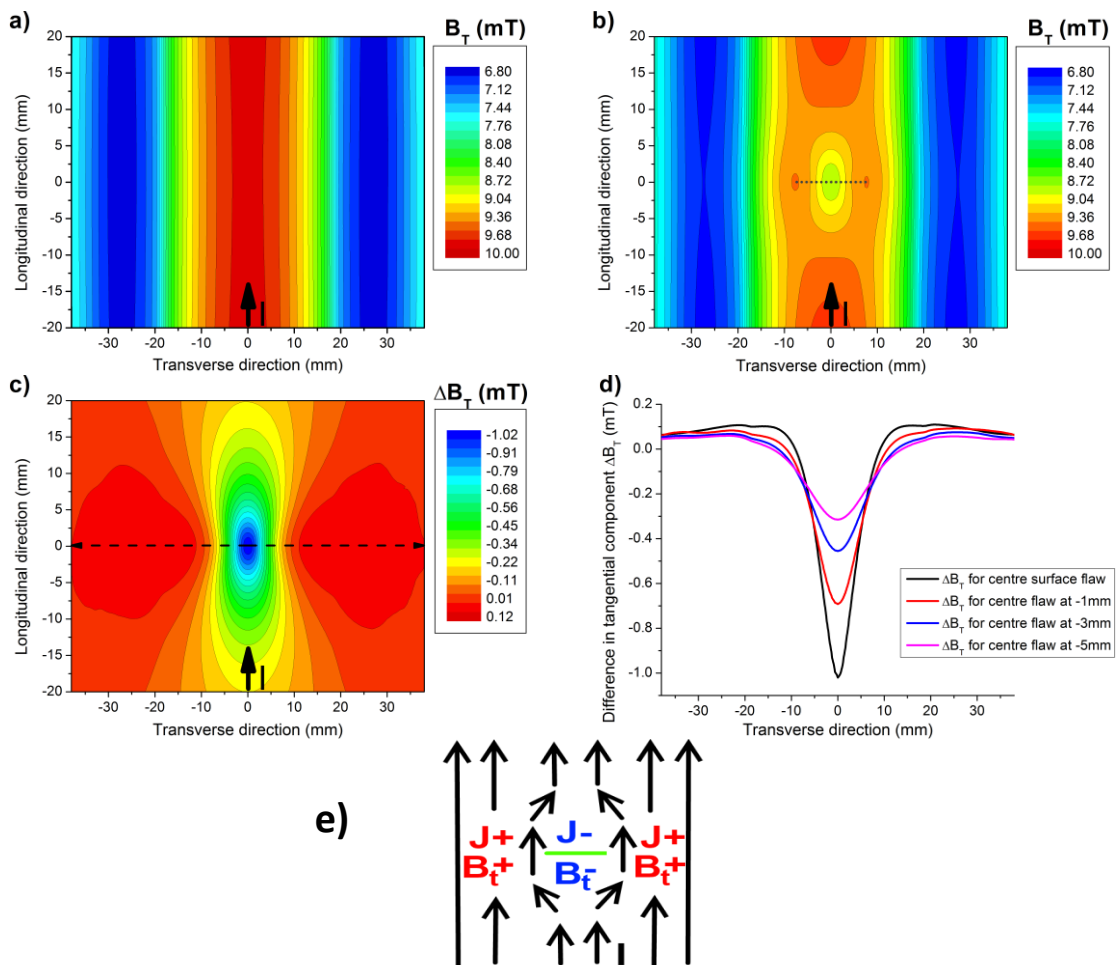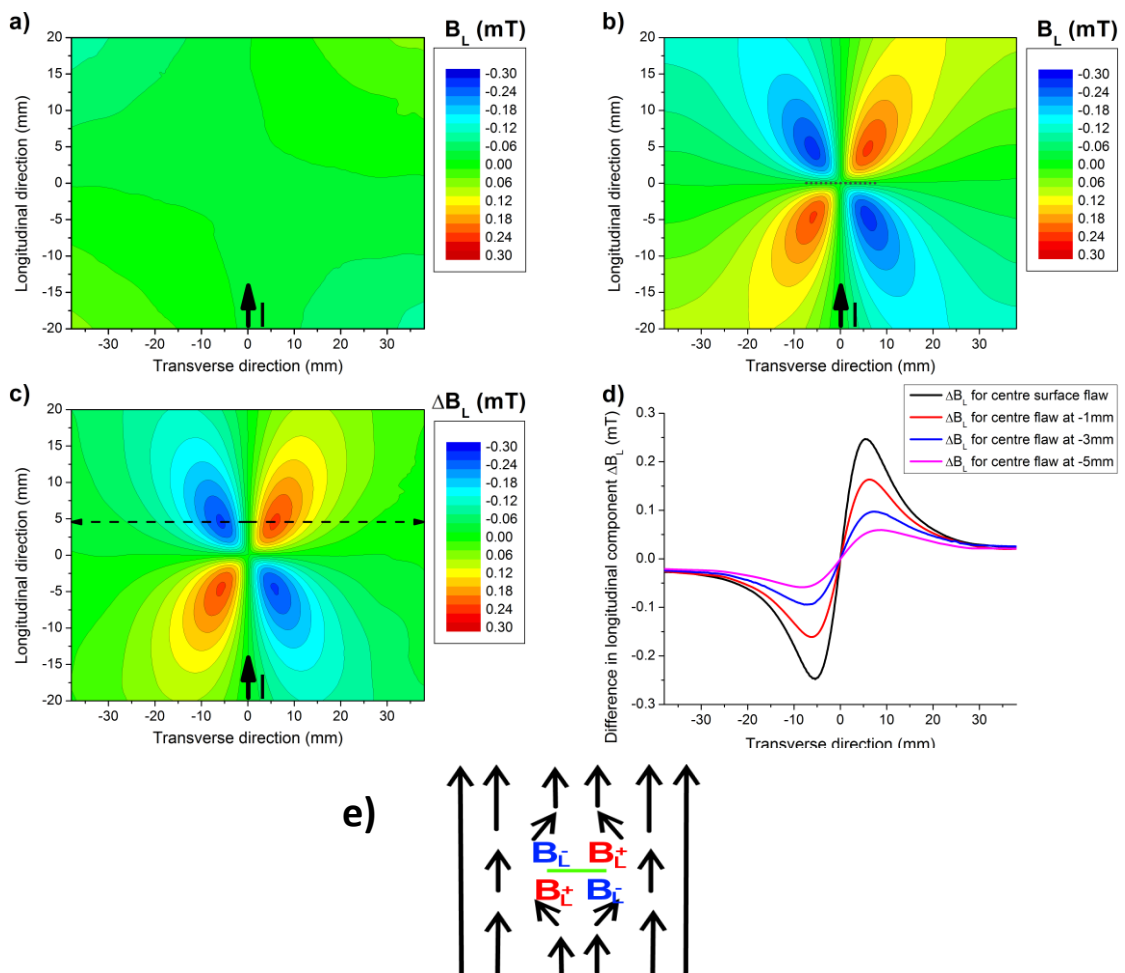

Fig. 5.21 Distributions of longitudinal component of magnetic field at 1mm above longitudinally energised: a) unflawed rail and b) flawed rail; c) Differential distribution $\Delta\mathbf{B_L}$ indicating effective perturbation in longitudinal component of magnetic field above surface flawed rail; d) Numerical profiles of differential perturbations in longitudinal component probed above longitudinally energised rails with surface and sub-surface flaws; e) Qualitative 2-D analysis of the current flow in the affected rail volume.

Unlike the B_L distribution above the unflawed rail which demonstrated negligible levels (Fig. 5.21a) the B_L distribution above flawed rail exhibited a distinctive symmetric four pole pattern with peak values of approximately +/- 0.25mT (Fig. 5.21b). The effective changes ΔB_L are shown in Fig. 5.21c. The appearance of the noticeable B_L levels would be attributed to the magnetic field generated by the re-routed currents flowing at non-zero angles to the longitudinal direction (Fig. 5.21e). At the front of the flaw the currents which diverged towards its right edge produced magnetic field in the negative longitudinal direction and therefore negative B_L. Consequently those currents which diverged to the left flaw edge produced field in positive longitudinal direction and hence positive B_L. At the rear of flaw, where the re-routed currents approached to return to the initial flow path, the magnetic field pattern was reversed. The decay in local maximum ΔB_L with increasing depth of flaw position was evaluated via numerical profiles presented in Fig. 5.21d.

An analogous type of analysis was performed for side flaws shifted 15 millimetres towards the left side of the rail. The shaded plots revealing increased levels of current density in vicinity of side surface flaw are shown in Figs. 5.22a and 5.22b.

Fig. 5.22 Distributions of current density **J** within a) transverse cross-section and b) longitudinal cross-section of side-flawed rail energised longitudinally.

The differential distributions of tangential B_T, normal B_N and longitudinal B_L components for rail with side surface flaw are shown in Figs. 5.23a, 5.23c and 5.23e. The corresponding numerical profiles of these components probed along the width of the rail are shown in Figs. 5.23b, 5.23d and 5.23f.

Fig. 5.23 Differential distributions of: a) tangential component; c) normal component and e) longitudinal component of magnetic field above surface side-flawed rail energised in longitudinal direction. Numerical profiles of differential perturbations in b) tangential component; d) normal component and f) longitudinal component of magnetic field probed above longitudinally energised rails with surface and sub-surface flaws.

It can be seen that the patterns of effective variations in B_T, B_N and B_L caused by side flaw were similar to those obtained for centre flaw. The only noticeable difference was the asymmetry in the differential distributions where the scale of perturbation was relatively lower on the left side of flaw, which could be clearly observed for case of ΔB_L

distribution. This asymmetry would be assigned to the fact that part of the currents which re-routed to the left flaw side were flowing within the curved rail section. The resulting greater air clearance between this section of rail and the plane of detection gave a smaller local perturbation than that generated by currents flowing within the flat top rail volume.

III. FEM results for rail with current flowing in the tangential direction.

The distributions of current density **J** in transverse and longitudinal planes of rail energised along the transverse direction are shown in Figs. 5.24a and 5.24b. The corresponding flux density **B** distribution is presented in Figs. 5.24c.
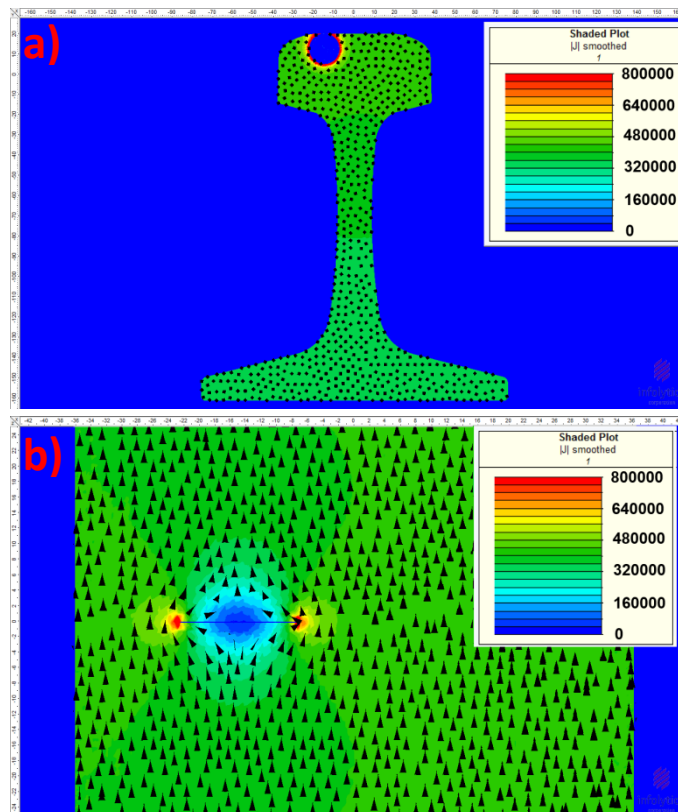

Fig. 5.24 Distributions of current density **J** within a) transverse cross-section and b) longitudinal cross-section of tangentially energised rail; c) Distribution of flux density **B** within transverse cross-section of tangentially energised rail.

As distinct from the case of rail energised in longitudinal direction, the current applied across the width of rail did not diverge within the full cross section but its flow remained within the rail head, as depicted in Fig. 5.24a. As a result the levels of current density **J** within most of the energised volume were approximately two to three times higher ($800kA/m^2$-$1200kA/m^2$) than those obtained in the previous case. The calculated distribution of **J** along the length of rail (Fig. 5.24b) indicated divergence of current from the electrodes in the longitudinal direction, with the parallel to transverse direction current flow only in the rail centre section. The corresponding flux density distribution (Fig. 5.24c) showed high levels of **B** within the range of 1.5T to 2T in the top half of the rail head, and the zero **B** region located within its lower section.

The resulting distributions of tangential component **B$_T$**, normal component **B$_N$** and longitudinal component **B$_L$** at 1mm above the rail are shown in Figs. 5.25a, 5.25b and 5.25c. The numerical profiles of these distributions taken along the length of rail in the regions indicated by the arrows are shown in Fig. 5.25d.
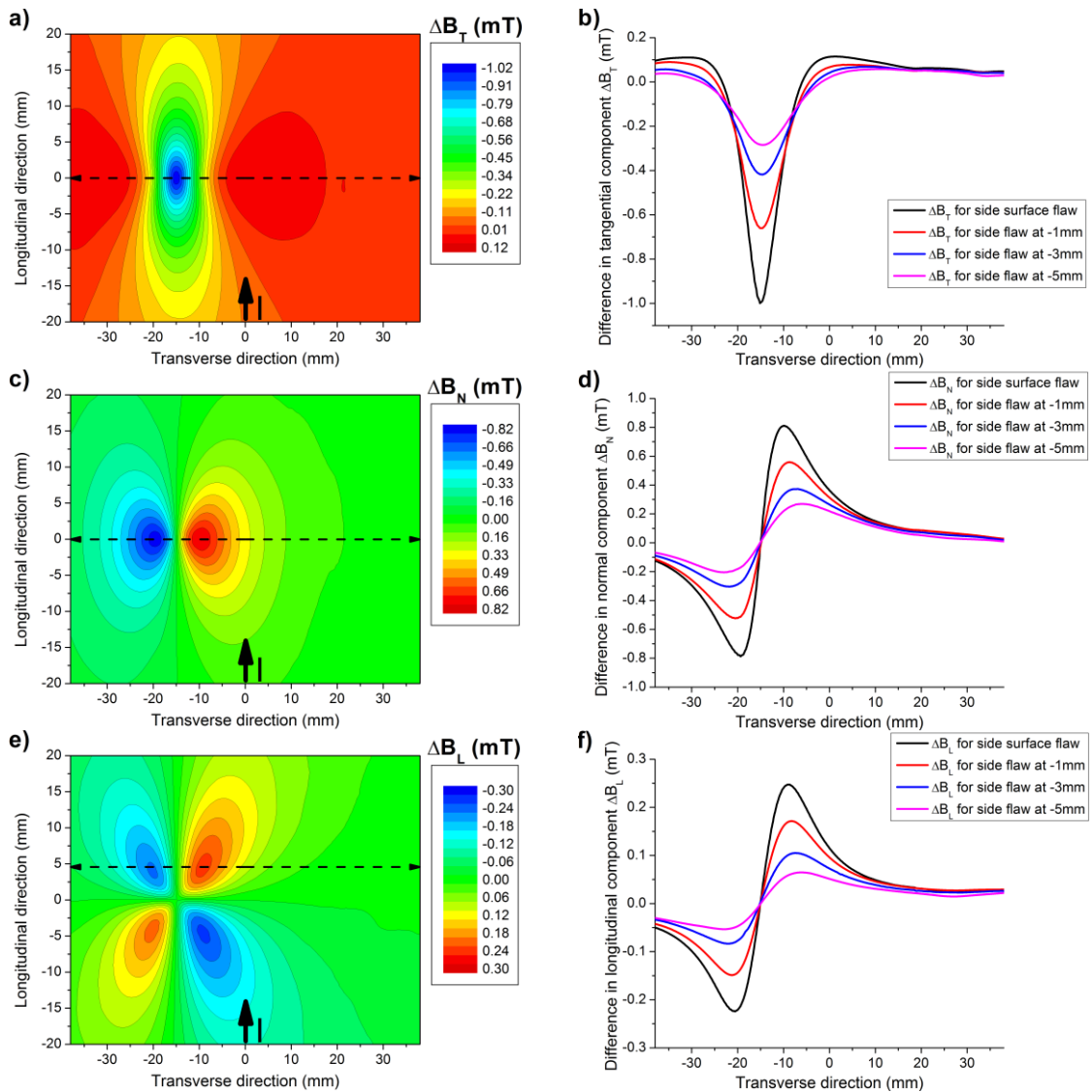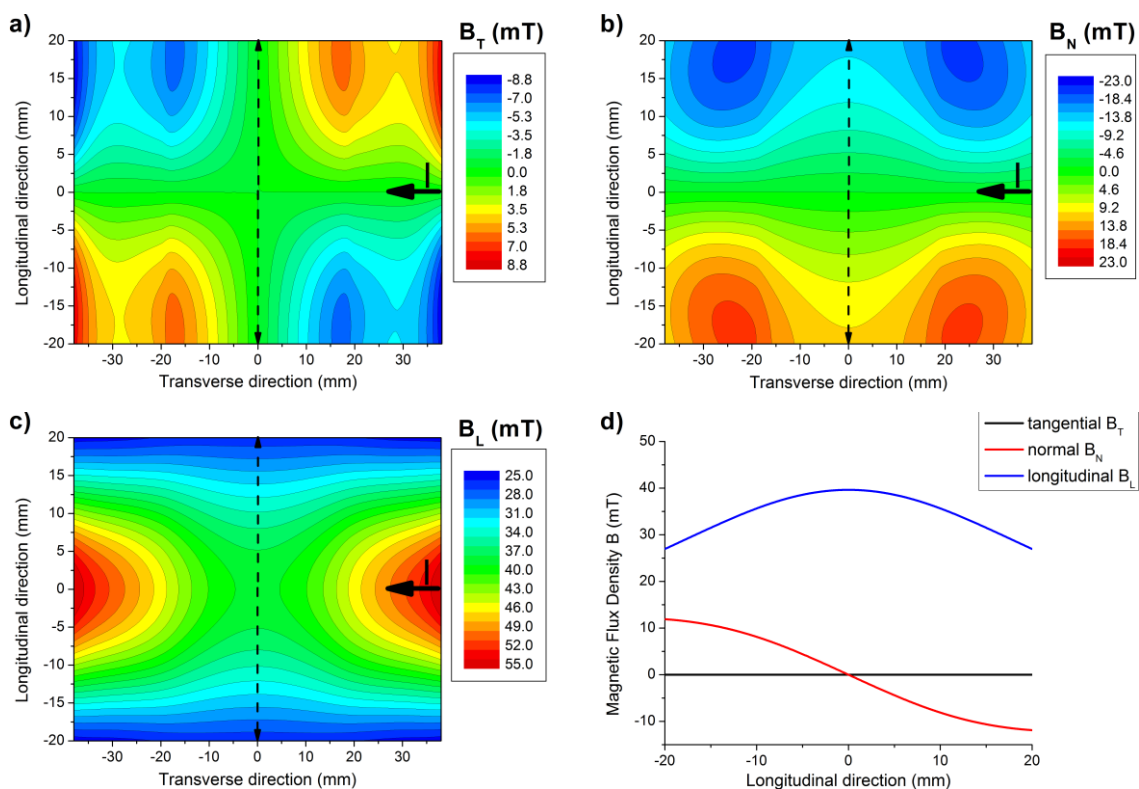

Fig. 5.25 Distributions of a) tangential component; b) normal component and c) longitudinal component of magnetic field at 1mm above central section of tangentially energised unflawed rail; d) Numerical profiles of these magnetic field components probed in the regions indicated by the arrows.

It can be seen in Fig. 5.25a that the B_T component exhibited as expected negligible levels above the centre regions of the energised volume, where the current flow was aligned with the transverse direction. This could be compared to the B_L component from the previous case of rail carrying current along its length. In the regions above the rail head side sections the current in electrodes and currents which diverged at non-zero angle to transverse direction produced noticeable levels of B_T within range from -8.8mT to 8.8mT.

The distribution of normal component B_N demonstrated a bi-polar pattern as shown in Fig. 5.25b. The highest values of B_N were calculated above the side rail head sections with coherent current flow. The subsequent current divergence in the centre of the rail head section resulted in a wider span and lower levels of B_N component.

The calculated B_L distribution revealed a single peak profile along the rail length. The highest values of B_L were obtained in regions adjacent to electrodes. These high B_L levels were produced by combination of coherent flow of current elements within the rail head and the current flowing in the electrodes.

The current density distributions in transverse and longitudinal planes of surface flawed rail energised along transverse direction are shown in Figs. 5.26a and 5.26b.

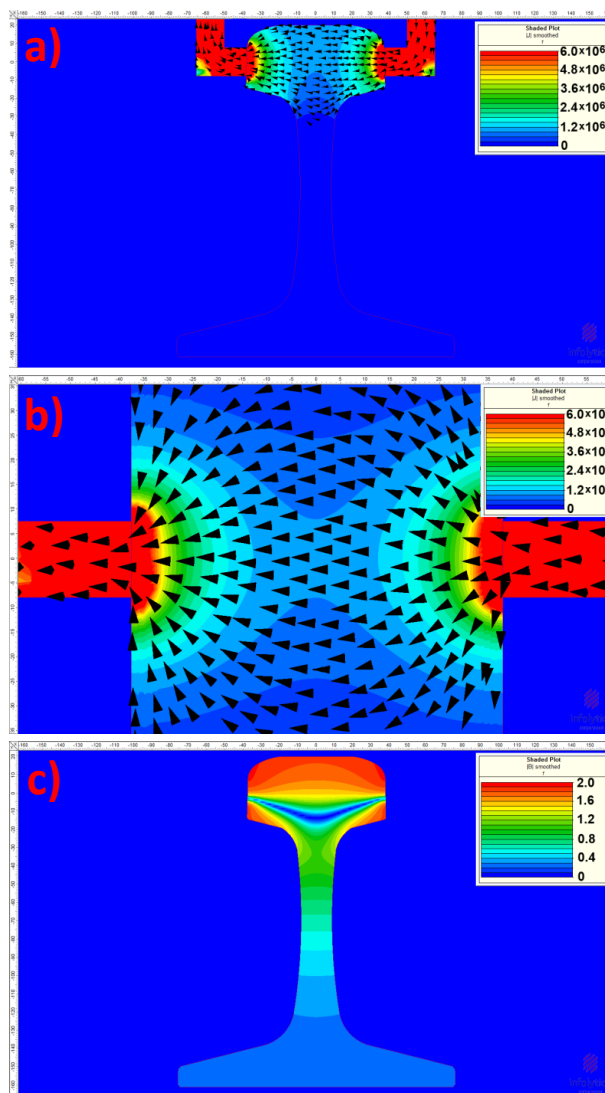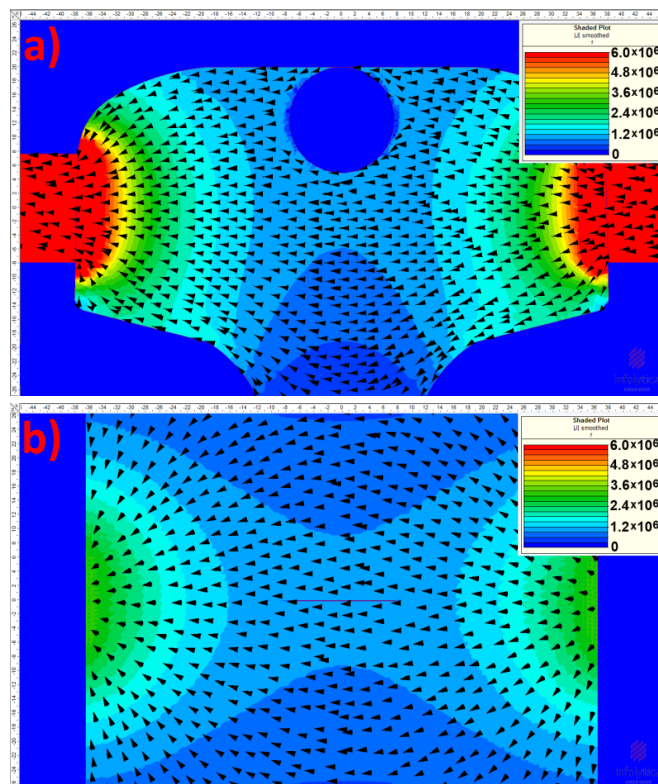Fig. 5.26 Distributions of current density **J** within a) transverse cross-section and b) longitudinal cross-section of tangentially energised rail with centre transverse flaw.

It can be seen in Fig. 5.26a that in the transverse plane the currents re-routed upwards and downwards along the edges of flaw. In the longitudinal plane (Fig. 5.26b) no meaningful alteration in current flow was observed.

The corresponding distribution of tangential component B_T is shown in Fig. 5.27b. When comparing it with the distribution above unflawed rail (Fig. 5.27a) it could be seen that a flaw related four pole leakage pattern was created in the centre section. This pattern was more pronounced in the differential distribution ΔB_T presented in Fig. 5.27c. The decay in local maximum ΔB_T with increasing depth of flaw position was evaluated via numerical profiles presented in Fig. 5.21d.

Fig. 5.27 Distributions of tangential component of magnetic field at 1mm above tangentially energised: a) unflawed rail and b) flawed rail; c) Differential distribution ΔB_T indicating effective perturbation in tangential component of magnetic field above surface flawed rail; d) Numerical profiles of differential perturbations in tangential component probed above tangentially energised rails with surface and sub-surface flaws; e) Qualitative 2-D analysis of the current flow in the affected rail volume.

The four-pole symmetrical perturbation in B_T was generated primarily by the current elements which diverged along top flaw edges closer to the surface of rail (as indicated with red arrows in Fig. 5.27e). The upward flow of this elements produced positive change $+ \Delta B_T$ in front of the flaw and negative change $-\Delta B_T$ at rear of flaw, and the downward flow produced opposite polarity of variations. When correlating this perturbation with the variations in longitudinal component from the previous case it can be seen that the scale of changes was more than eight times higher (approximate maximum variations of +/- 2.3mT comparing to +/-0.25mT).

The distributions of normal component B_N at 1mm above the unflawed and surface flawed rails energised along transverse direction are shown in Fig. 5.28a and 5.28b. The resulting changes ΔB_N presented in Fig. 5.28c showed a symmetrical bi-polar pattern of alterations.
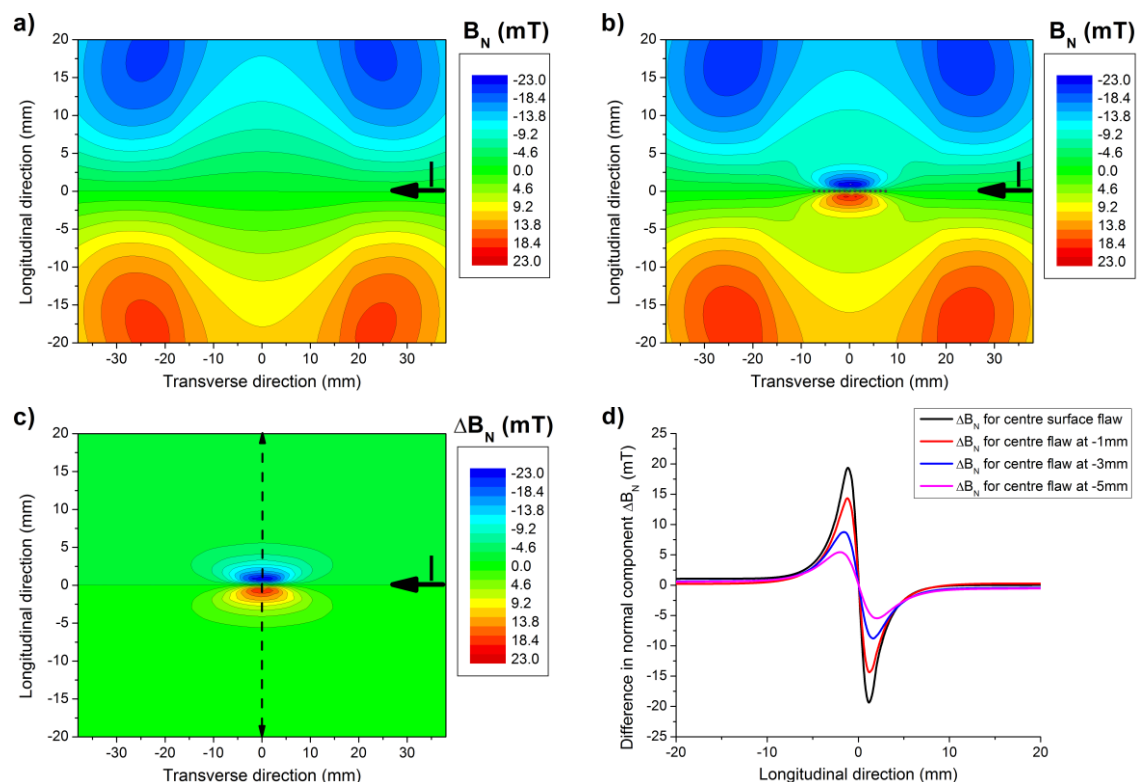
Fig. 5.28 Distributions of normal component of magnetic field at 1mm above tangentially energised: a) unflawed rail and b) flawed rail; c) Differential distribution ΔB_N indicating effective perturbation in normal component of magnetic field above surface flawed rail; d) Numerical profiles of differential perturbations in normal component probed above tangentially energised rails with surface and sub-surface flaws.

In this case the effective changes in B_N were not caused by re-routed currents but due to the fact that the generated magnetic flux was forced to close through the flaw

volume. As the permeability of the modelled transverse flaw was the same as surrounding air a relatively high magnetic flux leakage occurred leading to high B_N levels above the rail surface. The magnitude of this flux leakage was much higher than from the previously analysed ISU case (approximate maximum variations of +/-20mT compared with +/-0.8mT). The attenuation in the MFL signal with increasing depth of flaw position was evaluated via numerical profiles and is presented in Fig. 5.28d.

The B_L distributions above unflawed and flawed rails carrying current in transverse direction are shown in Figs. 5.29a and 5.29b. The effective changes ΔB_L and their decay with increasing flaw location depth are presented in Fig. 5.29c and 5.29d.
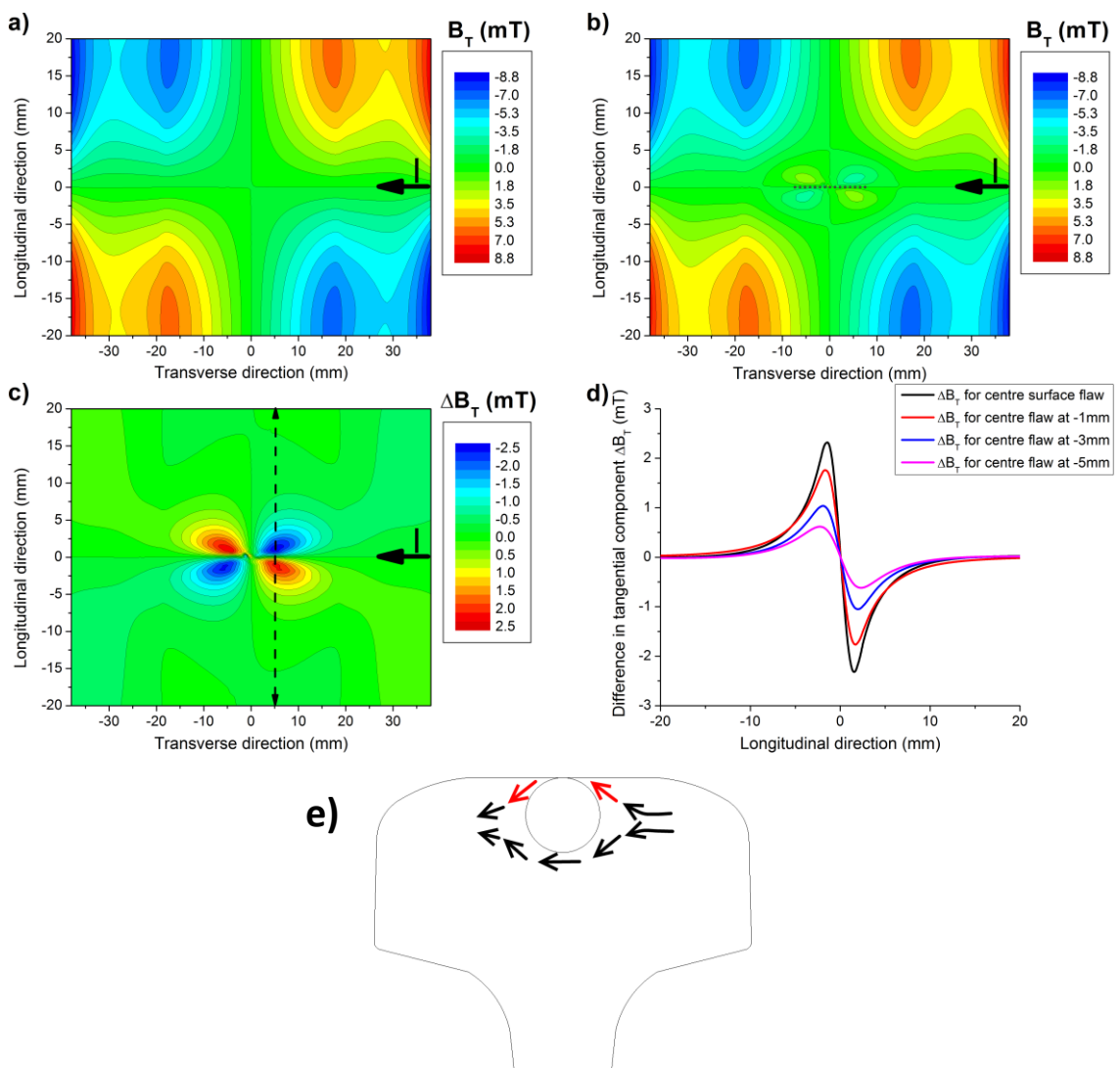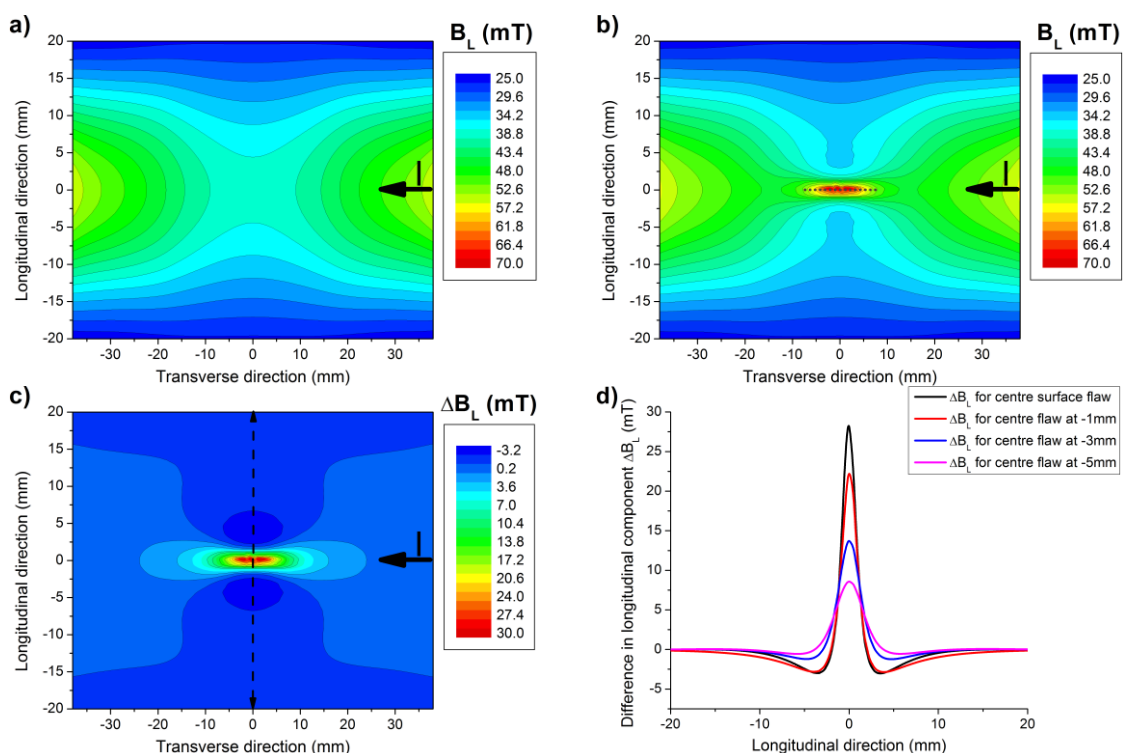

Fig. 5.29 Distributions of longitudinal component of magnetic field at 1mm above tangentially energised: a) unflawed rail and b) flawed rail; c) Differential distribution ΔB_L indicating effective perturbation in longitudinal component of magnetic field above surface flawed rail; d) Numerical profiles of differential perturbations in longitudinal component probed above rails with surface and sub-surface flaws.

The calculated B_L pattern indicated a relatively high stray field generated above the centre of the flaw where the flux lines cutting through the affected volume leaked into air. Additional visible perturbation ΔB_L was caused by the re-routed currents flowing along the top flaw edges, which broadened the area of perturbation. When comparing the variations ΔB_L from transverse current application with corresponding ΔB_T obtained with ISU electrodes it was noticed that the scale of perturbation was

significantly higher (max 30mT to 1mT above surface flaw). This has proven that the flux leakage effect caused by magnetic field applied perpendicular to the flaw would be much greater than that caused by the re-routing of currents in the ISU inspection.

A similar type of analysis was performed for side transverse flaws. The resulting current density distributions within transverse and longitudinal planes of rail with a side surface defect are shown in Figs. 5.30a and 5.30b.

Fig. 5.30 Distributions of current density **J** within a) transverse cross-section and b) longitudinal cross-section of tangentially energised rail with side transverse flaw.

The calculated differential distributions of tangential B_T, normal B_N and longitudinal B_L components above the surface of the side flawed rail are shown in Figs. 5.31a, 5.31c and 5.31e. The corresponding numerical profiles probed along the length of the rail are presented in Figs. 5.31b, 5.31d and 5.31f.
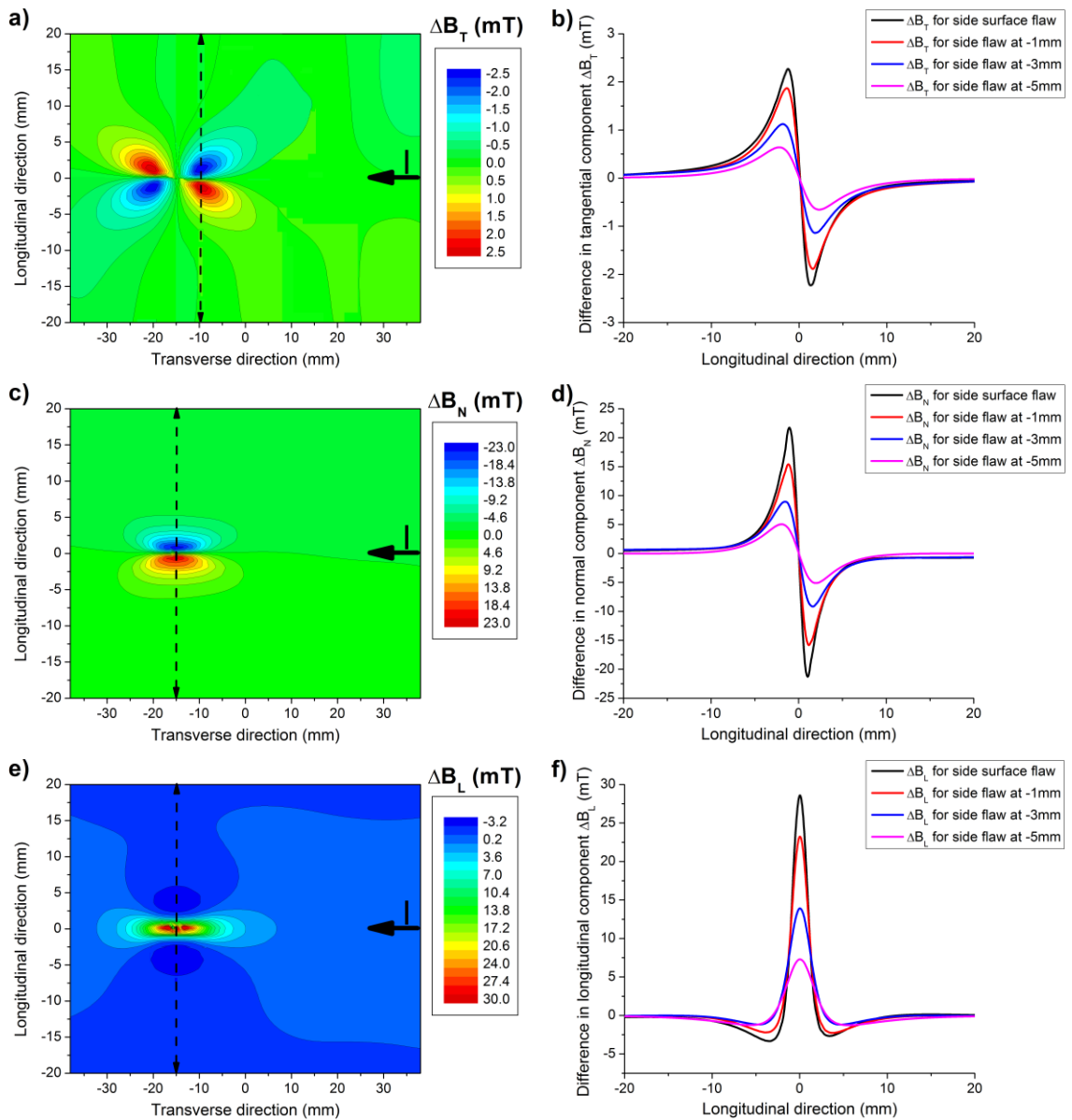
Fig. 5.31 Differential distributions of: a) tangential component; c) normal component and e) longitudinal component of magnetic field above surface side-flawed rail energised in tangential direction. Numerical profiles of differential perturbations in b) tangential component; d) normal component and f) longitudinal component of magnetic field probed above tangentially energised rails with surface and sub-surface flaws.

It can be seen that the patterns of variations in all three components obtained for side flaw were analogous to those observed for centre transverse flaw. The levels of calculated differential changes were also comparable, which implied an equivalent probability of detection of both of these flaws with this particular MFL technique.

IV. FEM results for rail with current flowing at 45° to its transverse and longitudinal planes.

The current density distributions in rail carrying current at 45° to its transverse and longitudinal planes are shown in Figs. 5.32a and 5.32b. The corresponding flux density **B** distribution is presented in Figs. 5.32c.
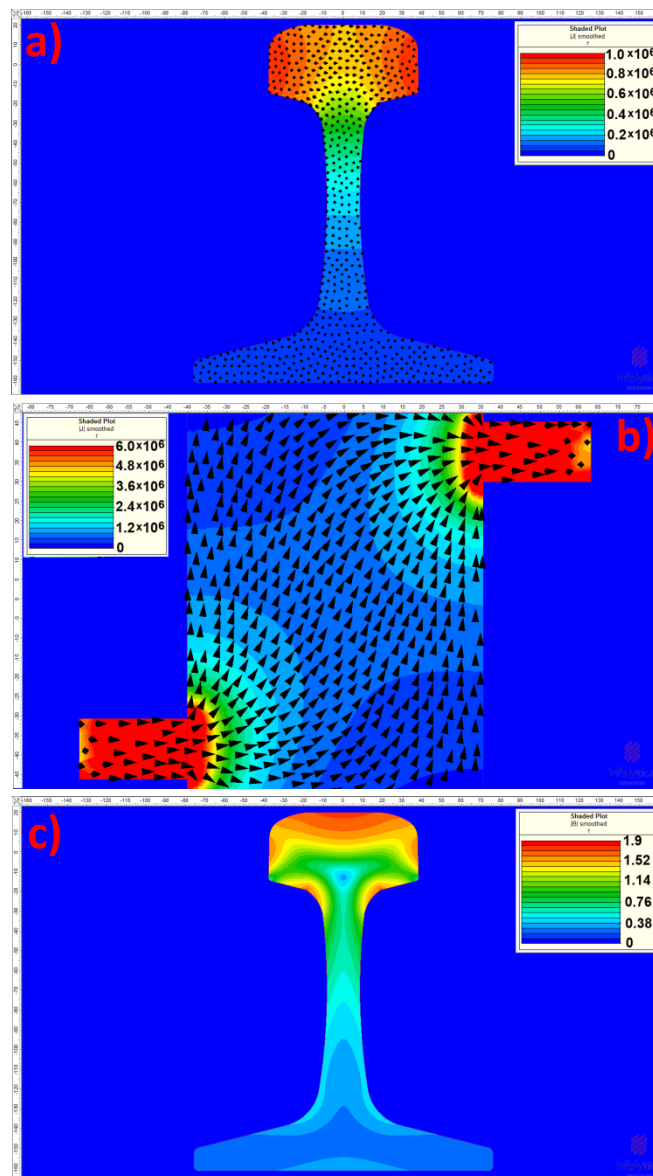
Fig. 5.32 Distributions of current density **J** within a) transverse cross-section and b) longitudinal cross-section of diagonally energised rail; c) Distribution of flux density **B** within transverse cross-section of diagonally energised rail.

As depicted in Figs. 5.32a and 5.32b the current diverged within both transverse and longitudinal sections of rail. The majority of currents flowed in the rail head where current density levels in its centre volume were within range of 700kA/m^2-1000kA/m^2

182

(Fig. 5.32a). The calculated distribution of **J** along the length of rail (Fig. 5.32b) indicated approximately 45° current flow only in the middle section. The corresponding flux density distribution (Fig. 5.24c) showed high levels of **B** within range of 1.3T to 1.9T in top half of rail head, and a relatively small zero **B** region located within its lower segment.

The calculated distributions of tangential component B_T, normal component B_N and longitudinal component B_L at 1mm above this rail are shown in Figs. 5.33a, 5.33b and 5.33c. The numerical profiles of these distributions taken along the width of rail in the regions indicated by the arrows are shown in Fig. 5.33d.
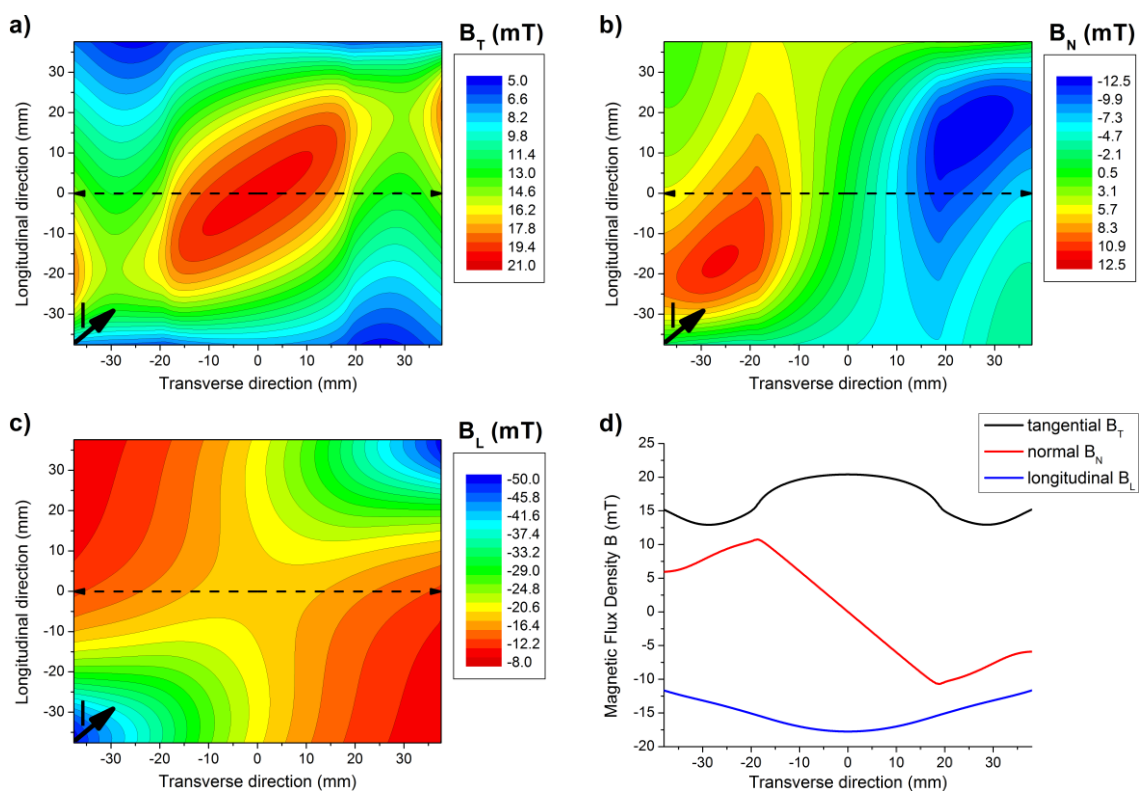
Fig. 5.33 Distributions of a) tangential component; b) normal component and c) longitudinal component of magnetic field at 1mm above central section of diagonally energised unflawed rail; d) Numerical profiles of these magnetic field components probed in the regions indicated by the arrows.

Due to the fact that the current was flowing at particular angles to major planes of rail all three components of **B** exhibited non-zero values above the centre section. As depicted in Fig. 5.33d the obtained profiles of tangential B_T and longitudinal B_L components presented a single peak above the mid-section whereas the normal component B_N exhibited a symmetrical double-peak distribution against the centre axis of rail.

The calculated current density distributions in transverse and longitudinal planes of surface flawed rail energised diagonally are shown in Figs. 5.34a and 5.34b.
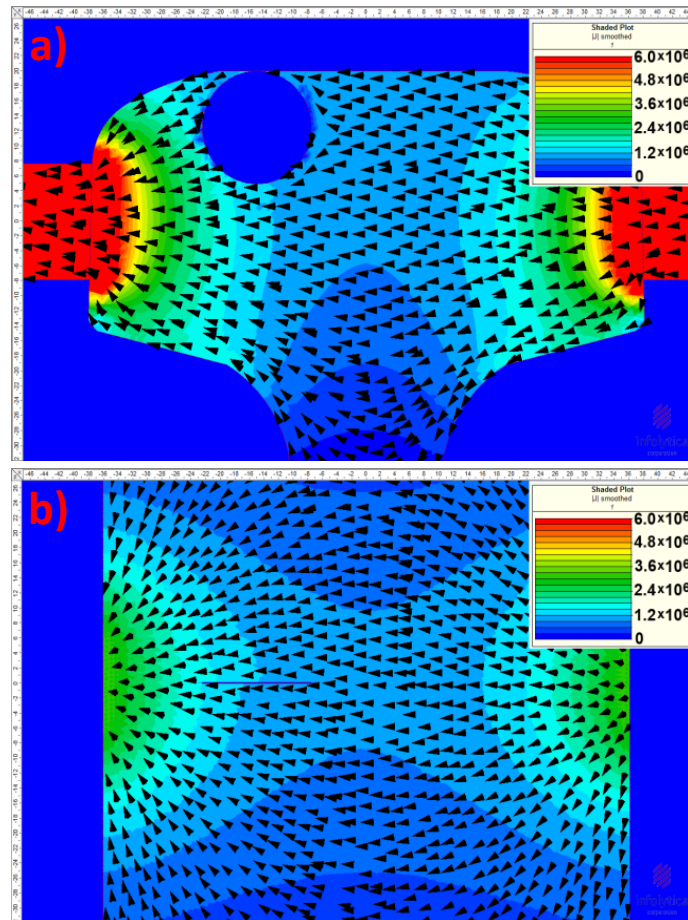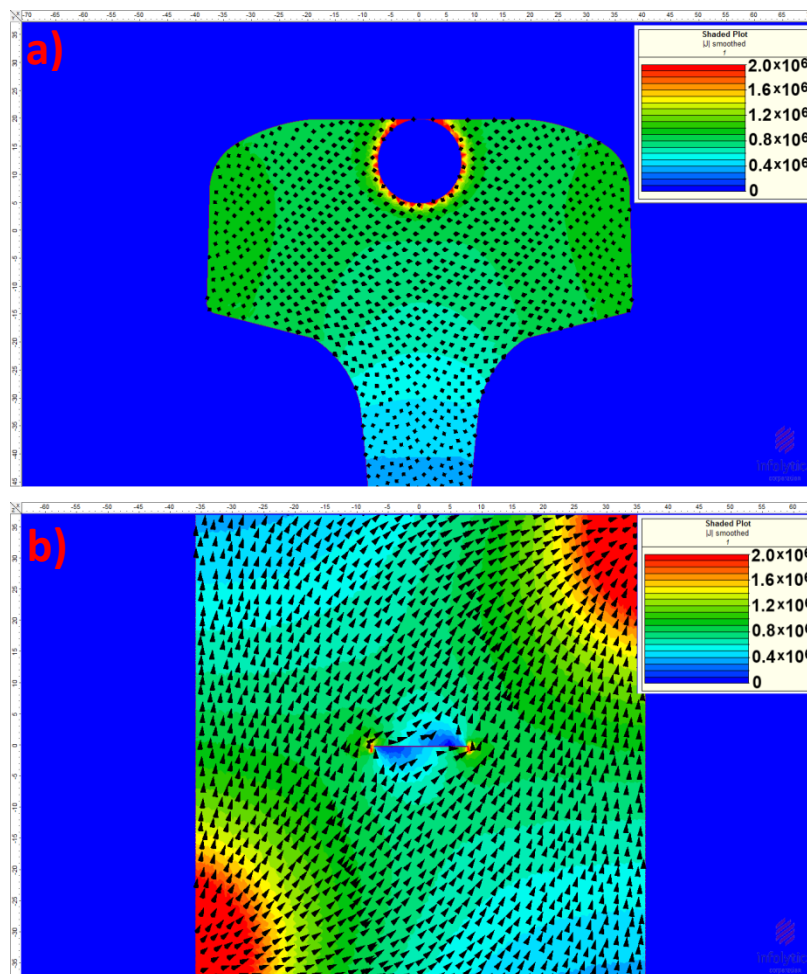

Fig. 5.34 Distributions of current density **J** within a) transverse cross-section and b) longitudinal cross-section of diagonally energised rail with centre transverse flaw.

It can be seen in Fig. 5.34a that the re-routed current elements increased the density **J** around the flaw to level of 2000kA/m^2, which was approximately three times higher than the level of **J** obtained within corresponding region of unflawed rail. The distribution of **J** in the longitudinal plane (Fig. 5.34b) revealed the asymmetrical re-routing pattern in vicinity of flaw. At the front of the flaw the currents which flowed near its left edge re-oriented towards the longitudinal direction and subsequently turned into the tangential direction at its rear. Those currents which flowed closer to flaw centre and right edge re-routed initially along tangential direction and re-oriented longitudinally to restore to their original flow pattern.

The corresponding distribution of tangential component B_T is shown in Fig. 5.35b. When comparing it with the distribution above the unflawed rail (Fig. 5.35a) it could be seen that a perturbation related to the flaw was created, as further pronounced in the differential distribution ΔB_T presented in Fig. 5.35c. The decay in the scale of this perturbation ΔB_T with increasing depth of flaw position was evaluated via numerical profiles shown in Fig. 5.35d.
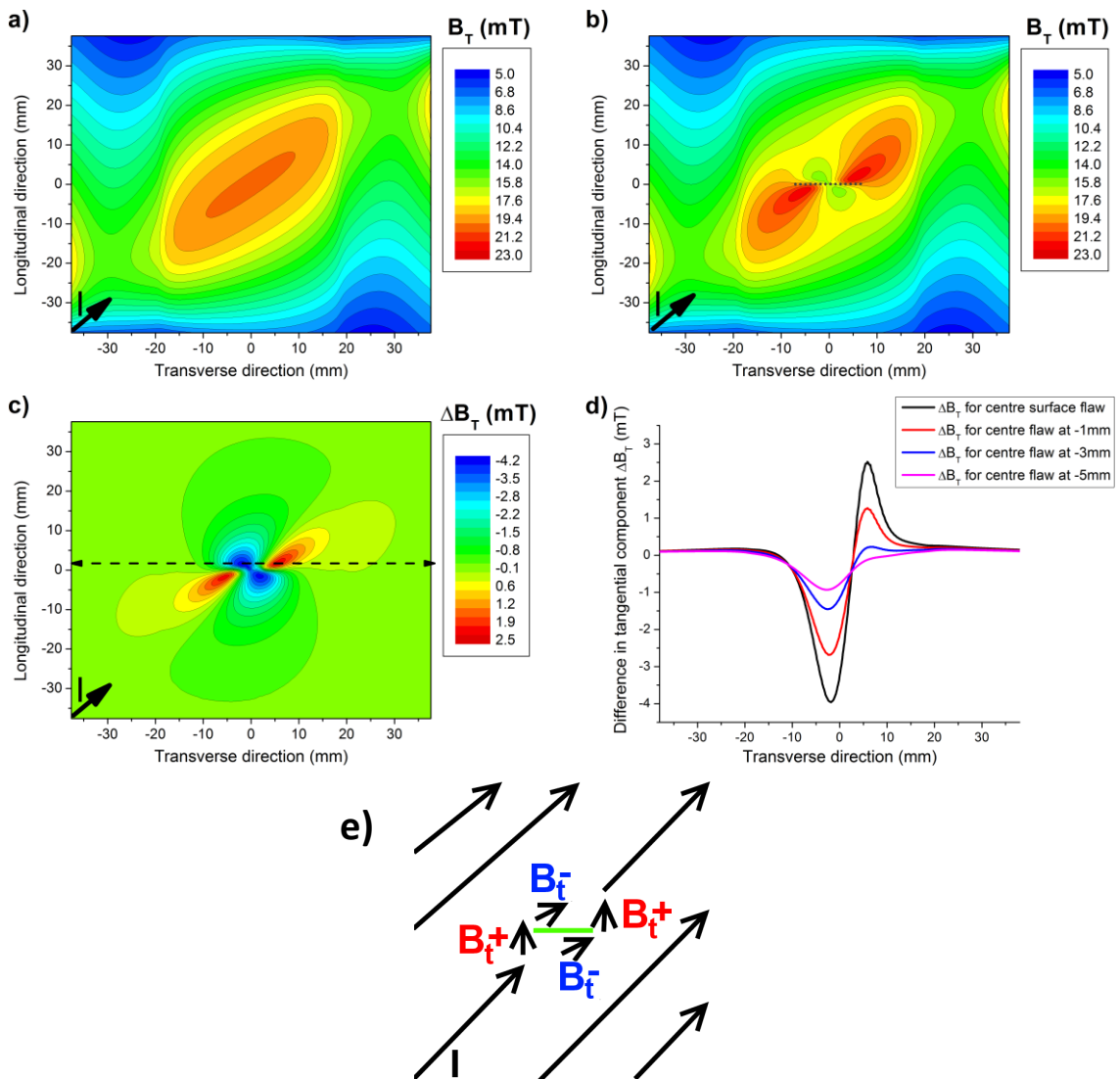
Fig. 5.35 Distributions of tangential component of magnetic field at 1mm above diagonally energised: a) unflawed rail and b) flawed rail; c) Differential distribution ΔB_T indicating effective perturbation in tangential component of magnetic field above surface flawed rail; d) Numerical profiles of differential perturbations in tangential component probed above diagonally energised rails with surface and sub-surface flaws; e) Qualitative 2-D analysis of the current flow in the affected rail volume.

The calculated pattern of B_T perturbation revealed four principal regions of variations in the vicinity of the flaw. Within two of these regions located in front and

rear of the flaw the reorientation of currents towards transverse direction (Fig. 5.35e) caused negative changes in B_T resulting in a local B_T minima. In the case of the other two regions located near the flaw side edges the currents which reoriented towards the longitudinal direction (Fig. 5.35e) generated higher values of B_T indicated by local positive variations $+\Delta B_T$, as depicted in Fig. 5.35c.

The distributions of the normal component B_N at 1mm above the unflawed and surface flawed rails energised along diagonal direction are shown in Fig. 5.36a and 5.36b. The resulting changes ΔB_N presented in Fig. 5.36c revealed a bi-polar pattern of alterations. The numerical profiles of effective changes ΔB_L and their decay with increasing flaw location depth are presented in Fig. 5.36d.
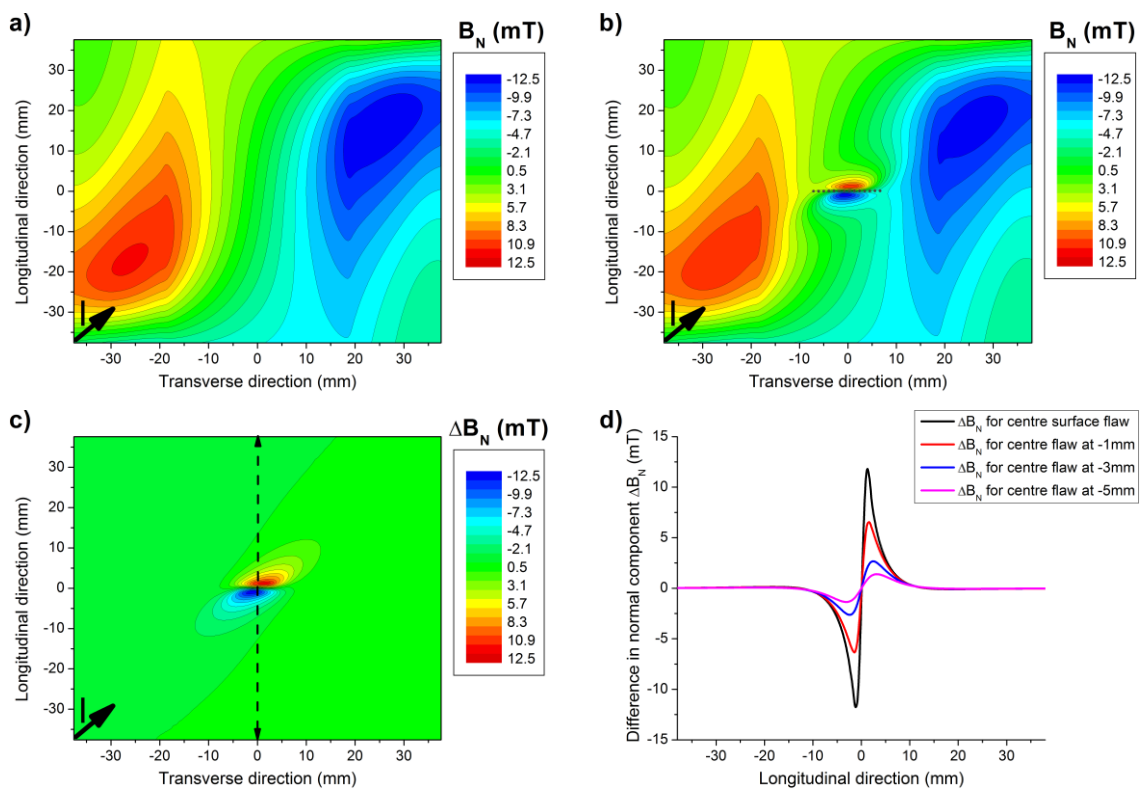
Fig. 5.36 Distributions of normal component of magnetic field at 1mm above diagonally energised: a) unflawed rail and b) flawed rail; c) Differential distribution ΔB_N indicating effective perturbation in normal component of magnetic field above surface flawed rail; d) Numerical profiles of differential perturbations in normal component probed above diagonally energised rails with surface and sub-surface flaws.

The calculated bi-polar flux leakage signal was generated by currents which re-routed towards the transverse direction in the front and rear of the flaw, as depicted in Fig 5.34b. This type of B_N perturbation was analogous to the one previously

observed for flawed rail energised along the transverse direction (Fig. 5.28c). However in this particular case the local extrema of ΔB_N were generated non-symmetrically against the flaw cross-sectional plane, as the current re-routing led to creation of zero J regions at the front left and rear right sides of the flaw (Fig. 5.34b). Moreover the maximum levels of B_N perturbation for diagonally energised rail could also be seen to be relatively lower than those corresponding to rail with transverse current flow.

The resulting distribution of longitudinal component B_L above surface flawed rail is shown in Fig. 5.37b. When comparing it with the distribution above unflawed rail (Fig. 5.37a) it could be seen that a considerable leakage pattern was created in the flaw vicinity. This pattern was clearly revealed in the differential distribution ΔB_L presented in Fig. 5.37c. The decay in local maximum ΔB_L with increasing depth of flaw position was evaluated via numerical profiles presented in Fig. 5.37d.
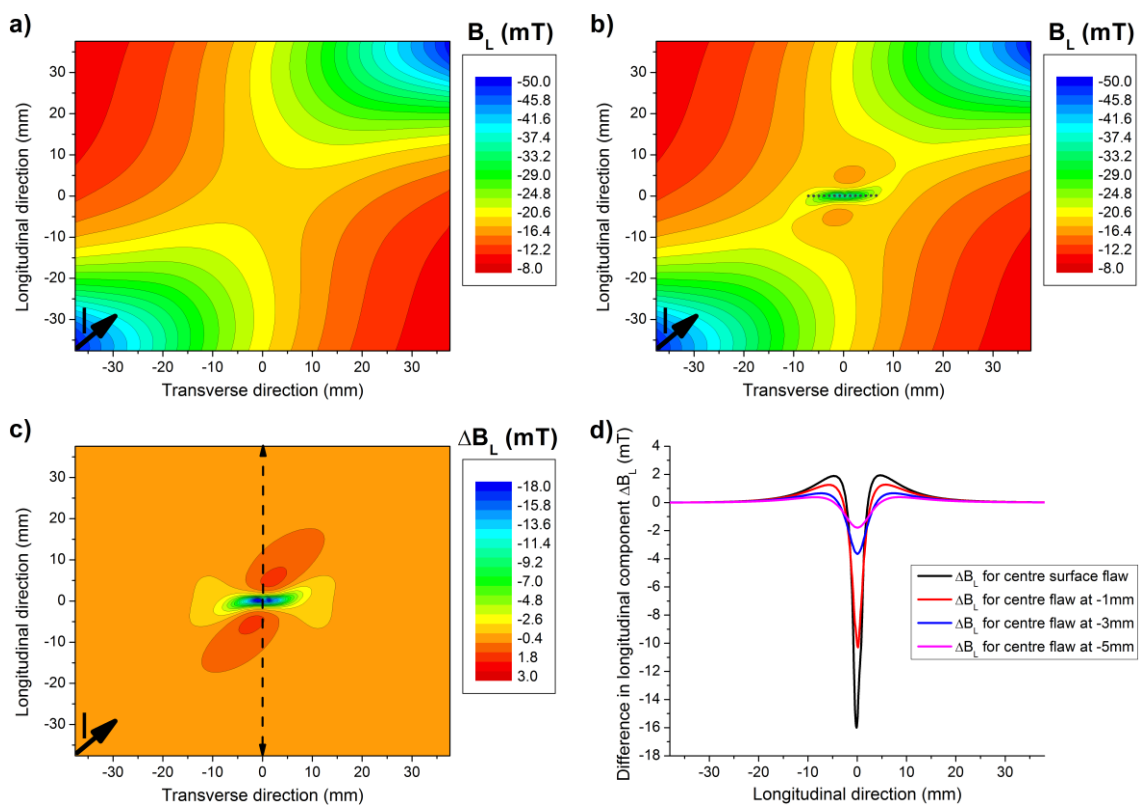
Fig. 5.37 Distributions of longitudinal component of magnetic field at 1mm above diagonally energised: a) unflawed rail and b) flawed rail; c) Differential distribution ΔB_L indicating effective perturbation in longitudinal component of magnetic field above surface flawed rail; d) Numerical profiles of differential perturbations in longitudinal component probed above diagonally energised rails with surface and sub-surface flaws.

Similar to the previous case of normal component B_N the generated perturbation in longitudinal component B_L could also be attributed to re-routed currents flowing along the flaw front and rear faces in transverse direction. The strongest stray field was generated above the centre of the flaw where the magnetic flux was forced to pass through the defect volume. The pattern of these ΔB_L variations was comparable to the case of ΔB_L for transversely energised rail (Fig, 5.29c) with a distinctive asymmetry due to different current re-routing possibilities. However, the effective levels of ΔB_L calculated for diagonally energised flawed rail were lower than those previously obtained for rail carrying current in the transverse direction.

A complementary FEM analysis was also performed for cases of side flaws incorporated into diagonally energised rail. The obtained **J** plots confirmed similar current re-orientation pattern in vicinity of side surface flaw, as shown in Figs. 5.38a and 5.38b.
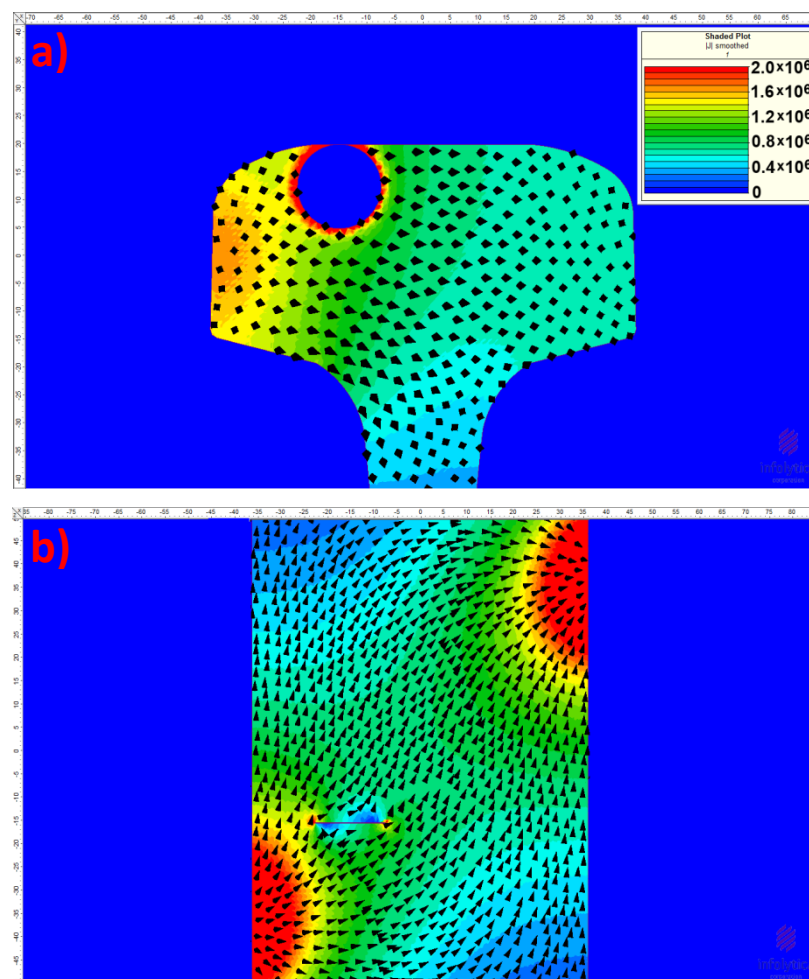
Fig. 5.38 Distributions of current density **J** within a) transverse cross-section and b) longitudinal cross-section of diagonally energised rail with side transverse flaw.

The corresponding differential distributions of tangential B_T, normal B_N and longitudinal B_L components above the analysed surface side flawed rail are shown in Figs. 5.39a, 5.39c and 5.39e. The numerical profiles probed in the indicated regions above rails with surface and subsurface side flaws are presented in Figs. 5.39b, 5.39d and 5.39f.
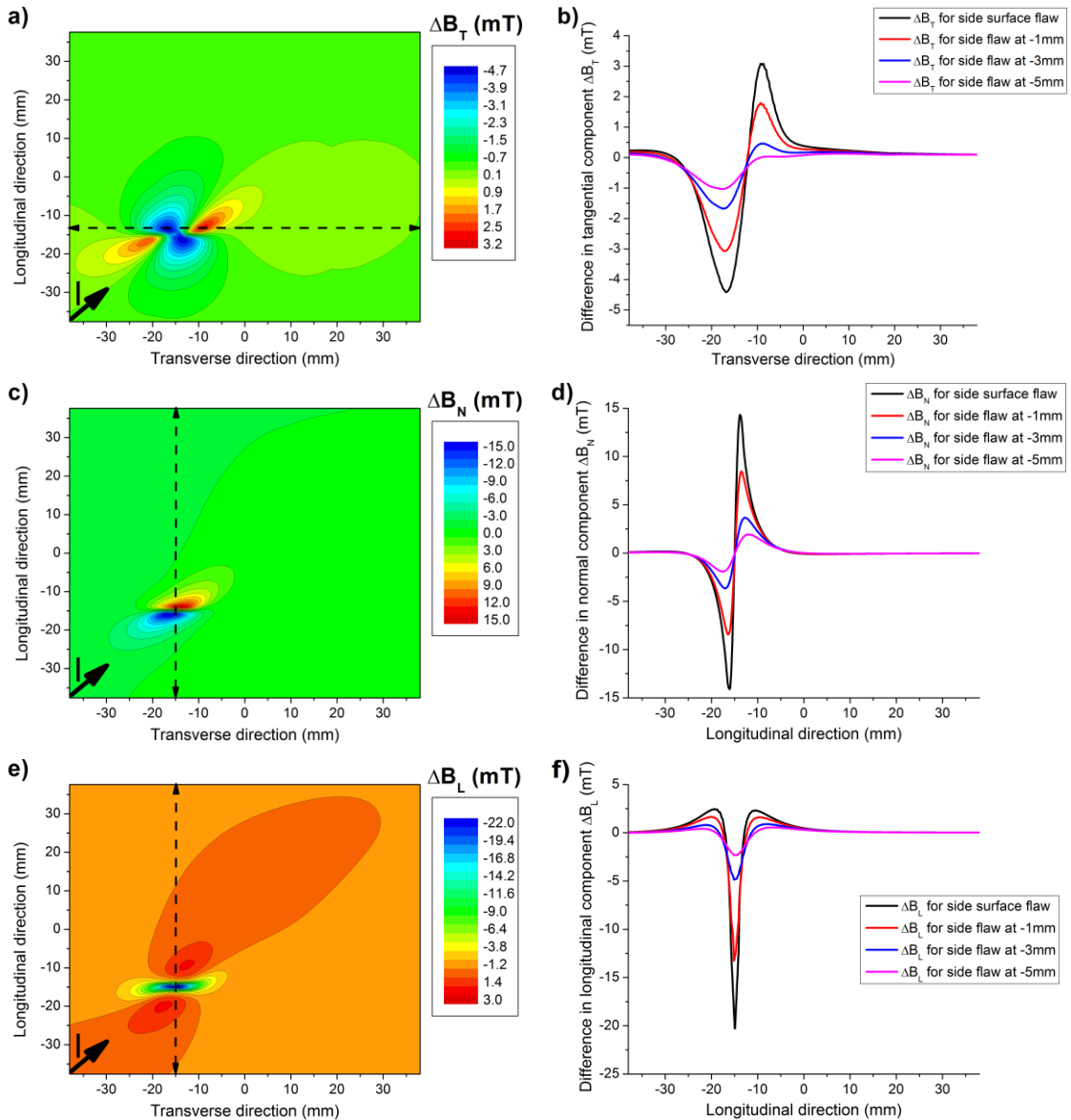
Fig. 5.39 Differential distributions of: a) tangential component; c) normal component and e) longitudinal component of magnetic field above surface side-flawed rail energised diagonally. Numerical profiles of differential perturbations in b) tangential component; d) normal component and f) longitudinal component of magnetic field probed above diagonally energised rails with surface and sub-surface flaws.

As it can be seen in the above graphs the perturbations in all three components were comparable to those previously observed for the centre flaw. Yet the numerical profiles indicated that the scale of effective variations (ΔB_T, ΔB_N, ΔB_L) due to the side

flaw in a diagonally energised rail were relatively higher than those calculated for the centre flaw. This is attributed to the fact that side flaw was located closer to the electrode-rail interface and therefore affected higher amount of current at an earlier stage of divergence within the energised rail volume.

In this section a comprehensive analysis of solutions from static FEM simulations of variously energised flawed and unflawed rails was presented. This analysis allowed the cause and character of detectable perturbations in the main components of magnetic field and flux leakage signals above the inspected rails to be analysed and explained.

The following Sections 5.4.2 and 5.4.3 are an extension of this analysis as they discuss FEM simulations of MFL scanning procedures above flawed rail sections with inductive sensors. They include visualization of the signatures of flux leakage and voltage signals acquired during inspection with Sperry ISU system, as well as MFL signals obtained from rail inspections with alternative current injection techniques.

5.4.2 Simulation of rail flaw inspection with Sperry Induction Sensing Unit

Development of the FEM model of Sperry ISU system involved creation of an equivalent set-up of inductive sensors located in between the current carrying electrodes, as shown in Fig. 5.40.
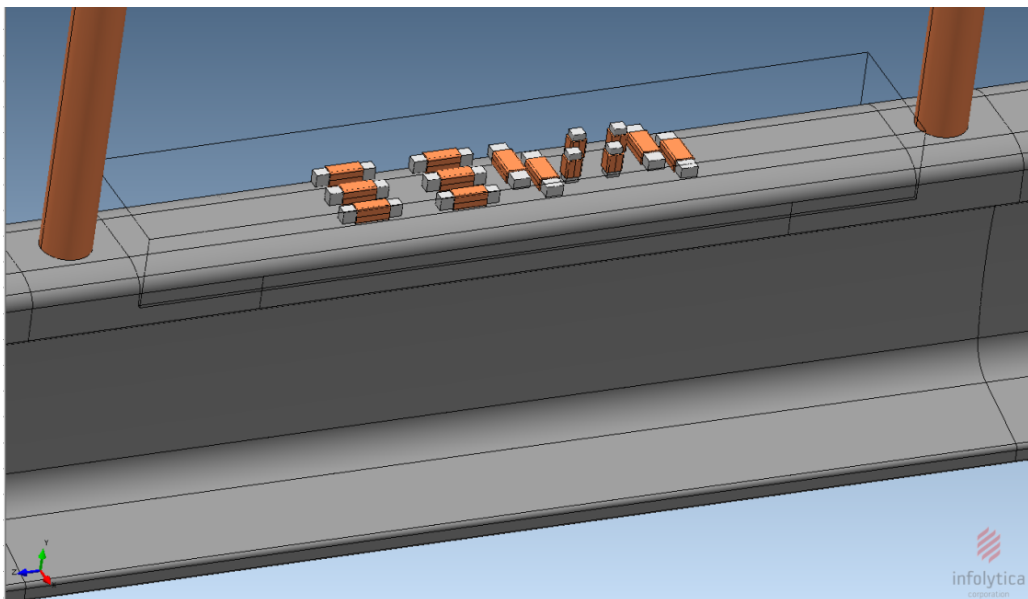
Fig. 5.40 FEM model of Sperry ISU system.

All sensors comprised ferromagnetic core made of M800-65A electrical steel wound with pick-up coil of 100 turns. The magnetisation curve of M800-65A steel used in the calculations is shown in Fig. 5.41.
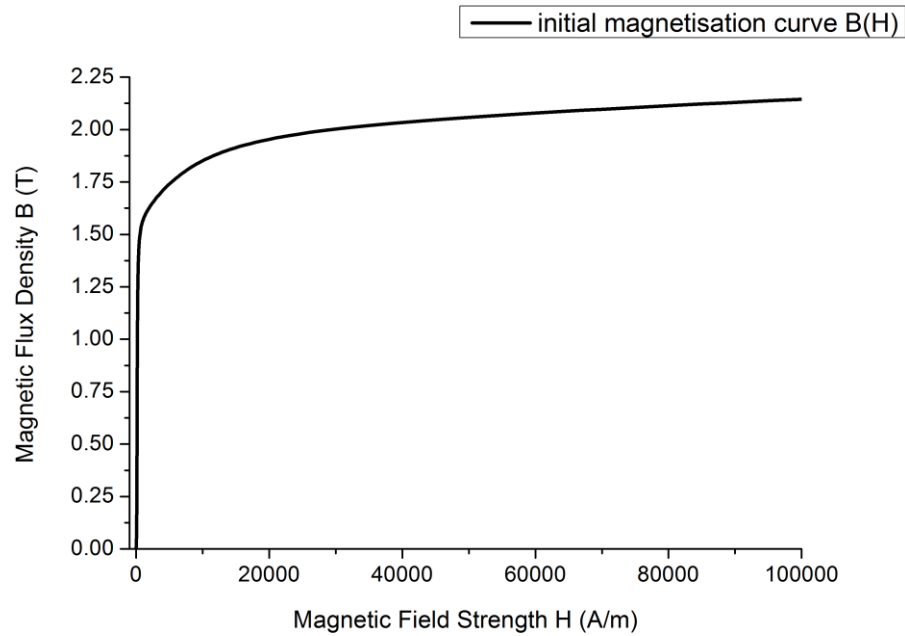
Fig. 5.41 Initial magnetisation curve of M800-65A sensor steel.

The FEM sensor set-up was made of three groups of directional sensors, as depicted in Fig. 5.42 and was analogous to the original Sperry ISU system
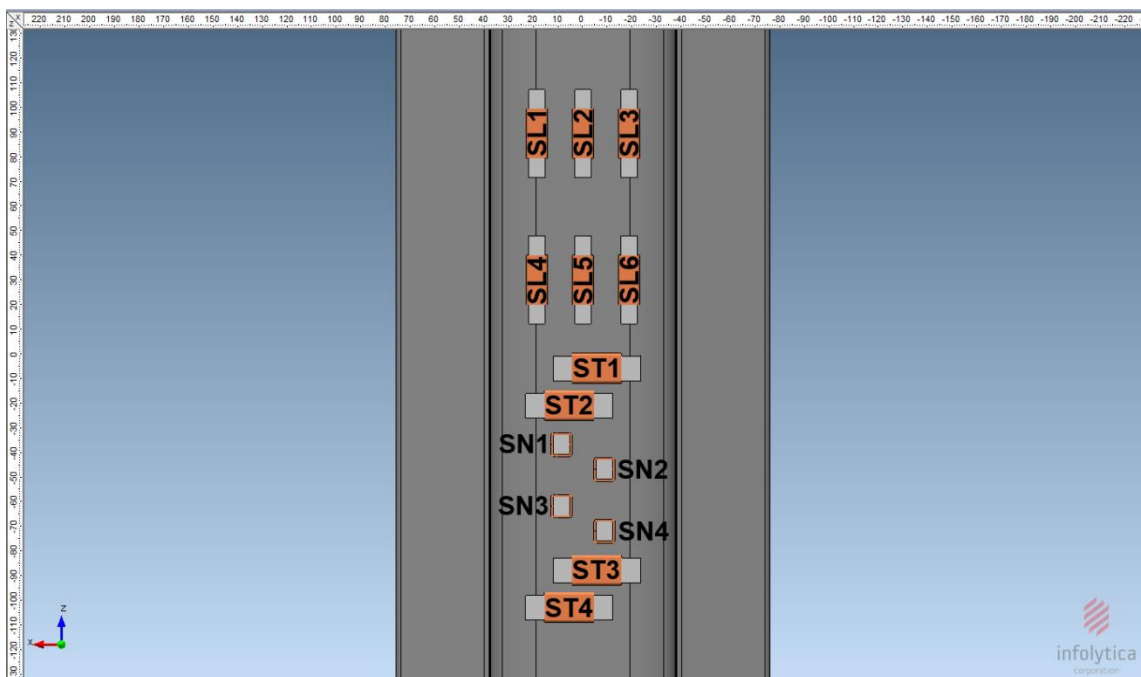
Fig. 5.42 FEM sensor set-up comprising three groups of directional sensors.

The first group of six directional sensors (SL1 to SL6) located in front of the unit were designed to probe the variations in longitudinal component (measured along the length of rail). The dimensions of the SL sensors were 35.6mm×7.6mm×6.4mm (length×height×width). The second group included four sensors (ST1 to ST4) positioned in the centre and rear of the unit. These ST sensors were used to detect the variations in tangential field component (along the width of rail). The dimensions of ST sensors were 35.6mm×6.4mm×10mm. The third group comprised four sensors (SN1 to SN4) assigned to probe the normal component of magnetic field (along rail height). These sensors had dimensions of 7.6mm×19mm×6.4mm. All sensors were enclosed within an air box of fine mesh for improving the solution accuracy. The lift-off of the sensor unit was set to 3mm which in real inspection includes the air gap between the ISU unit and rail, as well as the ISU unit casing thickness.

In the cases studied a typical surface and subsurface flaws of 0.1mm thickness and 15mm diameter were incorporated into the central cross section of rail. The modelling of the scanning procedure was performed by shifting the relative position of flaw along the longitudinal direction of rail, from its initial location of 125mm in front of ISU (Figs. 5.43a and 5.43b) to the final position of 125mm behind ISU (Figs. 5.43c and 5.43d) with fixed steps of 5mm increments. The total number of solved FEM problems for a given flaw was 94 which corresponded to a scanned distance of 465mm.

For each particular flaw position the physical quantity calculated by FEM software was the flux linkage φ_l of a given sensor being a product of flux cutting through its pick-up coil ϕ and number of coil turns N. Therefore by using the variations in φ_l with changing position (with fixed steps of 5mm) the induced voltage signal was obtained using the following equation:

$$V = -\frac{d\varphi_l}{dx}\frac{dx}{dt} \tag{5.12}$$

where $\frac{d\varphi_l}{dx}$ was the rate of change of magnetic flux linkage with distance and $\frac{dx}{dt}$ was the corresponding average ISU inspection speed rate of 30km/h equivalent to 5mm/0.6ms.

As the calculations of induced voltage signals were performed by differentiating flux linkage φ_l values obtained from set of subsequent static solutions rather than from continuous transient analysis, the dynamic effects related to generation of eddy

currents and related opposing magnetic fields in the rail and sensors were not considered. Nevertheless, by taking into account the relative position of sensor unit above the rail sections which experience stable level of direct current at moderate rate of inspection speed of 30km/h, these dynamic effects of time varying electromagnetic field on MFL signals could be assumed insignificant [62].
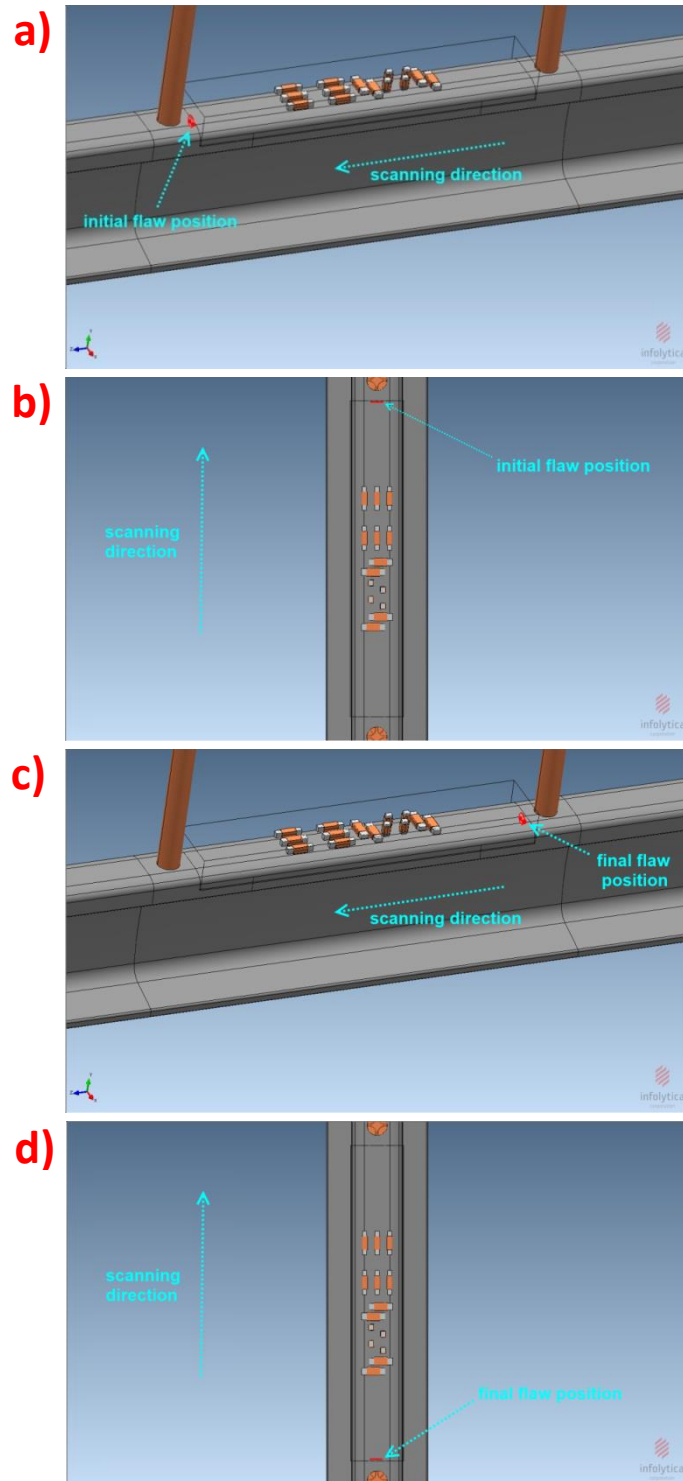
Fig. 5.43 Top and side views on FEM model used to simulate the dynamic flaw inspection with Sperry Induction Sensing Unit.

The flux linkage φ_l signals from the front longitudinal sensors SL1, SL2 and SL3 obtained for cases of rails with surface and subsurface centre transverse flaws are shown in Fig. 5.44a.
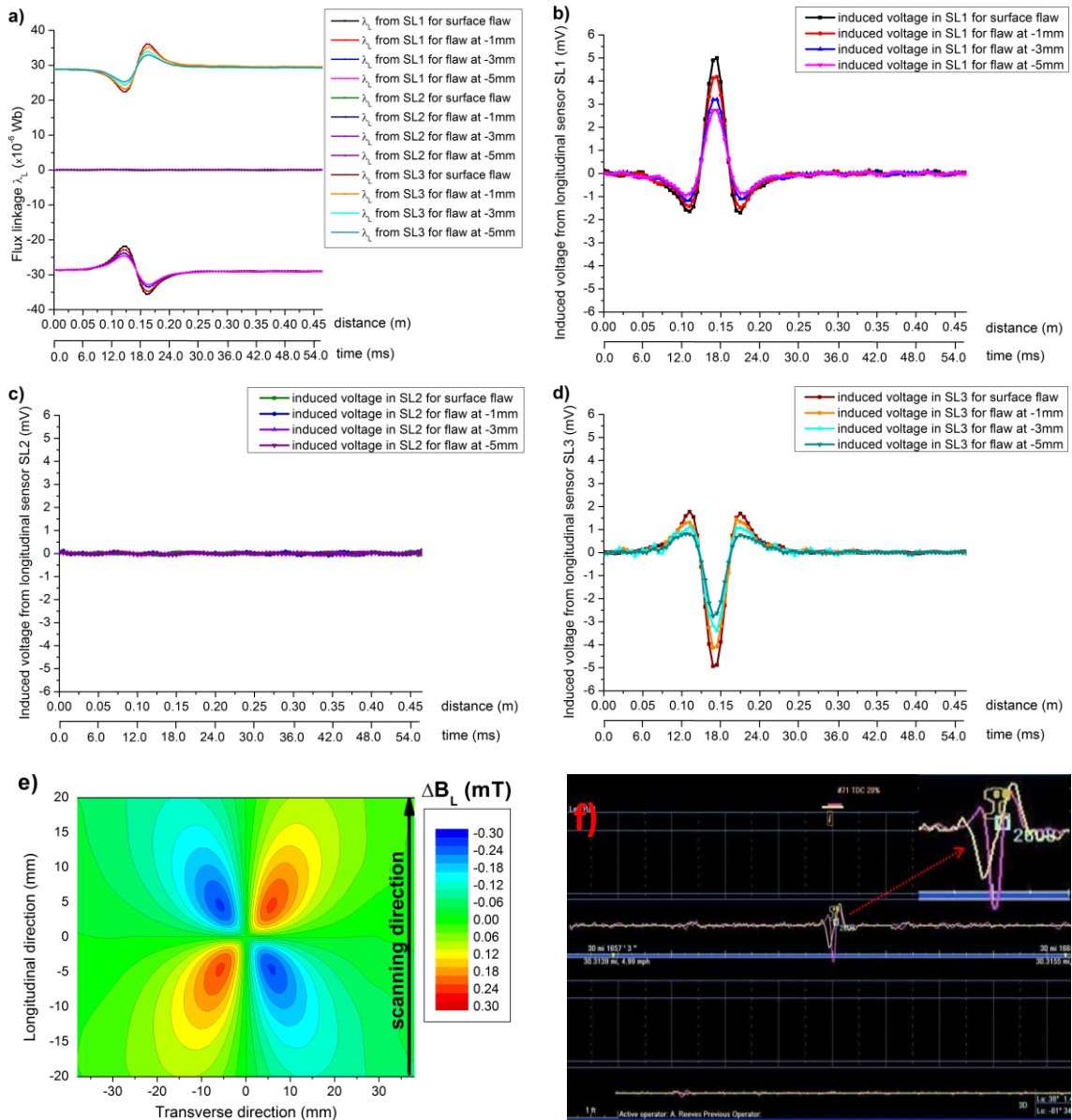
Fig. 5.44 a) Flux linkage signals from front ISU longitudinal sensors SL1, SL2 and SL3 probed above rails with surface and subsurface centre transverse flaws. Induced voltage signals from b) SL1 sensor, c) SL2 sensor and d) SL3 sensor obtained via differentiation of their flux linkage variations at speed rate of 30km/h; e) Distribution of effective changes in longitudinal component ΔB_L above longitudinally energised rail with surface centre flaw; f) Typical induced voltage signature indicating the presence of transverse flaw probed with longitudinal sensor SL (purple curve).

The signatures of these signals can be explained by referring to the previously described distribution of effective changes in longitudinal component ΔB_L from ISU inspection, reproduced in Fig. 5.44e. It can be seen that the sensor SL1 scanning

region above the left side of flaw probed initially positive changes in φ_l in front of the flaw and then subsequently detected a reversal in polarity of field variation at its rear. The negative offset of the SL1 flux linkage signal was generated by the current flowing in the nearby electrode. In the case of the SL3 sensor scanning the region above the right side of flaw the registered φ_l trends were opposite to those picked-up by SL1 sensor, as the negative changes in φ_l ahead of the flaw were probed first followed by detection of negative flux linkage variation behind the flaw. The calculated φ_l offset for SL2 was also of opposite polarity to that for SL1. Finally the sensor SL2 which scanned the region above the centre of the flaw determined negligible levels of flux linkage φ_l signals due to symmetry in MFL perturbation. The offset of SL2 flux linkage signal was also zero as it was positioned in the null zone of the longitudinal magnetic field created by the electrode current.

The resulting induced voltage signals in sensors SL1, SL2 and SL3 obtained via differentiation of their flux linkage time variation (Equation 5.12) are shown in Figs. 5.44b, 5.44c and 5.44d respectively. It can be seen that voltage waveforms of sensors SL1 and SL3 could be considered as mirror reflections due to symmetry of detected effective perturbation. Their peak voltage values for surface flaw were approximately +/-5mV and would gradually attenuate with increasing depth of flaw position to +/-2.7mV for innermost analysed flaw at -5mm from rail surface. In case of sensor SL3 the calculated induced voltage had fluctuation around zero level which would be assigned to inaccuracies in FEM meshing noise.

The calculated voltage waveforms for sensors SL1 and SL3 justified the signature of typical voltage signal from longitudinal sensor in Sperry ISU inspection indicating the presence of transverse defect which is represented by purple plot in Fig. 5.44f. This good agreement between calculated and measured voltage signals validated the effectiveness of the developed FEM MFL inspection model.

The analogous flux linkage signatures were obtained with the second set of longitudinal sensors SL4, SL5 and SL6, as depicted in Fig. 5.45a. The only distinctive feature was the asymmetry in the offset levels of φ_l signals from sensors SL4 and SL6 and non-zero offset of φ_l from SL5. These differences were attributed to the bias of local flux distribution at the rear of SL5 and SL6 sensors caused by vicinity of tangential sensor ST1, as shown in Fig. 5.45e.
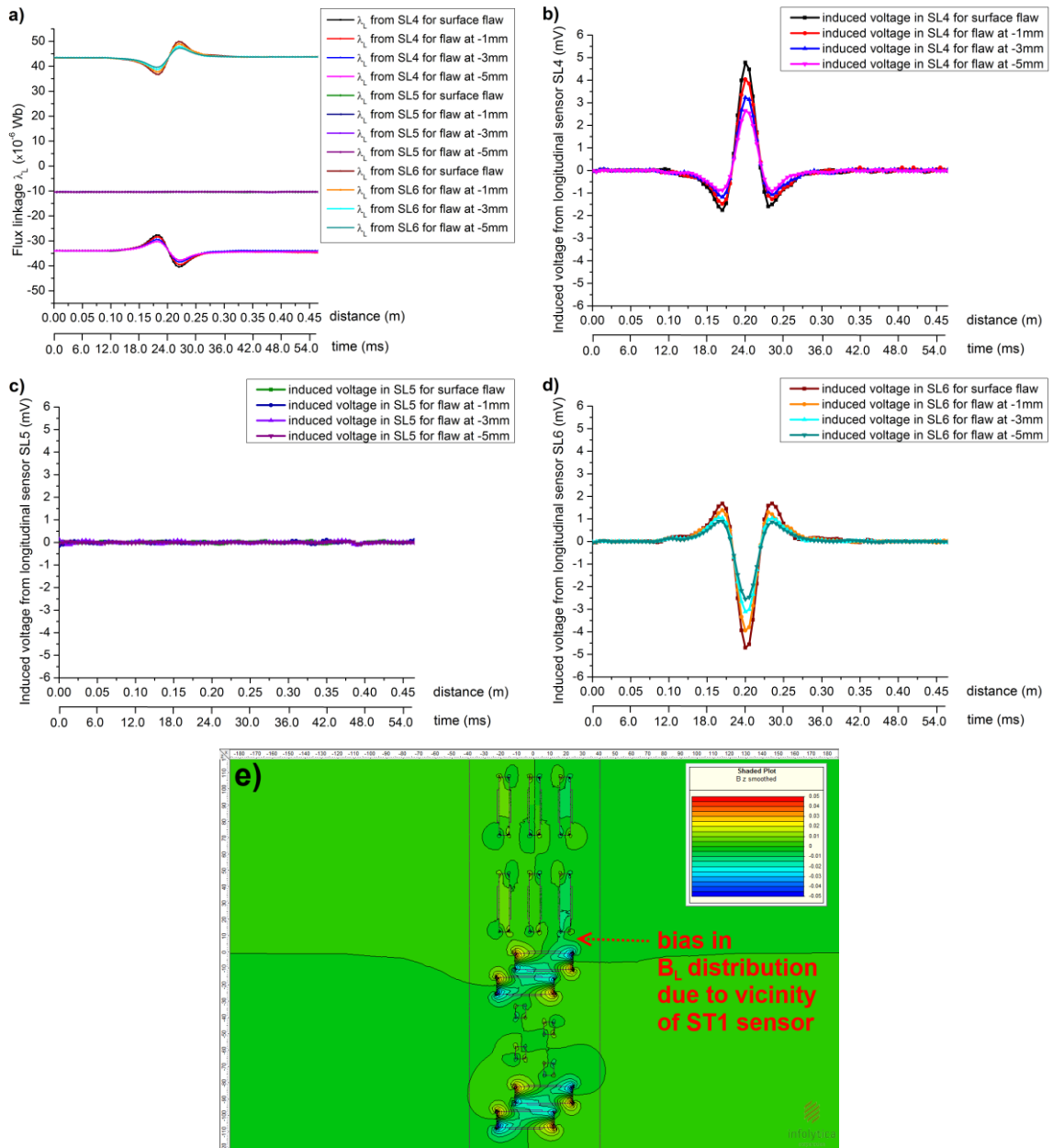
Fig. 5.45 a) Flux linkage signals from rear ISU longitudinal sensors SL4, SL5 and SL6 probed above rails with surface and subsurface centre transverse flaws. Induced voltage signals from b) SL4 sensor, c) SL5 sensor and d) SL6 sensor obtained via differentiation of their flux linkage variations at speed rate of 30km/h; e) Distribution of longitudinal component of magnetic field with indicated bias in local flux distribution at the rear of SL5 and SL6 sensors caused by vicinity of tangential sensor ST1.

Nevertheless, the discrepancies in the initial values of φ_l did not affect the MFL changes detected by SL4, SL5 and SL6 sensors and therefore their corresponding induced voltage signals were comparable to the output from the front longitudinal probes, as presented in Figs. 5.45b, 5.45c and 5.45d.

The flux linkage φ_l signals calculated for normal sensors SN1, SN2, SN3 and SN4 are shown in Figs. 5.46a, 5.46c, 5.46e and 5.46g respectively.

196
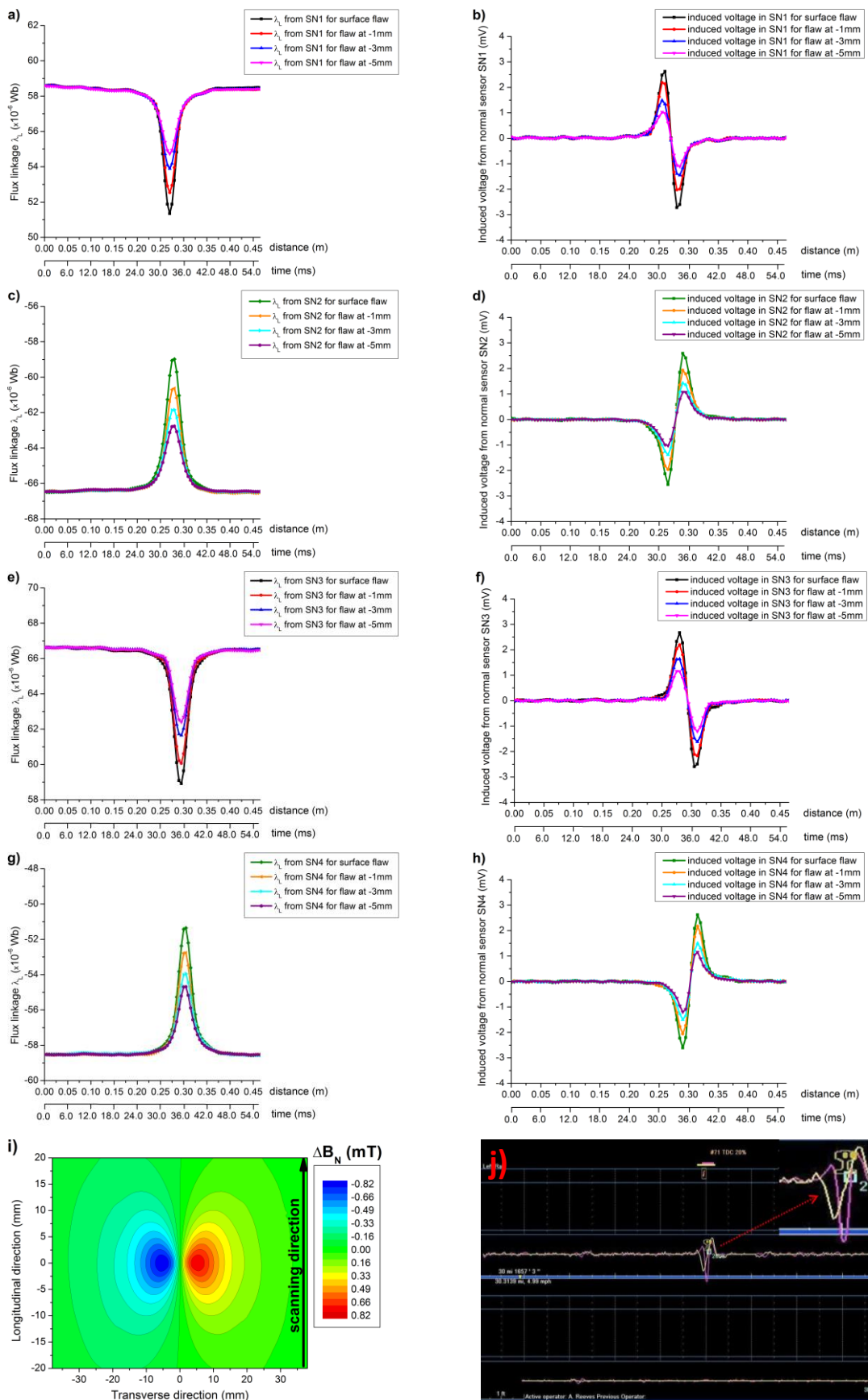
Fig. 5.46 Flux linkage signals probed with a) SN1 sensor, c) SN2 sensor, e) SN3 sensor and g) SN4 sensor. Induced voltage signals from: b) SN1 sensor, d) SN3 sensor, f) SN3 sensor and h) SN4 sensor at speed rate of 30km/h. i) Distribution of effective changes in normal component ΔB_N above longitudinally energised rail with surface centre flaw; j) Typical voltage signature indicating the presence of transverse flaw from ISU normal sensor SN (yellow curve).

The calculated flux linkage signals indicated that the normal sensors SN1 and SN3 which scanned the region above left side of flaw detected the local negative perturbation in MFL, whereas the right sensors SN2 and SN4 determined the local positive perturbation in MFL (Figs. 5.46c and 5.46g). The characteristics of these modelled signals corresponded directly to the previously discussed differential distribution of normal component ΔB_N above a longitudinally energised rail, as shown in Fig. 5.46i. From the plots of these signals it can also be seen that similarly to the preceding set of longitudinal sensors the offset MFL values of sensors SN1 and SN4 were biased by the presence of neighbouring tangential sensors ST2 and ST3.

The corresponding calculated voltage waveforms from SN sensors are shown in Figs. 5.46b, 5.46d, 5.46f and 5.46h. The resulting double peak profiles had values within approximate range from - 2.6mV to +2.6mV for a surface flaw, which would progressively decrease with increasing location depth to range from -1.1mV to +1.1mV for innermost subsurface flaw at -5mm. These calculated double peak profiles resembled the typical output voltage signatures from Sperry ISU SN sensors represented by the yellow plot in Fig. 5.46j. This further validated the agreement between qualitative outcome from modelled and practical MFL inspections.

The flux linkage φ_l signals calculated for tangential sensors ST1, ST2, ST3 and ST4 are shown in Figs. 5.47a, 5.47c, 5.47e and 5.47g respectively. It can be seen that each of these ST sensors detected the negative variation in MFL signal above the affected rail section. The calculated spatial perturbations in MFL signal probed by ST sensors were represented by shifted in phase single-peak signatures with the local flux minima corresponding to region above the centre of transverse flaw. This character of the probed perturbations had been expected based on the previously analysed differential distribution ΔB_T reproduced in Fig. 5.47i.

The calculated output voltage signals from tangential sensors ST1, ST2, ST3 and ST4 are shown in Figs. 5.47b, 5.47d, 5.47f and 5.47h respectively. The resulting waveforms of these signals comprised two symmetrical peaks with values of approximately +/- 6mV for surface flaw which would gradually be reduced with increasing location depth to level of +/-2.9mV for the furthest in subsurface flaw at -5mm.
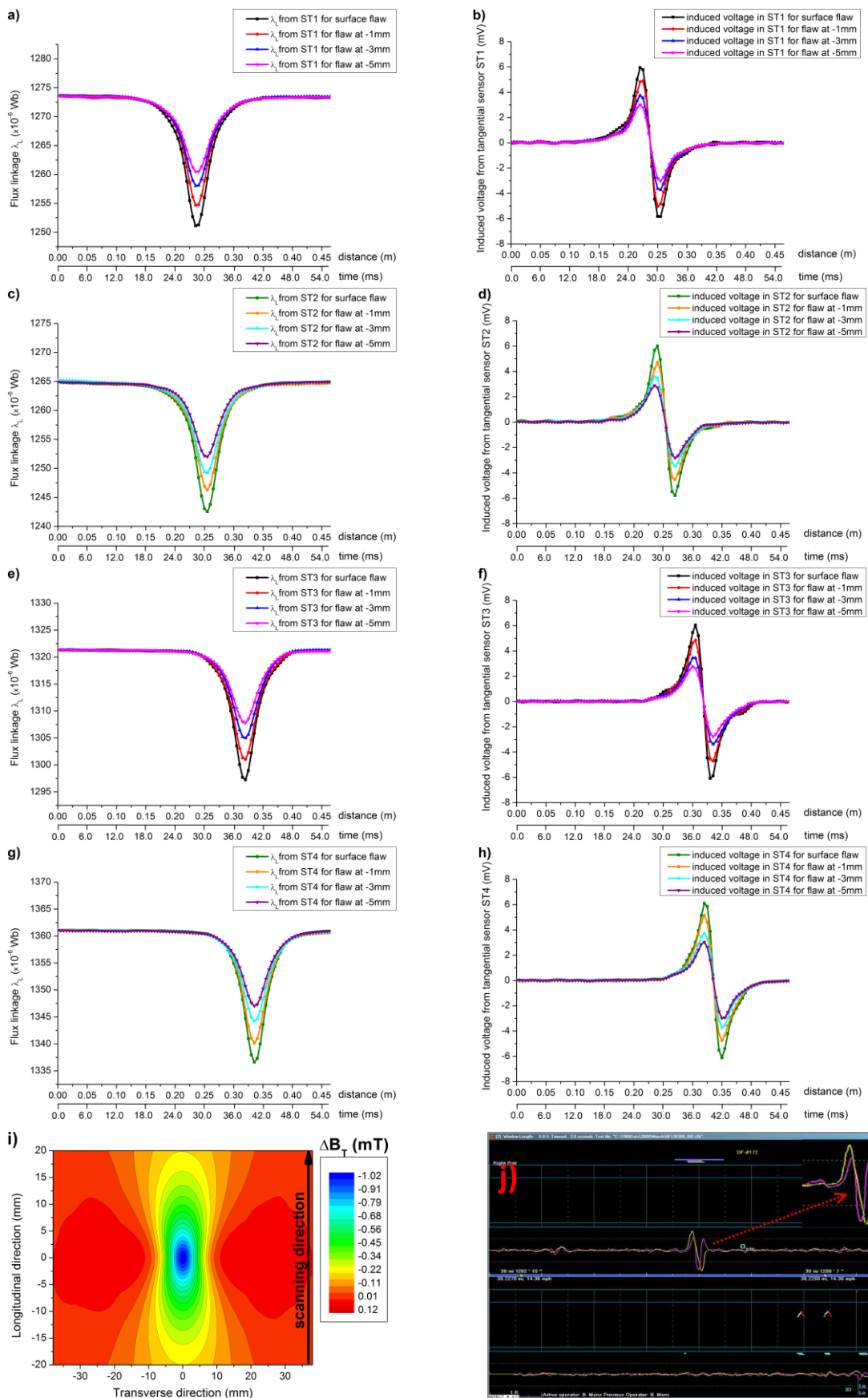
Fig. 5.47 Flux linkage signals probed with a) ST1 sensor, c) ST2 sensor, e) ST3 sensor and g) ST4 sensor. Induced voltage signals from: b) ST1 sensor, d) S23 sensor, f) ST3 sensor and h) ST4 sensor at speed rate of 30km/h. i) Distribution of effective changes in tangential component ΔB_T above longitudinally energised rail with surface centre flaw; j) Typical voltage signature indicating the presence of transverse flaw from ISU tangential sensor ST (yellow curve).

The modelled signatures of the voltage signals from ST sensors corresponded closely to the typical voltage waveforms from the same group of ISU sensors indicating presence of a transverse flaw. This is depicted by the yellow plot in Fig. 5.47j. This likewise confirmed the agreement between qualitative outputs from the simulated and actual Sperry MFL rail inspections.

5.4.3 Comparison of rail flaw inspection techniques with different current injection procedures

The final dynamic analysis of MFL signals above flawed rail with incorporated surface centre 15mm transverse defect was performed using three different current injection procedures. In these three alternative dynamic inspection cases the studied rails were energised along the longitudinal direction (Fig. 5.48a), the tangential direction (Fig. 5.48b) and at 45° to the flaw cross-section (Fig. 5.48c).
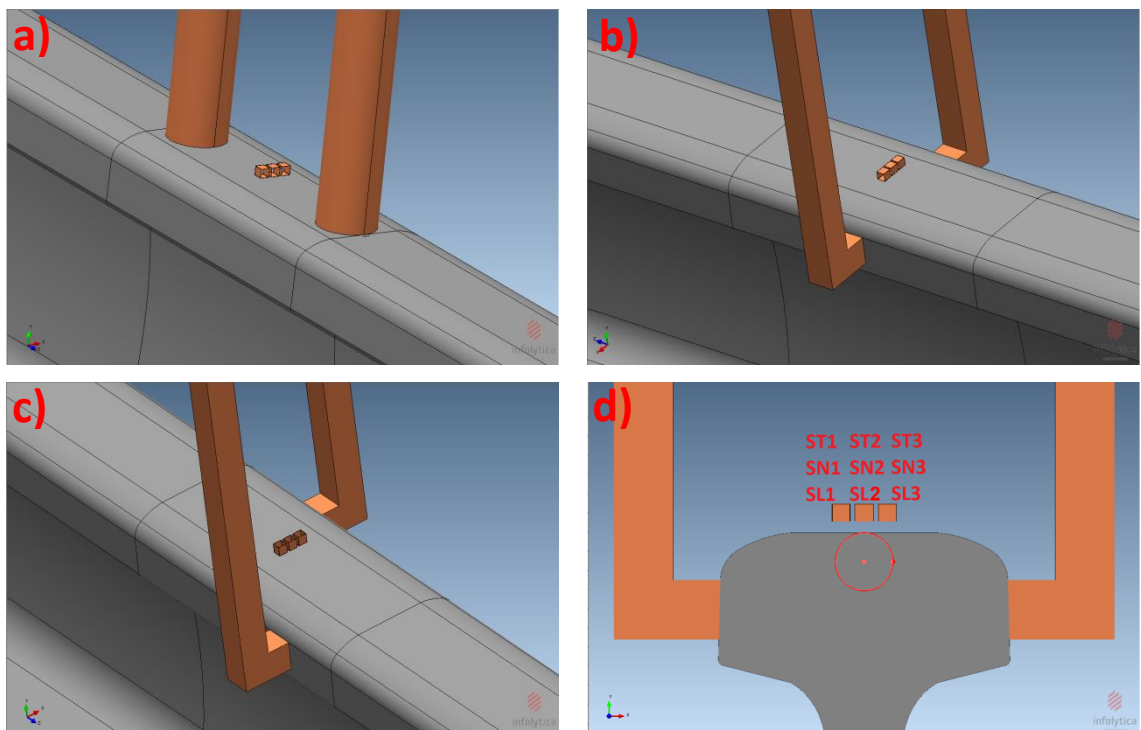
Fig. 5.48 Illustrations of modelled types of beryllium-copper electrodes for applying current in: a) longitudinal direction, b) tangential direction and c) at 45° to longitudinal and transverse planes of rail; d) Transverse view of the model with indicated positions of directional sensors.

In order to obtain a comparable current density **J** levels within the mid-section of investigated rail heads the distance between Sperry cylindrical electrodes was reduced to 100mm, as depicted in Fig. 5.48a. The resulting **J** distributions are shown in Fig. 5.49.

During each of the modelled rail inspections the resulting MFL signals were probed using a set of three-dimensional induction sensors (Fig. 5.48d) comprising three individual 5 turns coils used to pick-up flux variations of its longitudinal component (SL coils shown in Fig. 5.48a), tangential component (ST coils shown in Fig. 5.48b) and normal component (SN coils depicted in 5.48c).
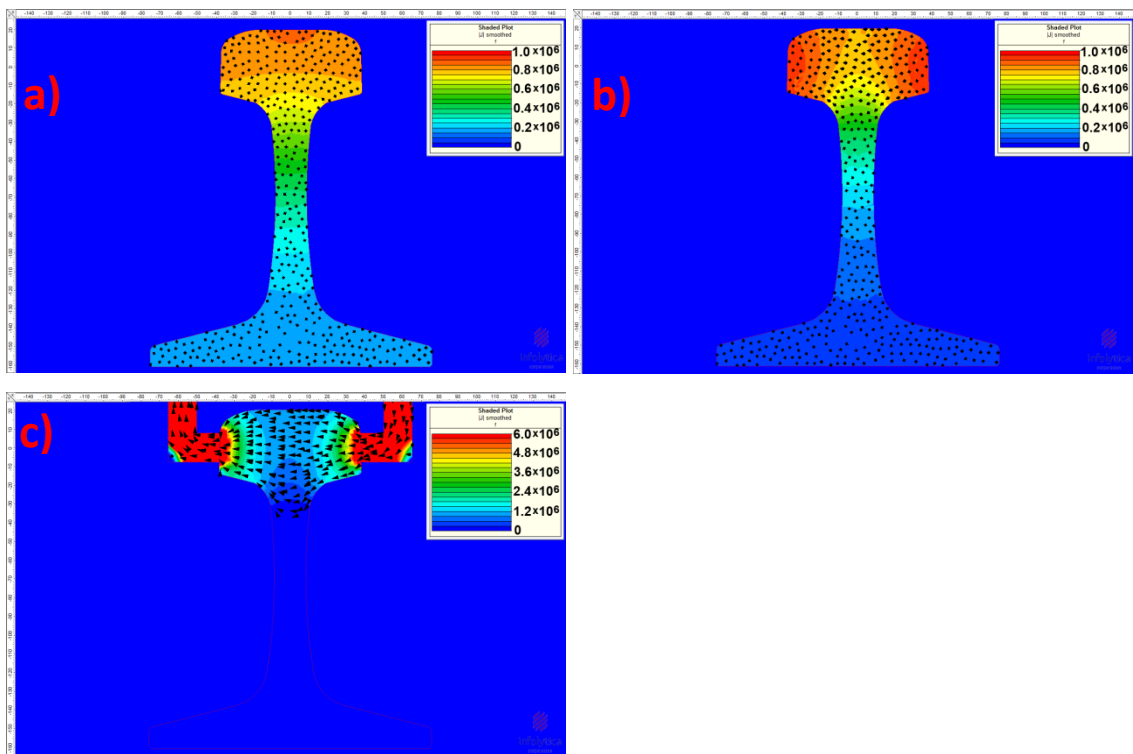
Fig. 5.49 Distribution of current density **J** in transverse cross-section of rails energised: a) longitudinally; b) diagonally and c) tangentially.

The three-dimensional sensors of dimensions 5mm×5mm×5mm were separated by distance of 1mm and positioned at 3mm above the centre of the energised rail sections. Their effective configuration was such that the first sensor with coils ST1, SN1 and SL1 scanned the region above the left side of the transverse flaw; the second sensor with coils ST2, SN2 and SL2 probed flux above centre of flaw and the third sensor with coils ST3, SN3 and SL3 examined the MFL signals above the right side of the defect, as indicated in Fig.5.48d.

Similarly to previously modelled Sperry ISU inspection, the simulation of scanning procedure was performed by shifting the relative position of flaw along the longitudinal direction of rail, from the initial front position of 50mm from the centre of 3-D sensors (Figs. 5.50a and 5.50b) to the final rear position of 50mm behind the sensor unit (Figs. 5.50c and 5.50d) with fixed step of 2mm.
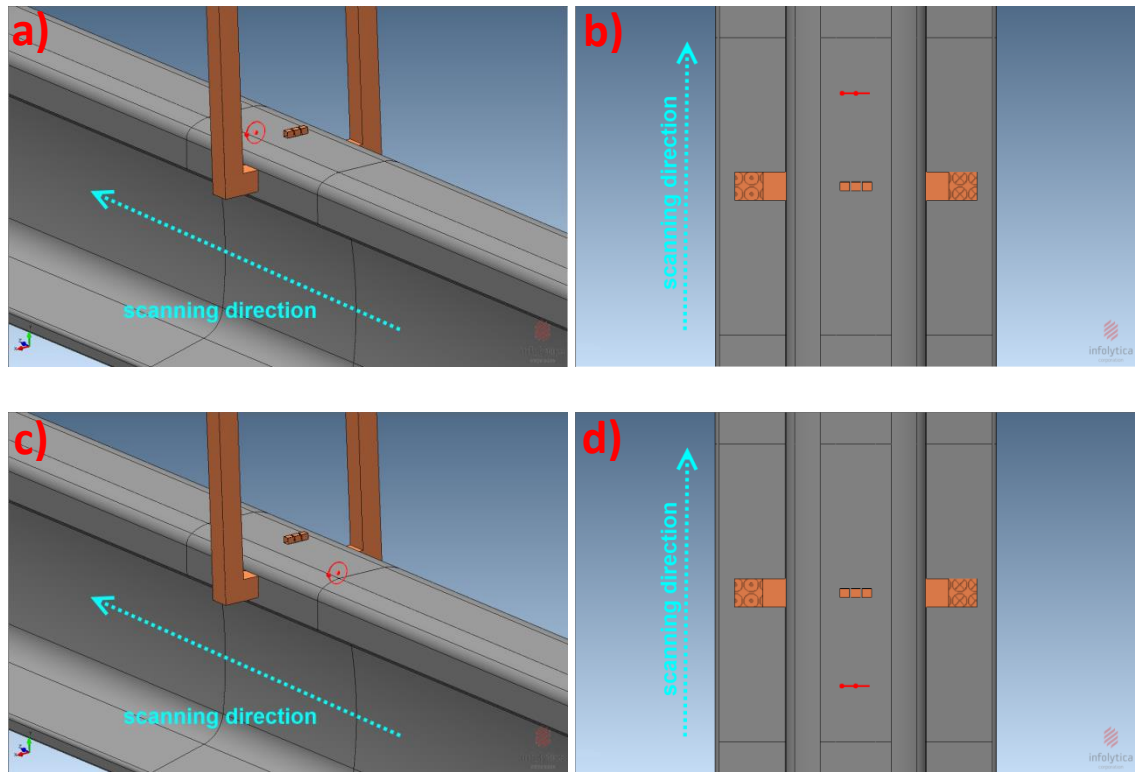
Fig. 5.50 Top and side views on FEM model with indicated initial and final flaw positions.

For each particular flaw position the flux linkage φ_l of a given sensor coil was calculated and the obtained dynamic variations in φ_l with distance were thoroughly used to determine the induced voltage output for an arbitrary inspection speed of 30km/h using Equation 5.12.

The resulting spatial and time variations in flux linkage φ_l probed by the ST sensors above flawed rails energised along longitudinal, tangential and diagonal directions are shown in Figs. 5.51a, 5.51c and 5.51e respectively. The corresponding static distributions of differential variations in tangential field component above these flawed rails are shown in Figs. 5.51b, 5.51d and 5.51f.

Fig. 5.51 Flux linkage signals from tangential sensors ST1, ST2 and ST3 probed above rails with surface centre flaws energised: a) longitudinally, c) tangentially and e) diagonally. Corresponding distributions of effective changes in tangential component $\Delta\mathbf{B_T}$ obtained above rails with surface centre flaws energised: b) longitudinally, d) tangentially and f) diagonally.

It can be seen in Fig. 5.51a that all three ST sensors detected the gradual decrease in tangential component of flux linkage above the longitudinally energised rail. Their registered MFL signals demonstrated single-peak profiles with minimum values corresponding to locations above the mid-section of the flaw. As expected from the static distributions, the greater effective change was indicated by the centre coil ST2 for which the φ_l level varied from initial value of 1.9385µWb to 1.885µWb above flaw centre, whereas the similar φ_l signals detected by the side coils ST1 and ST3 varied within approximate range from 1.9µWb to 1.87µWb and confirmed the symmetry of alterations in $\Delta\mathbf{B_T}$ spatial distribution.

In the case of transversely energised rail the side coils ST1 and ST3 probed a symmetrical double-peak flux linkage signal of reverse polarity, whereas the centre coil

203

ST2 indicated a negligible φ_l level due to a cancelling out effect of adjacent opposite flux variations. The calculated MFL signals for sensors ST1 and ST3 were within range of +/- 0.029µWb and the dynamic transition from the one peak to the other peak position took place within short distance of 8mm, corresponding to time span of 0.96ms.

When considering the outputs from the ST coils inspecting the rail with diagonal current flow a distinctive MFL signal profile could be noticed. The flank sensors ST1 and ST3 detected MFL signatures with three peaks corresponding to particular regions of negative and positive flux variations depicted in Fig. 5.51f. The reverse order in which those flux fluctuations were probed by a given sensor resulted in a mirror reflection of their MFL waveform with steepest transitions obtained above the mid-section of flaw. In the case of the centre coil ST2 it can be seen that only negative gradual variations were detected with an effective change from initial value of 1.67µWb to 1.57µWb above flaw centre. The calculated single-peak MFL profile of this sensor was symmetrical against the flaw mid-section.

The dynamics of the flux linkage variations detected by the ST coils during the rail inspections employing three alternative current injection procedures could be analysed by comparing their induced voltage outputs shown in in Figs. 5.52a, 5.52b and 5.52c.

Fig. 5.52 Induced voltage signals from tangential sensors ST1, ST2 and ST3 probed above rails with surface centre flaws energised: a) longitudinally, c) tangentially and e) diagonally at speed rate of 30km/h.

It can be seen in Fig. 5.52a that the output voltage signals from ST coils scanning the longitudinally energised rail comprised two peaks with approximate values of +/-11.5µV from side ST1 and ST3 coils, and +/-25.5µV from the centre ST2 sensor.

The calculated profiles from Fig. 5.52b showed that for the corresponding case of transversely energised rail the voltage signals from sensors ST1 and ST3 exhibited dominant central peaks of +/-91µV and two smaller side peaks of +/-24.5µV, whereas the ST2 voltage output was of zero level.

Finally, for the diagonally energised rail the calculated voltage signals from ST1 and ST3 coils revealed an asymmetric three peak profile with an extreme values at the centre of +/-87µV and adjacent local extrema of +/-21µV and +/-38µV. Simultaneously, the voltage waveform from the centre sensor ST2 exhibited double peaks of +/-44.6µV at locations corresponding to distances of 10mm away from flaw mid-section.

When comparing the characteristics of the above described ST voltage outputs it was noticed that the largest instantaneous amplitudes were obtained for the rail energised along its tangential direction (+/-91µV from coils ST1 and ST3). However, it was also noticed that for the diagonally energised rail the amplitudes from the same pair of coils were comparable (+/-87µV) and additionally the signal from the other sensor ST2 also clearly indicated the presence of a flaw. As a result this latter current injection procedure can be considered as more preferable when taking into account the flaw induced perturbation in tangential flux component individually.

The calculated variations in flux linkage φ_l probed by the SN coils above flawed rails energised along longitudinal, tangential and diagonal directions are shown in Figs. 5.53a, 5.53c and 5.53e, respectively. The corresponding static distributions of differential variations in normal field component above these flawed rails are shown in Figs. 5.53b, 5.53d and 5.53f.
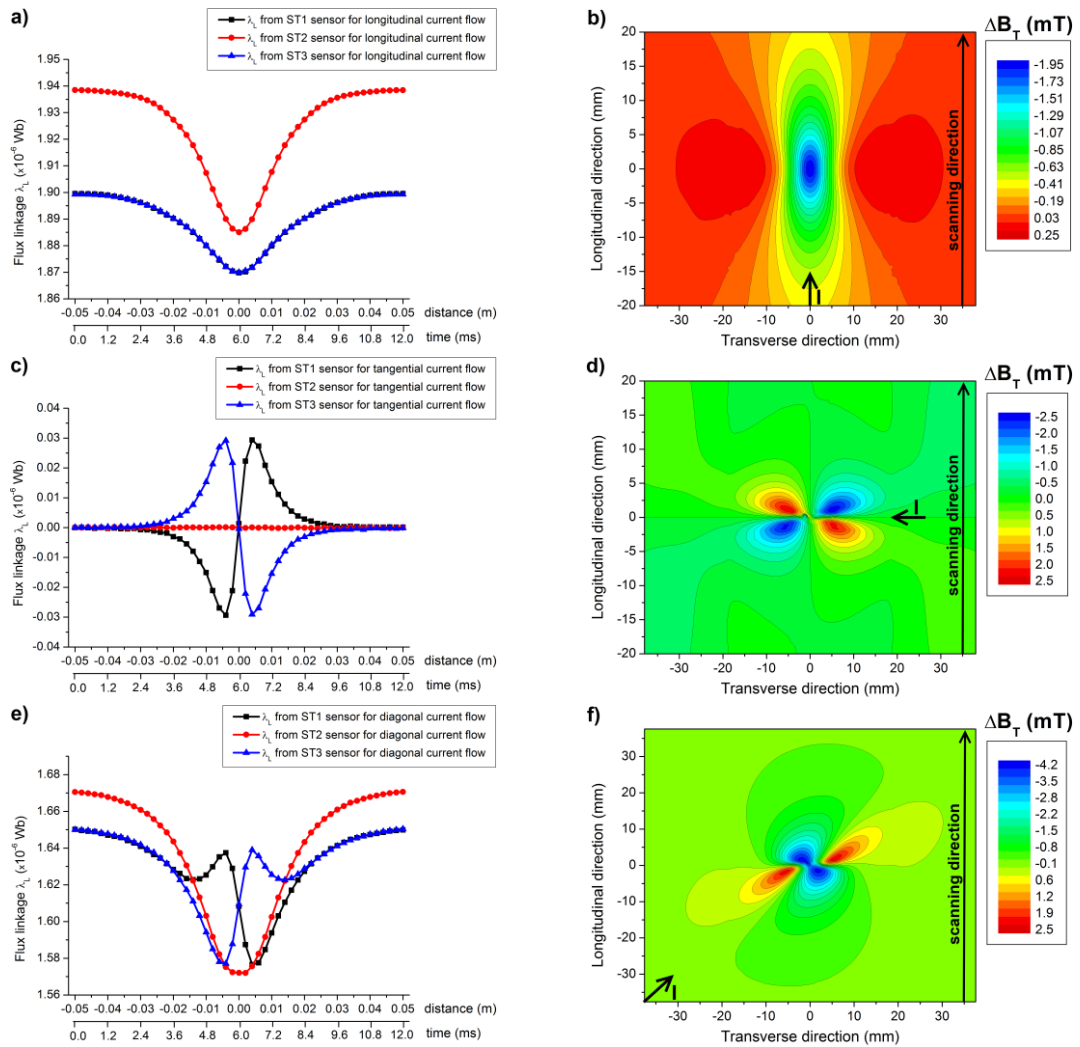
Fig. 5.53 Flux linkage signals from normal sensors SN1, SN2 and SN3 probed above rails with surface centre flaws energised: a) longitudinally, c) tangentially and e) diagonally. Corresponding distributions of effective changes in normal component ΔB_N obtained above rails with surface centre flaws energised: b) longitudinally, d) tangentially and f) diagonally.

It can be seen in Figs. 5.53b, 5.53d and 5.53f that in all three cases the static ΔB_N distributions were characterised by a two peak profiles of opposite polarities. The main distinctive features were the magnitudes of those peaks as well as the orientations of their particular symmetry planes. For longitudinally energised rail the symmetry plane was orthogonal to flaw transverse cross-section, for tangentially energised rail this symmetry plane was co-planar with flaw cross-section, and for diagonally energised rail it was at 45° to the flaw transverse plane. As a result the flux linkage signals of SN coils scanning the MFL distributions along the length of rail exhibited different time and spatial profiles.

In the case of longitudinally energised rail the side sensors SN1 and SN3 probed a single peak φ_l signal with opposite signs (Fig. 5.53a). The range of detected φ_l level

varied from initial value of 0.077µWb to 0.033µWb from SN1 coil, and from -0.077µWb to -0.033µWb from SN3 coil. The SN2 coil indicated a negligible φ_l level due to symmetry of sensed negative and positive $\mathbf{B_N}$ variations.

In case of tangentially energised rail all three SN coils probed the bi-polar MFL perturbations above the affected rail section. The greater variation magnitudes within range from -0.132µWb to 0.132µWb were detected by the centre sensor SN2, whereas those sensed by SN1 and SN3 coils were within scale from -0.1µWb to 0.1µWb (Fig. 5.53c). It was also noticed that the rates of change of sensed MFL signals were higher than for the previous case, due to smaller spatial span of detected changes.

The MFL signals detected by SN coils above diagonally energised rail could be described as a combination of SN signals from the other two alternative techniques. The side coils SN1 and SN3 probed pre-dominantly the unipolar variations equivalent to sensed φ_l levels from 0.22µWb to 0.1µWb by SN1 coil, and from -0.22µWb to -0.1µWb by SN3 coil. Simultaneously, the centre SN2 coil detected a bi-polar flux perturbation indicated by an MFL signal of double-peak profile within range from -0.096µWb to 0.096µWb.

Consequently, the dynamics of the MFL perturbations detected by the SN coils during alternative rail inspection techniques would be analysed by comparing their induced voltage outputs shown in Figs. 5.54a, 5.54b and 5.54c.
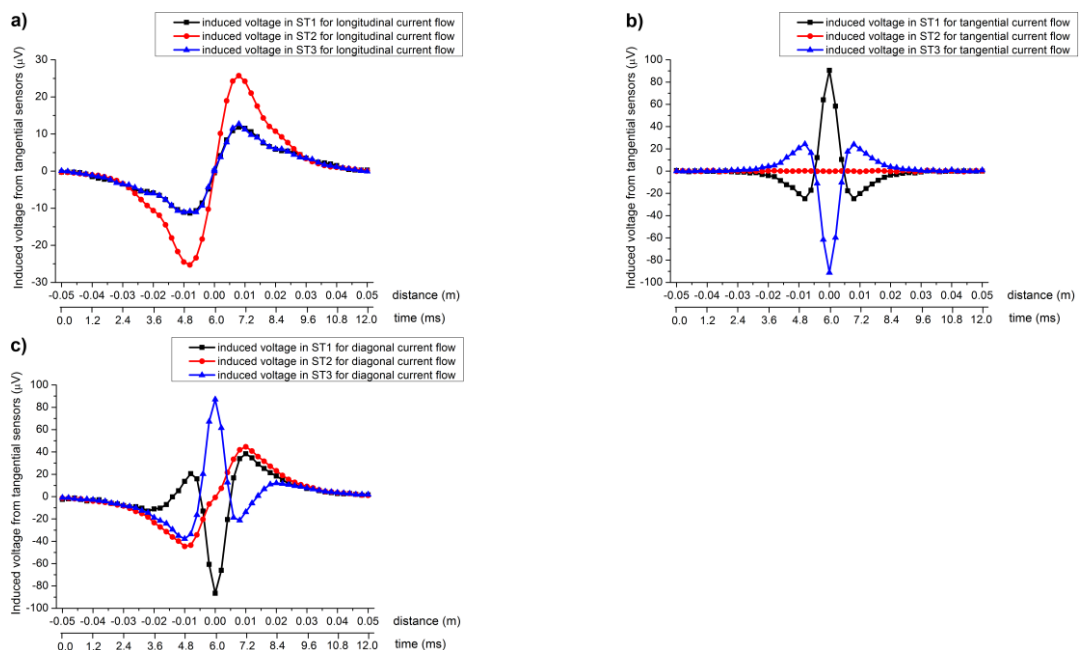

Fig. 5.54 Induced voltage signals from normal sensors SN1, SN2 and SN3 probed above rails with surface centre flaws energised: a) longitudinally, c) tangentially and e) diagonally at speed rate of 30km/h.

It can be seen in Fig. 5.54a that the output voltage signals from SN1 and SN3 coils inspecting the longitudinally energised rail comprised two peaks with approximate values of +/-24μV. The calculated SN2 voltage output had a form of fluctuation around zero level which was attributed to imperfections of FEM mesh.

The SN voltage signals presented in Fig. 5.54b for the case of tangentially energised rail exhibited signatures with dominant central peaks of -452.5μV from coil SN2 and -324.1μV from coils SN1 and SN3. The adjacent two smaller peaks had mean values of +128.5μV for coil SN2 and +95.4μV for coils SN1 and SN3.

Lastly, for the diagonally energised rail the calculated voltage signals from SN1 and SN3 coils revealed an asymmetric double peak profile with bi-polar amplitudes of -82μV and 163.1μV. The voltage waveform from SN2 coil exhibited dominant central peak of 301.9μV and two lower side peaks with values of -85μV.

Based on the above analysed profiles and strengths of induced voltages in SN sensors it was concluded that the rail inspection involving tangential current application would enable the highest probability of determining the presence of a transverse flaw from detected variations in normal component of MFL signals.

The calculated variations in flux linkage φ_l probed by the SL coils above flawed rails energised along longitudinal, tangential and diagonal directions are shown in Figs. 5.55a, 5.55c and 5.55e, respectively. The corresponding static distributions of differential variations in longitudinal field component $\Delta\mathbf{B_L}$ above these flawed rails are shown in Figs. 5.55b, 5.55d and 5.55f.

The signatures of φ_l signals detected by the SL sensors effectively indicated differences between the $\Delta\mathbf{B_L}$ distributions above the variously energised surface flawed rails.

In case of longitudinally energised rail the side sensors SL1 and SL3 detected a bi-polar flux linkage signals with peak amplitudes of approximately +/- 0.0165μWb, whereas the centre sensor SL2 determined negligible levels of φ_l signals due to symmetry in MFL perturbation (Figs. 5.55 and 5.55b). These calculated signals were consistent with those previously obtained by the ISU inspection unit, previously discussed in Section 5.4.2.
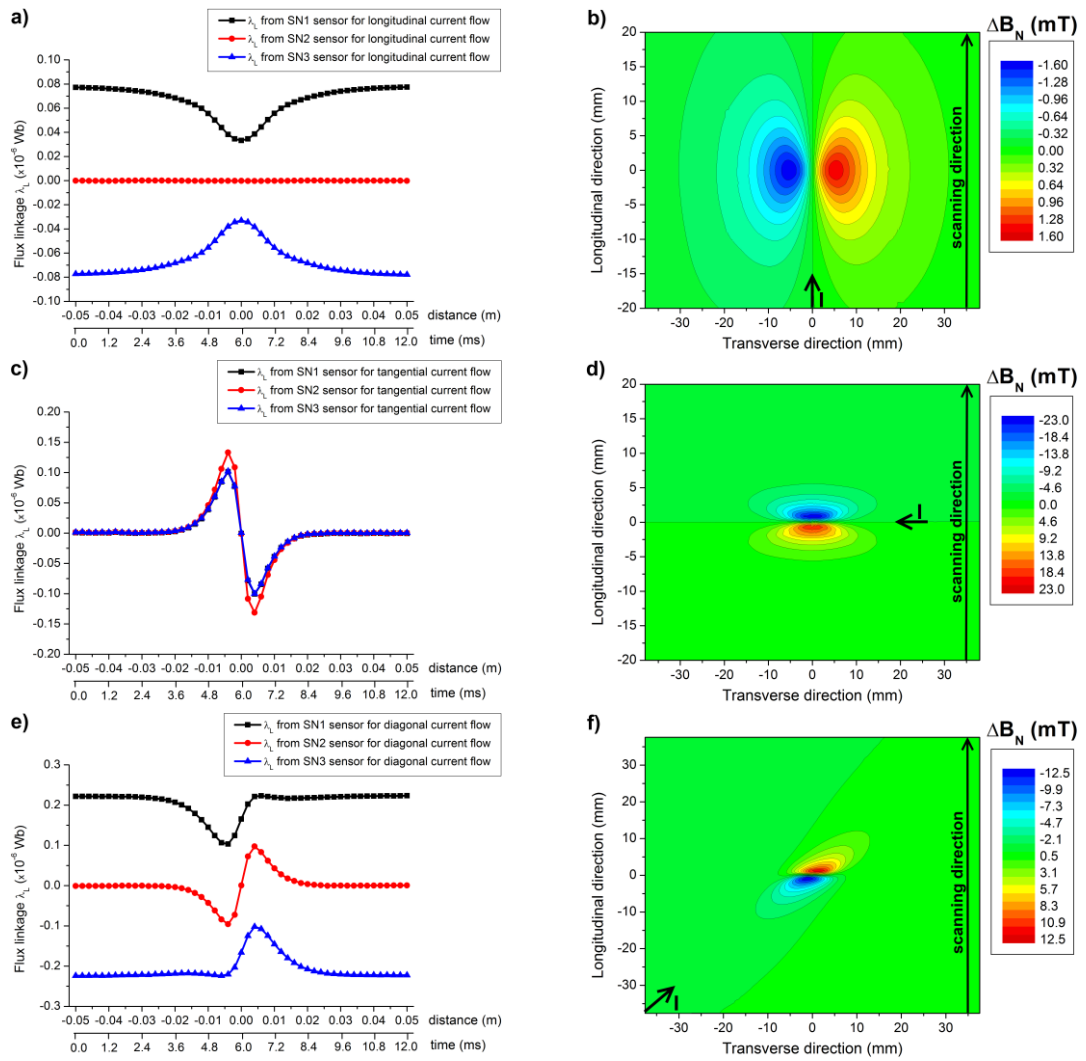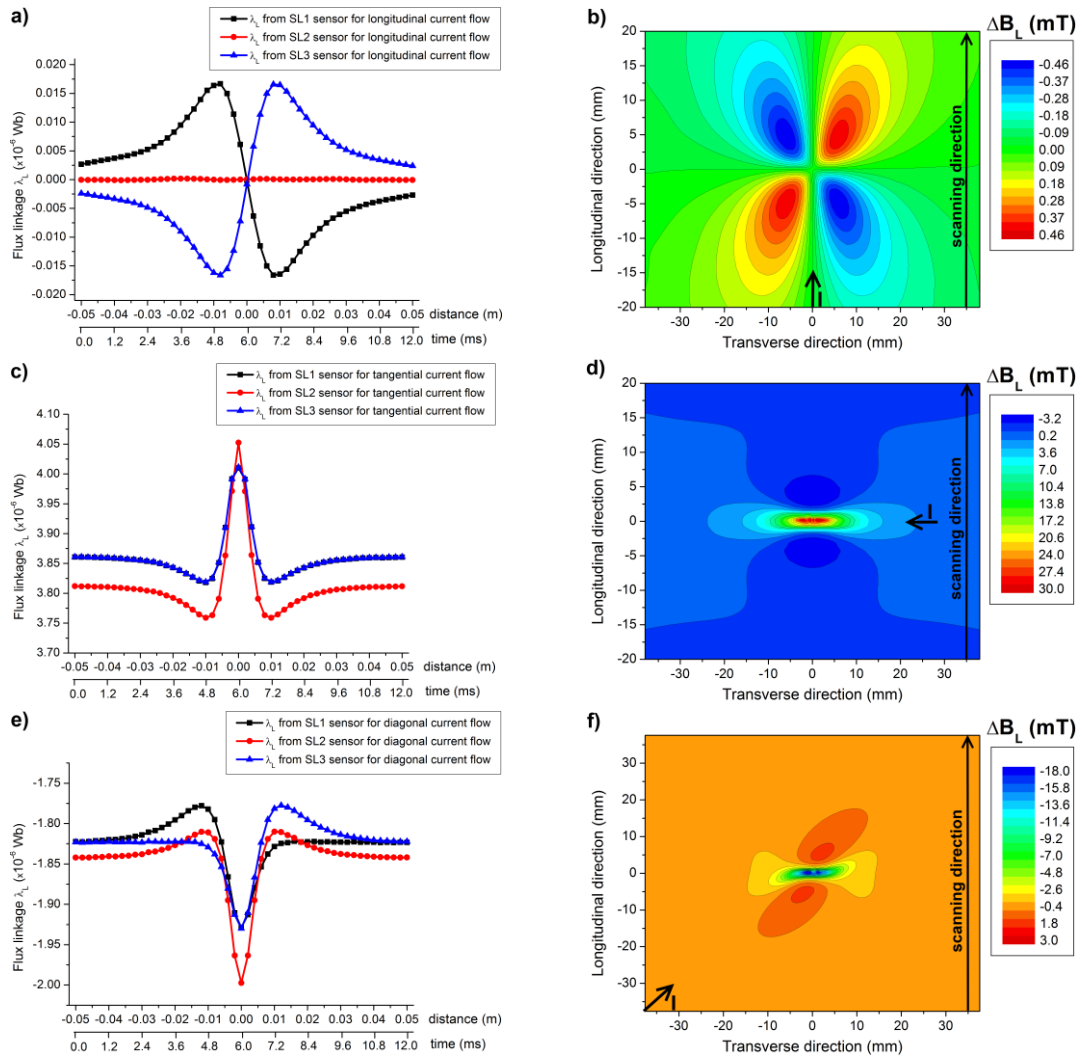
Fig. 5.55 Flux linkage signals from longitudinal sensors SL1, SL2 and SL3 probed above rails with surface centre flaws energised: a) longitudinally, c) tangentially and e) diagonally. Corresponding distributions of effective changes in longitudinal component ΔB_L obtained above rails with surface centre flaws energised: b) longitudinally, d) tangentially and f) diagonally.

In case of tangentially energised rail all three SL sensors probed similar flux linkage signals with dominant centre peak corresponding to local MFL maximum located above the mid-section of flaw, and two minor adjacent minima corresponding to regions above the front and rear of the flaw (Figs. 5.55c and 5.55d). The calculated values of major peaks had approximate values of 4.05μWb for centre SL2 sensor, and 4μWb for side SL1 and SL3 sensors; whereas their local probed MFL minima were equal to 3.76μWb from sensor SL2 and 3.82μWb from sensors SL1 and SL3. These values demonstrated that the scale of perturbation in longitudinal component of MFL above tangentially energised rail was more than six times higher than that detected above longitudinally energised rail (Fig. 5.55a).

Finally, in the case of diagonally energised rail the MFL signals detected by SL sensors exhibited both asymmetric and symmetric signatures (Fig. 5.55e). The symmetric signature of φ_l signal was obtained from the centre sensor SL2 and comprised dominant negative peak of -2µWb detected above flaw mid-section, and two adjacent local peaks of -1.8µWb probed at the front and rear of the flaw. Simultaneously, the side sensors SL1 and SL3 probed MFL signals of asymmetric signatures with major peaks of -1.93µWb above flaw centre, and minor peaks of -1.78µWb at the front (SL1) and rear (SL3) of the flaw. These calculated MFL profiles corresponded well with the previously determined differential distribution $\Delta\mathbf{B_L}$ presented in Fig. 5.55f. The effective scale of MFL perturbations probed by SL sensors above diagonally energised rail was relatively lower than that obtained for tangentially energised rail (Fig. 5.55c), but still more than four times higher than the one detected above rail carrying current along its longitudinal direction (Fig. 5.55a).

The dynamics of the flux linkage variations detected by the SL coils during the modelled inspections of variously energised flawed rails can be compared via analysis of their induced voltage outputs shown in in Figs. 5.56a, 5.56b and 5.56c.
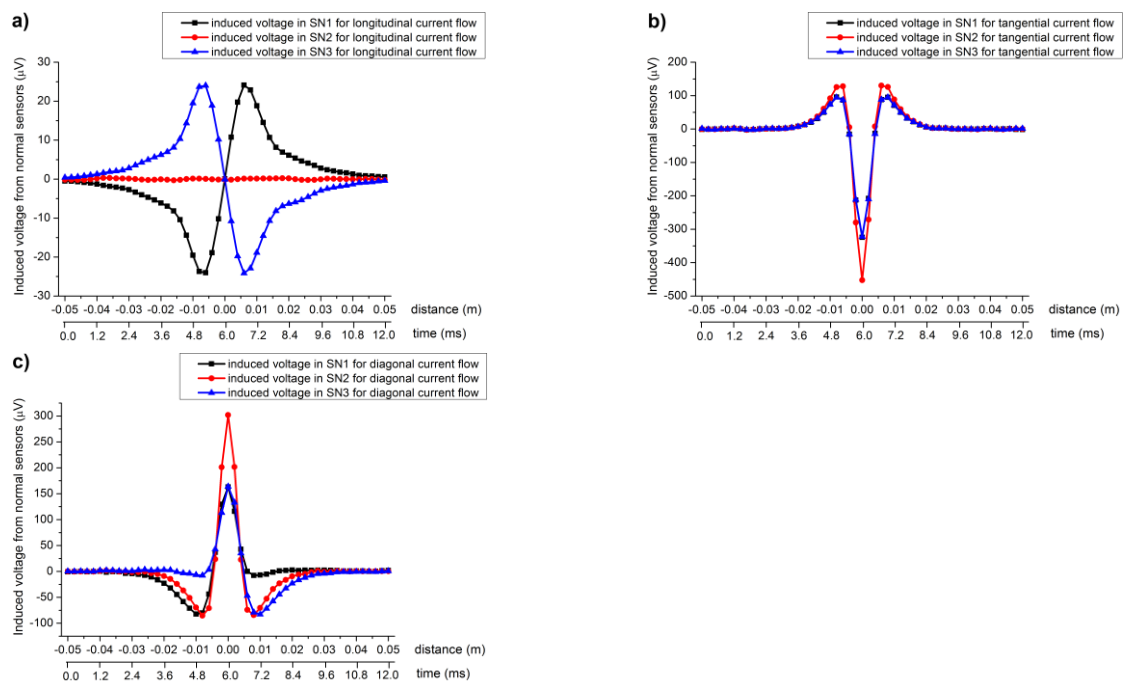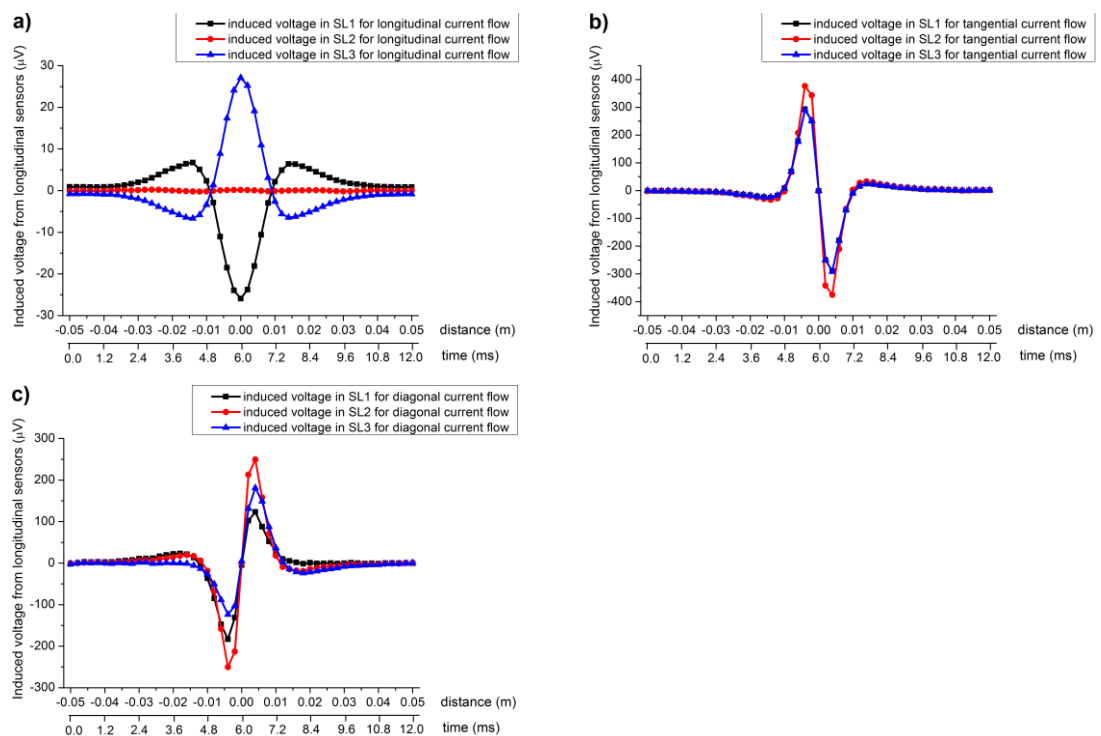

Fig. 5.56 Induced voltage signals from longitudinal sensors SL1, SL2 and SL3 probed above rails with surface centre flaws energised: a) longitudinally, c) tangentially and e) diagonally at speed rate of 30km/h.

It can be seen in Fig. 5.56a that the output voltage signals from sensors SL1 and SL3 inspecting the longitudinally energised rail comprised central dominant peaks with approximate values of +/-26µV and adjacent local minor peaks of approximately +/- 6.5 µV. The calculated SL2 voltage output had a form of minor fluctuations around zero level reflecting negligible changes in detected MFL signal.

The SL voltage signals presented in Fig. 5.56b for the case of tangentially energised rail exhibited symmetrical bi-polar signatures with approximate peak values of +/-375µV from centre SL2 sensor, and +/-291µV from the side sensors SL1 and SL3.

Subsequently, for the diagonally energised rail the calculated voltage signals from side SL1 and SL3 sensors revealed asymmetric double peak profiles with major amplitudes of +/-182µV and +/-123.5µV. The voltage waveform from the central SL2 sensor exhibited symmetrical bi-polar double-peak profile with approximate extrema of +/-250 µV.

The above presented voltage signals from SL sensors confirmed that the greatest spatial and time variations in longitudinal component of magnetic flux leakage were obtained in the rail inspection with tangential current application. Moreover a similar outcome was obtained for the previously analysed perturbations in normal component of stray magnetic flux. Distinctively, for the case of tangential component of MFL the detectable scale of perturbation was highest above the rail energised diagonally. Therefore by summarising the overall output from this comparative quantitative analysis it can be concluded that the most effective rail inspection should involve application of current in the tangential direction, which generates greatest flux leakage effect and consequently maximises the probability of transverse flaw detection.

5.5   Summary

- The analytical Equations 5.8 and 5.10 describing the generation of circulating magnetic field within and above current carrying rectangular conductor were derived. These mathematical expressions were subsequently used to calculate the values and attenuation of tangential and normal components of magnetic field **H** above a rail head conducting currents of different amplitudes.

- The flaw detection methodology of the Induction Sensing Unit currently used by Sperry Rail in rail inspection was characterised. Typical signatures of induced voltage signals indicating the presence of transverse flaws were calculated and presented.

- FEM rail models were developed in order to study the perturbation in magnetic field in vicinity of transverse flaws using numerical calculations.

- Distributions of tangential, normal and longitudinal components of the static magnetic field above unflawed and flawed rails were calculated. The obtained differential distributions revealed the effective changes in magnetic field profiles which were explained via the concept of a current re-routing mechanism. The comparative study of magnetic field perturbation above differently energised rails indicated the advantage of tangential and diagonal current application above the currently used longitudinal energisation.

- The dynamic flaw inspection method used in the Sperry Induction Sensing Unit was modelled. A good correspondence between calculated and measured signatures of sensed voltage signals was obtained. A correlation between modelled flaw induced field perturbation and probed signals was validated.

- The comparative analysis of dynamic flaw inspections involving different types of current application techniques was performed. This analysis confirmed that the most effective rail inspection involved application of current in the tangential direction, which generated the greatest flux leakage effect and consequently

maximised the probability of transverse flaw detection when using this particular method.

- The calculated levels of MFL signals justified the dependence of magnitude of flux leakage on the relative orientation of flaw with respect to magnetic field direction. The overall highest effective variations of flux leakage components were obtained for tangentially energised rail where the direction of local magnetic field was perpendicular to transverse flaw. In cases of diagonally and longitudinally energised rails the orientations of local magnetic fields at non-right angles to transverse flaws resulted in relatively lower MFL levels. The evaluated ranges of effective variations in MFL components probed above rail with surface centre transverse flaw, as well as corresponding peak levels of induced voltages from simulated dynamic inspections are summarised in Table 5.1.

	Effective variations in MFL components			Peak levels of induced voltage		
	tangential ΔB_T	normal ΔB_N	longitudinal ΔB_L	tangential sensors ST	normal sensors SN	longitudinal sensors SL
Tangential energisation	-2.3mT to +2.3mT	-19.4mT to +19.4mT	-3mT to +28.2mT	-91µV to +91µV	-452.5µV to +128.5µV	-375µV to +375µV
Diagonal energisation	-4mT to +2.5mT	-11.8mT to +11.8mT	-16mT to +1.9mT	-87µV to -87µV	-85µV to +301.9µV	-250 µV to +250 µV
Longitudinal energisation	-1.93mT to +0.2mT	-1.55mT to +1.55mT	-0.45mT to +0.45mT	-25.5µV to +25.5µV	-24µV to +24µV	-26µV to +26µV

Table 5.1 Comparison of the effective variations in MFL components and corresponding peak levels of induced voltages probed above rails with surface centre transverse flaw and energised tangentially, diagonally and longitudinally.

- Finally when considering the practical implementation of the tangential and diagonal current injection it must be noted that the geometries of electrodes would have to meet the constrained available spacing around the rail head at the railway level crossings. A potential solution to this limitation would require lifting the electrodes when inspecting these particular sections of rails.

6.   Conclusions and future work

6.1 Evaluation of stress using Magnetic Barkhausen Noise method

A new model describing dependence of magnetic Barkhausen noise peak amplitude on stress has been developed. This model predicted a linear relation between reciprocal of the peak Barkhausen noise MBN_{pk} and stress σ for ferromagnetic materials in which magnetostriction is relatively insensitive to stress. Moreover, it was shown that after incorporating the stress dependence of magnetostriction coefficients b and b' the proposed model could be further applied to describe the stress effects on MBN_{pk} in a wide variety of stress-sensitive magnetostrictive materials.

The anticipated linear behaviour of $1/ MBN_{pk}$ with stress based on the model was validated by experimental results obtained for carburised SAE9310 and nitrided SAE6481 samples. The analogous magnetoelastic effect of both applied stress and long range Type I residual macro-stress on MBN emissions in SAE9310 steel was justified. Significantly the model predictions were validated for materials with both positive and negative magnetostrictions. The generality of the proposed model was additionally confirmed by its successful application in the quantitative stress evaluation using Barkhausen emissions in other types of steel, such as pipeline and EN36 steels [91, 121, 122] and also in the recent results of other investigators for RAEX400, EN10084 and ASTM A36 steels [123, 124, 125].

It was discussed in Chapters 3 and 4 that both stress and microstructure influence the pinning of domain walls, and therefore the magnetostriction and Barkhausen noise in ferromagnetic materials. In order to further investigate the applicability of the MBN stress model a range of differently heat treated steels of various compositions could be studied providing a comprehensive set of information on the link between magnetic and mechanical properties. It would be beneficial to study the influence of various types and distributions of pinning sites, which can be altered by varying carbon content or/and alloy composition, on the dynamics of domain processes and consequently stress sensitivity of both magnetostriction and Barkhausen emissions in

different types of industrial steels. This kind of study would involve simultaneous magnetostriction, hysteresis and Barkhausen measurements of steel samples with known microstructure, hardness and under controlled stress. The results of such a study would allow a group of steels to be distinguished with magnetostriction relatively insensitive to stress, for which dependence of $1/\chi'_{Hc}$ and $1/MBN_{pk}$ on stress can be successfully evaluated using a linear function, and a group of materials of stress-sensitive magnetostriction for which additional stress dependence of coefficients b and b' has to be taken into account. The results of such study would provide basis for establishing a standard methodology, involving the developed MBN model, for stress evaluation using Magnetic Barkhausen Noise.

A new comprehensive method has been developed for determining depth profiles of properties such as residual stress using Magnetic Barkhausen Noise measurements. The developed underlying equations involve knowledge of the stress dependence of MBN amplitude and in addition knowledge of the attenuation of the original MBN signal. The proposed methodology shows how to mathematically extract the Barkhausen emissions and related stress information from different points of origin using some simplifying assumptions.

The research work on the practical implementation of developed stress depth-profiling method is currently being continued by a PhD candidate Orpheus Kypris at Iowa State University under supervision of professor David Jiles and in collaboration with AgustaWestland. The latest progress in this matter is reported in their recent publications [126,127,128]. The primary remaining challenge is the experimental validation of proposed mathematical and measurement methodologies. The supporting research would require preparation and evaluation of samples subjected to various levels of surface machining, such as grinding, turning or/and shot-peening, which exhibit different stress-depth profiles with no significant microstructural variation. The complementary methods for sample characterisation would involve X-ray diffraction for quantitative residual stress measurement and optical microscopy for microstructure examination. The MBN measurement system and procedure for application of the developed equations was proposed in Section 4.7. This procedure can be used for determining the variation of stress with depth in magnetic materials with the information being extracted from the frequency dependence of the detected

Barkhausen signals. The positive outcome of this affirmative research is required to further support this new Magnetic Barkhausen Noise method in gaining acceptance as a viable non-destructive stress depth-profiling tool.

6.2 Magnetic Flux Leakage method in detection of transverse flaws in rail structure

Distributions of magnetic field and magnetic flux leakage in the vicinity of flawed and unflawed current carrying rails were analysed via analytical and numerical calculations. This analysis involved derivation of mathematical expressions describing the generation of circulating magnetic field, characterisation of the flaw detection methodology of Induction Sensing Unit currently applied by Sperry Rail in the rail inspection, as well as development of FEM rail models for calculations of the perturbation in magnetic field in the vicinity of transverse flaws. The obtained differential distributions revealed the effective changes in magnetic field profiles which were explained via the concept of current re-routing mechanism. The comparative study of magnetic field perturbation above differently energised rails indicated the advantage of tangential and diagonal current application above the currently used longitudinal energisation. The dynamic flaw inspection with application of Sperry Induction Sensing Unit was also modelled. A good agreement between calculated and real signatures of sensed voltage signals was obtained. Moreover, a correlation between modelled flaw induced static field perturbation and probed signals was validated. The final comparative analysis of dynamic flaw inspections involving different current application techniques confirmed that the most effective rail inspection would involve application of current in a tangential direction, as it generated greatest flux leakage and would consequently maximise the probability of detection of a transverse flaw.

After identification of the optimal current application technique for MFL transverse flaw detection the future work should focus on development of the new complementary sensing unit. This work would therefore involve selection of the most suitable commercially available type of sensor, which are typically based on magnetic induction, Hall or magneto-resistive effects, as well as determining the most advantageous sensor configuration enabling optimum detection of flaw related MFL perturbation. In the initial development stage the sensing unit can be designed with help of numerical analysis, such as Finite Element Modelling, followed by experimental validation in the actual rail transverse flaw inspection.

In terms of practical implementation of the tangential and diagonal current injection, the geometries of electrodes should be designed with consideration of the constrained spacing around the rail head at the railway level crossings. Furthermore, the effects of mechanical factors, such as residual stress and rail deformation due to rolling contact fatigue, on the current distribution and MFL signals should be modelled and investigated. Finally, the analysis of the MFL signals in the dynamic rail inspection with current injection should be supported by the FEM transient analysis of induced eddy currents in rail. This would allow evaluation of the effect of inspection speed and time varying electromagnetic fields on the sensitivity and effectiveness of transverse flaw detection.

Bibliography

[1]   B. Cullity and C. Graham, "Introduction to magnetic material," John Wiley & Sons, 2008.

[2]   P. Weiss, "L'hypoth`ese du champ mol´eculaire et la propriet´e ferromagnetique". Journal de Physique, vol. 6, pp. 661–690, 1907.

[3]   E.S. Gorkunov, Yu.N. Dragoshansky, "Interaction between domain walls and structural defects as a background for magnetic inspection of steel structures", Proceedings of the 15th World Conference on Nondestructive Testing, Roma, Italy, 2000.

[4]   P. Curie, "Lois expérimentales du magnétisme. Propriétés magnétiques des corps à diverses temperatures", The Annual Review of Physical Chemistry, vol. 5, pp. 289-405, 1895.

[5]   D.C. Jiles, "Introduction to magnetism and magnetic materials", Second Edition, Chapman and Hall, 1998.

[6]   L. Landau and E. Lifshitz, "On the theory of the dispersion of magnetic permeability in ferromagnetic bodies", Die Physikalische Zeitschrift der Sowjetunion, vol. 8, pp. 153–169 , 1935.

[7]   F. Bloch, "Zur Theorie des Austauschproblems und der Remanenzerscheinung der Ferromagnetika", Zeitschrift für Physik, vol. 74, Issue 5-6, pp. 295-335, 1932.

[8]   J. A. Ewing, "Contributions to the molecular theory of induced magnetism", Philosophical Magazine, vol. 5, pp. 205-222, 1890.

[9]   D.C. Jiles and D. Atherton, "Ferromagnetic hysteresis", IEEE Transactions on Magnetics, vol. MAG19(5), pp. 2183-2185, 1983.

[10]   D.C. Jiles, "Theory of the magnetomechanical effect", Journal of Physics D-Applied Physics, vol. 17, pp. 1265-1281, 1995.

[11]   M. J. Sablik, H. Kwun, G. L. Burkhardt and D. C. Jiles, "Model for the effect of tensile and compressive stress on ferromagnetic hysteresis", Journal of Applied Physics, vol. 61, pp. 3799-3801, 1987.

[12]   P. Garikepati, T. T. Chang and D. C. Jiles, "Theory of Ferromagnetic Hysteresis: Evaluation of Stress from Hysteresis Curves", IEEE Transactions on Magnetics, vol. 24, pp. 2922-2924, 1988.

[13]   J. M. Makar and D. L. Atherton, "Effects of Stress on the Magnetostriction of 2% Mn
Pipeline Steel", IEEE Transactions on Magnetics, vol. 30, pp. 1388-1394, 1994.

[14]   B. E. Lorenz and C. D. Graham, "Magnetostriction versus magnetization of Hiperco 50 from 20°C to 700°C", IEEE Transactions on Magnetics, vol. 42, pp. 3886-3888, 2006.

[15]   Thu Trang Nguyen, F. Bouillault, L. Daniel, and X. Mininge, "Finite element modeling of magnetic field sensors based on nonlinear magnetoelectric effect", Journal of Applied Physics, vol. 109, 2011.

[16]   N. Galopin, X. Mininger, F. Bouillault and L. Daniel, "Finite element modeling of magnetoelectric sensors", IEEE Transactions on Magnetics, vol. 44, pp. 834-837, 2008.

[17]   H. Barkhausen,"Gerausche bien ummagnetisieren von eisen", Physikalishe Zeitschr, vol. 20, pp. 401-403, 1919.

[18]   Tsang, Ching H., "The origin of Barkhausen noise in small permalloy magnetoresistive sensors", Journal of Applied Physics, vol. 52, pp.2465-2467, 1981.

[19]   l. Neel, "Effet des cavités et des inclusions sur le champ coercitif", Cah. Phys., vol. 25, pp. 21-44, 1944.

[20]   H. Föll, "Defects in crystals", University of Kiel, 2006.

[21]   M. Blaow, J. T. Evans, B. A. Shaw , "Surface decarburisation of steel detected by magnetic Barkhausen emission", Journal of Materials Science, vol. 40, pp. 5517-5520, 2005.

[22]   B. Alessandro, C. Beatrice, G. Bertotti, and A. Montorsi, "Domain wall dynamics and Barkhausen effect in metallic ferromagnetic materials", Journal of Applied Physics, vol. 68, pp. 2908-2915, 1990.

[23]   D. C. Jiles, L. B. Sipahi, and G. Williams, "Modeling of micromagnetic Barkhausen activity using a stochastic process extension to the theory of hysteresis", Journal of Applied Physics, vol. 73, pp. 5830-5832, 1993.

[24]   S. J. Lee, B. Zhu, C. C. H. Lo, D. M. Clatterbuck, and D. C. Jiles, "Application of Non-Linear Barkhausen Model Incorporating Anhysteretic Susceptibility to Annealed Low Carbon Fe Sample", IEEE Transactions on Magnetics, vol. 37, pp. 2340-2342, 2001.

[25]   J. Reddy, "An Introduction to the Finite Element Method", McGraw-Hill Education, 2005.

[26]   R. Fitzpatrick, "Maxwell's Equations and the Principles of Electromagnetism", Infinity Science Press, 2008.

[27]   http://www.infolytica.com/en%5Cproducts/magnet/

[28]   C. A. Brebbia, "Structural integrity and passenger safety", WIT Press, 2000.

[29]   I. Milne, R. O. Ritchie, B.L. Karihaloo, "Comprehensive structural integrity", Newnes, 2003.

[30]   L. E. Steele, K. E. Stahlkopf, "Assuring structural integrity of steel reactor pressure vessels", Applied Science Publishers, 1980.

[31]   American Society for Metals (ASM) Handbook, vol. 1, "Properties and Selection: Irons steels and high performance alloys", ASM International, 1988.

[32]   J. D. Verhoeven, "Steel metallurgy for the non-metallurgist", ASM International, 2007.

[33] American Society for Metals (ASM) Handbook, vol. 4, "Heat treating", ASM International, 1991.

[34] P. J. Withers and H. K. D. H. Bhadeshia, "Residual Stress, Part 1 – Measurement Techniques", Materials Science and Technology, vol. 17, pp. 355-365, 2001.

[35] American Society for Metals (ASM), "Handbook of Residual Stress and Deformation of Steel", ASM International, 2002.

[36] W. Cui, "A state-of-the-art review on fatigue life prediction methods for metal structures", Journal of Marine Science and Technology, vol. 7, issue 1, pp. 43-56, 2002.

[37] D. C. Jiles, "Introduction to the principles of materials evaluation", CRC Press, 2007.

[38] Federal Railroad Administration, "Track inspector rail defect reference manual", First Edition, 2011.

[39] S. Kumar, "Study of rail breaks: Associated Risks and Maintenance Strategies", Lulea Railway Research Centre, 2007.

[40] R. M. Havira, "Detection of transverse defects under surface anomalies", Proceedings of the AREMA2009 Conference and Exposition, 2009.

[41] A. S. Birks and R. E. Green, "Handbook of nondestructive testing: ultrasonic testing", vol. 7, ASNT, 1991.

[42] J. Blitz and G. Simpson, "Ultrasonic methods for nondestructive testing", Chapman and Hall, 1995.

[43] M. G. Silk, "Ultrasonic transducers for nondestructive evaluation", Adam Hilger, 1984.

[44] W. S. Burkle and V. H. Isom, "Use of DAC curves and transfer lines to maintain ultrasonic test references level sensitivity", Materials Evaluation, vol. 41, pp.624-628, 1983.

[45]   B. Raj, T. Jayakumar and M. Thavasimuthu, "Practical non-destructive testing", Second Edition, Woodhead Publishing Ltd, 2002.

[46]   J. G. Martin, J. Gomez-Gil and E. Vazquez-Sanchez, "Non-destructive techniques based on eddy current testing", Sensors, vol. 11, pp. 2525-2565, 2011.

[47]   S. Qaimi, "The railway track manual", Second Edition, ThyssenKrupp Gft GleisTechnik, 2010.

[48]   W. Ricken, H. C. Schoenekess and W. J. Becker, "Improved multi-sensor for force measurement of pre-stressed steel cables by means of the eddy current technique", Sensors and Actuators A, vol. 129, pp. 80-85, 2006.

[49]   I. C. Noyan and J. B. Cohen, "Residual Stress Measurement by Diffraction and Interpretation", Springer-Verlag, 1987.

[50]   P. S. Prevey, "Metals Handbook", Ninth Edition, vol. 10, pp. 380-392, ASM International, 1986.

[51]   P. S. Prevey, "Current applications of x-ray diffraction residual stress measurement", Developments in Materials Characterization Technologies, pp. 103-110, ASM International, 1996.

[52]   T.M. Morton, R.M. Harrington and J.G. Bjeletich, "Acoustic Emission of fatigue crack growth", Engineering Fracture Mechanics, vol. 5, pp. 691-697, 1973.

[53]   A. E. Wehrmeister, "Weld Monitoring with Acoustic Emission", The Journal of The Minerals, Metals & Materials Society, vol. 30, issue 12, pp. 28-30, 1978.

[54]   S. Hewerdine, "Plant Integrity Assessment by Acoustic Emission Testing", Second Edition, Rugby, UK, 1993.

[55]   V. Leelalerkiet, T. Shimizu, Y. Tomoda and M. Ohtsu, "Estimation of corrosion in reinforced concrete by electrochemical techniques and acoustic emission", Journal of Advanced Concrete Technology, vol. 3, pp. 137-147, 2005.

[56]   N. N. Zatsepin and V. E. Shcherbinin, "Calculation of the magnetostatic field of surface defects", Defectoskopiya, vol. 5, pp. 50-65, 1966.

[57] C. R. Edwards and S. B. Palmer, "The magnetic leakage field of surface-breaking cracks", Journal of Physics D, Applied Physics vol. 19, pp. 657-673, 1986.

[58] M. Abe, S. Biwa and E. Matsumoto, "Three dimensional evaluation of parallel-piped flaw using amorphous MI sensor and neural network in biaxial MFLT", Proceedings of 3rd International Conference on Sensing Technology, pp.238-241, 2008.

[59] K. Mandal and D. L. Atherton, "A study of magnetic flux-leakage signals", Journal of Physics D, Applied Physics, vol. 31, pp. 3211–3217, 1998.

[60] H. Zuoying, Q. Peiwen and C. Liang, "3D FEM analysis in magnetic flux leakage method", NDT&E International, vol. 39, pp. 61–66, 2006.

[61] D. Zhiye, R. Jiangjun, P. Ying, Y. Shifeng, Z. Yu, G. Yan and L. Tianwei, "3-D FEM simulation of velocity effects on magnetic flux leakage testing signals", IEEE Transactions on Magnetics, vol. 44, pp. 1642-1645, 2008.

[62] A. G. Antipova and A. A. Markovb, "Evaluation of Transverse Cracks Detection Depth
in MFL Rail NDT", Russian Journal of Nondestructive Testing, Vol. 50, pp. 481–490, 2014.

[63] J. Wu, Y. Sun, Y. Kang and Y. Yang, "Theoretical Analyses of MFL Signal Affected by Discontinuity Orientation and Sensor-Scanning Direction", IEEE Transactions on Magnetics, vol. 51, article no 6200207, 2015.

[64] D. C. Jiles and D. L. Atherton, "Theory of the magnetisation process in ferromagnets and its application to the magnetomechanical effect", Journal of Physics D, Applied Physics, vol. 17, pp. 1265-1281, 1984.

[65] M. J. Sablik and B. Augustyniak, "The effect of mechanical stress on Barkhausen Noise signal integrated across a cycle of ramped magnetic field", Journal of Applied Physics, vol. 79, pp. 963-972, 1996.

[66] M. J. Sablik, H. Kwun, G. L. Burkhardt, D. C. Jiles, "Model for the effect of tensile and compressive stress on ferromagnetic hysteresis", Journal of Applied Physics, vol. 61, pp. 3799-3801, 1987.

[67] R. Langman, "Magnetic properties of mild steel under conditions of biaxial stress", IEEE Transactions on Magnetics, vol. 26, pp. 1246-1251, 1990.

[68] J. M. Makar and B. K. Tanner, "The effect of stresses approaching and exceeding the yield point on the magnetic properties of high strength pearlitic steels", NDT&E International, vol. 31, pp. 117–127, 1998.

[69] J. M. Makar and B. K. Tanner, "The in situ measurement of the effect of plastic deformation on the magnetic properties of steel, Part I – Hysteresis loops and magnetostriction", Journal of Magnetism and Magnetic Materials, vol. 184, pp. 193-208, 1998

[70] L. Vandenbossche, "Magnetic hysteretic characterization of ferromagnetic materials with objectives towards non-destructive evaluation of material degradation", PhD Dissertation, Ghent University, 2009.

[71] D. C. Jiles, "The effect of stress on magnetic Barkhausen activity in ferromagnetic steels", IEEE Transactions on Magnetics, vol. 25, pp. 3455-3457, 1989.

[72] D. C. Jiles, T. T. Chang, D. R. Hougen, and R. Ranjan, "Stress induced changes in the magnetic properties of some nickel-copper and nickel-cobalt alloys", Journal of Applied Physics, vol. 64, pp. 3620.-3628, 1988.

[73] C. C. H. Lo, S. J. Lee, L. Li, L. C. Kerdus, and D. C. Jiles, "Modeling stress effects on magnetic hysteresis and Barkhausen emission using a hysteretic–stochastic model", IEEE Transactions on Magnetics, vol. 38, pp. 2418-2420, 2002.

[74] C. C. H. Lo, E. Kinser and D. C. Jiles, "Modelling the interrelating effects of plastic deformation and stress on magnetic properties of materials", Journal of Applied Physics, vol. 93, pp. 6626-6628, 2003.

[75] M. J. Sablik and D. C. Jiles, "Coupled magnetoelastic theory of magnetic and magnetostrictive Hysteresis", IEEE Transactions on Magnetics, vol. 29, pp. 2113-2123, 1993.

[76] Y. Melikhov, D. C. Jiles, I. Tomás, C. C. H. Lo, O. Perevertov and J. Kadlecová, "Investigation of sensitivity of Preisach analysis for nondestructive testing", IEEE Transactions on Magnetics, vol. 37, pp. 3907-3912, 2001.

[77] A. Ktena and E. Hristoforou, "Stress dependent magnetization and vector Preisach modelling in low carbon steels", IEEE Transactions on Magnetics, vol. 48, pp. 1433-1436, 2012.

[78] E. S. Gorkunov, Y. N. Dragoshanskii and V. A. Khamitov, "Magnetoelastic acoustic emission in ferromagnetic materials II. Effect of elastic and plastic strains on parameters of magnetoelastic acoustic emission", Russian Journal of Nondestructive testing, vol. 37, pp. 835-858, 2001.

[79] C. H. Kim, C. G. Kim, "Effect of magnetising frequency and stress on magneto-acoustic emission from 3% Si-Fe crystals", Journal of Physics D, Applied Physics, vol. 22, pp. 192-198, 1989.

[80] R. Ranjan, D. C. Jiles, P. K. Rastogi, "Magnetic properties of decarburized steels: An investigation of the effects of grain size and carbon content", IEEE Transactions on Magnetics, MAG23 (3), pp. 1869-1876, 1987.

[81] C. Edwards and S.B. Palmer, "The Effect of Stress and Sample Shape on the Magnitude and Frequency of Magnetomechanical Acoustic Emission", Journal of the Acoustic Society of America, vol. 82, pp. 534-544, 1987.

[82] W.A. Theiner and H.H. Willems, "Determination of Microstructural Parameters by Magnetic and Ultrasonic Quantitative NDE", Nondestructive Methods for Materials Property Determination, pp. 249-258, Plenum Press, 1984.

[83] J. W. Wilson, G. Y. Tian, V. Moorthy, B. A. Shaw, "Magneto-acoustic emission and Magnetic Barkhausen emission for case depth measurement in En36 gear steel", IEEE Transactions on Magnetics, vol. 45 , pp. 177-183, 2009.

[84]   D. J. Griffiths, "Introduction to Electrodynamics", Third Edition, Addison Wesley, 1998.

[85]   S. Tumanski, "Induction coil sensors—a review", Measurement Science and Technology, vol. 18, pp. 31-46, 2007.

[86]   W. A. Fuller, "Introduction to Statistical Time Series", Second Edition, John Wiley&Sons, 1996.

[87]   A. Savitzky, M. Golay, "Smoothing and Differentiation of Data by Simplified Least Squares Procedures", Analytical Chemistry, vol. 36, pp. 1627–1639, 1964.

[88]   M. Kutz, "Handbook of materials selection", John Wiley&Sons, 2002.

[89]   X. Kleber and P. Barroso, "Investigation of shot-peened austenitic stainless steel 304L by means of magnetic Barkhausen noise", Materials Science and Engineering A, vol. 527, pp. 6046–6052, 2010.

[90]   C. H. Gür and I. Cam, "Comparison of magnetic Barkhausen noise and ultrasonic velocity measurements for microstructure evaluation of SAE 1040 and SAE 4140 steels", Materials Characterization, vol. 58, pp. 447–454, 2007.

[91]   V. Moorthy, B. A. Shaw and S, Day, "Evaluation of applied and residual stresses in case-carburised En36 steel subjected to bending using the magnetic Barkhausen emission technique", Acta Materialia, vol. 52, pp. 1927-1936, 2004.

[92]   M. Kuruzar and B. Cullity, "The magnetostriction of iron under tensile and compressive stress", International Journal on Magnetism, vol. 1, pp. 323-325, 1971.

[93]   R. Bozorth, "Ferromagnetism", D. Van Nostrand, 1951.

[94]   C. C. H. Lo, "Nondestructive evaluation of residual stresses in case hardened steels by magnetic anisotropy measurements", AIP Conference Proceedings, vol. 1430, pp. 1445-1451, 2012.

[95]   R.W. Leep, "The Barkhausen effect and its application in nondestructive testing", Proceedings of the Symposium on Physics and Nondestructive Testing, Gordon and Breach, pp. 439-453, 1967.

[96]   R. L. Pasley, "Barkhausen effect: An indication of stress", Materials Evaluation, vol.28, pp. 157-161, 1970.

[97]   S. Titto, "On the Mechanism of Magnetism Transitions in Steel", IEEE Transactions on Magnetics, vol. 14, pp. 527-529, 1978.

[98]   V. Moorthy , B. A. Shaw , P. Mountford and P. Hopkins, "Magnetic Barkhausen emission technique for evaluation of residual stress alteration by grinding in case-carburised En36 steel", Acta Materialia, vol. 53, pp. 4997–5006, 2005.

[99]   I. Altpeter, G. Dobmann, M. Kroning, M. Rabung and S. Szielasko, "Micro-magnetic evaluation of micro-residual stresses of the IInd and IIIrd order", NDT&E International, vol. 42, pp. 283–290, 2009.

[100] G. Dobmann, "Physical basics and industrial applications of 3MA – micromagnetic multiparameter microstructure and stress analysis", Proceedings of the 10th European Conference on Non-Destructive Testing, 2010.

[101] X. Kleber and A. Vincent, "On the role of residual internal stresses and dislocations on Barkhausen noise in plastically deformed steel", NDT&E International, vol. 37, pp. 439–445, 2004.

[102] S. F. Silva Jr. and T. R. Mansur, "Determining residual stresses in ferromagnetic materials by Barkhausen noise measurement", Proceedings of 15th World Conference on Nondestructive Testing, 2000.

[103] H. I. Yelbay, I. Cam and C. H. Gür, "Non-destructive determination of residual stress state in steel weldments by Magnetic Barkhausen Noise technique", NDT&E International, vol. 43, pp. 29–33, 2010.

[104] A. Mitra and D. C. Jiles, "Effects of tensile stress on the Magnetic Barkhausen Effect in 2605 CO amorphous alloy", IEEE Transactions on Magnetics, vol. 31, pp. 4020-4022, 1995.

[105] K. Mandal, A. Corey, M. E. Loukas, P. Weyman, J. Eichenberger and D. L. Atherton, "The effects of defect depth and bending stress on magnetic Barkhausen noise and flux-leakage signals", Journal of Physics D, Applied Physics, vol. 30, pp. 1976-1983, 1997.

[106] J. Gauthier, T. W. Krause and D. L. Atherton, "Measurement of residual stress in steel using the magnetic Barkhausen noise technique", NDT&E International, vol. 31, pp. 23–31, 1998.

[107] P. Wang, Y. Gao , Y. Yang , G. Tian , E. Yao and H. Wang, "Experimental studies and new feature extractions of MBN for stress measurement on rail tracks", IEEE Transactions on Magnetics, vol. 49 , pp. 4858-4864, 2013

[108] J. Thomas, J. Mohan, S. Kendrish and R. Fix, "Advanced techniques for the measure of microstructure and residual stress in components subject to rolling fatigue", SAE International Journal of Materials Manufacturing, vol. 2, pp. 206-210, 2009.

[109] H. Nishihara, S. Taniguchi, H. Maeda, I. Oguro, M. Harada, T. Ogino, S. Matsumoto, Y. Shindo and N. Ohtsuka, "The effect of mechanical stress on Barkhausen noises from heat-treated nickel plates", Proceedings of the 12th Asia-Pacific Conference on NDT, 2006.

[110] D. C. Jiles, "Magnetic properties and microstructure of AISI 1000 series carbon steels", Journal of Applied Physics, vol. 21, pp. 1186-1195, 1988.

[111] T. Yamasaki, S. Yamamoto and M. Hirao, "Effect of applied stresses on magnetostriction of low carbon steel", NDT&E International, vol. 29, pp. 263–268, 1996.

[112] American Standard, SAE AMS 6260R, 2012.

[113] American Standard, SAE AMS 6481C, 2012.

[114] http://www.lakeshore.com/products/hall-probes/transverse-probes/pages/Specifications.aspx

[115] http://www.omega.co.uk/index.html

[116] http://www.stresstechgroup.com/content/en/1034/1154/Rollscan%20300%20with%20MicroScan%20600%20software.html#

[117] http://www.analog.com/en/all-operational-amplifiers-op-amps/operational-amplifiers-op-amps/ad797/products/product.html

[118] http://www.instron.co.uk/wa/product/8801-Floor-Model-Fatigue-Systems.aspx

[119] L. Mierczak, D. C. Jiles and G. Fantoni, "A New Method for Evaluation of Mechanical Stress Using the Reciprocal Amplitude of Magnetic Barkhausen Noise", IEEE Transactions on Magnetics, vol. 47, pp. 459-465, 2011.

[120] L. Mierczak, D. C. Jiles, G. Fantoni and L. Merletti, "System and Method for Determining Stress of a Component Made of Magnetizable Material", World Intellectual Property Organization Patent WO/2011/144998, 2011.

[121] C. Jagadish, L. Clapham and D. L. Atherton, "The Influence of Stress on Surface Barkhausen Noise Generation in Pipeline Steels", IEEE Transactions on Magnetics, vol. 25, pp. 3452-3454, 1989.

[122] V. Moorthy, B. A. Shaw, P. Mountford and P. Hopkins, "Magnetic Barkhausen emission technique for evaluation of residual stress alteration by grinding in case-carburised En36 steel", Acta Materialia, vol. 53, pp. 4997-5006, 2005.

[123] S. Santa-aho, "Barkhausen Noise Method for Hardened Steel Surface Characterization – The Effect of Heat Treatments, Thermal Damages and Stresses", DSc Thesis, Tampere University of Technology, 2012.

[124] S. Santa-aho, M. Vippola, T. Saarinen, M. Isakov, A. Sorsa, M. Lindgren, K. Leiviskä and T. Lepistö, "Barkhausen noise characterisation during elastic bending and tensile-compression loading of case-hardened and tempered samples", Journal of Materials Science, vol. 47, pp. 6420-6428, 2012.

[125] O. Kypris, I. C. Nlebedim and D. C. Jiles, "Experimental Verification of the Linear Relationship between Stress and the Reciprocal of the Peak Barkhausen Voltage

in ASTM A36 Steel", IEEE Transactions on Magnetics, vol. 49, pp. 4148-4151, 2013.

[126] O. Kypris, I. C. Nlebedim and D. C. Jiles, "Mapping Stress as a Function of Depth at the Surface of Steel Structures Using a Frequency Dependent Magnetic Barkhausen Noise Technique", IEEE Transactions on Magnetics, vol. 48, pp. 4428-4431, 2012.

[127] O. Kypris, I. C. Nlebedim and D. C. Jiles, "A model for the Barkhausen frequency spectrum as a function of applied stress", Journal of Applied Physics, vol. 115, issue 8, 2014.

[128] O. Kypris, I. C. Nlebedim and D. C. Jiles, "Barkhausen spectroscopy: Non-destructive characterization of magnetic materials as a function of depth", Journal of Applied Physics, vol. 115, issue 17, 2014.

List of publications and conference presentations

[1]   L. Mierczak, Y. Melikhov, D. C. Jiles, "Detection of Damage in Ground Steel Components using Magnetic Barkhausen Noise Technique", conference digest presented at 11th International Magnetics Conference, Washington DC, US, 2010.

[2]   L. Mierczak, Y. Melikhov, D. C. Jiles, "A new way of determining residual stress in steels using the magnetic Barkhausen effect", conference digest presented at Review of Progress in Quantitative Nondestructive Evaluation Conference, San Diego, US,2010.

[3]   L. Mierczak, Y. Melikhov, D. C. Jiles, "Reconstructing Residual Stress Depth Profiles using the Magnetic Barkhausen Noise Effect", conference digest presented at 55th Annual Conference on Magnetism and Magnetic Materials, Atlanta, US, 2010.

[4]   L. Mierczak, D. C. Jiles and G. Fantoni, "A New Method for Evaluation of Mechanical Stress Using the Reciprocal Amplitude of Magnetic Barkhausen Noise", publication in IEEE Transactions on Magnetics, vol. 47, pp. 459-465, 2011.

[5]   L. Mierczak, D. C. Jiles, G. Fantoni and L. Merletti, "System and Method for Determining Stress of a Component Made of Magnetizable Material", World Intellectual Property Organization Patent WO/2011/144998, 2011.

[6]   L. Mierczak, Y. Melikhov, D. C. Jiles and O. Kypris, "Determining depth dependence of mechanical properties from micromagnetic emissions", conference digest presented at 56th Annual Conference on Magnetism and Magnetic Materials, Scottsdale, US, 2011.

[7]   L. Mierczak, Y. Melikhov, D. C. Jiles, "Residual stress depth profiling using Magnetic Barkhausen Noise method", conference digest presented at British Institute of Non-Destructive Testing Conference on Materials Testing, Telford, UK, 2011.

[8]   L. Mierczak, Y. Melikhov, "MBN Techniques for Quantitative Determination of Stress", conference digest presented at Review of Progress in Quantitative Nondestructive Evaluation Conference, Baltimore, US,2013.

[9]   L. Mierczak, Y. Melikhov, D. C. Jiles, "Determining Residual Stress Depth Profiles using the Magnetic Barkhausen Effect ", publication in IEEE Transactions on Magnetics, vol. 50, issue 10, 2014.

Appendix I

A New Method for Evaluation of Mechanical Stress Using the Reciprocal Amplitude of Magnetic Barkhausen Noise

L. Mierczak[1], D. C. Jiles[1], *Fellow, IEEE*, and G. Fantoni[2]

[1]Wolfson Centre for Magnetics, Cardiff University, Cardiff CF24 3AA, U.K.
[2]AgustaWestland, NDI Unit, Cascina Costa di Samarate, Italy

This paper describes a method for detecting stress in the surface of magnetic materials, such as steels, based on the measurement of magnetic Barkhausen emissions. The paper presents a simple practical linear calibration curve that can be used to determine stress, and also provides a theoretical explanation of the reason for such a relationship. The influence of elastic tensile and compressive stresses of various magnitudes on the magnetic Barkhausen emissions was studied, with the objective of developing a technique for quantitative measurements of surface stress in machined steels. The peak amplitude of the Barkhausen emissions was found to correlate with both residual and applied stress, showing a clear rising trend for transition from compressive to tensile stress. The relationship between stress dependence of the maximum differential anhysteretic susceptibility and Barkhausen peak amplitude was observed. Plots of reciprocal values $1/\chi'_{max}$ and $1/V_{MBN\ max}$ against stress showed a linear relationship providing a convenient method for detecting stress levels in near-surface regions from Barkhausen measurements.

Index Terms—Magnetic Barkhausen noise, nondestructive evaluation, residual stress, steels.

I. INTRODUCTION

MAGNETIC methods have been widely used for nonde-structive evaluation of steels and other ferrous compo-nents [1], [2]. In the present work, magnetic Barkhausen noise (MBN) was used to evaluate the effect of mechanical finishing operations on the surface condition of SAE9310 and 32CDV13 steels. Surface condition is the main factor affecting the fatigue life of industrial components subjected to varying stress. Fast, reliable and preferably nondestructive methods are needed for the assurance of desired conditions during and after compo-nent manufacture. Furthermore, evaluation of the surface and sub-surface conditions of components while in service permits detection of material degradation and can be used to determine the onset of failure of the component thereby giving advance warning of impending failure.

Grinding is a machining process commonly used in fabrica-tion of highly accurate aerospace and automotive components. In many instances, it is employed as a finishing process thus specifically affecting the final surface condition of the machined component in terms of properties such as fatigue strength, residual stress and wear resistance. During grinding, highly localized input of energy in the form of heat produced within the grinding zone can induce severe thermal damage in the surface layer if the grinding parameters are not well controlled.

If the temperature of the part exceeds the tempering tem-perature, grinding can produce softened regions in the surface, which are prone to accelerated wear. When the temperature of the component exceeds the austenitizing temperature, phase changes may also result. Regions of martensite, a brittle phase, may form on the surface which is then susceptible to cracking. The presence of tensile residual stress can also arise from thermal damage. It is generated when thermal gradients are large enough that the stress developed exceeds the yield strength of the material. These variations in the material condition are difficult to evaluate using conventional noninvasive techniques such as ultrasound and eddy currents. The evaluation is further complicated when the measurement is made on components with complex surface geometry and in confined regions, partic-ularly for "on-line" evaluation of components as they are being manufactured.

X-ray diffraction is a well known technique which can be used to evaluate the surface residual stress; however, it is time consuming when investigating components with relatively large surface areas. Due to the fact that it is a highly localized mea-surement, it involves repetitive measurements when examining a series of points at different locations.

Shot-peening is a mechanical treatment based on a cyclic cold-working of the surface, which is performed in order to gen-erate an exterior layer of isotropic residual compressive stress. The final amplitude and uniformity of distribution of this stress can vary. Therefore, a definitive assessment technique is needed to verify the final impact of the process.

Being able to identify the type and evaluate the magnitude of residual stress present in the surface is vital in the detection of impending failure of components. Compressive residual stresses generally enhance fatigue resistance whereas tensile stresses de-grade fatigue resistance and increase crack propagation leading to failure.

II. EFFECT OF STRESS ON MAGNETIC BARKHAUSEN NOISE EMISSION

Magnetic Barkhausen noise consists of discontinuous changes in flux density caused by sudden irreversible changes in magnetization as the magnetic field H changes. The principal

TABLE I
CHEMICAL COMPOSITION (WT %) OF THE SAE 9310 AND 32CDV13 STEELS

	C	Mn	Si	P	S	Cr	Ni	Mo	Cu
SAE 9310	0.07 – 0.13	0.4 – 0.7	0.15 – 0.35	0 – 0.015	0 – 0.015	1 – 1.4	3 – 3.5	0.08 – 0.15	0 – 0.35
	C	**Mn**	**Si**	**P**	**S**	**Cr**	**Ni**	**Mo**	**V**
32CDV13	0.29 – 0.36	0.4 – 0.7	0.1 – 0.4	0 – 0.015	0 – 0.005	2.8 – 3.3	0.3	0.7 – 1.2	0.15 – 0.35

TABLE II
DIMENSIONS, GRINDING PARAMETERS, AND RESIDUAL STRESS VALUES FOR CARBURIZED SAE 9310 SAMPLES

SAE 9310	Dimensions, diameter × length (in mm)	Speed of grinding wheel (turn/min)	Machining Advancement – feed rate (mm/turn)	Lubrication (in %)	Residual Stress from XRD (MPa)
Sample 1	25 × 35	25	0.15	0	+339
Sample 2	25 × 35	24	0.1	0	+292
Sample 3	25 × 35	24	0.15	0	+256
Sample 4	25 × 35	24	0.002	50	-281
Sample 5	25 × 35	24	0.04	50	-339
Sample 6	25 × 35	95	0.002	100	-482
Tensile Specimen	10 × 50 (gauge section)	95	0.002	100	- 805 (after shot-peening)

cause of magnetic Barkhausen effect emissions is the discontinuous motion of the domain walls when the material is subjected to a changing magnetic field. The amplitude distribution of such pulses has been shown to depend on the microstructure and stress state of the material [3]–[8].

Defects in the microstructure such as inclusions, dislocations and grain boundaries act as pinning sites which impede the motion of domain walls. The number density of these sites and their pinning strength determine the characteristics of MBN by affecting its amplitude, the field strength at which the peak amplitude occurs, and the total number of pulses generated during the magnetization process [9].

Long-range mechanical stress σ affects the anisotropy energies of domains due to the magnetoelastic coupling which acts like an effective magnetic field and results in changes of permeability. The direction of stress-induced anisotropy depends on the product of magnetostriction λ and σ. In materials with positive magnetostriction (e.g., steels) magnetic moments tend to align along the direction of tensile stress and perpendicular to the compressive stress axis, whereas in materials with negative magnetostriction (e.g., nickel) the opposite takes place. Therefore, in the case of steels, coaxial tensile stress can be treated as an equivalent magnetic field which enhances the total effective field, whereas coaxial compressive stress as an equivalent field which reduces it.

The effect of reorientation of magnetic domains affects the MBN signal by changing the local energy barrier that a domain wall has to overcome before it moves irreversibly from one pinning site to another. For materials with positive λ, the presence of tensile stress decreases the minimum strength of the internal field needed for a domain wall to break away from a pinning site, whereas compressive stress increases it. Thus, in steel surfaces with tensile stress domain walls overcome greater numbers of pinning sites and propagate through larger distances, generating MBN emission of higher amplitude and intensity than with compressive stress. Furthermore, the hysteresis and therefore the Barkhausen effect are affected by temperature [10], [11].

III. EXPERIMENTAL PROCEDURE

High-strength, case carburized SAE 9310 (AMS 6265M) and 32CDV13 (AMS 6481) low alloy steels are widely used in manufacturing of high-performance and critical components. Their chemical composition is given in Table I.

Cylindrical samples of both grades of steel together with a round dog-bone shaped SAE9310 tensile test specimen were ground in order to obtain different conditions in the machined surfaces. Three 32CDV13 samples and the tensile specimen were subsequently shot-peened in order to study regions with high compressive stress. Details of samples dimensions, grinding and shot-peening conditions, along with resulting amplitude of surface residual stress measured with X-ray diffraction $\sin^2 \psi$ technique are given in Tables II and III.

MBN measurements were taken using a sensor comprising the magnetizing ferrite C-core with cross-sectional area of 24 mm^2 (8 mm × 3 mm) with an encircling primary coil and a cubicoid ferrite probe with cross-sectional area of 3 mm^2 (3 mm × 1 mm) positioned centrally between the legs of the magnetizing yoke. A search coil wound around the probe was

32CDV13	Dimensions, diameter × length (in mm)	Speed of grinding wheel (turn/min)	Machining Advancement – feed rate (mm/turn)	Shot-peening parameters	Residual Stress from XRD (MPa)
Sample 1	30 × 110	30	0.5	All samples were shot-peened with SAE-170 balls, HRC42-52, intensity of 0.008 - 0.012 A	-145
Sample 2	30 × 110	30	1.5		-298
Sample 3	30 × 110	30	1		-533
Sample 4	30 × 110	30	0.5		-745
Sample 5	30 × 110	30	1.5		-765
Sample 6	30 × 110	30	1		-775

used to pick up the perpendicular component of the induced voltage signal. The maximum applied magnetic field strength measured at the centre of the poles of the electromagnet was equal to 4.5 kA/m. The size of the area being magnetized was 40 mm^2. This setup was designed for performing local measurements, from which results can be compared with the residual stress data obtained using X-ray diffraction.

The output of the search coil was amplified and high-band-pass filtered in order to remove the quasi-static hysteresis signal. Further filtering performed in data analysis was made using a digital filter software tool. The moving average method was implemented to obtain a smooth distribution of MBN signal in the form of envelope curves of the rectified bursts. Parameters extracted from these curves were used afterwards to quantify the detected MBN signal.

During tensile tests, stresses of various amplitudes within the elastic limit were applied using a servo-hydraulic mechanical testing system. MBN measurements were taken for a monotonically increasing load with increments of 100 MPa.

IV. RESULTS AND DISCUSSION

Envelope curves of the rectified MBN bursts for carburized SAE 9310 specimen for different amplitudes of applied stress are shown in Fig. 1. These curves represent MBN emission in the frequency range of 20 to 1250 kHz.

Progressive change in the width and peak amplitude of MBN envelopes was observed in response to increasing load. This type of behavior is consistent with the theory which describes the effects of applied stress in terms of equivalent magnetic field H_σ [12]. This additional field results from the magnetoelastic coupling and is given by the equation

$$H\sigma(\theta) = \frac{3}{2}\frac{\sigma}{\mu_o}(\cos^2\theta - \nu\sin^2\theta)\left(\frac{\partial\lambda}{\partial M}\right)_T \qquad (1)$$

where σ is the stress, λ is the magnetostriction, μ_0 is the permeability of free space, Θ is the angle between the stress axis and the direction of H_σ, and υ is Poisson's ratio. MBN is then a
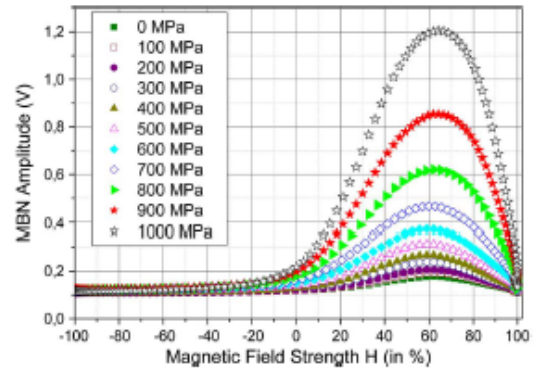

Fig. 1. Envelope curves of the rectified MBN bursts for carburized SAE 9310 specimen for different amplitudes of applied stress using a tensile test machine (residual stress value from XRD measured before stress application was −805 MPa).

response to an effective magnetic field which can be expressed as

$$H_e = H + H_\sigma + \alpha M \qquad (2)$$

where H is the applied external field, α is mean field parameter representing the interdomain coupling and H_σ is the stress equivalent field. In the measurements performed in the present study the external magnetic field applied during the measurements was coaxial with the applied stress; therefore, an increase of amplitude of applied tensile stress resulted in a higher value of total effective field sensed by domains.

In response to this effect the domain walls could break the local energy barriers at lower values of applied field H, which is consistent with an increase of MBN amplitude.

A rising trend of MBN peak amplitude for increasing applied stress is shown in Fig. 2. This type of stress dependence was previously observed for anhysteretic susceptibility at the origin $(\chi'_{an}(\sigma))_{H=0}$ for AISI 4130 steel in the work of Garikepati *et*
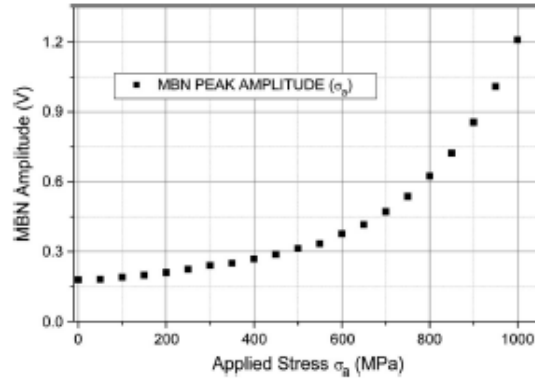
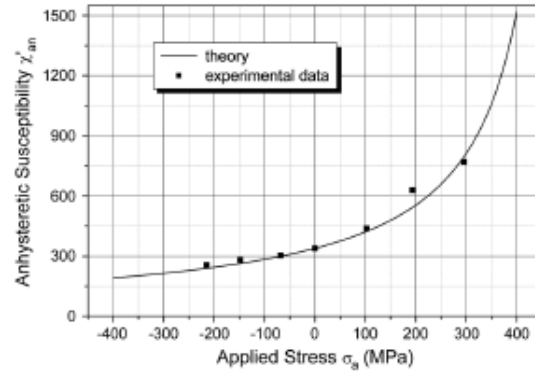Fig. 2. MBN peak amplitude for carburized SAE 9310 specimen as a function of applied stress.

Fig. 3. Anhysteretic susceptibility at the origin as a function of stress after Garikepati et al. [10].

al. [13] as shown in Fig. 3. The equation which predicts this relationship between stress σ and slope of the anhysteretic magnetization curve at the origin was derived from the Langevin function for magnetization in which the stress equivalent field had been added to the applied field and the internal coupling field.

The Langevin function used to represent the anhysteretic magnetization curve has the form

$$M_{an}(H) = M_s \left\{ \coth\left(\frac{H + \alpha M}{a}\right) - \left(\frac{a}{H + \alpha M}\right) \right\}. \quad (3)$$

After taking into account the effect of applied stress by the introduction of an equivalent magnetic field H_σ (1), the equation for the anhysteretic magnetization under stress becomes

$$M_{an}(H) = M_s \left\{ \coth\left(\frac{H + \alpha M + H_\sigma}{a}\right) - \left(\frac{a}{H + \alpha M + H_\sigma}\right) \right\}. \quad (4)$$

Magnetostriction at low values of magnetization, where λ is symmetric in M, can be expressed by the approximation

$$\lambda = bM^2 \quad (5)$$

and therefore

$$\frac{d\lambda}{dM} = 2bM. \quad (6)$$

The value of the coefficient b can be determined experimentally from magnetostriction measurements. The anhysteretic magnetization at the origin is linear in H and can be expressed as

$$\frac{M_{an}(H)}{M_s} = \frac{H + \left(\alpha + \frac{3b\sigma}{\mu_0}\right) M_{an}(H)}{3a} \quad (7)$$

for low values of H. This gives the equation for the differential susceptibility at the origin as

$$[\chi'_{an}(\sigma)]_{H=0} = \frac{M_s}{3a - \left(\alpha + \frac{3b\sigma}{\mu_0}\right) M_s} \quad (8)$$

which can be rewritten in the form

$$\frac{1}{[\chi'_{an}(0)]_{H=0}} - \frac{1}{[\chi'_{an}(\sigma)]_{H=0}} = \frac{3b\sigma}{\mu_0}. \quad (9)$$

Using the experimental data of reciprocal susceptibility for zero stress and the value of magnetostriction coefficient b, it was possible to calculate the predicted dependence of $[\chi'_{an}(\sigma)]_{H=0}$ on stress for AISI 4130 steel. It is also known from previous work that the maximum anhysteretic differential susceptibility χ'_{an} for many materials is equal to the maximum differential susceptibility at the coercive point χ'_{max} [14], so that based on (9) the maximum differential susceptibility, measured usually at the coercive point, is related to the stress σ by the equation

$$\frac{1}{[\chi'_{max}(0)]} - \frac{1}{[\chi'_{max}(\sigma)]} = \frac{3b\sigma}{\mu_0}. \quad (10)$$

The agreement between theory and experiment was tested by plotting the reciprocal anhysteretic susceptibility against stress as shown in Fig. 4.

It can be seen from Fig. 4 that the theoretical prediction represented by the linear function was in good agreement with the trend obtained from measurements. Therefore, the linear function given in (9) was confirmed as a convenient way for evaluating the stress from a measurable bulk magnetic property, specifically the slope of the anhysteretic magnetization curve at the origin. An alternative and often more practical alternative involves the use of the maximum differential susceptibility $\chi'_{max}(\sigma)$ at the coercive point as shown in (10).
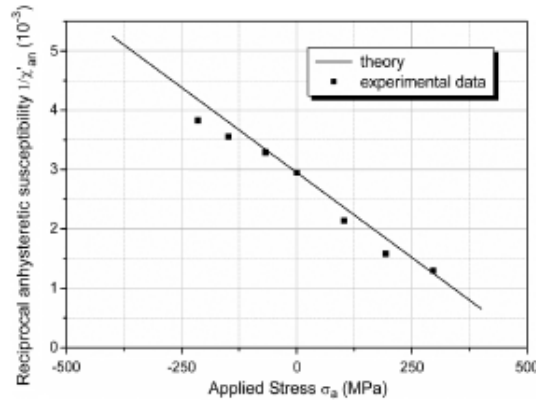
Fig. 4.   Reciprocal anhysteretic susceptibility at the origin as a function of applied stress after Garikepati *et al*. [10].

Fig. 5.   Reciprocal of MBN peak amplitude for carburized SAE 9310 specimen as a function of applied stress. Compare with Fig. 4.

The MBN peak amplitude showed a similar stress dependence to that obtained for the maximum differential susceptibility $\chi'_{max}(\sigma)$. Hence, there should be a relation linking these two results. The first assumption which can be made is that both of them correspond to the same stage of the magnetization process where values of dM/dH and consequently dB/dH are the highest. These regions are represented by the steepest slope of the magnetization curve at the coercive point. The second assumption is that the level of Barkhausen activity in a given time interval dM_{JS}/dt is proportional to the rate of change of magnetization in time $dM/dt = (dM/dH)(dH/dt) = \chi' dH/dt$. This relationship was described before by the model of micromagnetic Barkhausen activity based on the theory of hysteresis [15]. According to that model, the sum of Barkhausen jumps in a given period Δt is proportional to the total change in magnetization ΔM in that period. This can be expressed by the following equation:

$$M_{JS} = \gamma \Delta M = \gamma \left(\frac{dM}{dt} \right) \Delta t$$
$$= \gamma \left(\frac{dM}{dH} \right) \left(\frac{dH}{dt} \right) \Delta t = \gamma \chi' \left(\frac{dH}{dt} \right) (\Delta t) \quad (11)$$

where γ is simply a coefficient of proportionality $(0 \leq \gamma \leq 1)$, which represents the ratio of discontinuous magnetization change to total magnetization change. This equation defines the link between the MBN and differential susceptibility at any point of hysteresis loop, and consequently confirms the direct relation between peak amplitude of the Barkhausen emissions $V_{MBN\ max}$ and maximum differential susceptibility χ'_{max}. Therefore, the plot of reciprocal MBN peak amplitude can also be represented as a linear function of applied stress, as shown in Fig. 5.

The effect of surface residual stress on MBN was studied in the second stage of this work. First, residual stress gradients were measured in ground and shot-peened regions of SAE 9310 and 32CDV13 steel samples using X-ray diffraction. Afterwards, these regions were evaluated with the MBN technique.
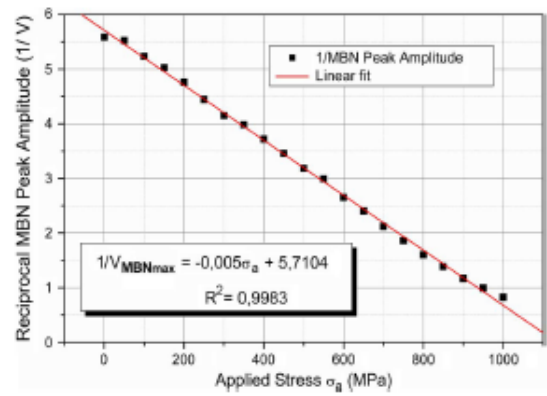
The direction of the applied field during Barkhausen measurements was coaxial with the axis of the residual stress measured with the XRD method.

In order to correlate the MBN results with the surface residual stress from XRD measurements, the Barkhausen signal was analyzed by passing it through a high-pass filter. The depth of penetration δ was calculated for the lower analyzing frequency limit of the frequency range of Barkhausen emissions using the skin depth formula (12)

$$f = \frac{1}{\pi \sigma_e \mu \delta^2} \quad (12)$$

where $\mu = \mu_0 \mu_r$ is the magnetic permeability, σ_e is the electrical conductivity, and f is the frequency of Barkhausen noise signal. The lower limit of the analyzing frequency range was determined for δ equal to 10 μm, which corresponds approximately to the penetration depth of X-rays [16]. Values of conductivity used for calculations were 4.57×10^6 S/m for carburized SAE 9310 and 4.03×10^6 S/m for 32CDV13. Values of differential magnetic permeability at the coercive point were obtained experimentally from the measured BH loops and were equal to 0.00115 for SAE 9310 and 0.00251 for 32CDV13. The frequency ranges used in analysis were 605.7–1250 kHz for carburized SAE 9310 steel and 314.7–250 kHz for 32CDV13 steel. Detecting only Barkhausen emissions with frequencies in these ranges, it can be assumed that the majority of these emissions originate from the surface and near-subsurface regions, and therefore can be directly related to the stress values in the surface evaluated by XRD.

MBN envelope curves for both groups of samples for various amplitudes of residual stress are shown in Figs. 6 and 7.

MBN peak amplitudes for both sets of specimens for various magnitudes of residual stress are shown in Fig. 8. Differences in MBN peak amplitude indicated differences in residual stress in the surface. The amplitude of MBN obtained with compressive stress was lower than that obtained for tensile stress. Moreover, it was possible to distinguish regions with different stress levels
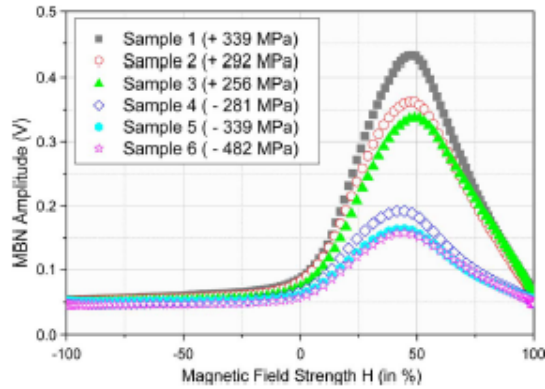
237

Fig. 6. Envelope curves of the rectified MBN bursts for carburized SAE 9310 specimens for different amplitudes of residual stress.
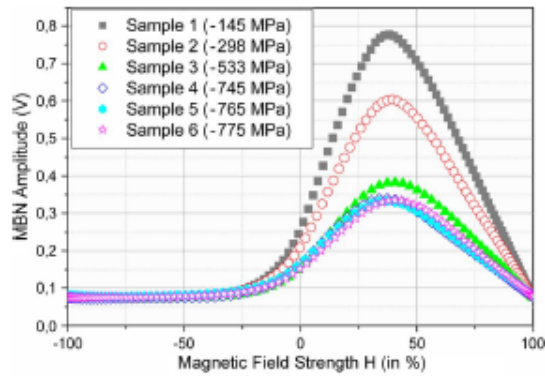

Fig. 8. MBN peak amplitude for carburized SAE 9310 and 32CDV13 specimens as a function of residual stress.

Fig. 7. Envelope curves of the rectified MBN bursts for 32CDV13 specimens for different amplitudes of residual stress.

Fig. 9. Reciprocal of MBN peak amplitude for carburized SAE 9310 and 32CDV13 specimens as a function of residual stress.

within both positive and negative ranges of stress. These results are consistent with the theory of the magnetoelastic effect as well as results obtained from tensile tests.

The measured variations of $V_{\text{MBN max}}$ with residual stress for both materials are analogous to those obtained with applied stress. Therefore, it can be seen that both residual and applied stresses influence differential susceptibility and consequently MBN in the same way. Plots of reciprocal $V_{\text{MBN max}}$ against residual stress in Fig. 9 confirmed these linear relationships.

It should be noted that the slope of the curve of reciprocal MBN peak amplitude $1/V_{\text{MBN max}}$ for SAE 9310 steel is the same for both applied stress and residual stress. This confirmed that the magnetoelastic effect is the same for both types of stress. The linear stress dependence of $1/V_{\text{MBN max}}$ for 32CDV13 suggests the generality of the method for stress evaluation.

V. CONCLUSION

This paper describes a method for detecting stress in the surface of magnetic materials, such as steels, based on the measurement of Barkhausen emissions. The reciprocal of the peak amplitude of the Barkhausen emissions $1/V_{\text{MBN max}}$ has been
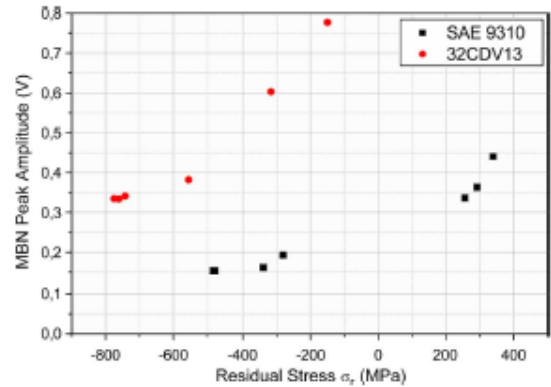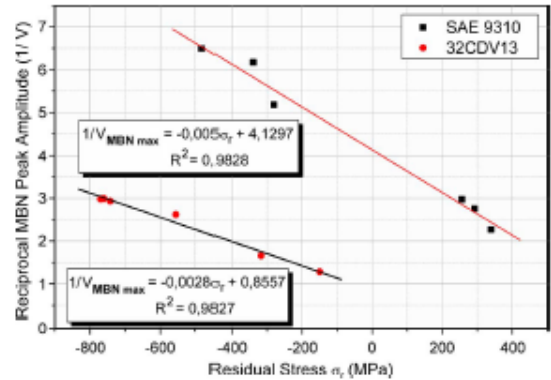
experimentally shown here to vary linearly with stress. This provides a useful calibration curve for determining stress.

The amplitude of the Barkhausen emissions has been shown in a previous theoretical analysis to depend on the maximum differential susceptibility $\chi'_{\text{max}}(\sigma)$ at the coercive point. Furthermore, it has also been shown previously that the anhysteretic differential susceptibility χ'_{an} is for many materials equal to χ'_{max}. Therefore, a direct link between $V_{\text{MBN max}}$ and χ'_{an} is suggested. Since previous work had already shown that $1/\chi'_{\text{an}}$ is a linear function of stress, we have arrived at an explanation of the observed linear relation between stress σ and the measurable quantity $1/V_{\text{MBN max}}$. This relation has been shown to be true for two different types of steel, SAE 9310 and 32CDV13.

ACKNOWLEDGMENT

REFERENCES

[1] D. C. Jiles, "Review of magnetic methods for nondestructive evaluation," *NDT Int.*, vol. 21, p. 311, 1988.

[2] D. C. Jiles, "Review of magnetic methods for nondestructive evaluation (Part 2: Flux leakage and related methods)," *NDT Int.*, vol. 23, p. 83, 1990.

[3] M. J. Sablik, "A model for the Barkhausen noise power as a function of applied magnetic field and stress," *J. Appl. Phys.*, vol. 74, no. 9, pp. 5898–5900, 1993.

[4] M. J. Sablik and B. Augustyniak, "The effect of mechanical stress on a Barkhausen noise signal integrated across a cycle of ramped magnetic field," *J. Appl. Phys.*, vol. 79, no. 2, pp. 963–972, 1996.

[5] R. Ranjan, D. C. Jiles, O. Buck, and R. B. Thompson, "Grain-size measurement using magnetic and acoustic Barkhausen noise," *J. Appl. Phys.*, vol. 61, p. 3199, 1987.

[6] E. R. Kinser, C. C. H. Lo, A. J. Barsic, and D. C. Jiles, "Modeling microstructural effects on Barkhausen emission in surface-modified magnetic materials," *IEEE Trans. Magn.*, vol. 41, no. 10, pp. 3292–3294, Oct. 2005.

[7] C. C. H. Lo, S. J. Lee, L. Li, L. C. Kerdus, and D. C. Jiles, "Modeling stress effects on magnetic hysteresis and Barkhausen emission using a hysteretic-stochastic model," *IEEE Trans. Magn.*, vol. 38, no. 5, pp. 2418–2420, Sep. 2002.

[8] V. Moorthy, B. A. Shaw, and P. Hopkins, "Surface and subsurface stress evaluation in case-carburized steel using high and low frequency magnetic Barkhausen emission measurements," *J. Magn. Magn. Mater.*, vol. 299, pp. 362–375, 2006.

[9] E. R. Kinser, C. C. H. Lo, and D. C. Jiles, "Analysis of Barkhausen effect signals in surface-modified magnetic materials using a hysteretic—Stochastic model," *J. Appl. Phys.*, vol. 99, p. 08B705, 2006.

[10] A. Raghunathan, Y. Melikhov, J. E. Snyder, and D. C. Jiles, "Modeling the temperature dependence of hysteresis based on Jiles-Atherton theory," *IEEE Trans. Magn.*, vol. 45, no. 10, pp. 3954–3957, Oct. 2009.

[11] G. Vertesy, T. Uchimoto, I. Tomas, and T. Takagi, "Temperature dependence of magnetic descriptors of magnetic adaptive testing," *IEEE Trans. Magn.*, vol. 46, no. 2, pp. 509–512, Feb. 2010.

[12] M. J. Sablik and D. C. Jiles, "Coupled magnetoelastic theory of magnetic and magnetostrictive hysteresis," *IEEE Trans. Magn.*, vol. 29, no. 4, pp. 2113–2123, Jul. 1993.

[13] P. Garikepati, T. T. Chang, and D. C. Jiles, "Theory of ferromagnetic hysteresis: Evaluation of stress from hysteresis curves," *IEEE Trans. Magn.*, vol. 24, no. 6, pp. 2922–2924, Nov. 1988.

[14] D. C. Jiles, "Magnetic properties and microstructure of AISI 1000 series carbon steels," *J. Appl. Phys.*, vol. 21, p. 1186, 1988.

[15] D. C. Jiles, L. B. Sipahi, and G. Williams, "Modeling of micromagnetic Barkhausen activity using a stochastic process extension to the theory of hysteresis," *J. Appl. Phys.*, vol. 73, p. 5830, 1993.

[16] P. S. Prevéy, "Current application of x-ray diffraction residual stress measurement," Developments in Materials Characterization Technologies, ASM International, Materials Park, OH, pp. 103–110, 1996.

Appendix II

Determining Residual Stress Depth Profiles Using the Magnetic Barkhausen Effect

Lukasz P. Mierczak[1], Yevgen Melikhov[1], and David C. Jiles[2], *Fellow, IEEE*

[1]Wolfson Centre for Magnetics, Cardiff University, Cardiff CF24 3AA, U.K.
[2]Department of Electrical and Computer Engineering, Iowa State University, Ames, IA 50011 USA

A new method for determining depth dependence of residual stress from measured magnetic Barkhausen signals is proposed. This method improves on the previously accepted practice, which rather loosely used Barkhausen measurements at different frequencies for nondestructively determining the depth dependence of properties. This paper develops a complete set of equations for describing the detected Barkhausen signals in terms of the actual emissions that are generated inside the material and how these appear when they propagate to the surface. The underlying equations consider the Barkhausen emission signal amplitude and its decay with distance and frequency. The variation of Barkhausen emission amplitude with stress is also described. A case study of depth profiling in a specimen that consists of multiple layers with different, but uniform, physical properties is presented.

Index Terms—Depth profiling, magnetic Barkhausen noise (MBN), nondestructive evaluation, residual stress.

I. INTRODUCTION

MAGNETIC Barkhausen noise (MBN) consists of discontinuous changes in magnetic flux density caused by sudden irreversible changes in magnetization inside the material as the applied magnetic field H changes continuously. These changes can be measured at the surface in the form of voltage pulses using a pickup coil. The measured voltages are representative of, but not identical to, the emissions occurring inside the material. The amplitude of such measured Barkhausen signals has been shown to depend on the state of stress, microstructure, or hardness of the material [1]–[4]. Models have been developed to describe these dependencies [5], [6].

Attenuation of magnetic Barkhausen emissions in magnetic materials is frequency dependent and therefore information from different depths inside the material is contained in the frequency spectrum of the detected Barkhausen signal. The depth dependent information about material conditions, such as variations in microstructure and/or the presence of residual stress in steel components (e.g., load bearings, gears, and camshafts), is of great technical interest. However, this depth dependent information, although present in the Barkhausen emissions needs to be deconvolved from the measurement results. Previous attempts at this have not been exact or complete as they were considering only a simplified exponential attenuation of Barkhausen emission only, while neglecting its depth dependence and complexity when evaluating specimens with nonuniform mechanical properties from layer to layer [7]. This paper presents a new comprehensive method for extracting this information from measured MBN signals at different emission frequencies.

II. THEORETICAL STUDY

In this paper, the measured MBN V_{MBNmeas} is considered to arise as a result of the rate of change of magnetic flux density that emerges at the surface when a Barkhausen emission event occurs at a location at depth x inside the material. If we denote the surface as $x = 0$ then, assuming for simplicity that the signal is not diverging and that the passage of the Barkhausen signal does not change its frequency, even though it changes its amplitude, the signal $V_{\text{MBNmeas}}(x, \omega)$ that is detected at the surface will be the original signal at depth x, $V_{\text{MBNorigin}}(x, \omega)$ attenuated by the exponential decay term as shown in

$$V_{\text{MBNmeas}}(x, \omega) = V_{\text{MBNorigin}}(x, \omega) * \exp\left(\frac{-x}{\sqrt{\frac{2\rho}{\omega\mu_0\mu_r}}}\right) \quad (1)$$

where x is a depth at which $\text{MBN}_{\text{origin}}(x,\omega)$ was emitted [m], ρ is the electrical resistivity [Ω*m], $\omega = 2\pi f$ is the MBN signal frequency [Hz], μ_0 is the permeability of free space [$4\pi \times 10^{-7}$ H/m], and μ_r is the relative permeability. If the Barkhausen emission signal is diverging then the terms of the right hand side (RHS) of (1) need to be multiplied by a further term that depends on the inverse square of the distance between the location of emission and the location of measurement. An example attenuation curves for MBN signals with original amplitudes of 1 mV and frequencies of 20, 100, and 500 kHz propagating within ferromagnetic material with resistivity of $\rho = 5 \times 10^{-7}$ [Ω*m] and relative permeability of $\mu_r = 100$ are shown in Fig. 1.

For a multiple number of Barkhausen events, which occur throughout the volume of material, the detected signal at a given frequency ω will be a sum of all these events at different depths within the volume of inspection from $x = 0$ to $x = x_{\text{max}}$ as shown in

$$V_{\text{MBNmeas}}(0, x_{\text{max}}, \omega) = \sum_{x=0}^{x=x_{\text{max}}} V_{\text{MBNorigin}}(x, \omega)$$
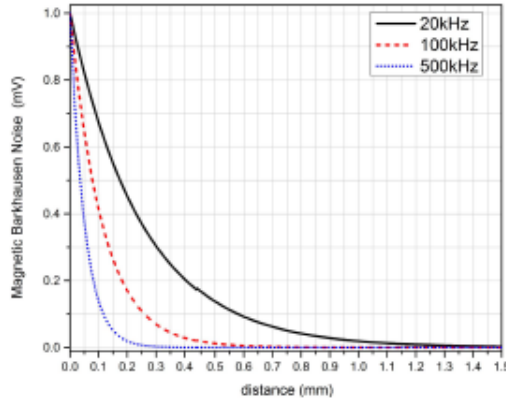$$* \exp(-\alpha x \sqrt{\omega}) \quad (2)$$

Fig. 1. Attenuation curves for MBN signals with frequencies of 20, 100, and 500 kHz propagating within ferromagnetic material.

where $\alpha = \sqrt{\frac{\mu_0 \mu_r}{2\rho}}$.

When treating the distribution as continuous it can be expressed in the integral form as shown in

$$V_{\text{MBNmeas}}(0, x_{\max}, \omega)$$
$$= \int_0^{x_{\max}} V_{\text{MBNorigin}}(x, \omega) * \exp(-\alpha x \sqrt{\omega}) dx. \quad (3)$$

The above expression deals only with one frequency, but Barkhausen emissions occur over a range of frequencies. If the frequency band of detection is from ω_L (lower) to ω_U (upper) then the expression for the measured Barkhausen noise will be

$$V_{\text{MBNmeas}}(0, x_{\omega_L}, \omega_L, \omega_U)$$
$$= \int_{\omega_L}^{\omega_U} \int_0^{x_{\omega_L}} V_{\text{MBNorigin}}(x, \omega) * \exp(-\alpha x \sqrt{\omega}) dx d\omega. \quad (4)$$

This is the basic equation that we have developed for the nondivergent Barkhausen signal detected at the surface. The depth $x_{\omega L}$ from which MBN signal can be detected depends on the lower frequency limit ω_L. Control of this measurement parameter ω_L can therefore be used to preferentially sample Barkhausen emissions from different depths in the material. In particular, a set of measurements with the same high-frequency cutoff, but a series of low-frequency cutoffs, allows differentiation of the measured signal with respect to the lower frequency and hence allows the Barkhausen emissions and related properties to be probed as a function of depth.

By way of example, we consider a test specimen which consists of two layers with different stress levels, as shown in Fig. 2. In this specimen, the depths of x_1 and x_2 correspond to low-frequency cutoffs of ω_1 and ω_2. The terms $V_{\text{MBNorigin}_1}$ and $V_{\text{MBNorigin}_2}$ are representative of the local Barkhausen emissions in the first and second layer before attenuation.
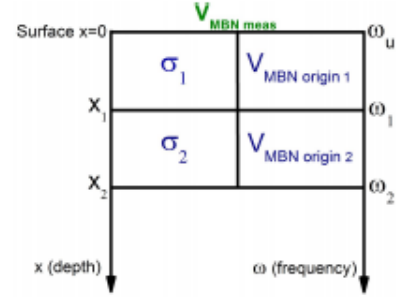

Fig. 2. Schematic diagram of layered specimen.

A. For the First Layer

In the case where the stress is uniform throughout, the amplitude of $V_{\text{MBNorigin}}$ will not change with depth x. Furthermore, for the purpose of simplification here we assume that in this particular case the amplitude of the emissions at their origin, $V_{\text{MBNorigin}}$, before they get attenuated is the same for all frequencies. This is the white noise assumption. Different frequency spectra such as $1/f$ or other types of pink noise are also possible. With the white noise assumption at the point of origin, the expression for the measured Barkhausen voltage V_{MBNmeas} for the first layer becomes

$$V_{\text{MBNmeas}}(0, x_1, \omega_1, \omega_U)$$
$$= \int_{\omega_1}^{\omega_u} \int_0^{x_1} V_{\text{MBNorigin}_1} * \exp(-\alpha x \sqrt{\omega}) dx d\omega \quad (5)$$

where x_1 is the depth of the first layer, and ω_1 and ω_u are the lower and upper bounds of the range of detection frequencies. The term $V_{\text{MBNorigin}_1}$ is representative of the local Barkhausen emissions in the first layer before attenuation. The result of the integration is

$$V_{\text{MBNmeas}}(0, x_1, \omega_1, \omega_u) = \frac{2 * V_{\text{MBNorigin}_1}}{x_1 \alpha^2}$$
$$* (\exp(-x_1 \alpha \sqrt{\omega_u}) - \exp(-x_1 \alpha \sqrt{\omega_1}) + x_1 \alpha (\sqrt{\omega_u} - \sqrt{\omega_1})). \quad (6)$$

From (6), it is possible to calculate $V_{\text{MBNorigin}_1}$, which is the unattenuated Barkhausen emission occurring inside the sample in terms of the measurable Barkhausen emission voltage V_{MBNmeas}. Therefore, if the first layer in the layered specimen of Fig. 1 has a uniform stress σ_1 the expression for the Barkhausen emission voltage inside the material will be

$$V_{\text{MBNorigin}_1}(\sigma_1)$$
$$= \frac{V_{\text{MBNmeas}}(0, x_1, \omega_1, \omega_u) \frac{\alpha^2}{2}}{\frac{1}{x_1}(\exp(-x_1 \alpha \sqrt{\omega_u}) - \exp(-x_1 \alpha \sqrt{\omega_1}) + x_1 \alpha(\sqrt{\omega_u} - \sqrt{\omega_1}))} \quad (7)$$

and therefore

$$\frac{1}{V_{\text{MBNorigin}_1}(\sigma_1)}$$
$$=\frac{\frac{1}{x_1}\left(\exp\left(-x_1 a\sqrt{\omega_u}\right)-\exp\left(-x_1 a\sqrt{\omega_1}\right)+x_1 a\left(\sqrt{\omega_u}-\sqrt{\omega_1}\right)\right)}{V_{\text{MBNmeas}}(0,x_1,\omega_1,\omega_u)\frac{a^2}{2}}.$$

$$(8)$$

It is this term $V_{\text{MBNorigin}}$ that needs to be determined for correct depth profiling of the condition of the material, not V_{MBNmeas}. This arises because it is $V_{\text{MBNorigin}}$ that is primarily dependent on stress (V_{MBNmeas} is only secondarily dependent on stress because of the stress dependence of $V_{\text{MBNorigin}}$). Therefore, $V_{\text{MBNorigin}}$ can be used to determine the level of stress locally at different depths provided it can be calculated from the measurements.

B. For the Combined First and Second Layer

To take measurements from both layer 1 and layer 2, the lower cutoff frequency needs to be reduced to allow detection of emissions from deeper inside the sample. Let this new lower cut off frequency be ω_2, such that $\omega_2 < \omega_1$ and let the depth of penetration be x_2 such that $x_2 > x_1$

$$V_{\text{MBNmeas}}(0,x_2,\omega_2,\omega_u)$$
$$=\int_{\omega_2}^{\omega_u}\int_0^{x_2} V_{\text{MBNorigin}}(x)*\exp(-ax\sqrt{\omega})dxd\omega.$$

$$(9)$$

Splitting this into two terms, the separate integrals which represent the detected emissions from each of the two layers are

$$V_{\text{MBNmeas}}(0,x_2,\omega_2,\omega_u)$$
$$=\int_{\omega_2}^{\omega_u}\int_0^{x1} V_{\text{MBNorigin}_1}^*\exp(-ax\sqrt{\omega})dxd\omega$$
$$+\int_{\omega_2}^{\omega_u}\int_{x1}^{x2} V_{\text{MBNorigin}_2}*e\exp(-ax\sqrt{\omega})dxd\omega$$

$$(10)$$

where we now allow the properties of the two layers to be different so that the unattenuated Barkhausen emissions, $V_{\text{MBNorigin}_1}$ and $V_{\text{MBNorigin}_2}$, while the same for any particular layer location from which they originate (assuming the layer is uniform throughout), will exhibit differences between the two layers. This difference in properties could be caused for example by differences in stress or microstructure from one layer to the next.

C. For the Second Layer Alone

The emissions from the second layer at frequencies between ω_1 and ω_u will not reach the surface, so that we are only interested in emissions from that layer with frequencies between ω_2 and ω_1. Therefore for the second layer, for which the frequency bounds are ω_2 ($<\omega_1$) and ω_u, the expression for

the measured Barkhausen emission is

$$V_{\text{MBNmeas}}(x_1,x_2,\omega_2,\omega_1)$$
$$=\int_{\omega_2}^{\omega_1}\int_{x1}^{x_2} V_{\text{MBNorigin}_2}*\exp(-ax\sqrt{\omega})dxd\omega.$$

$$(11)$$

Therefore, (10) must be modified to

$$V_{\text{MBNmeas}}(0,x_2,\omega_2,\omega_u)$$
$$=\int_{\omega_2}^{\omega_u}\int_0^{x1} V_{\text{MBNorigin}_1}*\exp(-ax\sqrt{\omega})dxd\omega$$
$$+\int_{\omega_2}^{\omega_1}\int_{x1}^{x2} V_{\text{MBNorigin}_2}*\exp(-ax\sqrt{\omega})dxd\omega$$

$$(12)$$

where the values of $V_{\text{MBNorigin}_1}$ and $V_{\text{MBNorigin}_2}$ are assumed constant in each layer, but different from layer to layer. The first integral on the RHS of (12) represents the emissions from the first layer. This can also be split into two parts. The integral from ω_1 to ω_u represents the measurement V_{MBNmeas} in (5), while the integral from ω_2 to ω_1 represents additional emissions measured from the first layer that arise because of the increased bandwidth from ω_1 to ω_2 in the second measurement. This can be written as follows:

$$V_{\text{MBNmeas}}(0,x_2,\omega_2,\omega_u)$$
$$=\int_{\omega_1}^{\omega_u}\int_0^{x_1} V_{\text{MBNorigin}_1}\exp(-ax\sqrt{\omega})dxd\omega$$
$$+\int_{\omega_2}^{\omega_1}\int_0^{x_1} V_{\text{MBNorigin}_1}\exp(-ax\sqrt{\omega})dxd\omega$$
$$+\int_{\omega_2}^{\omega_1}\int_{x1}^{x_2} V_{\text{MBNorigin}_2}\exp(-ax\sqrt{\omega})dxd\omega$$

$$(13)$$

and since the first term on the RHS of the above (13) is equivalent to the first measurement $V_{\text{MBNmeas}}(0,x_1,\omega_1,\omega_u)$ given in (5)

$$V_{\text{MBNmeas}}(0,x_2,\omega_2,\omega_u)$$
$$= V_{\text{MBNmeas}}(0,x_1,\omega_1,\omega_U)$$
$$+\int_{\omega_2}^{\omega_1}\int_0^{x_1} V_{\text{MBNorigin}_1}\exp(-ax\sqrt{\omega})dxd\omega$$
$$+\int_{\omega_2}^{\omega_1}\int_{x1}^{x_2} V_{\text{MBNorigin}_2}\exp(-ax\sqrt{\omega})dxd\omega.$$

$$(14)$$

To determine $V_{\text{MBNorigin}_2}$ we need to find

$$\int_{\omega_2}^{\omega_1}\int_0^{x_1} V_{\text{MBNorigin}_1}\exp(-ax\sqrt{\omega})dxd\omega.$$

$$(15)$$

The white noise approximation, which we make is that the amplitude spectrum of emissions in the range of frequencies of interest is white noise. This means that $V_{\text{MBNorigin}}$ is

independent of frequency. We can therefore use the result of (6) to solve this integral

$$\int_{\omega_2}^{\omega_1} \int_0^{x_1} V_{\text{MBNorigin}_1} * \exp(-ax\sqrt{\omega}) dx d\omega$$
$$= \frac{2 * V_{\text{MBNorigin}_1}}{x_1 a^2} * (\exp(-x_1 a\sqrt{\omega_1})$$
$$- \exp(-x_1 a\sqrt{\omega_2}) + x_1 a(\sqrt{\omega_1} - \sqrt{\omega_2})) \quad (16)$$

and substituting this into (14) gives

$$V_{\text{MBNmeas}}(0, x_2, \omega_2, \omega_u)$$
$$= V_{\text{MBNmeas}}(0, x_1, \omega_1, \omega_U) + \frac{2 * V_{\text{MBNorigin}_1}}{x_1 a^2}$$
$$* (\exp(-x_1 a\sqrt{\omega_1}) - \exp(-x_1 a\sqrt{\omega_2})$$
$$+ x_1 a(\sqrt{\omega_1} - \sqrt{\omega_2}))$$
$$+ \int_{\omega_2}^{\omega_1} \int_{x_1}^{x_2} V_{\text{MBNorigin}_2} \exp(-ax\sqrt{\omega}) dx d\omega. \quad (17)$$

We also know from (7) that we get

$$V_{\text{MBNorigin}_1}$$
$$= \frac{V_{\text{MBNmeas}}(0, x_1, \omega_1, \omega_u) \frac{a^2}{2}}{\frac{1}{x_1}(\exp(-x_1 a\sqrt{\omega_u}) - \exp(-x_1 a\sqrt{\omega_1}) + x_1 a(\sqrt{\omega_u} - \sqrt{\omega_1}))}. \quad (18)$$

Substituting into (17) gives

$$V_{\text{MBNmeas}}(0, x_2, \omega_2, \omega_U)$$
$$= V_{\text{MBNmeas}}(0, x_1, \omega_1, \omega_U) + V_{\text{MBNmeas}}(0, x_1, \omega_1, \omega_U)$$
$$* \frac{(\exp(-x_1 a\sqrt{\omega_1}) - \exp(-x_1 a\sqrt{\omega_2}) + x_1 a(\sqrt{\omega_1} - \sqrt{\omega_2}))}{(\exp(-x_1 a\sqrt{\omega_u}) - \exp(-x_1 a\sqrt{\omega_1}) + x_1 a(\sqrt{\omega_u} - \sqrt{\omega_1}))}$$
$$+ \int_{\omega_2}^{\omega_1} \int_{x_1}^{x_2} V_{\text{MBNorigin}_2} \exp(-ax\sqrt{\omega}) dx d\omega. \quad (19)$$

Therefore, from the two measurements $V_{\text{MBNmeas}}(0, x_1, \omega_1, \omega_u)$ and $V_{\text{MBNmeas}}(0, x_2, \omega_2, \omega_u)$ it should be possible to calculate $V_{\text{MBNorigin}_2}$ and thereby determine the condition of the material in the second layer from depth x_1 to x_2.

Next we need to evaluate the double integral on the RHS of (19)

$$\int_{\omega_2}^{\omega_1} \int_{x_1}^{x_2} V_{\text{MBNorigin}_2} \exp(-ax\sqrt{\omega}) dx d\omega$$
$$= \frac{2 V_{\text{MBNorigin}_2}}{a^2} \left(\frac{1}{x_2} \exp(-ax_2\sqrt{\omega_1}) - \exp{-ax_2\sqrt{\omega_2}} \right)$$
$$- \frac{1}{x_1} (\exp(-ax_1\sqrt{\omega_1}) - \exp{-ax_1\sqrt{\omega_2}}) \quad (20)$$

and from (19) and (20), an expression can be obtained for VMBNmeas(0, x2, ω2, ωu), similar to (6), because the solution to the integral on the left hand side of (20) is known. This

then represents the measurement

$$V_{\text{MBNmeas}}(0, x_2, \omega_2, \omega_u)$$
$$= V_{\text{MBNmeas}}(0, x_1, \omega_1, \omega_u) + V_{\text{MBNmeas}}(0, x_1, \omega_1, \omega_u)$$
$$* \frac{(\exp(-x_1 a\sqrt{\omega_1}) - \exp(-x_1 a\sqrt{\omega_2}) + x_1 a(\sqrt{\omega_1} - \sqrt{\omega_2}))}{(\exp(-x_1 a\sqrt{\omega_u}) - \exp(-x_1 a\sqrt{\omega_1}) + x_1 a(\sqrt{\omega_u} - \sqrt{\omega_1}))}$$
$$+ \frac{2 V_{\text{MBNorigin}_2}}{a^2} \left(\frac{1}{x_2} (\exp(-ax_2\sqrt{\omega_1}) - \exp(-ax_2\sqrt{\omega_2})) \right.$$
$$\left. - \frac{1}{x_1} (\exp(-ax_1\sqrt{\omega_1}) - \exp(-ax_1\sqrt{\omega_2})) \right). \quad (21)$$

Therefore, the unattenuated Barkhausen emissions occurring inside layer 2 of the sample $V_{\text{MBNorigin}_2}$ can be expressed in terms of the two Barkhausen noise voltages measured at the surface $V_{\text{MBNmeas}}(0, x_2, \omega_2, \omega_u)$ and $V_{\text{MBNmeas}}(0, x_1, \omega_1, \omega_u)$, as shown in (22), at the top of the next page, and therefore (23), also shown at the top of the next page.

In [8], an exact analytic expression for the variation of V_{MBN} amplitude with stress was derived

$$\frac{1}{[V_{\text{MBN}}(0)]} - \frac{1}{[V_{\text{MBN}}(\sigma)]} = \frac{3 b' \sigma}{\mu_0} \quad (24)$$

where $V_{\text{MBN}}(0)$ is the MBN amplitude for zero stress, $V_{\text{MBN}}(\sigma)$ is the MBN amplitude for a given stress σ, μ_0 is the permeability of free space, σ is the mechanical stress and b' is a coefficient relating magnetostriction λ to magnetization M. It follows that:

$$\frac{1}{[V_{\text{MBN}}(\sigma_2)]} - \frac{1}{[V_{\text{MBN}}(\sigma_1)]} = \frac{3 b' (\sigma_1 - \sigma_2)}{\mu_0}. \quad (25)$$

By combining equations (8), (23), and (25) the differences in stress between the two layers can be calculated from (26), shown at the top of the next page [before that, however, here we need to relate $V_{\text{MBN}}(\sigma)$ of (25) with $V_{\text{MBNorigin}}$ of (8) and (23)].

III. PRACTICAL IMPLEMENTATION

The MBN measurement set-up required for stress depth profiling should comprise the following components.

1) A magnetizing unit in a form of U-shape yoke with wound coil energized by low-frequency current to ensure uniform magnetization within the investigated depth range of the specimen.
2) An MBN sensing probe with linear characteristic which can be induction sensor, Hall probe, or any other suitable type of magnetic sensor. When an induction sensor is used it should have its resonant frequency outside the analyzed MBN frequency range.
3) A data acquisition card with high-sampling frequency and postprocessing software containing a filter for extracting MBN data within various ranges of frequency.

In the initial experimental stage the values of $V_{\text{MBNorigin}_1}$ for the first layers of two reference specimens with known but different stress states need to be measured. This can be done by correlating the stress obtained from X-ray diffraction (XRD) with the $V_{\text{MBNorigin}_1}$ calculated from (18) where the low-frequency limit ω_1 should correspond to the XRD penetration depth.

$$V_{\text{MBNorigin}_2} = \frac{a^2}{2} \frac{V_{\text{MBNmeas}}(0, x_2, \omega_2, \omega_u) - V_{\text{MBNmeas}}(0, x_1, \omega_1, \omega_u)\left(1 + \frac{(\exp(-x_1 a\sqrt{\omega_1}) - \exp(-x_1 a\sqrt{\omega_2}) + x_1 a(\sqrt{\omega_1} - \sqrt{\omega_2}))}{(\exp(-x_1 a\sqrt{\omega_u}) - \exp(-x_1 a\sqrt{\omega_1}) + x_1 a(\sqrt{\omega_u} - \sqrt{\omega_1}))}\right)}{\frac{1}{x_2}(\exp(-a x_2\sqrt{\omega_1}) - \exp(-a x_2\sqrt{\omega_2})) - \frac{1}{x_1}(\exp(-a x_1\sqrt{\omega_1}) - \exp(-a x_1\sqrt{\omega_2}))} \quad (22)$$

$$\frac{1}{V_{\text{MBNorigin}_2}} = \frac{2}{a^2} \frac{\left(\frac{1}{x_2}(\exp(-a x_2\sqrt{\omega_1}) - \exp(-a x_2\sqrt{\omega_2})) - \frac{1}{x_1}(\exp(-a x_1\sqrt{\omega_1}) - \exp(-a x_1\sqrt{\omega_2}))\right)}{V_{\text{MBNmeas}}(0, x_2, \omega_2, \omega_u) - V_{\text{MBNmeas}}(0, x_1, \omega_1, \omega_u)\left(1 + \frac{(\exp(-x_1 a\sqrt{\omega_1}) - \exp(-x_1 a\sqrt{\omega_2}) + x_1 a(\sqrt{\omega_1} - \sqrt{\omega_2}))}{(\exp(-x_1 a\sqrt{\omega_u}) - \exp(-x_1 a\sqrt{\omega_1}) + x_1 a(\sqrt{\omega_u} - \sqrt{\omega_1}))}\right)}. \quad (23)$$

$$\sigma_1 - \sigma_2 = \frac{\mu_0}{3b'} \frac{2}{a^2}\left[\frac{\left(\frac{1}{x_2}(\exp(-a x_2\sqrt{\omega_1}) - \exp(-a x_2\sqrt{\omega_2})) - \frac{1}{x_1}(\exp(-a x_1\sqrt{\omega_1}) - \exp(-a x_1\sqrt{\omega_2}))\right)}{V_{\text{MBNmeas}}(0, x_2, \omega_2, \omega_u) - V_{\text{MBNmeas}}(0, x_1, \omega_1, \omega_u) * \left(1 + \frac{(\exp(-x_1 a\sqrt{\omega_1}) - \exp(-x_1 a\sqrt{\omega_2}) + x_1 a(\sqrt{\omega_1} - \sqrt{\omega_2}))}{(\exp(-x_1 a\sqrt{\omega_u}) - \exp(-x_1 a\sqrt{\omega_1}) + x_1 a(\sqrt{\omega_u} - \sqrt{\omega_1}))}\right)}\right]$$
$$- \frac{\mu_0}{3b'} \frac{2}{a^2}\left[\frac{\frac{1}{x_1}\left(\exp(-x_1 a\sqrt{\omega_u}) - \exp(-x_1 a\sqrt{\omega_1}) + x_1 a(\sqrt{\omega_u} - \sqrt{\omega_1})\right)}{V_{\text{MBNmeas}}(0, x_1, \omega_1, \omega_u)}\right] \quad (26)$$

The established quantitative relation for first layer can be further used to determine the stress in the second layer as the functions $1/V_{\text{MBNorigin}_1}(\sigma_1)$ and $1/V_{\text{MBNorigin}_2}(\sigma_2)$ are analogous.

IV. CONCLUSION

A new comprehensive method has been developed for determining depth profiles of properties, such as residual stress using MBN measurements. The underlying equations involve knowledge of the stress dependence of MBN amplitude and in addition knowledge of the attenuation of the original MBN signal.

The complete set of equations has been derived for the first time here in this paper, and for the purposes of demonstration a particular case has been presented in which the stress is uniform in each of two layers, but different from one layer to the next. The proposed practical implementation, utilizing the developed equations, can be used for determining the variation of stress with depth in magnetic materials with the information being extracted from the frequency dependence of the detected Barkhausen signals.

REFERENCES

[1] W. A. Theiner and I. Altpeter, "Determination of residual stresses using micromagnetic parameters," in *New Procedures in NDT*, P. Holler, Ed. New York, NY, USA: Spinger, 1983, pp. 575–585.

[2] M. J. Sablik, "A Model for the Barkhausen noise power as a function of applied magnetic field and stress," *J. Appl. Phys.*, vol. 74, no. 9, pp. 5898–5900, 1993.

[3] R. Ranjan, D. C. Jiles, O. Buck, and R. B. Thompson, "Grain-size measurement using magnetic and acoustic Barkhausen noise," *J. Appl. Phys.*, vol. 61, no. 8, pp. 3199–3202, 1987.

[4] G. Bach, K. Goebbels, and W. A. Theiner, "Characterization of hardening depth using Barkhausen noise measurement," *Mater. Eval.*, vol. 46, pp. 1576–1580, Sep. 1988.

[5] E. R. Kinser, C. C. H. Lo, A. J. Barsic, and D. C. Jiles, "Modeling microstructural effects on Barkhausen emission in surface-modified magnetic materials," *IEEE Trans. Magn.*, vol. 41, no. 10, pp. 3292–3294, Oct. 2005.

[6] C. C. H. Lo, S. J. Lee, L. Li, L. C. Kerdus, and D. C. Jiles, "Modeling stress effects on magnetic hysteresis and Barkhausen emission using a hysteretic-stochastic model," *IEEE Trans. Magn.*, vol. 38, no. 5, pp. 2418–2420, Sep. 2002.

[7] S. Tiitto and S. Saynajakangas, "Spectral damping in Barkhausen noise," *IEEE Trans. Magn.*, vol. 11, no. 6, pp. 1666–1672, Nov. 1975.

[8] L. Mierczak, D. C. Jiles, and G. Fantoni, "A new method for evaluation of mechanical stress using the reciprocal amplitude of magnetic Barkhausen noise," *IEEE Trans. Magn.*, vol. 47, no. 2, pp. 459–465, Feb. 2011.